THESIS FOR THE DEGREE OF DOCTOR OF PHILOSOPHY

Analysis, Modeling and Control of Doubly-Fed Induction Generators for Wind Turbines

ANDREAS PETERSSON

Division of Electric Power Engineering
Department of Energy and Environment
CHALMERS UNIVERSITY OF TECHNOLOGY
Göteborg, Sweden 2005

Analysis, Modeling and Control of Doubly-Fed Induction Generators for Wind Turbines
ANDREAS PETERSSON
ISBN 91-7291-600-1

Doktorsavhandlingar vid Chalmers tekniska högskola
Ny serie nr. 2282
ISSN 0346-718x

Division of Electric Power Engineering
Department of Energy and Environment
Chalmers University of Technology
SE-412 96 Göteborg
Sweden
Telephone + 46 (0)31-772 1000

Chalmers Bibliotek, Reproservice
Göteborg, Sweden 2005

Analysis, Modeling and Control of Doubly-Fed Induction Generators for Wind Turbines
ANDREAS PETERSSON
Division of Electric Power Engineering
Department of Energy and Environment
Chalmers University of Technology

Abstract

This thesis deals with the analysis, modeling, and control of the doubly-fed induction generator (DFIG) for wind turbines. Different rotor current control methods are investigated with the objective of eliminating the influence of the back electromotive force (EMF), which is that of, in control terminology, a load disturbance, on the rotor current. It is found that the method that utilizes both feed forward of the back EMF and so-called "active resistance" manages best to suppress the influence of the back EMF on the rotor current, particularly when voltage sags occur, of the investigated methods. This method also has the best stability properties. In addition it is found that this method also has the best robustness to parameter deviations.

The response of the DFIG wind turbine system to grid disturbances is simulated and verified experimentally. A voltage sag to 80% (80% remaining voltage) is handled very well. Moreover, a second-order model for prediction of the response of small voltage sags of the DFIG wind turbines is derived, and its simulated performance is successfully verified experimentally.

The energy production of the DFIG wind turbine is investigated and compared to that of other wind turbine systems. The result found is that the energy capture of the DFIG wind turbine is almost the same as for an active stall-controlled fixed-speed (using two fixed speeds) wind turbine. Compared to a full-power-converter wind turbine the DFIG wind turbine can deliver a couple of percentage units more energy to the grid.

Voltage sag ride-through capabilities of some different variable-speed wind turbines has been investigated. It has been found that the energy production cost of the investigated wind turbines with voltage sag ride-through capabilities is between 1–3 percentage units higher than that of the ordinary DFIG wind turbine without the ride-through capability.

Finally, a flicker reduction control law for stall-controlled wind turbines with induction generators, using variable rotor resistance, is derived. The finding is that it is possible to reduce the flicker contribution by utilizing the derived rotor resistance control law with 40–80% depending on the operating condition.

Keywords: Doubly-fed induction generator, wind turbine, wind energy, current control, voltage sag, power quality.

Acknowledgements

This research project has been carried out at the Department of Energy and Environment (and the former Department of Electric Power Engineering) at Chalmers University of Technology. The financial support provided by the Swedish National Energy Agency is gratefully acknowledged.

I would like to thank my supervisors Dr. Torbjörn Thiringer and Prof. Lennart Harnefors for help, inspiration, and encouragement. I would also like to thank my examiner Prof. Tore Undeland for valuable comments and encouragement. Thanks goes to my fellow Ph.D. students who have assisted me: Stefan Lundberg for a pleasant collaboration with the efficiency calculations, Dr. Rolf Ottersten for many interesting discussions and a nice cooperation, especially with the analysis of the full-power converter, Dr. Tomáš Petrů for valuable and time saving collaboration with practical field measurement set-ups, and Oskar Wallmark for a good companionship and valuable discussions.

Many thanks go to the colleagues at the Division of Electric Power Engineering and the former Department of Electric Power Engineering, who have assisted me during the work of this Ph.D. thesis.

Finally, I would like to thank my family for their love and support.

Table of Contents

Chapter 1

Introduction

The Swedish Parliament adopted new energy guidelines in 1997 following the trend of moving towards an ecologically sustainable society. The energy policy decision states that the objective is to facilitate a change to an ecologically sustainable energy production system. The decision also confirmed that the 1980 and 1991 guidelines still apply, i.e., that the nuclear power production is to be phased out at a slow rate so that the need for electrical energy can be met without risking employment and welfare. The first nuclear reactor of Barsebäck was shut down 30th of November 1999. Nuclear power production shall be replaced by improving the efficiency of electricity use, conversion to renewable forms of energy and other environmentally acceptable electricity production technologies [97]. According to [97] wind power can contribute to fulfilling several of the national environmental quality objectives decided by Parliament in 1991. Continued expansion of wind power is therefore of strategic importance. The Swedish National Energy Agency suggest that the planning objectives for the expansion of wind power should be 10 TWh/year within the next 10–15 years [97]. In Sweden, by the end of 2004, there was 442 MW of installed wind power, corresponding to 1% of the total installed electric power in the Swedish grid [23, 98]. These wind turbines produced 0.8 TWh of electrical energy in 2004, corresponding to approximately 0.5% of the total generated and imported electrical energy [23, 98].

Wind turbines (WTs) can either operate at fixed speed or variable speed. For a fixed-speed wind turbine the generator is directly connected to the electrical grid. For a variable-speed wind turbine the generator is controlled by power electronic equipment. There are several reasons for using variable-speed operation of wind turbines; among those are possibilities to reduce stresses of the mechanical structure, acoustic noise reduction and the possibility to control active and reactive power [11]. Most of the major wind turbine manufactures are developing new larger wind turbines in the 3-to-5-MW range [3]. These large wind turbines are all based on variable-speed operation with pitch control using a direct-driven synchronous generator (without gearbox) or a doubly-fed induction generator (DFIG). Fixed-speed induction generators with stall control are regarded as unfeasible [3] for these large wind turbines. Today, doubly-fed induction generators are commonly used by the wind turbine industry (year 2005) for larger wind turbines [19, 29, 73, 105].

The major advantage of the doubly-fed induction generator, which has made it popular, is that the power electronic equipment only has to handle a fraction (20–30%) of the total system power [36, 68, 110]. This means that the losses in the power electronic equipment can

be reduced in comparison to power electronic equipment that has to handle the total system power as for a direct-driven synchronous generator, apart from the cost saving of using a smaller converter.

1.1 Review of Related Research

According to [12] the energy production can be increased by 2–6% for a variable-speed wind turbine in comparison to a fixed-speed wind turbine, while in [112] it is stated that the increase in energy can be 39%. In [69] it is shown that the gain in energy generation of the variable-speed wind turbine compared to the most simple fixed-speed wind turbine can vary between 3–28% depending on the site conditions and design parameters. Efficiency calculations of the DFIG system have been presented in several papers, for instance [52, 86, 99]. A comparison to other electrical systems for wind turbines are, however, harder to find. One exception is in [16], where Datta *et al.* have made a comparison of the energy capture for various WT systems. According to [16] the energy capture can be significantly increased by using a DFIG. They state an increased energy capture of a DFIG by over 20% with respect to a variable-speed system using a cage-bar induction machine and by over 60% in comparison to a fixed-speed system. One of the reasons for the various results is that the assumptions used vary from investigation to investigation. Factors such as speed control of variable-speed WTs, blade design, what kind of power that should be used as a common basis for comparison, selection of maximum speed of the WT, selected blade profile, missing facts regarding the base assumptions etc, affect the outcome of the investigations. There is thus a need to clarify what kind of energy capture gain there could be when using a DFIG WT, both compared to another variable-speed WT and towards a traditional fixed-speed WT.

Control of the DFIG is more complicated than the control of a standard induction machine. In order to control the DFIG the rotor current is controlled by a power electronic converter. One common way of controlling the rotor current is by means of field-oriented (vector) control. Several vector control schemes for the DFIG have been proposed. One common way is to control the rotor current with stator-flux orientation [46, 61, 80, 99], or with air-gap-flux orientation [107, 110]. If the stator resistance can be considered small, stator-flux orientation gives in principle orientation also with the stator voltage (grid-flux orientation) [17, 61, 68]. Wang *et al.* [107] have by simulations found that the flux is influenced both by load changes and stator power supply variations. The flux response to a disturbance is a damped oscillation. Heller *et al.* [43] and Congwei *et al.* [13] have investigated the stability of the DFIG analytically, showing that the dynamics of the DFIG have poorly damped eigenvalues (poles) with a corresponding natural frequency near the line frequency, and, also, that the system is unstable for certain operating conditions, at least for a stator-flux-oriented system. These poorly damped poles influence the rotor current dynamics through the back electromotive force (EMF). The author has, however, not found in the literature any evaluation of the performance of different rotor current control laws with respect to eliminating the influence of the back EMF, which is dependent on the stator voltage, rotor speed, and stator flux, in the rotor current.

The flux oscillations can be damped in some different ways. One method is to reduce the bandwidth of the current controllers [43]. Wang *et al.* [107] have introduced a flux differentiation compensation that improves the damping of the flux. Kelber *et al.* [54] have used

another possibility; to use an extra (third) converter that substitutes the Y point of the stator winding, i.e., an extra degree of freedom is introduced that can be used to actively damp the flux oscillations. Kelber has in [55] made a comparison of different methods of damping the flux oscillations. It was found that the methods with a flux differentiation compensation and the method with an extra converter manage to damp the oscillations best.

The response of wind turbines to grid disturbances is an important issue, especially since the rated power of wind-turbine installations steadily increases. Therefore, it is important for utilities to be able to study the effects of various voltage sags and, for instance, the corresponding wind turbine response. For calculations made using grid simulation programs, it is of importance to have as simple models as possible that still manage to model the dynamics of interest. In [22, 26, 60, 84], a third-order model has been proposed that neglects the stator-flux dynamics of the DFIG. This model gives a correct mean value [22] but a drawback is that some of the main dynamics of the DFIG system are also neglected. In order to preserve the dynamic behavior of the DFIG system, a slightly different model approach must be made. As described earlier a dominating feature of the DFIG system is the natural frequency of the flux dynamics, which is close to the line frequency. Since the dynamics of the DFIG are influenced by two poorly damped eigenvalues (poles) it would be natural to reduce the model of the DFIG to the flux dynamics described by a second-order model. This is a common way to reduce the DFIG model in classical control theory stability analysis [13, 43]. The possibility to use it as simulation model remains to be shown. In order to preserve the behavior of an oscillatory response, it is obvious that a second-order model is the simplest that can be used.

New grid codes will require WTs and wind farms to ride through voltage sags, meaning that normal power production should be re-initiated once the nominal grid voltage has been recovered. Such codes are in progress both in Sweden [96] and in several other countries [8]. These grid codes will influence the choice of electrical system in future WTs, which has initiated industrial research efforts [8, 20, 28, 30, 42, 72] in order to comply. Today, the DFIG WT will be disconnected from the grid when large voltage sags appear in the grid. After the DFIG WT has been disconnected, it takes some time before the turbine is reconnected to the grid. This means that new WTs have to ride through these voltage sags. The DFIG system, of today, has a crowbar in the rotor circuit, which at large grid disturbances has to short circuit the rotor circuit in order to protect the converter. This leads to that the turbine must be disconnected from the grid, after a large voltage sag.

In the literature there are some different methods to modify the DFIG system in order to accomplish voltage sag ride-through proposed. In [20] anti-parallel thyristors is used in the stator circuit in order to achieve a quick (within 10 ms) disconnection of the stator circuit, and thereby be able to remagnetize the generator and reconnect the stator to the grid as fast as possible. Another option proposed in [72] is to use an “active” crowbar, which can break the short circuit current in the crowbar. A third method, that has been mentioned earlier, is to use an additional converter to substitute the Y point of the stator circuit [54, 55]. In [55], Kelber has shown that such a system can effectively damp the flux oscillations caused by voltage sags. All of these systems have different dynamical performance. Moreover, the efficiency and cost of the different voltage sag ride-through system might also influence the choice of system. Therefore, when modifying the DFIG system for voltage sag ride-

through it is necessary to evaluate consequences for cost and efficiency. Any evaluation of different voltage sag ride-through methods for DFIG wind turbines and how they affect the efficiency is hard to find in the literature. Consequences for the efficiency is an important issue since, as mentioned earlier, one of the main advantage with the DFIG system was that losses of the power electronic equipment is reduced in comparison to a system where the power electronic equipment has to handle the total power. Moreover, it is necessary to compare the ride-through system with a system that utilizes a full-power converter, since such a system can be considered to have excellent voltage sag ride-through performance (as also will be shown in Chapter 7) [74].

1.2 Purpose and Contributions

The main purpose of this thesis is the analysis of the DFIG for a WT application both during steady-state operation and transient operation. In order to analyze the DFIG during transient operation both the control and the modeling of the system is of importance. Hence, the control and the modeling are also important parts of the thesis. The main contribution of this thesis is dynamic and steady-state analysis of the DFIG, with details being as follows.

- In Chapter 3 an investigation of the influence of the converter's size on the energy production for a DFIG system is analyzed. A smaller converter implies that the converter losses will be lower. On the other hand it also implies a smaller variable-speed range, which influences the aerodynamical efficiency. Further, in Chapter 3, a comparison of the energy efficiency of DFIG system to other electrical systems is presented. The investigated systems are two fixed-speed induction generator systems and three variable-speed systems. The variable-speed systems are: a doubly-fed induction generator, an induction generator (with a full-power converter) and a direct-driven permanent-magnet synchronous generator system. Important electrical and mechanical losses of the systems are included in the study. In order to make the comparison as fair as possible the base assumption used in this work is that the maximum (average) shaft torque of the wind turbine systems used should be the same. Finally, two different methods of reducing the magnetizing losses of the DFIG system are compared.

- In Chapter 4 a general rotor current control law is derived for the DFIG system. Terms are introduced in order to allow the possibility to include feed-forward compensation of the back EMF and/or "active resistance." "Active resistance" has been used for the squirrel-cage induction machines to damp disturbances, such as varying back EMF [18, 41]. The main contribution of Chapter 5 is an evaluation of different rotor current control laws with respect to eliminating the influence of the back EMF. Stability analysis of the system is performed for different combinations of the terms introduced in the current control law, in both the stator-flux-oriented and the grid-flux-oriented reference frames, for both correctly and erroneously known parameters.

- In Chapter 6, the grid-fault response of a DFIG wind turbine system is studied. Simulations are verified with experimental results. Moreover, another objective is also to study how a reduced-order (second-order) model manages to predict the response of the DFIG system.

- The contribution of Chapter 7 is to analyze, dynamically and in the steady state, two different voltage sag ride-through systems for the DFIG. Moreover, these two methods are also compared to a system that utilizes a full-power converter. The reason for comparing these two systems with a system that utilizes a full-power converter is that the latter system is capable of voltage sag ride-through.
- Finally, in Chapter 8, a rotor resistance control law for a stall-controlled wind turbine is derived and analyzed. The objective of the control law is to minimize torque fluctuations and flicker.

1.3 List of Publications

Some of the results presented in this thesis have been published in the following publications.

1. A. Petersson and S. Lundberg, "Energy efficiency comparison of electrical systems for wind turbines," in *Proc. IEEE Nordic Workshop on Power and Industrial Electronics (NORpie/2002)*, Stockholm, Sweden, Aug. 12–14, 2002.

   The efficiency of some different electrical systems for wind turbines are compared. This paper is an early version of the material presented in Chapter 3.

2. T. Thiringer, A. Petersson, and T. Petrů, "Grid Disturbance Response of Wind Turbines Equipped with Induction Generator and Doubly-Fed Induction Generator," in *Proc. IEEE Power Engineering Society General Meeting*, vol. 3, Toronto, Canada, July 13–17, 2003, pp. 1542–1547.

   The grid disturbance response to fixed-speed wind turbines and wind turbines with DFIG were presented.

3. A. Petersson, S. Lundberg, and T. Thiringer, "A DFIG Wind-Turbine Ride-Through System Influence on the Energy Production," in *Proc. Nordic Wind Power Conference*, Göteborg, Sweden, Mar. 1–2, 2004.

   In this paper a voltage sag ride-through system for a DFIG WT based on increased rating of the valves of the power electronic converter was investigated. This paper presents one of the voltage sag ride-through system for a DFIG wind turbine that is compared in Chapter 7.

   The organizing committee of the conference recommended submission of this paper to *Wind Energy*. The paper has been accepted for publication.

4. A. Petersson, T. Thiringer, and L. Harnefors, "Flicker Reduction of Stall-Controlled Wind Turbines using Variable Rotor Resistances," in *Proc. Nordic Wind Power Conference*, Göteborg, Sweden, Mar. 1–2, 2004.

   In this paper a rotor resistance control law is derived for a stall-controlled wind turbine. The objective of the control law is to minimize the flicker (or voltage fluctuations) contribution. This study is presented in Chapter 8.

5. T. Thiringer and A. Petersson, "Grid Integration of Wind Turbines," *Przeglad Elektrotechniczny*, no. 5, pp. 470–475, 2004.

   This paper gives an overview of the three most common wind turbine systems, their power quality impact, and its the response to grid disturbances.

6. R. Ottersten, A. Petersson, and K. Pietiläinen, "Voltage Sag Response of PWM Rectifiers for Variable-Speed Wind Turbines," in *Proc. IEEE Nordic Workshop on Power and Industrial Electronics (NORpie/2004)*, Trondheim, Norway, June 14–16, 2004.

   The voltage sag response of a PWM rectifier for wind turbines that utilizes a full-power converter were studied. This paper serves as a basis for the comparison of ride-through systems of wind turbines in Chapter 7.

   The organizing committee of the conference recommended submission of this paper to *EPE Journal*. The paper has been accepted for publication.

7. A. Petersson, L. Harnefors, and T. Thiringer, "Comparison Between Stator-Flux and Grid-Flux Oriented Rotor-Current Control of Doubly-Fed Induction Generators," in *Proc. IEEE Power Electronics Specialists Conference (PESC'04)*, vol. 1, Aachen, Germany, June 20–25, 2004, pp. 482–486.

   The comparison between grid-flux and stator-flux-oriented current control of the DFIG presented in Chapter 5 were studied in this paper.

8. A. Petersson, L. Harnefors, and T. Thiringer, "Evaluation of Current Control Methods for Wind Turbines Using Doubly-Fed Induction Machines," *IEEE Trans. Power Electron.,* vol. 20, no. 1, pp. 227–235, Jan. 2005.

   In this paper the analysis of the stator-flux oriented current control of the DFIG presented in Chapter 5 was studied.

9. A. Petersson, T. Thiringer, L. Harnefors, and T. Petrů, "Modeling and Experimental Verification of Grid Interaction of a DFIG Wind Turbine," *IEEE Trans. Energy Conversion* (accepted for publication)

   Here a full-order model and a reduced-order model of the DFIG is compared during grid disturbances. The models are experimentally verified with an 850 kW DFIG wind turbine. These results are also presented in Chapter 6.

Chapter 2

Wind Energy Systems

2.1 Wind Energy Conversion

In this section, properties of the wind, which are of interest in this thesis, will be described. First the wind distribution, i.e., the probability of a certain average wind speed, will be presented. The wind distribution can be used to determine the expected value of certain quantities, e.g. produced power. Then different methods to control the aerodynamic power will be described. Finally, the aerodynamic conversion, i.e., the so-called $C_p(\lambda, \beta)$-curve, will be presented. The interested reader can find more information in, for example, [11, 53].

2.1.1 Wind Distribution

The most commonly used probability density function to describe the wind speed is the Weibull functions [53]. The Weibull distribution is described by the following probability density function

$$f(w) = \frac{k}{c}\Big(\frac{w}{c}\Big)^{k-1} e^{-(w/c)^k} \tag{2.1}$$

where k is a shape parameter, c is a scale parameter and w is the wind speed. Thus, the average wind speed (or the expected wind speed), $\overline{w}$, can be calculated from

$$\overline{w} = \int_0^\infty w f(w) dw = \frac{c}{k}\Gamma\Big(\frac{1}{k}\Big) \tag{2.2}$$

where Γ is Euler's gamma function, i.e.,

$$\Gamma(z) = \int_0^\infty t^{z-1} e^{-t} dt. \tag{2.3}$$

If the shape parameter equals 2, the Weibull distribution is known as the Rayleigh distribution. For the Rayleigh distribution the scale factor, c, given the average wind speed can be found from (k=2, and $\Gamma(\frac{1}{2}) = \sqrt{\pi}$)

$$c = \frac{2}{\sqrt{\pi}}\overline{w}. \tag{2.4}$$

In Fig. 2.1, the wind speed probability density function of the Rayleigh distribution is plotted. The average wind speeds in the figure are 5.4 m/s, 6.8 m/s, and 8.2 m/s. A wind speed of 5.4 m/s correspond to a medium wind speed site in Sweden [100], while 8–9 m/s are wind speeds available at sites located outside the Danish west coast [24].

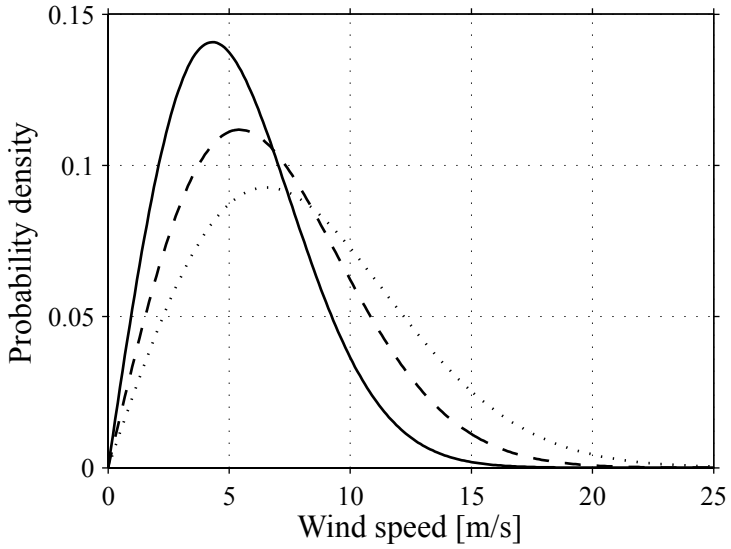

Fig. 2.1. Probability density of the Rayleigh distribution. The average wind speeds are 5.4 m/s (solid), 6.8 m/s (dashed) and 8.2 m/s (dotted).

2.1.2 Aerodynamic Power Control

At high wind speeds it is necessary to limit the input power to the wind turbine, i.e., aerodynamic power control. There are three major ways of performing the aerodynamic power control, i.e., by stall, pitch, or active stall control. Stall control implies that the blades are designed to stall in high wind speeds and no pitch mechanism is thus required [11].

Pitch control is the most common method of controlling the aerodynamic power generated by a turbine rotor, for newer larger wind turbines. Almost all variable-speed wind turbines use pitch control. Below rated wind speed the turbine should produce as much power as possible, i.e., using a pitch angle that maximizes the energy capture. Above rated wind speed the pitch angle is controlled in such a way that the aerodynamic power is at its rated [11]. In order to limit the aerodynamic power, at high wind speeds, the pitch angle is controlled to decrease the angle of attack, i.e., the angle between the chord line of the blade and the relative wind direction [53]. It is also possible to increase the angle of attack towards stall in order to limit the aerodynamic power. This method can be used to fine-tune the power level at high wind speeds for fixed-speed wind turbines. This control method is known as *active stall* or *combi stall* [11].

2.1.3 Aerodynamic Conversion

Some of the available power in the wind is converted by the rotor blades to mechanical power acting on the rotor shaft of the WT. For steady-state calculations of the mechanical power from a wind turbine, the so called $C_p(\lambda, \beta)$-curve can be used. The mechanical power, P_{mech}, can be determined by [53]

$$P_{\text{mech}} = \frac{1}{2}\rho A_r C_p(\lambda, \beta) w^3 \tag{2.5}$$

$$\lambda = \frac{\Omega_r r_r}{w} \tag{2.6}$$

where C_p is the power coefficient, β is the pitch angle, λ is the tip speed ratio, w is the wind speed, Ω_r is the rotor speed (on the low-speed side of the gearbox), r_r is the rotor-plane radius, ρ is the air density and A_r is the area swept by the rotor. In Fig. 2.2, an example of a $C_p(\lambda, \beta)$ curve and the shaft power as a function of the wind speed for rated rotor speed, i.e., a fixed-speed wind turbine, can be seen. In Fig. 2.2b) the solid line corresponds to a fixed

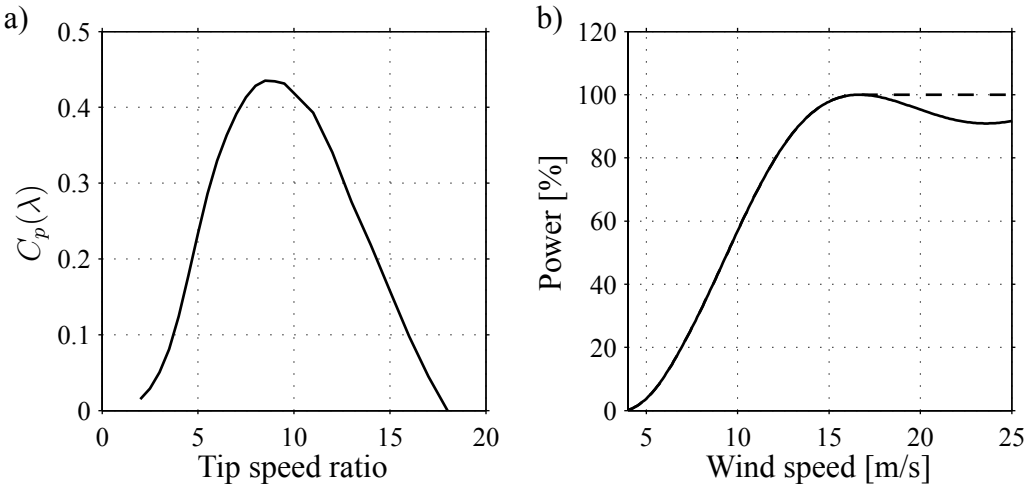

Fig. 2.2. a) The power coefficient, C_p, as a function of the tip speed ratio, λ. b) Mechanical power as a function of wind speed at rated rotor speed (solid line is fixed pitch angle, i.e., stall control and dashed line is active stall).

pitch angle, β, while dashed line corresponds to a varying β (active stall).

Fig. 2.3 shows an example of how the mechanical power, derived from the $C_p(\lambda, \beta)$ curve, and the rotor speed vary with the wind speed for a variable-speed wind turbine. The rotor speed in the variable-speed area is controlled in order to keep the optimal tip speed ratio, λ, i.e., C_p is kept at maximum as long as the power or rotor speed is below its rated values. As mentioned before, the pitch angle is at higher wind speeds controlled in order to limit the input power to the wind turbine, when the turbine has reached the rated power. As seen in Fig. 2.3b) the turbine in this example reaches the rated power, 1 p.u., at a wind speed of approximately 13 m/s. Note that there is a possibility to optimize the radius of the wind turbines rotor to suit sites with different average wind speeds. For example, if the rotor radius, r_r, is increased, the output power of the turbine is also increased, according to (2.5). This implies that the nominal power will be reached for a lower wind speed, referred to Fig. 2.3b). However, increasing the rotor radius implies that for higher wind speed the output power must be even more limited, e.g., by pitch control, so that the nominal power of the generator is not exceeded. Therefore, there is a trade-off between the rotor radius and the nominal power of the generator. This choice is to a high extent dependent on the average wind speed of the site.

2.2 Wind Turbine Systems

Wind turbines can operate with either fixed speed (actually within a speed range about 1 %) or variable speed. For fixed-speed wind turbines, the generator (induction generator) is di-

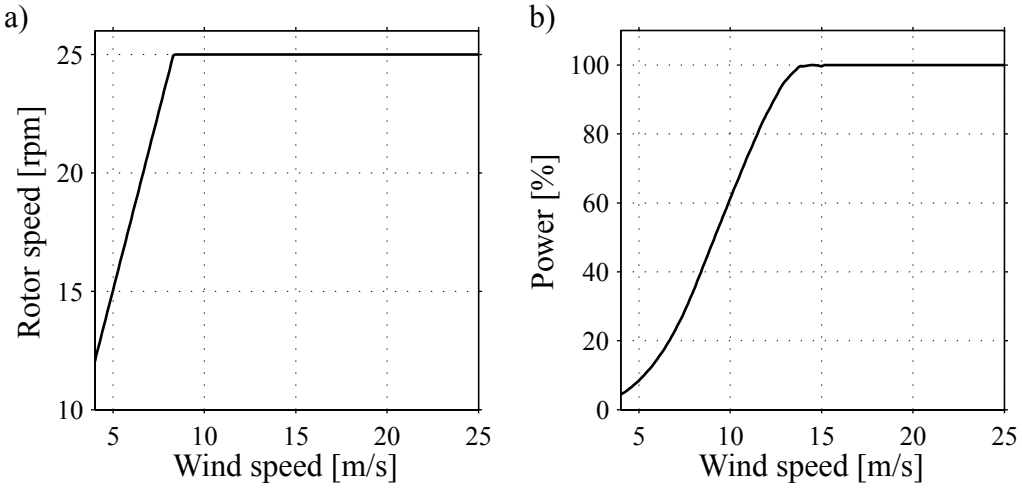

Fig. 2.3. Typical characteristic for a variable-speed wind turbine. a) Rotor speed as a function of wind speed. b) Mechanical power as a function of wind speed.

rectly connected to the grid. Since the speed is almost fixed to the grid frequency, and most certainly not controllable, it is not possible to store the turbulence of the wind in form of rotational energy. Therefore, for a fixed-speed system the turbulence of the wind will result in power variations, and thus affect the power quality of the grid [77]. For a variable-speed wind turbine the generator is controlled by power electronic equipment, which makes it possible to control the rotor speed. In this way the power fluctuations caused by wind variations can be more or less absorbed by changing the rotor speed [82] and thus power variations originating from the wind conversion and the drive train can be reduced. Hence, the power quality impact caused by the wind turbine can be improved compared to a fixed-speed turbine [58].

The rotational speed of a wind turbine is fairly low and must therefore be adjusted to the electrical frequency. This can be done in two ways: with a gearbox or with the number of pole pairs of the generator. The number of pole pairs sets the mechanical speed of the generator with respect to the electrical frequency and the gearbox adjusts the rotor speed of the turbine to the mechanical speed of the generator.

In this section the following wind turbine systems will be presented:

1. Fixed-speed wind turbine with an induction generator.

2. Variable-speed wind turbine equipped with a cage-bar induction generator or synchronous generator.

3. Variable-speed wind turbine equipped with multiple-pole synchronous generator or multiple-pole permanent-magnet synchronous generator.

4. Variable-speed wind turbine equipped with a doubly-fed induction generator.

There are also other existing wind turbine concepts; a description of some of these systems can be found in [36].

2.2.1 Fixed-Speed Wind Turbine

For the fixed-speed wind turbine the induction generator is directly connected to the electrical grid according to Fig. 2.4. The rotor speed of the fixed-speed wind turbine is in principle

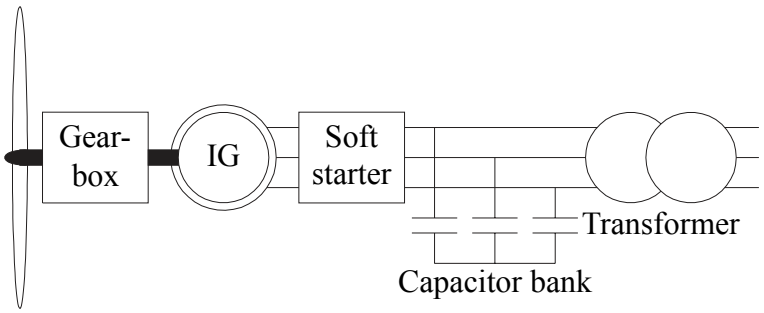

Fig. 2.4. Fixed-speed wind turbine with an induction generator.

determined by a gearbox and the pole-pair number of the generator. The fixed-speed wind turbine system has often two fixed speeds. This is accomplished by using two generators with different ratings and pole pairs, or it can be a generator with two windings having different ratings and pole pairs. This leads to increased aerodynamic capture as well as reduced magnetizing losses at low wind speeds. This system (one or two-speed) was the "conventional" concept used by many Danish manufacturers in the 1980s and 1990s [36].

2.2.2 Variable-Speed Wind Turbine

The system presented in Fig. 2.5 consists of a wind turbine equipped with a converter connected to the stator of the generator. The generator could either be a cage-bar induction

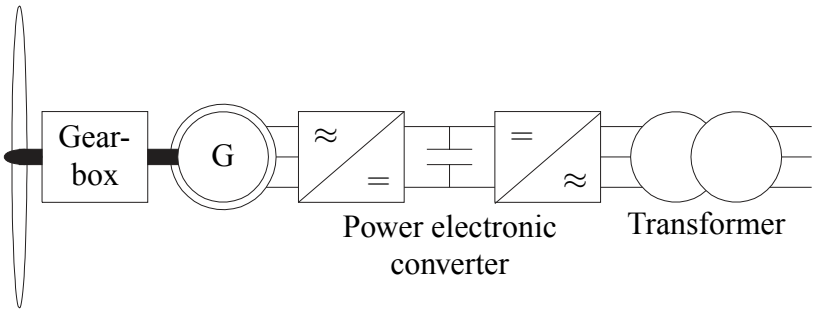

Fig. 2.5. Variable-speed wind turbine with a synchronous/induction generator.

generator or a synchronous generator. The gearbox is designed so that maximum rotor speed corresponds to rated speed of the generator. Synchronous generators or permanent-magnet synchronous generators can be designed with multiple poles which implies that there is no need for a gearbox, see Fig. 2.6. Since this "full-power" converter/generator system is commonly used for other applications, one advantage with this system is its well-developed and robust control [7, 39, 61]. A synchronous generator with multiple poles as a wind turbine generator is successfully manufactured by Enercon [25].

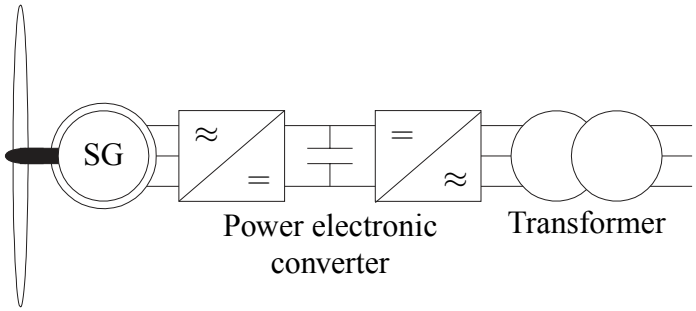

Fig. 2.6. Variable-speed direct-driven (gear-less) wind turbine with a synchronous generator (SG).

2.2.3 Variable-Speed Wind Turbine with Doubly-Fed Induction Generator

This system, see Fig. 2.7, consists of a wind turbine with doubly-fed induction generator. This means that the stator is directly connected to the grid while the rotor winding is connected via slip rings to a converter. This system have recently become very popular as gen-

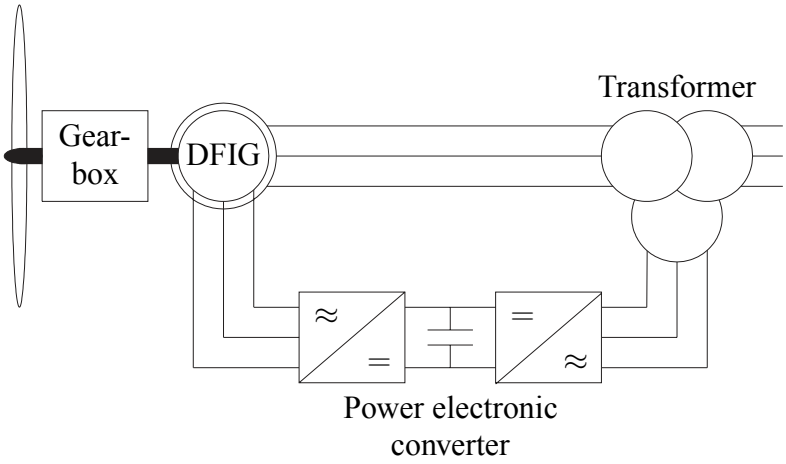

Fig. 2.7. Variable-speed wind turbine with a doubly-fed induction generator (DFIG).

erators for variable-speed wind turbines [36]. This is mainly due to the fact that the power electronic converter only has to handle a fraction (20–30%) of the total power [36, 110]. Therefore, the losses in the power electronic converter can be reduced, compared to a system where the converter has to handle the total power, see Chapter 3. In addition, the cost of the converter becomes lower.

There exists a variant of the DFIG method that uses controllable external rotor resistances (compare to slip power recovery). Some of the drawbacks of this method are that energy is unnecessary dissipated in the external rotor resistances and that it is not possible to control the reactive power.

Manufacturers, that produce wind turbines with the doubly-fed induction machine as generator are, for example, DeWind, GE Wind Energy, Nordex, and Vestas [19, 29, 73, 105].

2.3 Doubly-Fed Induction Generator Systems for Wind Turbines

For variable-speed systems with limited variable-speed range, e.g. ±30% of synchronous speed, the DFIG can be an interesting solution [61]. As mentioned earlier the reason for this is that power electronic converter only has to handle a fraction (20–30%) of the total power [36, 110]. This means that the losses in the power electronic converter can be reduced compared to a system where the converter has to handle the total power. In addition, the cost of the converter becomes lower. The stator circuit of the DFIG is connected to the grid while the rotor circuit is connected to a converter via slip rings, see Fig. 2.8. A more detailed picture

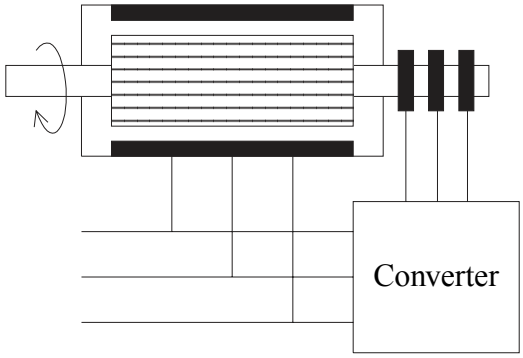

Fig. 2.8. Principle of the doubly-fed induction generator.

of the DFIG system with a back-to-back converter can be seen in Fig. 2.9. The back-to-back converter consists of two converters, i.e., machine-side converter and grid-side converter, that are connected "back-to-back." Between the two converters a dc-link capacitor is placed, as energy storage, in order to keep the voltage variations (or ripple) in the dc-link voltage small. With the machine-side converter it is possible to control the torque or the speed of

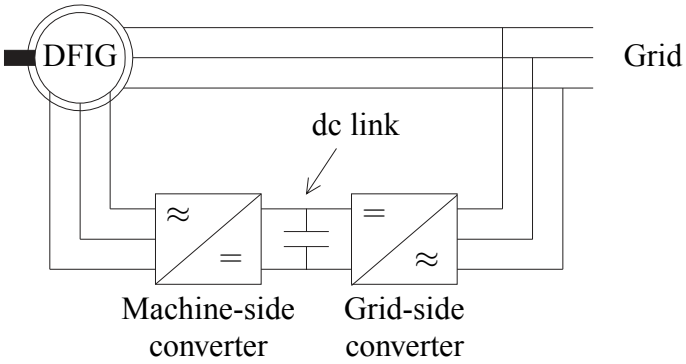

Fig. 2.9. DFIG system with a back-to-back converter.

the DFIG and also the power factor at the stator terminals, while the main objective for the grid-side converter is to keep the dc-link voltage constant. The speed–torque characteristics of the DFIG system can be seen in Fig. 2.10 [61]. As also seen in the figure, the DFIG can operate both in motor and generator operation with a rotor-speed range of $\pm\Delta\omega_r^{\max}$ around the synchronous speed, ω_1.

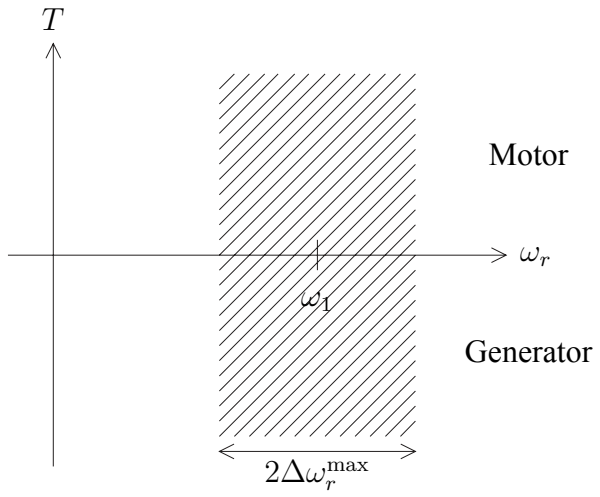

Fig. 2.10. Speed–torque characteristics of a DFIG.

A typical application, as mentioned earlier, for DFIG is wind turbines, since they operate in a limited speed range of approximately ±30%. Other applications, besides wind turbines, for the DFIG systems are, for example, flywheel energy storage system [4], stand-alone diesel systems [78], pumped storage power plants [6, 43], or rotating converters feeding a railway grid from a constant frequency public grid [61].

2.3.1 Equivalent Circuit of the Doubly-Fed Induction Generator

The equivalent circuit of the doubly-fed induction generator, with inclusion of the magnetizing losses, can be seen in Fig. 2.11. This equivalent circuit is valid for one equivalent Y phase and for steady-state calculations. In the case that the DFIG is Δ-connected the machine can still be represented by this equivalent Y representation. In this section the $j\omega$-method is adopted for calculations. Note, that if the rotor voltage, $\mathbf{V}_r$, in Fig. 2.11, is short circuited

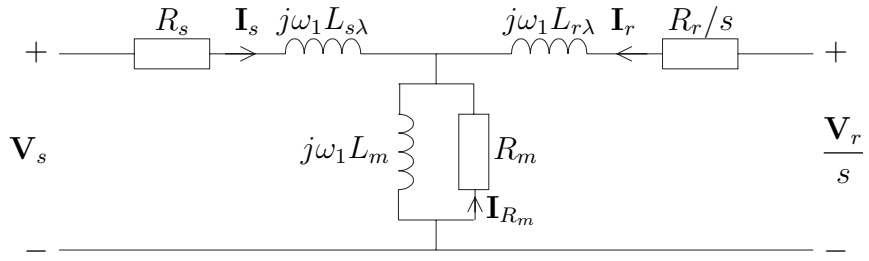

Fig. 2.11. Equivalent circuit of the DFIG.

the equivalent circuit for the DFIG becomes the ordinary equivalent circuit for a cage-bar induction machine. Applying Kirchhoff's voltage law to the circuit in Fig. 2.11 yields [87]

$$\mathbf{V}_s = R_s\mathbf{I}_s + j\omega_1 L_{s\lambda}\mathbf{I}_s + j\omega_1 L_m(\mathbf{I}_s + \mathbf{I}_r + \mathbf{I}_{R_m}) \tag{2.7}$$

$$\frac{\mathbf{V}_r}{s} = \frac{R_r}{s}\mathbf{I}_r + j\omega_1 L_{r\lambda}\mathbf{I}_r + j\omega_1 L_m(\mathbf{I}_s + \mathbf{I}_r + \mathbf{I}_{R_m}) \tag{2.8}$$

$$0 = R_m\mathbf{I}_{R_m} + j\omega_1 L_m(\mathbf{I}_s + \mathbf{I}_r + \mathbf{I}_{R_m}) \tag{2.9}$$

where the following notation is used.

$\mathbf{V}_s$	stator voltage;	R_s	stator resistance;
$\mathbf{V}_r$	rotor voltage;	R_r	rotor resistance;
$\mathbf{I}_s$	stator current;	R_m	magnetizing resistance;
$\mathbf{I}_r$	rotor current;	$L_{s\lambda}$	stator leakage inductance;
$\mathbf{I}_{R_m}$	magnetizing resistance current;	$L_{r\lambda}$	rotor leakage inductance;
ω_1	stator frequency;	L_m	magnetizing inductance;
s	slip.		

The slip, s, equals

$$s = \frac{\omega_1 - \omega_r}{\omega_1} = \frac{\omega_2}{\omega_1} \tag{2.10}$$

where ω_r is the rotor speed and ω_2 is the slip frequency. Moreover, if the air-gap flux, stator flux and rotor flux are defined as

$$\Psi_m = L_m(\mathbf{I}_s + \mathbf{I}_r + \mathbf{I}_{R_m}) \tag{2.11}$$
$$\Psi_s = L_{s\lambda}\mathbf{I}_s + L_m(\mathbf{I}_s + \mathbf{I}_r + \mathbf{I}_{R_m}) = L_{s\lambda}\mathbf{I}_s + \Psi_m \tag{2.12}$$
$$\Psi_r = L_{r\lambda}\mathbf{I}_r + L_m(\mathbf{I}_s + \mathbf{I}_r + \mathbf{I}_{R_m}) = L_{r\lambda}\mathbf{I}_r + \Psi_m \tag{2.13}$$

the equations describing the equivalent circuit, i.e., (2.7)–(2.9), can be rewritten as

$$\mathbf{V}_s = R_s\mathbf{I}_s + j\omega_1\Psi_s \tag{2.14}$$
$$\frac{\mathbf{V}_r}{s} = \frac{R_r}{s}\mathbf{I}_r + j\omega_1\Psi_r \tag{2.15}$$
$$0 = R_m\mathbf{I}_{R_m} + j\omega_1\Psi_m. \tag{2.16}$$

The resistive losses of the induction generator are

$$P_{\text{loss}} = 3\left(R_s|\mathbf{I}_s|^2 + R_r|\mathbf{I}_r|^2 + R_m|\mathbf{I}_{R_m}|^2\right) \tag{2.17}$$

and it is possible to express the electro-mechanical torque, T_e, as

$$T_e = 3n_p\text{Im}\left[\Psi_m\mathbf{I}_r^*\right] = 3n_p\text{Im}\left[\Psi_r\mathbf{I}_r^*\right] \tag{2.18}$$

where n_p is the number of pole pairs. Table 2.1 shows some typical parameters of the induction machine in per unit (p.u.).

TABLE 2.1. TYPICAL PARAMETERS OF THE INDUCTION MACHINE IN P.U., [101].

		Small Machine 4 kW	Medium Machine 100 kW	Large Machine 800 kW
Stator and rotor resistance	R_s and R_r	0.04	0.01	0.01
Leakage inductance	$L_{s\lambda} + L_{r\lambda} \approx L_\sigma$	0.2	0.3	0.3
Magnetizing inductance	$L_m \approx L_M$	2.0	3.5	4.0

2.3.2 Power Flow

In order to investigate the power flow of the DFIG system the apparent power that is fed to the DFIG via the stator and rotor circuit has to be determined. The stator apparent power $\mathbf{S}_s$ and rotor apparent power $\mathbf{S}_r$ can be found as

$$\mathbf{S}_s = 3\mathbf{V}_s\mathbf{I}_s^* = 3R_s\left|\mathbf{I}_s\right|^2 + j3\omega_1 L_{s\lambda}\left|\mathbf{I}_s\right|^2 + j3\omega_1\Psi_m\mathbf{I}_s^* \tag{2.19}$$

$$\mathbf{S}_r = 3\mathbf{V}_r\mathbf{I}_r^* = 3R_r\left|\mathbf{I}_r\right|^2 + j3\omega_1 sL_{r\lambda}\left|\mathbf{I}_r\right|^2 + j3\omega_1 s\Psi_m\mathbf{I}_r^* \tag{2.20}$$

which can be rewritten, using the expressions in the previous section, as

$$\mathbf{S}_s = 3R_s\left|\mathbf{I}_s\right|^2 + j3\omega_1 L_{s\lambda}\left|\mathbf{I}_s\right|^2 + j3\omega_1\frac{\left|\Psi_m\right|^2}{L_m} + 3R_m\left|\mathbf{I}_{R_m}\right|^2 - j3\omega_1\Psi_m\mathbf{I}_r^* \tag{2.21}$$

$$\mathbf{S}_r = 3R_r\left|\mathbf{I}_r\right|^2 + j3\omega_1 sL_{r\lambda}\left|\mathbf{I}_r\right|^2 + j3\omega_1 s\Psi_m\mathbf{I}_r^*. \tag{2.22}$$

Now the stator and rotor power can be determined as

$$P_s = \mathrm{Re}\left[\mathbf{S}_s\right] = 3R_s\left|\mathbf{I}_s\right|^2 + 3R_m\left|\mathbf{I}_{R_m}\right|^2 + 3\omega_1\mathrm{Im}\left[\Psi_m\mathbf{I}_r^*\right] \approx 3\omega_1\mathrm{Im}\left[\Psi_m\mathbf{I}_r^*\right] \tag{2.23}$$

$$P_r = \mathrm{Re}\left[\mathbf{S}_r\right] = 3R_r\left|\mathbf{I}_r\right|^2 - 3\omega_1 s\mathrm{Im}\left[\Psi_m\mathbf{I}_r^*\right] \approx -3\omega_1 s\mathrm{Im}\left[\Psi_m\mathbf{I}_r^*\right] \tag{2.24}$$

where the approximations are because the resistive losses and the magnetizing losses have been neglected. From the above equations the mechanical power produced by the DFIG can be determined as the sum of the stator and rotor power as

$$P_{\mathrm{mech}} = 3\omega_1\mathrm{Im}\left[\Psi_m\mathbf{I}_r^*\right] - 3\omega_1 s\mathrm{Im}\left[\Psi_m\mathbf{I}_r^*\right] = 3\omega_r\mathrm{Im}\left[\Psi_m\mathbf{I}_r^*\right]. \tag{2.25}$$

Then, by dividing P_{mech} with mechanical rotor speed, $\omega_m = \omega_r/n_p$, the produced electromechanical torque, as given in (2.18), can be found. Moreover, this means that $P_s \approx P_{\mathrm{mech}}/(1-s)$ and $P_r \approx -sP_{\mathrm{mech}}/(1-s)$. In Fig. 2.12 the power flow of a "lossless" DFIG system can be seen. In the figure it can be seen how the mechanical power divides

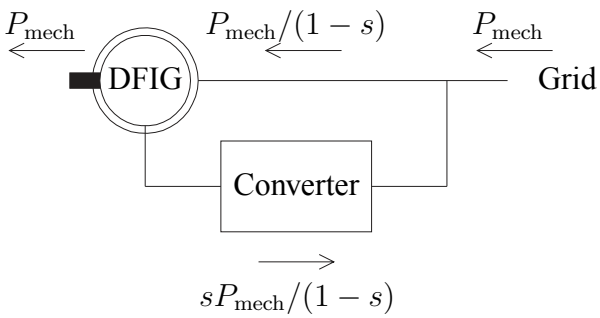

Fig. 2.12. Power flow of a "lossless" DFIG system.

between the stator and rotor circuits and that it is dependent on the slip. Moreover, the rotor power is approximately minus the stator power times the slip: $P_r \approx -sP_s$. Therefore, as mentioned earlier, the rotor converter can be rated as a fraction of the rated power of the DFIG if the maximum slip is low.

An example of how the stator and rotor powers depend on the slip is shown in Table 2.2. It can be seen in the table that the power through the converter, given the mechanical power,

TABLE 2.2. EXAMPLE OF THE POWER FLOW FOR DIFFERENT SLIPS OF THE DFIG SYSTEM.

slip, s, [%]	rotor speed, ω_r, [p.u.]	rotor power, P_r	stator power, P_s
0.3	0.7	$-0.43 \cdot P_{\text{mech.}}$	$1.43 \cdot P_{\text{mech.}}$
0	1.0	0	$P_{\text{mech.}}$
-0.3	1.3	$0.23 \cdot P_{\text{mech.}}$	$0.77 \cdot P_{\text{mech.}}$

is higher for positive slips ($\omega_r < \omega_1$). This is due to the factor $1/(1-s)$ in the expressions for the rotor power. However, for a wind turbine, the case is not as shown in Table 2.2. For a wind turbine, in general, at low mechanical power the slip is positive and for high mechanical power the slip is negative, as seen in Fig. 2.13. The figure is actually the same as Fig. 2.3, but the stator and rotor power of the DFIG system is also shown and instead of the rotor speed the slip is shown. In the figure it is assumed that the gearbox ratio is set in such a way that

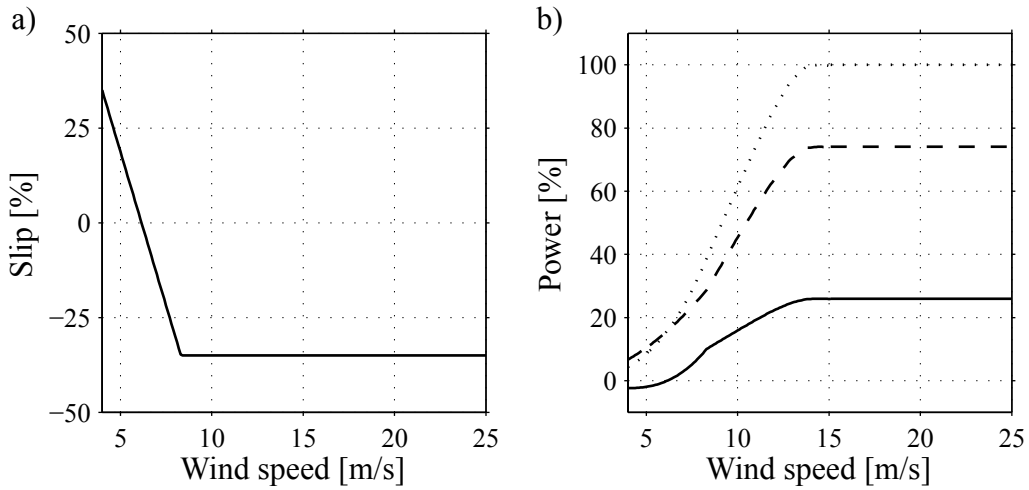

Fig. 2.13. Typical characteristic for a variable speed DFIG wind turbine. a) Slip as a function of wind speed. b) Mechanical power (dotted), rotor power (solid) and stator power (dashed) as a function of wind speed.

the average value of the rotor-speed range corresponds to synchronous speed of the DFIG. Moreover, for the wind turbine in Fig. 2.13 the stator power is at maximum only 0.7 times the rated power.

2.3.3 Stator-to-Rotor Turns Ratio

Since the losses in the power electronic converter depend on the current through the valves, it is important to have a stator-to-rotor turns ratio of the DFIG that minimizes the rotor current without exceeding the maximum available rotor voltage. In Fig. 2.14 a transformer is placed between the rotor circuit and the converter. The transformer is to highlight and indicate the stator-to-rotor turns ratio, but it does not exist in reality.

For example, if the stator-to-rotor turns ratio, n_s/n_r, is 0.4, the rotor current is approximately 0.4 times smaller than the stator current, if the magnetizing current is neglected. Moreover, if the slip s of the DFIG is 30%, the rotor voltage will approximately be $V_R^{\text{rotor}} = s/(n_s/n_r)V_s = 0.3/0.4V_s = 0.75V_s$, i.e., 75% of the stator voltage, which leaves room for a dynamic control reserve. Note that $V_R^{\text{rotor}} = (n_r/n_s)V_R$ is the actual (physical)

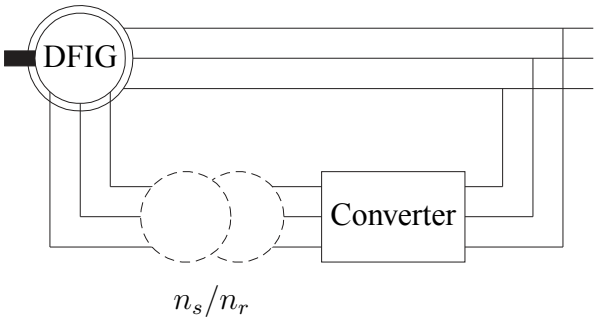

Fig. 2.14. Stator-to-rotor turns ratio indicated with a "virtual" transformer.

rotor voltage, while V_R is rotor voltage referred to the stator circuit. In this thesis, all rotor variables and parameters are referred to the stator circuit if not otherwise stated.

2.3.4 Lowering Magnetizing Losses

In an ordinary induction machine drive the stator is fed by a converter, which means that it is possible to reduce the losses in the machine by using an appropriate flux level. At low loads it is possible to reduce the flux level, which means that the magnetizing losses are lowered, leading to a better efficiency. However, in the DFIG system the stator is connected to the grid, and accordingly the flux level is closely linked to the stator voltage. Still, for the DFIG system there are, at least, two methods to lower the magnetizing losses of the DFIG. This can be done by:

1. short-circuiting the stator of the induction generator at low wind speeds, and transmitting all the turbine power through the converter. This set-up is referred to as the *short-circuited DFIG*.

2. having the stator Δ-connected at high wind speeds and Y-connected at low wind speeds; referred to as the *Y-Δ-connected DFIG*.

The influence that these two methods have on the overall efficiency of a DFIG system will be further analyzed in Chapter 3. A brief description of these two systems follows:

"Short-Circuited DFIG"

Fig. 2.15 shows a diagram of the "short-circuited DFIG." In the figure two switches can be seen. Switch S2 is used to disconnect the turbine from the grid and switch S1 is then used to short-circuit the stator of the DFIG. Now the turbine is operated as a cage-bar induction machine, except that the converter is connected to the rotor circuit instead of the stator circuit. This means, that in this operating condition, the DFIG can be controlled in a similar way as an ordinary cage-bar induction generator. For instance, at low wind speeds the flux level in the generator can be lowered.

Y-Δ-connected DFIG

Fig. 2.16 presents a set-up of the Y-Δ-connected DFIG. As shown in the figure, a device for changing between Y and Δ connection has been inserted in the stator circuit. Before a

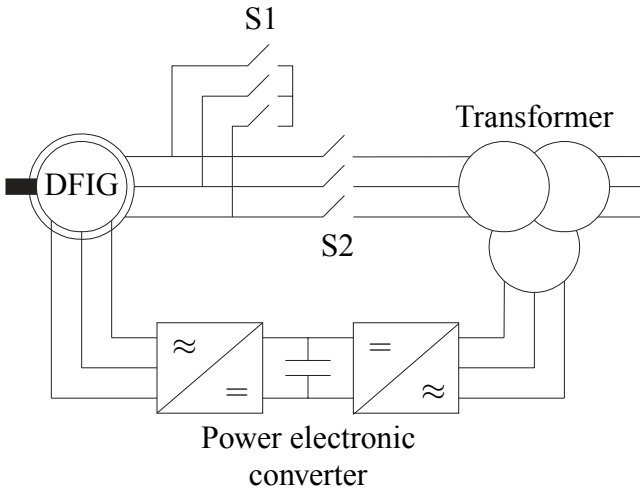

Fig. 2.15. Principle of the "short-circuited DFIG."

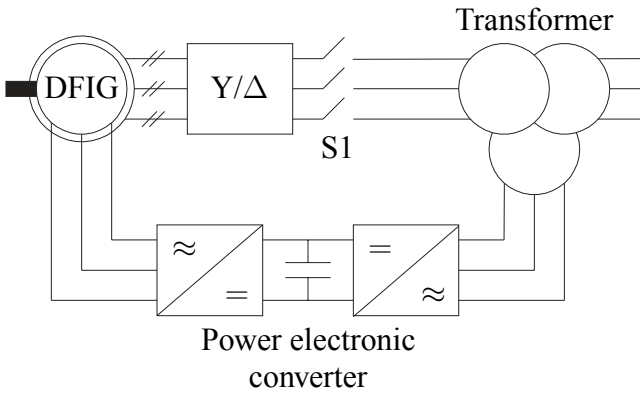

Fig. 2.16. Principle of the Y-Δ-connected DFIG.

change from Y to Δ connection (or vice versa) the power of the turbine is reduced to zero and the switch S1 disconnects the stator circuit from the grid. Then the stator circuit is connected in Δ (or vice versa) and the turbine is synchronized to the grid.

2.3.5 Other Types of Doubly-Fed Machines

In this section a short presentation of other kinds of doubly-fed machines is made: a cascaded doubly-fed induction machine, a single-frame cascaded doubly-fed induction machine, a brushless doubly-fed induction machine, and a doubly-fed reluctance machine.

Cascaded Doubly-Fed Induction Machine

The cascaded doubly-fed induction machine consists of two doubly-fed induction machines with wound rotors that are connected mechanically through the rotor and electrically through the rotor circuits. See Fig. 2.17 for a principle diagram. The stator circuit of one of the machines is directly connected to the grid while the other machine's stator is connected via a

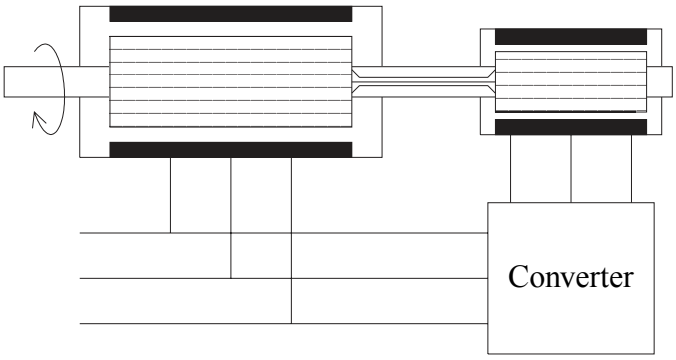

Fig. 2.17. Principle of cascaded doubly-fed induction machine.

converter to the grid. Since the rotor voltages of both machines are equal, it is possible to control the induction machine that is directly connected to the grid with the other induction machine.

It is possible to achieve decoupled control of active and reactive power of the cascaded doubly-fed induction machine in a manner similar to the doubly-fed induction machine [47].

It is doubtful whether it is practical to combine two individual machines to form a cascaded doubly-fed induction machine, even though it is the basic configuration of doubly-fed induction machine arrangement. Due to a large amount of windings, the losses are expected to be higher than for a standard doubly-fed induction machine of a comparable rating [48].

Single-Frame Cascaded Doubly-Fed Induction Machine

The single-frame cascaded doubly-fed induction machine is a cascaded doubly-fed induction machine, but with the two induction machines in one common frame. Although this machine is mechanically more robust than the cascaded doubly-fed induction machine, it suffers from comparatively low efficiency [48].

Brushless Doubly-Fed Induction Machine

This is an induction machine with two stator windings in the same slot. That is, one winding for the power and one winding for the control. See Fig. 2.18 for a principle sketch. To avoid a direct transformer coupling between the two-stator windings, they can not have the same number of pole pairs. Furthermore, to avoid unbalanced magnetic pull on the rotor the difference between the pole pairs must be greater than one [106]. The number of poles in the rotor must equal the sum of the number of poles in the two stator windings [106]. For further information and more details, see [106, 108, 111].

Doubly-Fed Reluctance Machine

The stator of the doubly-fed reluctance machine is identical to the brushless doubly-fed induction machine, while the rotor is based on the principle of reluctance. An equivalent circuit with constant parameters can be obtained for the doubly-fed reluctance machine, in spite the

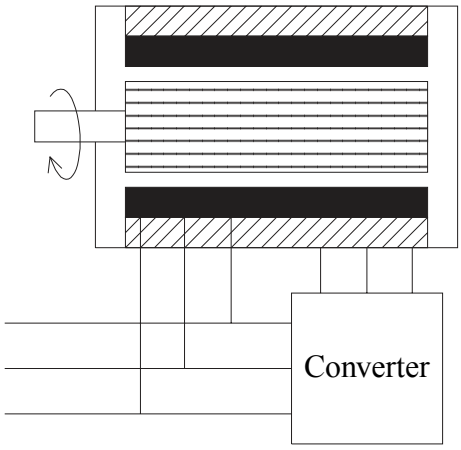

Fig. 2.18. Principle of the brushless doubly-fed induction machine.

fact that the machine is characterized by a pulsating air-gap flux. It has almost the same equivalent circuit as the standard doubly-fed induction generator [109].

Chapter 3

Energy Efficiency of Wind Turbines

The purpose of this chapter is to investigate the energy efficiency of the DFIG system and to relate this study to other types of WTs with various electrical systems. This study focuses on 1) reducing the magnetizing losses of the DFIG system, 2) influence of the converter's size on the energy production (i.e., smaller converter implies a smaller variable-speed range for the DFIG system) and finally 3) comparison of the DFIG system to other electrical systems.

In order to make the comparison as fair as possible the base assumption used in this work is that the maximum (average) shaft torque of the wind turbine systems used should be the same. Moreover, the rated WT power used in this chapter is 2 MW.

3.1 Determination of Power Losses

Steady-state calculations are carried out in this section in order to determine the power losses of the DFIG system. Moreover, in order to compare the performance of the DFIG system, the power losses of other systems with induction generators will also be presented. The following systems are included in this study:

- *FSIG 1 system* — Fixed-speed system, as described in Section 2.2.1, with one generator.
- *FSIG 2 system* — Fixed-speed system, as described in Section 2.2.1, with two generators or a pole-pair changing mechanism.
- *VSIG system* — Variable-speed system with an induction generator and a full-power converter, as described in Section 2.2.2.
- *DFIG system* — Variable-speed system with a DFIG, as described in Section 2.2.3.

The following losses are taken into account: aerodynamic losses, gearbox losses, generator losses and converter losses.

3.1.1 Aerodynamic Losses

Fig. 3.1 shows the turbine power as a function of wind speed both for the fixed-speed and variable-speed systems. In the figure it is seen that the fixed-speed system with only one generator has a lower input power at low wind speeds. The other systems produce almost

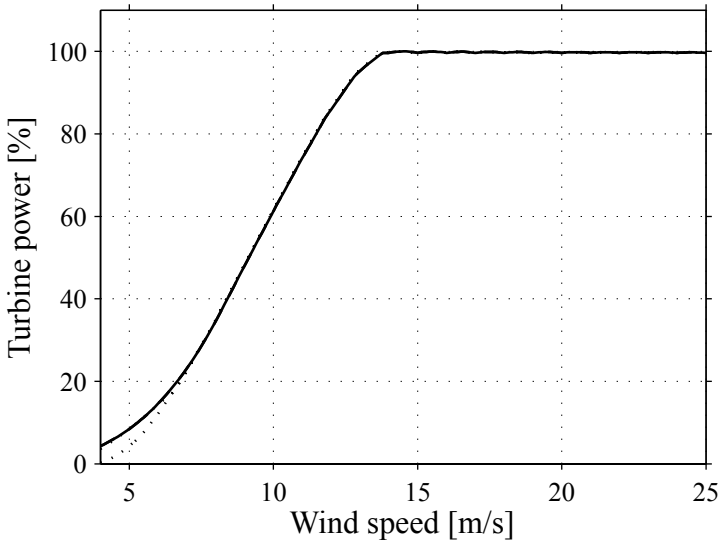

Fig. 3.1. Turbine power. The power is given in percent of maximum shaft power. The solid line corresponds to the variable-speed systems (VSIG and DFIG) and the two-speed system (FSIG 2). The dotted line corresponds to a fixed-speed system (FSIG 1).

identical results. In order to calculate the power in Fig. 3.1, a so-called $C_p(\lambda, \beta)$-curve, as described in Section 2.1.3, derived using blade-element theory has been used used.

In order to avoid making the results dependent on the torque, speed and pitch control strategy, that vary from turbine to turbine, and anyway the settings used by the manufacturers are not in detail known by the authors, only the average wind speed is used in the calculations, i.e., the influence of the turbulence is ignored. The interested reader can find information of the influence of the turbulence on the energy production in [69].

3.1.2 Gearbox Losses

One way to estimate the gearbox losses, $P_{\text{loss,GB}}$, is, [33],

$$P_{\text{loss,GB}} = \eta P_{\text{lowspeed}} + \xi P_{\text{nom}} \frac{\Omega_r}{\Omega_{r,\text{nom}}} \tag{3.1}$$

where η is the gear-mesh losses constant and ξ is a friction constant. According to [34], for a 2-MW gearbox, the constants $\eta = 0.02$ and $\xi = 0.005$ are reasonable. In Fig. 3.2 the gearbox losses are shown for the investigated systems.

3.1.3 Induction Generator Losses

In order to calculate the losses of the generator, the equivalent circuit of the induction generator, with inclusion of magnetizing losses, has been used, see Section 2.3.1.

For the DFIG system, the voltage drop across the slip rings has been neglected. Moreover, the stator-to-rotor turns ratio for the DFIG is adjusted so that maximum rotor voltage is 75% of the rated grid voltage. This is done in order to have safety margin, i.e., a dynamic reserve to handle, for instance, a wind gust. Observe that instead of using a varying turns ratio, the same effect can also be obtained by using different rated voltages on the rotor and stator [81].

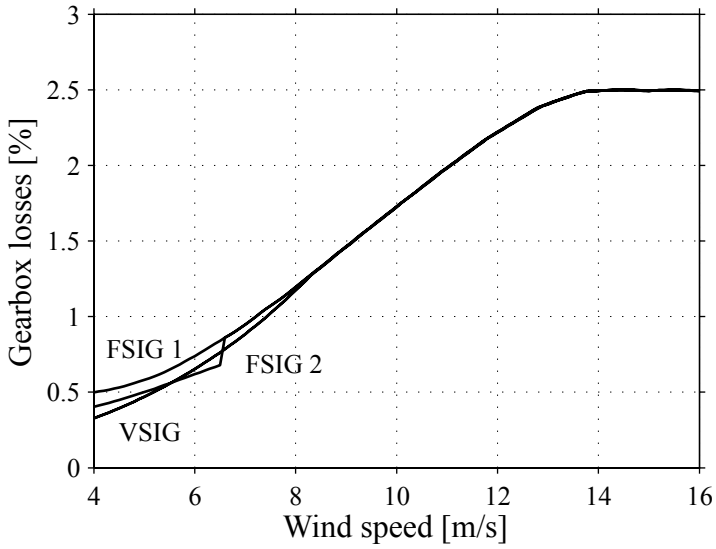

Fig. 3.2. Gearbox losses. The losses are given in percent of maximum shaft power. The solid line corresponds to the variable-speed systems (VSIG and DFIG). The dotted lines correspond to fixed-speed systems, i.e., FSIG 1 and 2 (both one-speed and two-speed generators).

In Fig. 3.3 the induction generator losses of the DFIG system are shown. The reason that the generator losses are larger for high wind speeds for the VSIG system compared to the DFIG system is that the gearbox ratio is different between the two systems. This implies that the shaft torque of the generators will be different for the two systems, given the same input power. It can also be noted that the losses of the DFIG are higher than those of the

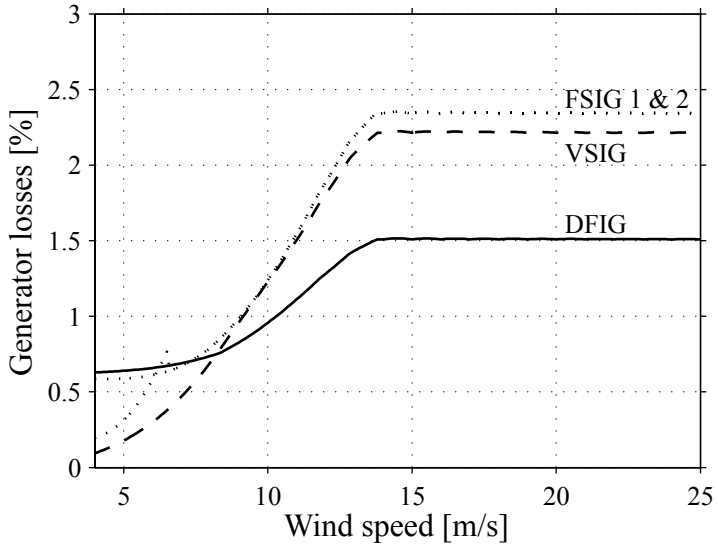

Fig. 3.3. Induction generator losses. The losses are given in percent of maximum shaft power. DFIG is solid, dashed is the variable-speed system (VSIG) and dotted are the fixed-speed systems (FSIG 1 and 2).

VSIG for low wind speeds. The reason for this is that the flux level of the VSIG system has been optimized from an efficiency point of view while for the DFIG system the flux level is almost fixed to the stator voltage. This means that for the VSIG system a lower flux level is

used for low wind speeds, i.e., the magnetizing losses are reduced.

For the IGs used in this chapter operated at 690 V 50 Hz and with a rated current of 1900 A and 390 A, respectively, the following parameters are used:

2-MW power: See Appendix B.1.

0.4-MW power: $R_s = 0.04$ p.u., $R_r = 0.01$ p.u., $R_m = 192$ p.u., $L_{s\lambda} = 0.12$ p.u., $L_{r\lambda} = 0.04$ p.u., $L_m = 3.7$ p.u. and $n_p = 3$.

3.1.4 Converter Losses

In order to be able to feed the IG with a variable voltage and frequency source, the IG can be connected to a pulse-width modulated (PWM) converter. In Fig. 3.4, an equivalent circuit of the converter is drawn, where each transistor, T1 to T6, is equipped with a reverse diode. A PWM circuit switches the transistors to on and off states. The duty cycle of the transistor and the diode determines whether the transistor or a diode is conducting in a transistor leg (e.g., T1 and T4).

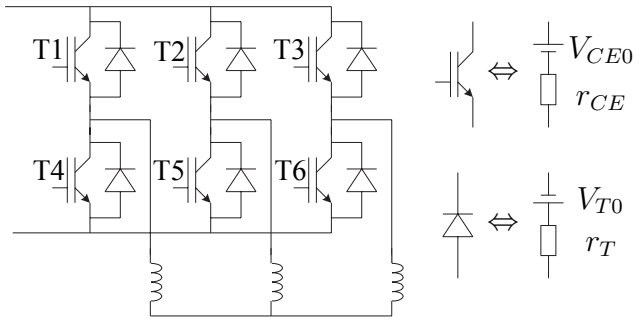

Fig. 3.4. Converter scheme.

The losses of the converter can be divided into switching losses and conducting losses. The switching losses of the transistors are the turn-on and turn-off losses. For the diode the switching losses mainly consist of turn-off losses [103], i.e., reverse-recovery energy. The turn-on and turn-off losses for the transistor and the reverse-recovery energy loss for a diode can be found from data sheets. The conducting losses arise from the current through the transistors and diodes. The transistor and the diode can be modeled as constant voltage drops, V_{CE0} and V_{T0}, and a resistance in series, r_{CE} and r_T, see Fig. 3.4. Simplified expressions of the transistor's and diode's conducting losses, for a transistor leg, are (with a third harmonic voltage injection) [2]

$$\begin{aligned} P_{\mathrm{c,T}} =& \frac{V_{CE0} I_{\mathrm{rms}} \sqrt{2}}{\pi} + \frac{I_{\mathrm{rms}} V_{CE0} m_i \cos(\phi)}{\sqrt{6}} + \frac{r_{CE} I_{\mathrm{rms}}^2}{2} \\ &+ \frac{r_{CE} I_{\mathrm{rms}}^2 m_i}{\sqrt{3}\cos(\phi) 6\pi} - \frac{4 r_{CE} I_{\mathrm{rms}}^2 m_i \cos(\phi)}{45\pi\sqrt{3}} \end{aligned} \tag{3.2}$$

$$\begin{aligned} P_{\mathrm{c,D}} =& \frac{V_{T0} I_{\mathrm{rms}} \sqrt{2}}{\pi} - \frac{I_{\mathrm{rms}} V_{T0} m_i \cos(\phi)}{\sqrt{6}} + \frac{r_T I_{\mathrm{rms}}^2}{2} \\ &- \frac{r_T I_{\mathrm{rms}}^2 m_i}{\sqrt{3}\cos(\phi) 6\pi} + \frac{4 r_T I_{\mathrm{rms}}^2 m_i \cos(\phi)}{45\pi\sqrt{3}} \end{aligned} \tag{3.3}$$

where I_{rms} is the root mean square (RMS) value of the (sinusoidal) current to the grid or the generator, m_i is the modulation index, and ϕ is the phase shift between the voltage and the current.

Since, for the values in this chapter, which are based on [89, 90, 91, 92] (see Table 3.1 for actual values), $r_{IGBT} = r_{CE} \approx r_T$ and $V_{IGBT} = V_{CEO} \approx V_{TO}$. Hence, it is possible to reduce the loss model of the transistor and the diode to the same model. The conduction

TABLE 3.1. CONVERTER CHARACTERISTIC DATA (IGBT AND INVERSE DIODE).

Nominal current	$I_{C,\mathrm{nom}}$	500 A	1200 A	1800 A	2400 A
Operating dc-link voltage	V_{CC}	1200 V	1200 V	1200 V	1200 V
	V_{CEO}	1.0 V	1.0 V	1.0 V	1.0 V
Lead resistance (IGBT)	r_{CE}	3 mΩ	1.5 mΩ	1 mΩ	0.8 mΩ
Turn-on and turn-off energy (IGBT)	$E_{\mathrm{on}} + E_{\mathrm{off}}$	288 mJ	575 mJ	863 mJ	1150 mJ
	V_{TO}	1.1 V	1.1 V	1.1 V	1.1 V
Lead resistance (diode)	r_T	2.6 mΩ	1.5 mΩ	1.0 mΩ	0.8 mΩ
Reverse recovery energy (diode)	E_{rr}	43 mJ	86 mJ	128 mJ	171 mJ

losses can, with the above-mentioned approximation, be written as

$$P_{\mathrm{c}} = P_{\mathrm{c,T}} + P_{\mathrm{c,D}} = V_{IGBT}\frac{2\sqrt{2}}{\pi}I_{\mathrm{rms}} + r_{IGBT}I_{\mathrm{rms}}^2. \tag{3.4}$$

The switching losses of the transistor can be considered to be proportional to the current, for a given dc-link voltage, as is assumed here [2]. This implies that the switching losses from the transistor and the inverse diode can be expressed as

$$P_{\mathrm{s,T}} = (E_{\mathrm{on}} + E_{\mathrm{off}})\frac{2\sqrt{2}}{\pi}\frac{I_{\mathrm{rms}}}{I_{C,nom}}f_{sw} \approx V_{sw,T}\frac{2\sqrt{2}}{\pi}I_{\mathrm{rms}} \tag{3.5}$$

$$P_{\mathrm{s,D}} = E_{rr}\frac{2\sqrt{2}}{\pi}\frac{I_{\mathrm{rms}}}{I_{C,nom}}f_{sw} \approx V_{sw,D}\frac{2\sqrt{2}}{\pi}I_{\mathrm{rms}} \tag{3.6}$$

where E_{on} and E_{off} are the turn-on and turn-off energy losses, respectively, for the transistor, E_{rr} is the reverse recovery energy for the diode and $I_{C,nom}$ is the nominal current through the transistor. In the equations above, two voltage drops, $V_{sw,T}$ and $V_{sw,D}$, have been introduced. This is possible since the ratios $(E_{\mathrm{on}} + E_{\mathrm{off}})/I_{C,nom}$ and $E_{rr}/I_{C,nom}$ are practically constant for all the valves in Table 3.1. This means that for a given dc-link voltage and switching frequency (which both are assumed in this thesis), the switching losses of the IGBT and diode can be modeled as a constant voltage drop that is independent of the current rating of the valves. The switching frequency used in this thesis is 5 kHz. Moreover, since the products $r_{CE}I_{C,\mathrm{nom}}$ and $r_T I_{C,\mathrm{nom}}$ also are practically constant and equal to each other, it is possible to determine a resistance, $r_{IGBT,1\,\mathrm{A}}$, that is valid for a nominal current $I_{C,\mathrm{nom}} = 1$ A. Then, the resistance of a specific valve can be determined from $r_{IGBT} = r_{IGBT,1\,\mathrm{A}}/I_{C,\mathrm{nom}}$, where $I_{C,\mathrm{nom}}$ is the nominal current of the valve. In this thesis, $I_{C,\mathrm{nom}}$ is chosen as $I_{C,\mathrm{nom}} = 2I_{\mathrm{rms}}^{\mathrm{max}}$ where $I_{\mathrm{rms}}^{\mathrm{max}}$ is the maximum RMS value of the current in the valve. By performing the above simplification the model of the IGBT and valve can be scaled to an arbitrary rating. Using

the values given in Table 3.1 it is possible to determine the voltage drops $V_{sw,T} = 2.5$ V and $V_{sw,D} = 0.38$ V, assuming a switching frequency of 5 kHz and the resistance $r_{IGBT,1\,\mathrm{A}} = 1.76\ \Omega$. When determining $V_{sw,T}$, $V_{sw,D}$, and $r_{IGBT,1\,\mathrm{A}}$ the average values of all of the valves in Table 3.1 has been used. Now, the total losses from the three transistor legs of the converter become

$$\begin{aligned} P_{\mathrm{loss}} &= 3(P_{\mathrm{c}} + P_{\mathrm{s,T}} + P_{\mathrm{s,D}}) \\ &= 3\left((V_{IGBT} + V_{sw,T} + V_{sw,D}) \frac{2\sqrt{2}}{\pi} I_{\mathrm{rms}} + r_{IGBT} I_{\mathrm{rms}}^2 \right). \end{aligned} \tag{3.7}$$

The back-to-back converter can be seen as two converters which are connected together: the machine-side converter (MSC) and the grid-side converter (GSC). For the MSC, the current through the valves, I_{rms}, is the stator current for the VSIG system or the rotor current for the DFIG system. One way of calculating I_{rms} for the GSC is by using the active current that is produced by the machine, adjusted with the ratio between machine-side voltage and the grid voltage. The reactive current can be freely chosen. Thus it is now possible to calculate the losses of the back-to-back converter as

$$P_{\mathrm{loss,converter}} = P_{\mathrm{loss,GSC}} + P_{\mathrm{loss,MSC}}. \tag{3.8}$$

The total converter losses are now presented as a function of wind speed in Fig. 3.5. From the figure it can, as expected, be noted that the converter losses in the DFIG system are

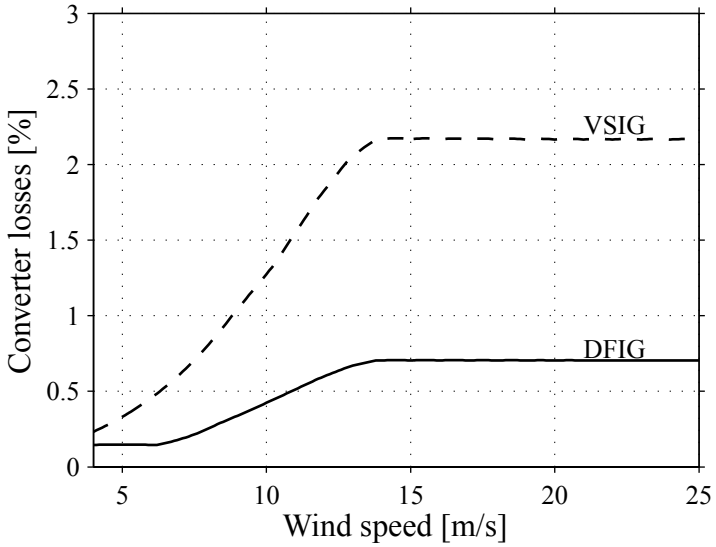

Fig. 3.5. Converter losses. The losses are given in percent of maximum shaft power. DFIG is solid and VSIG is dashed.

much lower compared to the full-power converter system.

3.1.5 Total Losses

The total losses (aerodynamic, generator, converter, gearbox) are presented in Fig. 3.6. From the figure it can be noted that the DFIG system and the two-speed system (FSIG 2) has roughly the same total losses while the full-power converter system has higher total losses.

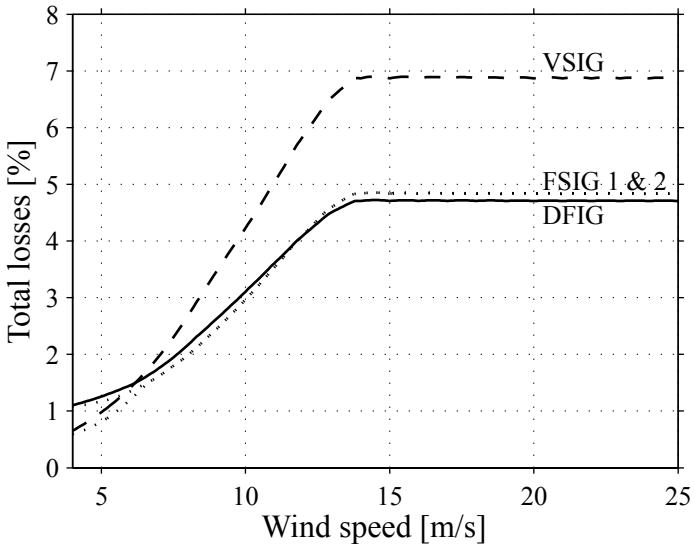

Fig. 3.6. Total losses. The losses are given in percent of maximum shaft power. DFIG is solid, FSIG 1 and 2 is dotted and VSIG is dashed.

3.2 Energy Production of the DFIG System

In the previous section, the power loss as a function of transmitted power (or wind speed) was determined. However, for the wind-turbine application, the most important quantity is the energy delivered to the grid (electric energy capture). Accordingly, in this section the results in the previous section have been used to determine the energy capture (or energy efficiency) of the various systems.

In order to do this, the distribution of wind speeds must be known. As mentioned earlier one commonly used probability density functions to describe the wind speed is the Rayleigh function [53]. Given a probability density functions, $f(w)$, the average (or expected) value of the power, $P(w)$, can be found as

$$P_{\text{avg}} = \int_0^\infty P(w) f(w) dw \tag{3.9}$$

where w is the wind speed.

3.2.1 Investigation of the Influence of the Converter's Size on the Energy Production

As was mentioned earlier, it is not possible to obtain a full speed range with the DFIG system if the converter is smaller than the rated power of the turbine. This means that the smaller the converter is, the more the WT will operate at a non-ideal tip-speed ratio, λ, for low wind speeds. Fig. 3.7 illustrates the impact of having a smaller converter and thus a smaller rotor-speed range, i.e., the aerodynamic losses become higher.

In Fig. 3.8 the converter losses are presented for different designs of the rotor-speed range, i.e., a smaller rotor-speed range implies smaller ratings of the converter. It can be seen in the figure that the converter losses are lower for smaller rotor-speed ranges (or smaller converter ratings). Note, as mentioned earlier, that the stator-to-rotor turns ratio has to be

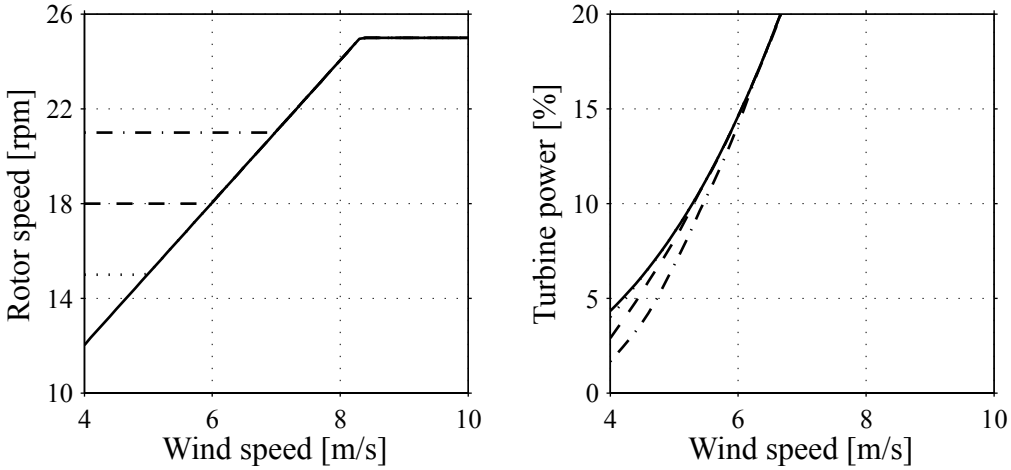

Fig. 3.7. Rotor speed and the corresponding turbine power.

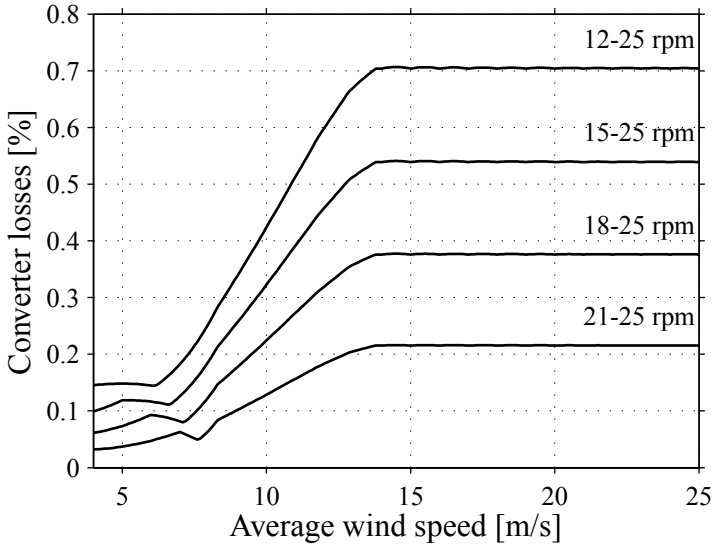

Fig. 3.8. Converter losses for some different rotor-speed ranges as a function of the wind speed.

designed according to desired variable-speed range in order to minimize the converter losses. However, the most interesting information is the total energy efficiency. In Fig. 3.9 the energy efficiency of the DFIG for different rotor-speed ranges (or converter sizes) can be seen. It can be seen in the figure that the gain in energy increases with the rotor-speed range (converter size), even though the converter losses of the DFIG system increase with the rotor-speed range (converter size), as shown in Fig. 3.8. The increased aerodynamic capture has thus a larger impact than the increased converter losses. If the rotor-speed range is set to 12–25, it is possible to run at optimal tip-speed ratio in the whole variable-speed area. It can be seen in the figure, as expected, that the rotor-speed range is of greater importance for a low average wind-speed compared to a high average wind speed.

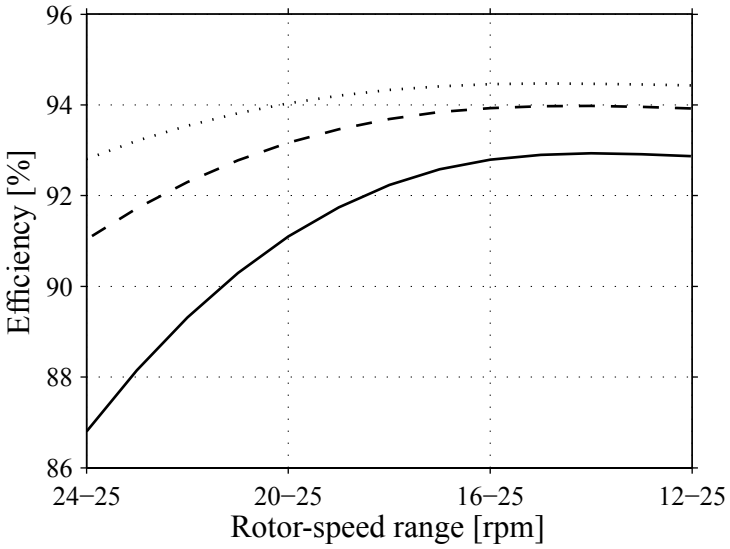

Fig. 3.9. Efficiency, for average wind speeds of 5.4 m/s (solid), 6.8 m/s (dashed) and 8.2 m/s (dotted), of the DFIG system as a function of the rotor-speed range. Note that the aerodynamic efficiency is also taken into account.

3.2.2 Reduction of Magnetizing Losses

As presented in Section 2.3.4 there are at least two ways of lowering the magnetizing losses, i.e., this can be done by:

1. short-circuiting the stator of the induction generator at low wind speeds, and transmitting all the turbine power through the converter. This set-up is referred to as the *short-circuited DFIG*.

2. having the stator Δ-connected at high wind speeds and Y-connected at low wind speeds; referred to as the *Y-Δ-connected DFIG*.

The break-even point of the total losses or the rated values of the equipment determines the switch-over point for the doubly-fed generators, i.e., the Y-Δ coupling or the synchronization of the stator voltage to the grid.

In Fig. 3.10 the energy gain using the two methods are presented. It can be seen in the figure that the Y-Δ-connected DFIG system produces approximately 0.2 percentage units more energy than the short-circuited DFIG system, at least for low average wind speeds.

Since the Y-Δ-connected DFIG system performs better than the short-circuited DFIG system the Y-Δ-connected DFIG system will henceforth be referred to as the *DFIG system*, and the other variants will not be subjected to any further studies.

3.3 Comparison to Other Wind Turbine Systems

The base assumption made here is that all wind turbine systems have the same average maximum shaft torque as well as the same mean upper rotor speed. In Fig. 3.11 the produced grid power together with the various loss components for an average wind speed of 6 m/s are presented for the various systems. The systems are the DFIG system, the full variable-speed

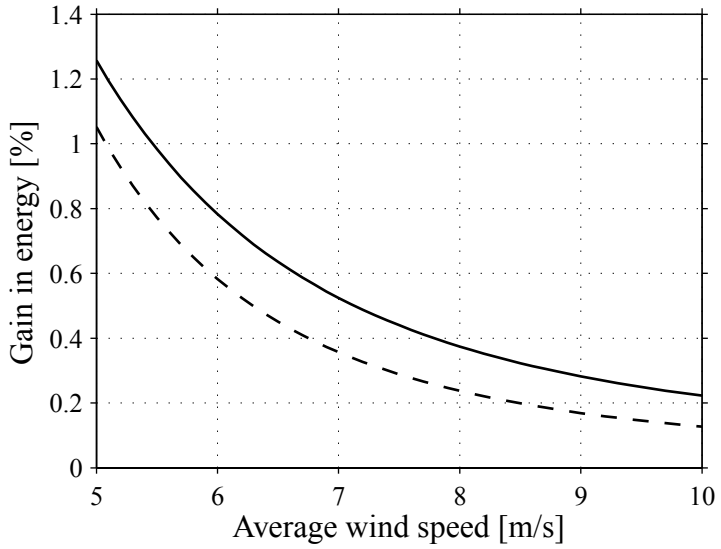

Fig. 3.10. Gain in energy production by lowering the magnetizing losses for a DFIG system as a function of the average wind speed. Solid line is the Y-Δ-connected DFIG and dashed line is short-circuited DFIG.

system (VSIG), one-speed system (FSIG 1), two-speed system (FSIG 2), and, a variable-speed system equipped with a permanent magnet synchronous generator (PMSG). The average efficiency for the PMSG is taken from [34]. The converter losses of the PMSG system are assumed equal to that of the VSIG system. It would also be possible to have the PMSG connected to a diode rectifier with series or shunt compensating capacitors, which may give a possibility to reduce the converter losses [32]. However, a transistor rectifier has the potential to utilize the generator best [32]. In the figure it can be seen that the one-speed system

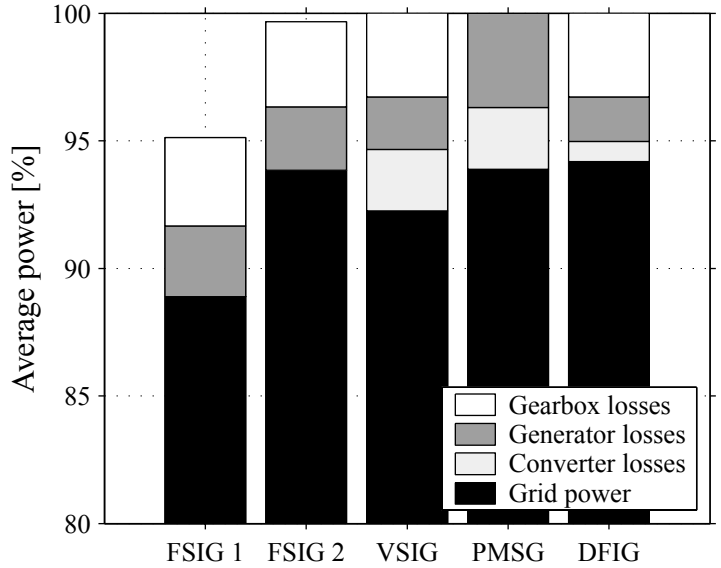

Fig. 3.11. The produced average grid power and generator, converter and gearbox losses for an average wind speed of 6 m/s. 100% correspond to the input turbine power at optimal, with respect to the rotor speed, aerodynamic efficiency.

(FSIG 1) has the disadvantage of poor aerodynamic efficiency. However, with the two-speed system (FSIG 2) the aerodynamic efficiency is improved and close to the variable speed systems (VSIG, PMSG and DFIG).

In Fig. 3.12 the produced energy of the different systems, for various average wind speeds, are presented. In the figure, the DFIG is operated with a rotor-speed range set to 12–25 rpm.

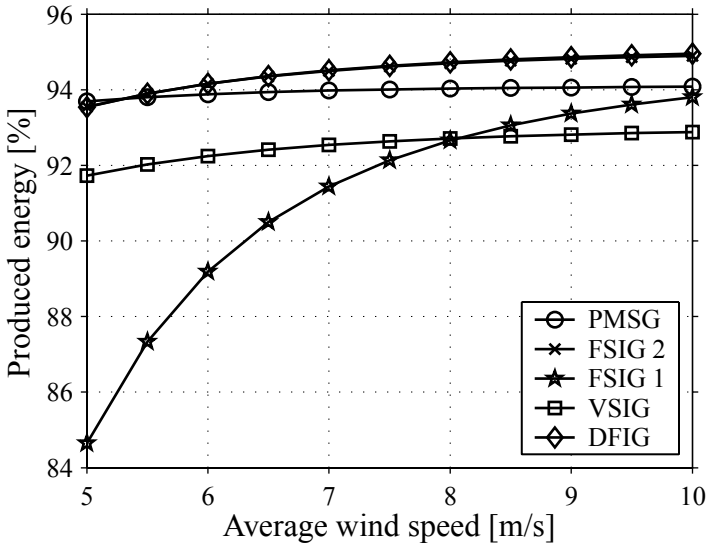

Fig. 3.12. Energy efficiency of the FSIG 1, FSIG 2, VSIG, PMSG and the DFIG system as a function of the average wind speed.

Detailed information of the gearless electrically magnetized generator system was not available. However, it is reasonable to assume that the losses in the diode rectifier connected to the stator, the boost converter on the dc-link, transistor converter towards the grid and the magnetizing system of the generator are in the same range as the PMSG system. In [35], a lower fixed-speed IG WT efficiency was reported than in this study. The reason for this is that the IG in this study has two generators and lower iron losses.

3.4 Discussion

In Fig. 3.12 it can be seen that the two-generator system (FSIG 2), the DFIG system, and the PMSG system have almost the same efficiency. In [16] it was found that the DFIG system produced 60% more energy compared to a fixed-speed system. However, in this study the produced energy of the systems was found to be similar. The difference between the result here and in [16] is due to the different base assumptions used. Further, it was found in this investigation that there is a possibility to gain a few percentage units (approximately 2%) in energy using the DFIG system compared to the full variable-speed system. This can be compared to a gain of 20% for the DFIG system compared to the variable-speed system reported in [16]. The reason for the difference is again, that the base assumptions differ. Reference [16] sets the rating of the stator windings equal while we choose the shaft power and maximum speed instead.

The focus in this chapter is on the electrical energy efficiency of the DFIG-system in relation to other systems. However, aerodynamics must be accounted for when fixed-speed and variable-speed turbines are compared. In order to reduce the number of uncertainties, only the average wind speed has been used and the influence of turbulence has not been treated. Reference [69] showed that a two-speed active stall turbine and a variable-speed pitch turbine is fairly unaffected by the turbulence intensity for turbulence intensities up to 15%. For the more unusual turbulence intensities of 20–25% the variable-speed turbines gained a couple of percentage units in energy production compared to the two-speed active stall-regulated system.

Of great importance to point out is that when comparing the DFIG system to the full variable system, the turbulence intensity, regardless of value plays an unimportant role since the torque and speed control of the turbines are in principle the same. (The rotor-speed range of the DFIG system is assumed to be almost the same as for the full-variable speed system). Another problem when incorporating the effect of the turbulence intensity is that the selection of torque, speed and pitch control influences the result. Also, among other factors, the time delay between generator switchings for the fixed-speed systems, start and stop, Δ-Y-reconnections for the DFIG-systems must be known, in order to perform a detailed energy capture calculation. So, in order not to include uncertainties that might not be the best chosen, the ambition has instead been to make the comparison as clean as possible, using only the facts that can be presented clearly and with best certainty.

3.5 Conclusion

In this chapter, it has been found that there is a possibility to gain a few percentage units in energy efficiency for a doubly-fed induction generator system compared to a cage-bar induction generator, controlled by a full-power converter. In comparison to a direct-driven permanent-magnet synchronous generator, controlled by a converter or a two-speed generator system the difference in energy efficiency was found to be small.

Moreover, two methods to reduce the magnetizing losses (and thereby increase the gain in energy) of the DFIG system, have been investigated. It was found that the method utilizing a Y-Δ switch in the stator circuit had the largest gain in energy of the two investigated methods.

Finally, it was found that the converter losses of the DFIG can be reduced if the available rotor-speed range is made smaller. However, the aerodynamic capture of the wind turbine is reduced with a smaller rotor-speed range. This means that the increased aerodynamic capture that can be achieved by a larger converter has, thus, a greater impact than the increased converter losses.

Worth stressing is that the main reason for using a variable-speed turbine instead of a fixed-speed turbine is not the energy efficiency, instead it is the possibility of lowering the mechanical stresses [53] and also improving the power quality [58].

Chapter 4

Control of Doubly-Fed Induction Generator System

4.1 Introduction

In this section, different aspects of designing and implementing control systems for doubly-fed induction generators (DFIGs) are treated.

4.1.1 Space Vectors

The idea behind space vectors is to describe the induction machine with two phases instead of three. Space vectors were originally invented to describe the spatial flux of an ac machine [39]. A three-phase stator winding, which is supplied with three-phase currents, forms a rotating flux in the air gap. The same rotating flux could also be formed with only two phases, as seen in Fig. 4.1. This is the principle of space vectors. In order to determine the

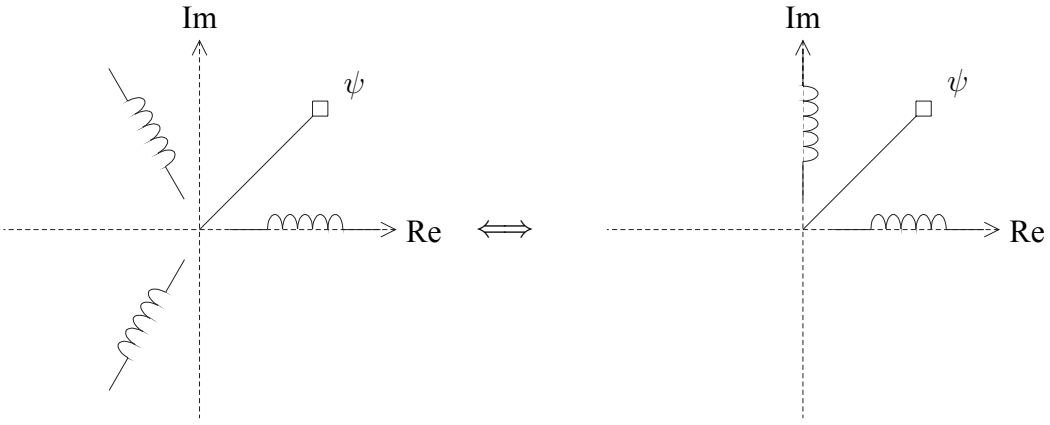

Fig. 4.1: Principle of space vectors.

space vector, $\mathbf{s}^s$, of the three-phase quantities, s_a, s_b, and s_c, the following transformation is applied [39]

$$\mathbf{s}^s = s_\alpha + j s_\beta = \frac{2K}{3}\left(s_a + \mathbf{a} s_b + \mathbf{a}^2 s_c\right) \tag{4.1}$$

where K is the space-vector scaling constant and $\mathbf{a} = e^{j2\pi/3}$. Superscript "s" indicates that the space vectors are referred to the reference frame of the stator of the induction machine. The constant K can be chosen arbitrary, though if it is chosen as

$$K = \frac{1}{\sqrt{2}} \tag{4.2}$$

the space vector will be scaled according to the RMS value of the three-phase quantities. This choice of K will be used throughout this thesis.

A general space vector can be expressed as

$$\mathbf{s}^s = se^{j(\theta_1+\phi)} \tag{4.3}$$

where ϕ is a phase shift and θ_1 is the synchronous angle corresponding to the synchronous frequency, ω_1, as $d\omega_1/dt = \theta_1$. It is possible to transform the vector to synchronous coordinates (dq coordinates) as

$$\mathbf{s} = s_d + js_q = e^{-j\theta_1}\mathbf{s}^s = se^{j\phi}. \tag{4.4}$$

The synchronous coordinate system is not indicated by a superscript. The synchronous coordinate system has to be aligned with a quantity, normally the stator or rotor flux of an induction machine. However, it is also possible to align the synchronous coordinate system with, for example, the grid voltage. Space vectors in synchronous coordinates will be dc quantities in the steady state.

4.1.2 Power and Reactive Power in Terms of Space Vectors

The instantaneous power, P, in a three-phase system is given by

$$P = v_a i_a + v_b i_b + v_c i_c = \frac{3}{2K^2}\mathrm{Re}\left[\mathbf{v}^s(\mathbf{i}^s)^*\right] = \frac{3}{2K^2}\mathrm{Re}\left[\mathbf{v}\mathbf{i}^*\right]. \tag{4.5}$$

The above-mentioned scaling, i.e. $K = 1/\sqrt{2}$, yields

$$P = 3\mathrm{Re}\left[\mathbf{v}\mathbf{i}^*\right]. \tag{4.6}$$

In (4.6) the instantaneous power is the real part of voltage times the complex conjugate of the current, i.e., the same as active power in terms of phasors. It is also possible to define a quantity the instantaneous reactive power, Q, as the corresponding imaginary part of the above equation [5]:

$$Q = 3\mathrm{Im}\left[\mathbf{v}\mathbf{i}^*\right]. \tag{4.7}$$

4.1.3 Phase-Locked Loop (PLL)-Type Estimator

A PLL-type estimator can be used for estimation of the angle and frequency of a signal, e.g., the synchronous frequency, ω_1, and its corresponding angle, θ_1. The PLL-type estimator used in this thesis is described by [37]

$$\frac{d\hat{\omega}_1}{dt} = \gamma_1\varepsilon \tag{4.8}$$

$$\frac{d\hat{\theta}_1}{dt} = \hat{\omega}_1 + \gamma_2\varepsilon \tag{4.9}$$

where $\varepsilon = \sin(\theta_1 - \hat{\theta}_1)$ and $\theta_1 - \hat{\theta}_1$ is the error in the estimated angle. In the above equations γ_1 and γ_2 are gain parameters. The notation "$\hat{}$" indicates an estimated variable or parameter. If the true frequency and position are given by $d\omega_1/dt = 0$ and $d\theta_1/dt = \omega_1$, then it is shown in [37] that the estimation error equations for $\tilde{\omega}_1 = \omega_1 - \hat{\omega}_1$ and $\tilde{\theta}_1 = \theta_1 - \hat{\theta}_1$ are asymptotically stable if $\{\gamma_1, \gamma_2\} > 0$. This implies that $\hat{\omega}_1$ and $\hat{\theta}_1$ will converge to ω_1 and θ_1 respectively, asymptotically. If the difference $\theta_1 - \hat{\theta}_1$ is small, it is possible to approximate $\sin(\theta_1 - \hat{\theta}_1) \approx \theta_1 - \hat{\theta}_1$, and the following characteristic polynomial of the system described by (4.8) and (4.9) can be found:

$$p^2 + \gamma_2 p + \gamma_1 \tag{4.10}$$

where $p = d/dt$. If the parameters are chosen as

$$\gamma_1 = \rho^2 \qquad \gamma_2 = 2\rho \tag{4.11}$$

then ρ can be adjusted to the desired bandwidth of the PLL-type estimator.

Modified PLL-Type Estimator

If the PLL-type estimator should synchronize to a constant (or at least close to constant) frequency, such as the grid frequency, it is possible to simplify the PLL-type estimator in (4.8)–(4.9). This is done by neglecting (4.8); then the modified PLL-type estimator becomes [76]

$$\frac{d\hat{\theta}_1}{dt} = \omega_1 = \omega_g + \rho\varepsilon. \tag{4.12}$$

In [76] it is shown that the modified PLL-type estimator rejects better voltage harmonics than the PLL-type estimator in (4.8)–(4.9). For small bandwidths the rejection is twice as good.

4.1.4 Internal Model Control (IMC)

Due to the simplicity of IMC for designing controllers, this method will be used throughout this thesis. IMC can, for instance, be used for designing current or speed control laws of any ac machine [40, 44, 102]. The idea behind IMC is to augment the error between the process, $G(p)$ and a process model, $\hat{G}(p)$, by a transfer function $C(p)$, see Fig. 4.2. Controller design is then just a matter of choosing the "right" transfer function $C(p)$. One common way is [31]

$$C(p) = \Big(\frac{\alpha}{p+\alpha}\Big)^n \hat{G}^{-1}(p) \tag{4.13}$$

where n is chosen so that $C(p)$ become proper, i.e., the order of the denominator is equal to or greater than that of the numerator. The closed-loop system will be

$$G_{cl}(p) = G(p)\Big(1 + C(p)[G(p) - \hat{G}(p)]\Big)^{-1} C(p) \tag{4.14}$$

which simplifies to

$$G_{cl}(p) = G(p)C(p) = \Big(\frac{\alpha}{p+\alpha}\Big)^n \tag{4.15}$$

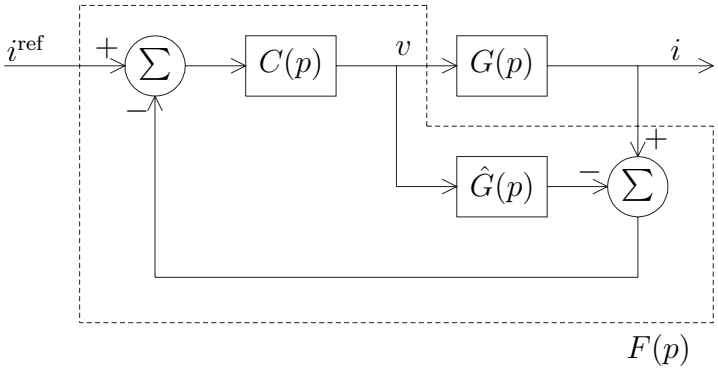

Fig. 4.2. Principle of IMC.

when $G(p) = \hat{G}(p)$. The parameter α is a design parameter, which for $n = 1$, is set to the desired bandwidth of the closed-loop system. The relationship between the bandwidth and the rise time (10%–90%) is $\alpha = \ln 9/t_{\text{rise}}$. The controller, $F(p)$, (inside the dashed area in Fig. 4.2) becomes

$$F(p) = \left(1 - C(p)\hat{G}(p)\right)^{-1} C(p). \tag{4.16}$$

For a first-order system, $n = 1$ is sufficient. The controller then typically becomes an ordinary PI controller:

$$F(p) = \frac{\alpha}{p}\hat{G}^{-1}(p) = k_p + \frac{k_i}{p}. \tag{4.17}$$

4.1.5 "Active Damping"

For a first-order system designed with IMC, the transfer function from the load disturbance E to output signal i is given by

$$G_{Ei}(p) = \frac{G(p)}{1 + G(p)F(p)} = \frac{p}{p + \alpha}G(p) \tag{4.18}$$

if all parameters are assumed to be known. If the dynamics of $G(p)$ are fast, the load disturbance rejection should be sufficient. However, as the dynamics of the process, $G(p)$, are normally much slower than the dynamics of the closed-loop system, the disturbance rejection is to a large extent determined by the process [76]. Therefore, addition of an inner feed-back loop, see Fig. 4.3, can improve the disturbance rejection. Then, the transfer function in (4.18) is changed to

$$G_{Ei}(p) = \frac{p}{p + \alpha}\frac{G(p)}{1 + G(p)R} = \frac{p}{p + \alpha}\frac{1}{G^{-1}(p) + R}. \tag{4.19}$$

For a first-order system it is possible to choose R so that the above transfer function can be reduced to

$$G_{Ei}(p) = K\frac{p}{(p + \alpha)^2} \tag{4.20}$$

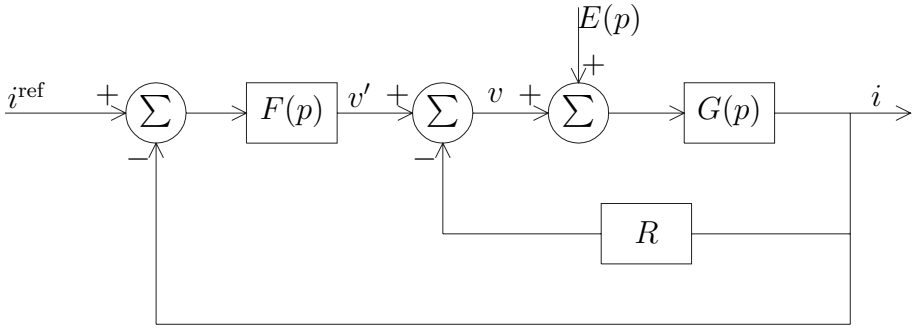

Fig. 4.3. Principle of "active damping."

where K is a constant. This means that a load disturbance E is damped with the same time constant as the control loop. This will be refereed to as "active damping" or "active resistance." "Active damping" has been used for the cage-bar induction machine to damp disturbances, such as varying back EMF [18, 41].

For example, consider the following first-order system (e.g., a dc machine)

$$L\frac{di}{dt} = v - Ri + e \tag{4.21}$$

where i is the state (current), v is the input signal (applied voltage), and e is a load disturbance (back emf). Then the "active damping" can be introduced by letting $v = v' - R_a i$, where the term $R_a i$ is the "active damping" term. Then, the system can be rewritten as

$$L\frac{di}{dt} = v' - (R + R_a)i + e \tag{4.22}$$

which has the following transfer function

$$G(p) = \frac{i(p)}{v'(p)} = \frac{1}{Lp + R + R_a}. \tag{4.23}$$

By using IMC, the following PI controller can be found:

$$F(p) = \frac{\alpha}{p}G^{-1}(p) = \alpha L + \alpha\frac{R + R_a}{p}. \tag{4.24}$$

Then, from (4.19), the transfer function from the load disturbance e to the output i can be determined as

$$G_{ei}(p) = \frac{p}{p + \alpha}\frac{1}{G^{-1}(p) + R_a}. \tag{4.25}$$

By choosing $R_a = \alpha L - R$, the transfer function is reduced to

$$G_{ei}(p) = \frac{p}{L\,(p + \alpha)^2}. \tag{4.26}$$

This means that the disturbance is damped with the same time constant as the dynamics of the control loop.

4.1.6 Saturation and Integration Anti-Windup

When designing control laws, the control signal cannot be arbitrary large due to design limitations of the converter or the machine. Therefore, the control signal must be limited (saturated). This causes the integral part of the PI controller to accumulate the control error during the saturation, so called integrator wind-up. This might cause overshoots in the controlled variable since the integration part of control law will keep the ideal control signal high even when the controlled variable is getting closer to the reference value [39].

One method to avoid integration wind-up is to use the "back-calculation" method [39]. The idea behind the back-calculation method is to modify the reference value in case of saturation, so that the ideal control signal, u, does not exceed the maximum value, i.e., $|u| = u_{\max}$. The algorithm can be described as [39]

$$u = k_p e + k_i I \tag{4.27}$$

$$u_{\text{sat}} = \text{sat}(u) \tag{4.28}$$

$$\frac{dI}{dt} = e + \frac{u_{\text{sat}} - u}{k_p} \tag{4.29}$$

where e is the control error and I is the integral of the control error.

4.1.7 Discretization

Throughout the thesis, differential equations and control laws will be described in continuous time. However, when implementing control laws in computers, they have to be discretized. The forward Euler method will be used, i.e., a derivative is approximated as

$$\frac{dx}{dt} \approx \frac{x(n+1) - x(n)}{T_{\text{sample}}} \tag{4.30}$$

where n indicates the sample number, at time $t = nT_{\text{sample}}$. For a continuous system given as

$$\dot{x}(t) = Ax(t) + Bu(t) \tag{4.31}$$

$$y(t) = Cx(t) \tag{4.32}$$

the discrete equivalent using the forward Euler method becomes

$$x(n+1) = (I + AT_{\text{sample}})x(n) + T_{\text{sample}}Bu(n) \tag{4.33}$$

$$y(n) = Cx(n). \tag{4.34}$$

The forward Euler discretization can also be written as

$$p \longrightarrow \frac{q-1}{T_{\text{sample}}} \tag{4.35}$$

where q is the forward shift operator. Stability of a linear time-invariant continuous system requires that the poles are in the left half plane. For a linear time-invariant discrete system the corresponding stability region is inside the unit circle [88]. Mapping the unit circle

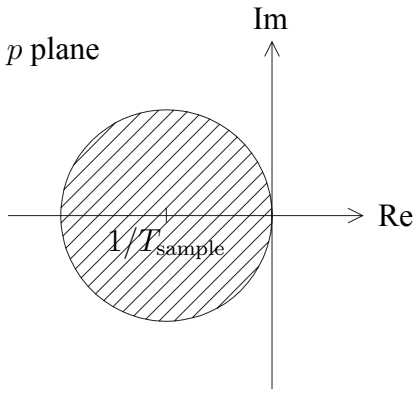

Fig. 4.4: Region of stability.

onto the continuous p plane using (4.35) gives the region in the p plane where the poles of the continuous system must be located in order to get a stable discretization [38]. Fig. 4.4 shows where the poles of continuous system must be located so that the forward Euler discretization, in (4.35), becomes stable. As seen in the figure the poles must be inside a circle with the radius of $1/T_{\text{sample}}$ with the center point located at $(-1/T_{\text{sample}}, 0)$ in order for the forward Euler discretization to be stable.

4.2 Mathematical Models of the DFIG System

In Fig. 4.5 an equivalent circuit of the DFIG system can be seen. As mentioned earlier, the system consists of a DFIG and a back-to-back voltage source converter with a dc link. The back-to-back converter consists of a grid-side converter (GSC) and a machine-side converter (MSC). Moreover, a grid filter is placed in between the GSC and the grid, since both the grid and the voltage source converter are voltage stiff and to reduce the harmonics caused by the converter. For voltage source converters the grid filter used is mainly an L-filter or an LCL-filter [62]. However, in this thesis the L-grid filter will be used, as shown in Fig. 4.5. More detailed description of the models of the components of the DFIG system will be performed in the following sections. In addition, the variables and the parameters in Fig. 4.5 will also be explained.

4.2.1 Machine Model

Due to its simplicity for deriving control laws for the DFIG, the Γ representation of the IG model will be used. Note, that from a dynamic point of view, the rotor and the stator leakage inductance have the same effect. Therefore, it is possible to use a different representation of the Park model in which the leakage inductance is placed in the rotor circuit, the so-called Γ *representation* of the induction machine [94]. The name is due to the formation of a "Γ" of the inductances; see Fig. 4.6. This model is described by the following space-vector

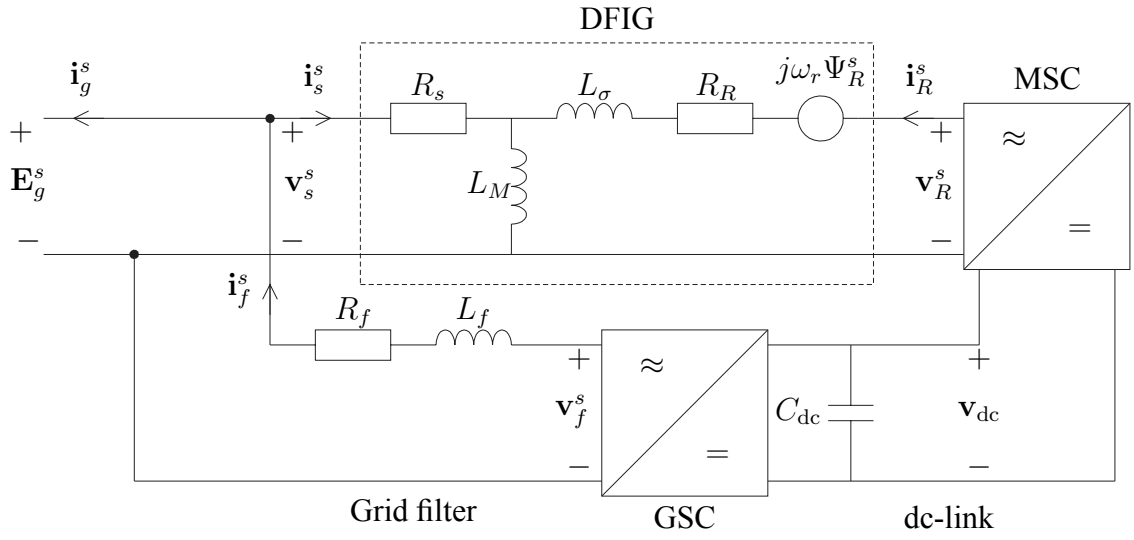

Fig. 4.5. Equivalent circuit of the DFIG system.

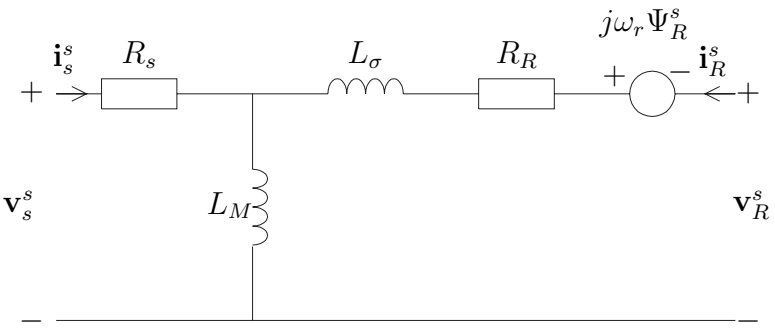

Fig. 4.6. Γ representation of the IG in stator coordinates. Superscript "s" indicates that the space vectors are referred to the reference frame of the stator of the DFIG.

equations in stator coordinates [94]:

$$\mathbf{v}_s^s = R_s\mathbf{i}_s^s + \frac{d\Psi_s^s}{dt} \tag{4.36}$$

$$\mathbf{v}_R^s = R_R\mathbf{i}_R^s + \frac{d\Psi_R^s}{dt} - j\omega_r\Psi_R^s \tag{4.37}$$

where superscript s indicates stator coordinates. The model can also be described in synchronous coordinates as

$$\mathbf{v}_s = R_s\mathbf{i}_s + \frac{d\Psi_s}{dt} + j\omega_1\Psi_s \tag{4.38}$$

$$\mathbf{v}_R = R_R\mathbf{i}_R + \frac{d\Psi_R}{dt} + j\omega_2\Psi_R \tag{4.39}$$

where the following notation is used:

$\mathbf{v}_s$	stator voltage;	Ψ_s	stator flux;
$\mathbf{v}_R$	rotor voltage;	Ψ_R	rotor flux;
$\mathbf{i}_s$	stator current;	R_s	stator resistance;
$\mathbf{i}_R$	rotor current;	R_R	rotor resistance;
ω_1	synchronous frequency;	ω_2	slip frequency.

The stator flux, rotor flux, and electromechanical torque are given by

$$\Psi_s = L_M(\mathbf{i}_s + \mathbf{i}_R) \tag{4.40}$$

$$\Psi_R = (L_M + L_\sigma)\mathbf{i}_R + L_M\mathbf{i}_s = \Psi_s + L_\sigma\mathbf{i}_R \tag{4.41}$$

$$T_e = 3n_p\mathrm{Im}\left[\Psi_s\mathbf{i}_R^*\right] \tag{4.42}$$

where L_M is the magnetizing inductance, L_σ is the leakage inductance, and n_p is the number of pole pairs. Finally, the mechanical dynamics of the induction machine are described by

$$\frac{J}{n_p}\frac{d\omega_r}{dt} = T_e - T_s \tag{4.43}$$

where J is the inertia and T_s is the shaft torque. The quantities and parameters of the Γ model relate to the Park model (or the T representation) as follows:

$$\mathbf{v}_R = \gamma\mathbf{v}_R \qquad \mathbf{i}_R = \frac{\mathbf{i}_r}{\gamma} \qquad \Psi_R = \gamma\Psi_r \qquad \gamma = \frac{L_{s\lambda} + L_m}{L_m}$$
$$R_R = \gamma^2 R_r \qquad L_\sigma = \gamma L_{s\lambda} + \gamma^2 L_{r\lambda} \qquad L_M = \gamma L_m.$$

4.2.2 Grid-Filter Model

In Fig. 4.7 the equivalent circuit of the grid filter in stator coordinates can be seen. The filter consists of an inductance L_f and its resistance R_f. Applying Kirchhoffs voltage law to the

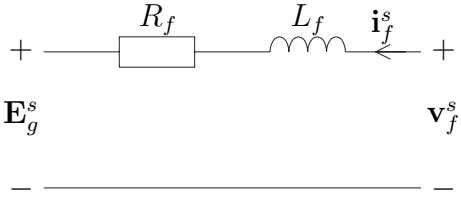

Fig. 4.7. Grid-filter model in stator coordinates.

circuit in the figure the following model in synchronous coordinates can be found:

$$\mathbf{E}_g = -\left(R_f + j\omega_1 L_f\right)\mathbf{i}_f - L_f\frac{d\mathbf{i}_f}{dt} + \mathbf{v}_f \tag{4.44}$$

where $\mathbf{E}_g$ is the grid voltage, $\mathbf{i}_f$ is the grid-filter current, and $\mathbf{v}_f$ is the grid-filter voltage supplied from the grid-side converter.

Harmonics

The transfer function, $G_f(p)$, of the grid filter can be expressed as

$$G_f(p) = \frac{\mathbf{i}_f^s(p)}{\mathbf{v}_f^s(p)} = \frac{1}{L_f p + R_f}. \tag{4.45}$$

This means that the damping of the grid filter is given by

$$|G_f(j\omega)| = \frac{1}{\sqrt{L_f^2\omega^2 + R_f^2}}. \tag{4.46}$$

If $L_f\omega \gg R_f$, the gain can be approximated as $|G_f(j\omega)| \approx 1/(L_f\omega)$. For example, if the switching frequency of the converter is $\omega = 100$ p.u. and $L_f = 0.2$ p.u., then the gain of the grid filter is $|G_f(j100)| \approx 0.05$ p.u. (corresponding to a damping of 26 dB) if R_f can be neglected.

4.2.3 DC-Link Model

The energy, W_{dc}, stored in the dc-link capacitor, C_{dc}, is given by

$$W_{\mathrm{dc}} = \frac{1}{2} C_{\mathrm{dc}} v_{\mathrm{dc}}^2 \tag{4.47}$$

where v_{dc} is the dc-link voltage. In Fig. 4.8 an equivalent circuit of the dc-link model, where the definition of the power flow through the grid-side converter (GSC) and the machine-side converter (MSC, can be seen. Moreover, if the losses in the actual converter can be

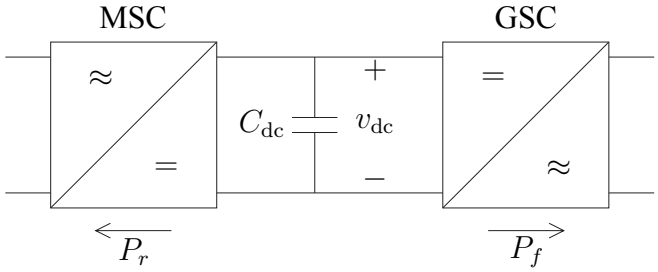

Fig. 4.8. DC-link model.

considered small and thereby be neglected, the energy in the dc-link capacitor is dependent on the power delivered to the grid filter, P_f, and the power delivered to the rotor circuit of the DFIG, P_r, as [76]

$$\frac{dW_{\mathrm{dc}}}{dt} = \frac{1}{2} C_{\mathrm{dc}} \frac{d}{dt} v_{\mathrm{dc}}^2 = -P_f - P_r. \tag{4.48}$$

This means that the dc-link voltage will vary as

$$C_{\mathrm{dc}} v_{\mathrm{dc}} \frac{dv_{\mathrm{dc}}}{dt} = -P_f - P_r \tag{4.49}$$

which means that $P_f = -P_r$ for a constant dc-link voltage.

4.2.4 Summary

The total model of the DFIG system, presented in Fig. 4.5 can now be summarized in synchronous coordinate, as

$$\frac{d\Psi_s}{dt} = \mathbf{E}_g - R_s\mathbf{i}_s - j\omega_1\Psi_s \tag{4.50}$$

$$\frac{d\Psi_R}{dt} = \mathbf{v}_R - R_R\mathbf{i}_R - j\omega_2\Psi_R \tag{4.51}$$

$$L_f\frac{d\mathbf{i}_f}{dt} = \mathbf{v}_f - (R_f + j\omega_1 L_f)\,\mathbf{i}_f - \mathbf{E}_g \tag{4.52}$$

$$C_{\mathrm{dc}}v_{\mathrm{dc}}\frac{dv_{\mathrm{dc}}}{dt} = -P_f - P_r \tag{4.53}$$

$$\frac{J}{n_p}\frac{d\omega_r}{dt} = T_e - T_s \tag{4.54}$$

where

$$\Psi_s = L_M\left(\mathbf{i}_s + \mathbf{i}_R\right) \tag{4.55}$$

$$\Psi_R = L_\sigma\mathbf{i}_R + L_M\left(\mathbf{i}_s + \mathbf{i}_R\right) \tag{4.56}$$

$$T_e = 3n_p\mathrm{Im}\left[\Psi_s\mathbf{i}_R^*\right] \tag{4.57}$$

$$P_r = 3\mathrm{Re}\left[\mathbf{v}_R\mathbf{i}_R^*\right] \tag{4.58}$$

$$P_f = 3\mathrm{Re}\left[\mathbf{v}_f\mathbf{i}_f^*\right]. \tag{4.59}$$

Note that in (4.50) that the stator voltage, $\mathbf{v}_s$, has been changed to the grid voltage, $\mathbf{E}_g$.

4.3 Field Orientation

In order to control the rotor current of a DFIG by means of vector control, the reference frame has to be aligned with a flux linkage. One common way is to control the rotor currents with stator-flux orientation [46, 61, 80, 99], or with air-gap-flux orientation [107, 110]. If the stator resistance is considered to be small, stator-flux orientation gives orientation also with the stator voltage [17, 61, 68]. According to [17], pure stator-voltage orientation can be done without any significant error. Note that in this thesis stator-voltage orientation will be, from now on, referred to as grid-flux orientation [21], i.e., the machine is aligned with a virtual grid flux.

Fig. 4.9 shows an example of the space vectors of the grid voltage and the stator flux. As illustrated by the figure there is only a small angular difference between the grid-voltage and stator-flux space vectors in the stator-flux reference frame compared to the grid-flux reference frame.

4.3.1 Stator-Flux Orientation

For a stator-flux-oriented system the synchronous angle θ_1 is defined as

$$\theta_1 = \angle\Psi_s^s \tag{4.60}$$

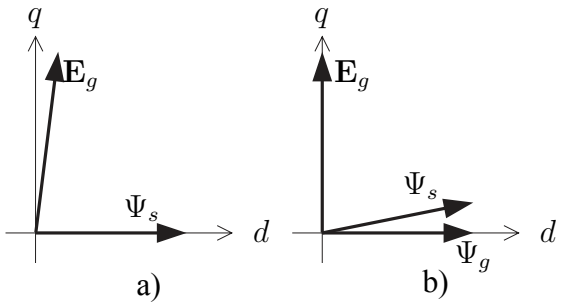

Fig. 4.9. Space-vector diagram of grid voltage and stator flux. a) Stator-flux orientation. b) Grid-flux orientation.

where Ψ_s^s is the stator flux in stator coordinates. Then the stator flux can be transformed to synchronous coordinates as

$$\Psi_s = \Psi_s^s e^{-j\hat{\theta}_1} = \psi_s e^{j\tilde{\theta}_1} \tag{4.61}$$

where $\hat{\theta}_1$ is the estimate of θ_1, ψ_s is the stator flux magnitude, and $\tilde{\theta}_1 = \theta_1 - \hat{\theta}_1$ is the error between the synchronous angle and its estimate. This means that for perfect field orientation, i.e. $\theta_1 = \hat{\theta}_1$, that $\Psi_s = \psi_s$, i.e., the space vector of the flux is real valued. Moreover, if the stator current, rotor current and the rotor position are measured, the stator flux can be calculated and thus the transformation angle can be found.

4.3.2 Grid-Flux Orientation

The basic idea behind grid-flux orientation is to define a virtual grid flux, Ψ_g^s, as [21, 76]

$$\Psi_g^s = \frac{\mathbf{E}_g^s}{j\omega_g} = -\frac{jE_g e^{j\theta_g}}{\omega_g} \tag{4.62}$$

where ω_g is the frequency of the grid voltage and θ_g is the corresponding angle. Since ω_g is close to constant, the virtual grid flux is linked to the grid voltage. This means that the relationship between the synchronous angle, θ_1, and the grid voltage angle, θ_g, for a grid-flux oriented (or stator-voltage oriented) system, is

$$\theta_1 = \angle\Psi_g^s = \angle - j\mathbf{E}_g^s = \theta_g - \frac{\pi}{2}. \tag{4.63}$$

Then, the grid voltage can be transformed to synchronous coordinates as

$$\mathbf{E}_g = \mathbf{E}_g^s e^{-j\hat{\theta}_1} = jE_g e^{j\tilde{\theta}_1} \tag{4.64}$$

where E_g is the grid voltage magnitude. This means that for perfect field orientation, i.e., $\theta_1 = \hat{\theta}_1$, that $\mathbf{E}_g = jE_g$, i.e., the space vector of the grid voltage is imaginary. Note that the grid-flux orientation is equal to the stator-flux orientation in the steady state, if the stator resistance can be neglected, since then

$$\mathbf{v}_s = \mathbf{E}_g = R_s\mathbf{i}_s + \frac{d\Psi_s}{dt} + j\omega_1\Psi_s \approx j\omega_1\Psi_s \tag{4.65}$$

and $\omega_1 = \omega_g$. The transformation angle for a grid-flux oriented system can be found directly from measurements of the stator voltage. However, in order to have some filtering effect a PLL-estimator, as described in Section 4.1.3, can be used to track the grid frequency and its corresponding angle.

4.4 Control of Machine-Side Converter

The main task of the machine-side converter is, of course, to control the machine. This is done by having an inner fast field-oriented current control loop that controls the rotor current. The field orientation could, for example, either be aligned with the stator flux of the DFIG or the grid flux. For both reference frames the q component of the rotor current largely determines the produced torque while the d component can be used to control, for instance, the reactive power at the stator terminals.

4.4.1 Current Control

As mentioned earlier, it is common to control the rotor current with either stator-flux orientation or grid-flux orientation. In order to derive the rotor-current control law, it is advantageous to eliminate $\mathbf{i}_s$ and Ψ_R from (4.38) and (4.39), which yields

$$\mathbf{v}_s = -R_s\mathbf{i}_R + \frac{d\Psi_s}{dt} + \Big(\frac{R_s}{L_M} + j\omega_1\Big)\Psi_s \tag{4.66}$$

$$\begin{aligned}\mathbf{v}_R &= (R_R + j\omega_2 L_\sigma)\mathbf{i}_R + L_\sigma\frac{d\mathbf{i}_R}{dt} + \frac{d\Psi_s}{dt} + j\omega_2\Psi_s \\ &= (R_R + R_s + j\omega_2 L_\sigma)\mathbf{i}_R + L_\sigma\frac{d\mathbf{i}_R}{dt} + \mathbf{E}\end{aligned} \tag{4.67}$$

$$\mathbf{E} = \mathbf{v}_s - \Big(\frac{R_s}{L_M} + j\omega_r\Big)\Psi_s \tag{4.68}$$

where $\mathbf{E}$ is the back EMF. It is possible to decouple the cross coupling between the d and q components of the rotor current—$j\omega_2 L_\sigma\mathbf{i}_R$ in (4.67)—in the control law [17, 80]. Further, it is possible to include a feed-forward compensating term in the control law that will compensate for the tracking error caused by variations in the back EMF. In [46, 61, 80] this is done by feed forward of the term $j\omega_2\Psi_s$ and neglecting the derivative of the flux in (4.67). Here, an estimate of the whole back EMF, $\hat{\mathbf{E}}$, will be used:

$$\begin{aligned}\mathbf{v}_R &= \mathbf{v}'_R + (j\hat{\omega}_2\hat{L}_\sigma - R_a)\mathbf{i}_R + k_E\hat{\mathbf{E}} \\ &= k_p\mathbf{e} + k_i\int\mathbf{e}\,dt + (j\hat{\omega}_2\hat{L}_\sigma - R_a)\mathbf{i}_R + k_E\hat{\mathbf{E}}.\end{aligned} \tag{4.69}$$

where "$\hat{}$" indicates an estimated quantity. A coefficient k_E is introduced in order to make the control law more general and to simplify the analysis in Chapter 5:

$$k_E = \begin{cases} 0 & \text{for control without feed forward of } \mathbf{E} \\ 1 & \text{for control with feed forward of } \mathbf{E}. \end{cases} \tag{4.70}$$

Furthermore, in (4.69), an "active resistance," R_a, has been introduced. The "active resistance" is used to increase the damping of disturbances and variations in the back EMF.

Similar approaches have been used for the squirrel-cage IG [18, 41]. How to choose the "active resistance" will be shown in next section. If the estimate of the slip frequency, $\hat{\omega}_2$, is put to zero in (4.69), the d and the q components of the rotor current will not be decoupled. In [46] it is stated that the influence of the decoupling term $j\omega_2 L_\sigma \mathbf{i}_R$ is of minor importance, since it is an order of magnitude smaller than the term $j\omega_2 \Psi_s$. Nevertheless, here the d and q components of the rotor current will be decoupled, since for a DSP-based digital controller it is easy to implement.

Substituting (4.69) in (4.67), the rotor current dynamics formed by the inner loop in Fig. 4.10 are now given by

$$L_\sigma \frac{d\mathbf{i}_R}{dt} = \mathbf{v}'_R - (R_R + R_s + R_a)\mathbf{i}_R \tag{4.71}$$

where the estimated parameters in the control law are assumed to have the correct values. If the back EMF is not compensated for, i.e., $k_E = 0$ in (4.69), it is treated as a disturbance to the rotor current dynamics. The transfer function from $\mathbf{v}'_R$ to $\mathbf{i}_R$ is

$$G(p) = \frac{1}{pL_\sigma + R_R + R_s + R_a}$$

which via (4.17) yields the following controller parameters

$$k_p = \alpha_c \hat{L}_\sigma \qquad k_i = \alpha_c(\hat{R}_R + \hat{R}_s + R_a) \tag{4.72}$$

where α_c is closed-loop bandwidth of the current dynamics, giving

$$G_{cl}(p) = \frac{p}{p + \alpha_c}. \tag{4.73}$$

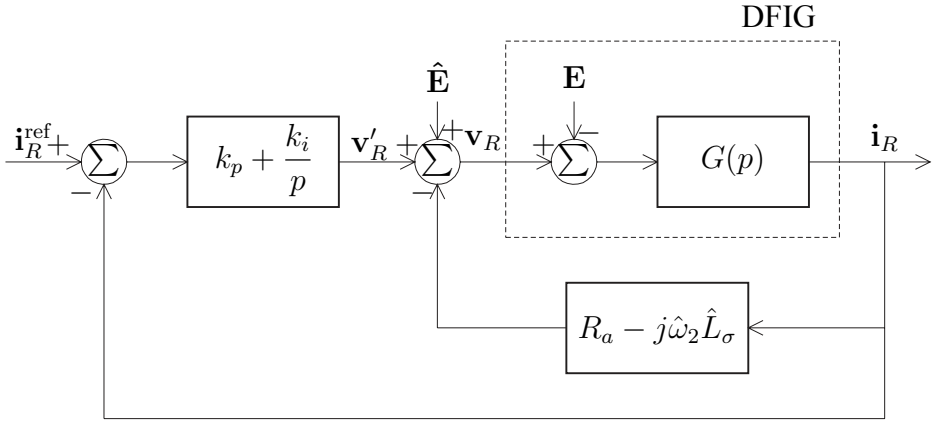

Fig. 4.10. Block diagram of the current control system. The dashed box is the model for the doubly-fed induction generator.

Selection of the "Active Resistance"

If the "active resistance" is set to $R_a = k_R(\alpha_c \hat{L}_\sigma - \hat{R}_R - \hat{R}_s)$, the transfer function from the back EMF, $\mathbf{E}$, to the current, $\mathbf{i}_R$, cf. Fig. 4.10, is given as

$$G_{\mathbf{Ei}}(p) = \frac{-p/(p+\alpha_c)}{pL_\sigma + L_\sigma \alpha_c k_R + (1-k_R)(R_r + R_s)} \tag{4.74}$$

if all model parameters are assumed to be accurate. A parameter k_R is introduced in a fashion similar to (4.70):

$$k_R = \begin{cases} 0 & \text{for control without "active resistance"} \\ 1 & \text{for control with "active resistance."} \end{cases} \tag{4.75}$$

This yields

$$G_{\mathbf{Ei}}(p) = \begin{cases} \dfrac{-p}{(p+\alpha_c)(pL_\sigma + R_R + R_s)} & k_R = 0 \\ \dfrac{-p}{L_\sigma(p+\alpha_c)^2} & k_R = 1 \end{cases} \tag{4.76}$$

This means that the above choice of R_a will force a change in the back EMF to be damped with the same bandwidth as the closed-loop current dynamics. Since R_a should be greater than zero, the minimum bandwidth of the current control loop when using "active resistance" becomes

$$\alpha_{c,\min} = (R_R + R_s)/L_\sigma. \tag{4.77}$$

For the investigated system, $\alpha_{c,\min}$ equals 0.08 p.u., which can be considered as a low value since for modern drive, a current control loop bandwidth of 7 p.u. is reasonable [40], corresponding to a rise time of 1 ms at a base frequency of 50 Hz.

In order to investigate the performance of the "active resistance" with regards to damping of disturbances, we study the ratio between the moduli of the frequency function corresponding to (4.74), with and without "active resistance":

$$G_r(\omega) = \frac{|G_{\mathbf{Ei}}(j\omega)|_{k_R=1}}{|G_{\mathbf{Ei}}(j\omega)|_{k_R=0}} = \sqrt{\frac{(R_R+R_s)^2 + \omega^2 L_\sigma^2}{(\alpha_c^2 + \omega^2)L_\sigma^2}}. \tag{4.78}$$

The following two extreme values of the above ratio are worth noting:

$$G_r(\omega) = \begin{cases} \dfrac{R_R + R_s}{\alpha_c L_\sigma} & \text{when } \omega \longrightarrow 0 \\ 1 & \text{when } \omega \longrightarrow \infty \end{cases} \tag{4.79}$$

which shows that while the "active resistance" has little impact on high-frequency disturbances, the damping of low-frequency disturbances is significantly improved, since, typically, $R_R + R_s \ll \alpha_c L_\sigma$. In Fig. 4.11, $G_r(\omega)$, is depicted for a current control loop bandwidth of 7 p.u. It can be seen that when using "active resistance," the damping of low-frequency disturbances has been significantly improved.

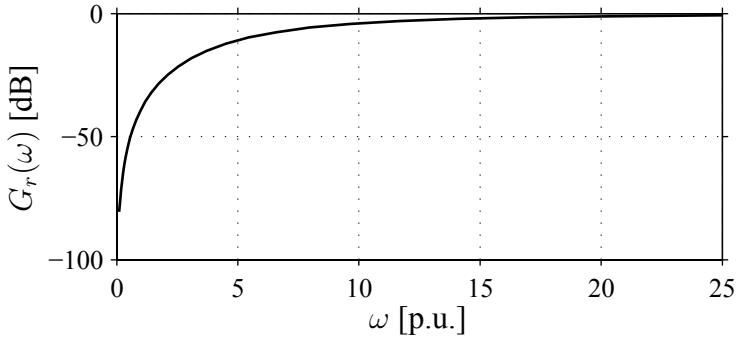

Fig. 4.11. Ratio of the damping improvement when using "active resistance" as a function of the frequency, ω, of the back EMF. The bandwidth of the current control loop is set to 7 p.u.

4.4.2 Torque Control

The electromechanical torque can be found from (4.42) as

$$T_e = 3n_p \mathrm{Im}\left[\Psi_s \mathbf{i}_R^*\right] \approx -3n_p \psi_s i_{Rq}. \tag{4.80}$$

For a stator-flux-oriented system the above approximation is actually an equality. Since the stator flux, ψ_s, is almost fixed to the stator voltage, the torque can be controlled by the q component of the rotor current, i_{Rq}. Since it is difficult to measure the torque, it is most often controlled in an open-loop manner. Therefore, the q component reference current, i_{Rq}^{ref}, can be determined from the reference torque, T_e^{ref}, as

$$i_{Rq}^{\mathrm{ref}} = -\frac{T_e^{\mathrm{ref}}}{3n_p \hat{\psi}_s}. \tag{4.81}$$

Instead of using the actual flux in (4.81), the approximation $\hat{\psi}_s \approx E_{g,\mathrm{nom}}/\omega_1$ can be used. Fig. 4.12 shows a block diagram of the open-loop torque control scheme.

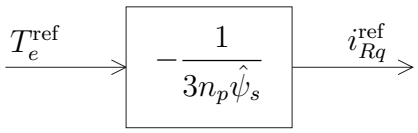

Fig. 4.12: Block diagram of the open-loop torque control.

4.4.3 Speed Control

Since the current dynamics, i.e., with the bandwidth α_c, should be set much faster than the speed dynamics, the speed can be controlled in cascade with the current. The mechanical dynamics are described by

$$\frac{J}{n_p}\frac{d\omega_r}{dt} = T_e - T_s \tag{4.82}$$

where T_e is the electromechanical torque and T_s is the shaft torque. The electromechanical torque can be expressed, under the assumption that the current dynamics are much faster than the speed dynamics, as

$$T_e = T_e^{\text{ref}} \tag{4.83}$$

where the reference torque is set to

$$T_e^{\text{ref}} = T_e'^{\text{ref}} - B_a\omega_r \tag{4.84}$$

where an "active damping" term, B_a, is introduced. This is, as mentioned earlier, an inner feedback loop [41], that can be used to improve the damping of disturbances. How to determine the "active damping" will be shown in the next section. The transfer function from $T_e'^{\text{ref}}$ to ω_r, treating the shaft torque, T_s, as a disturbance, then becomes

$$G(p) = \frac{\omega_r(p)}{T_e'^{\text{ref}}(p)} = \frac{1}{\frac{J}{n_p}p + B_a}. \tag{4.85}$$

Using IMC, as described in Section 4.1.4, the following PI controller can be found:

$$F(p) = \frac{\alpha_s}{p}G^{-1}(p) = k_p + \frac{k_i}{p} = \frac{\hat{J}\alpha_s}{n_p} + \frac{B_a\alpha_s}{p} \tag{4.86}$$

where α_s is the desired closed-loop bandwidth of the speed-control loop and the notation "^" indicates an estimated quantity. Fig. 4.13 shows a block diagram of the speed control system.

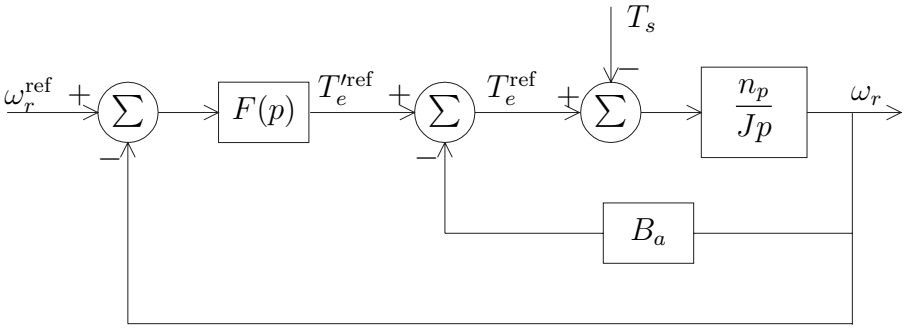

Fig. 4.13. Speed control loop.

Choosing the "Active Damping"

The transfer function from the shaft torque, T_s, to the rotational speed can be described by, see Fig. 4.13,

$$\frac{\omega_r(p)}{T_s} = \frac{p}{\frac{\hat{J}}{n_p}p^2 + (B_a + k_p)p + k_i} \tag{4.87}$$

if the active damping term is chosen as $B_a = \alpha_s \hat{J}/n_p$, (4.87), becomes

$$\frac{\omega_r(p)}{T_s} = \frac{p}{\frac{J}{n_p}(p+\alpha_s)^2} \tag{4.88}$$

i.e., change in the shaft torque, T_s, is damped with the same time constant as the bandwidth of the speed-control loop. In (4.88) all parameters are assumed to be ideal.

Evaluation

Fig. 4.14 shows a simulation of the speed control loop with rated driving torque. The bandwidth of the current control loop is set to 1.4 p.u. and the bandwidth of the speed control loop, α_s, is set to 0.014 p.u. A bandwidth of 1.4 p.u. corresponds to a rise time of 5 ms and 0.014 p.u. corresponds to 0.5 s. Initially the speed reference is set to 1.25 p.u., after 1 s it is changed to 0.75 p.u. After 4 s it is changed back to 1.25 p.u., and after 7 s the reference is ramped down during 3 s to 1 p.u. Finally, after 13 s the driving torque is changed to 50% of its rated value. The simulations shows that the speed-control loop behaves as expected. Moreover, it can be seen in the simulation that the speed reference step at 1 s forces limitation of the rotor current, since the maximum rotor current has been reached. This causes the rise time of the rotor speed to be longer than the ideal.

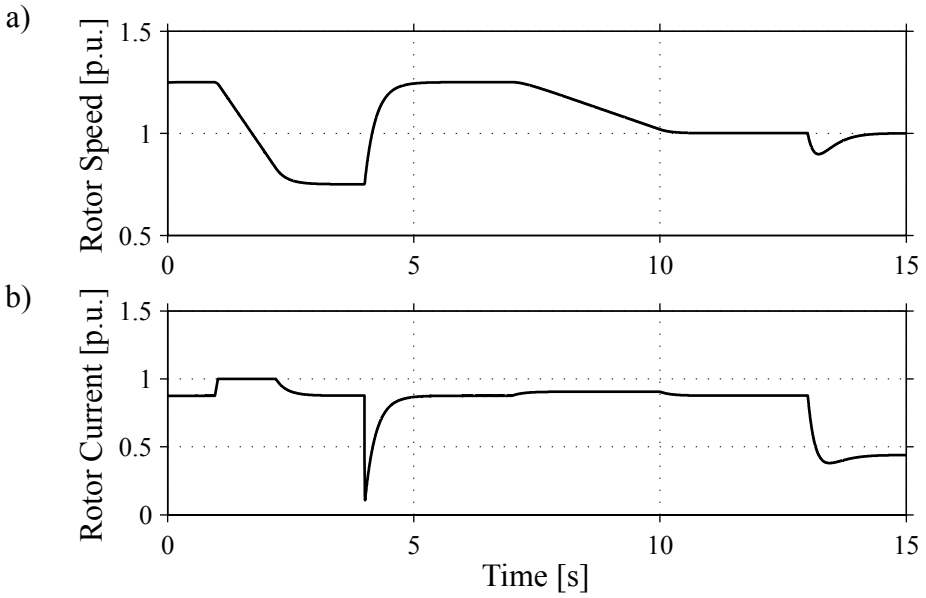

Fig. 4.14. Simulation of the speed-control loop. a) Rotor speed. b) Rotor current (q component).

4.4.4 Reactive Power Control

The instantaneous apparent power at the stator terminals, $\mathbf{S}_s = P_s + jQ_s$, can now be found as

$$\mathbf{S}_s = 3\mathbf{v}_s\mathbf{i}_s^* = 3\left(R_s\mathbf{i}_s + \frac{d\Psi_s}{dt} + j\omega_1\Psi_s\right)\mathbf{i}_s^* \tag{4.89}$$

Then the active and reactive power, neglecting the derivative of the stator flux, can thus be written as

$$P_s = 3R_s|\mathbf{i}_s|^2 + 3\omega_1\left(\psi_{sd}i_{sq} - \psi_{sq}i_{sd}\right) \tag{4.90}$$

$$Q_s = 3\omega_1\left(\psi_{sd}i_{sd} + \psi_{sq}i_{sq}\right). \tag{4.91}$$

For a stator-flux-oriented system, i.e., $\psi_{sd} = \psi_s$ and $\psi_{sq} = 0$, the above is reduced to

$$P_s = 3R_s|\mathbf{i}_s|^2 + 3\omega_1\psi_s i_{sq} = 3R_s\left(|\mathbf{i}_R|^2 - 2\frac{\psi_s}{L_M}i_{Rd} + \frac{\psi_s^2}{L_M^2}\right) - 3\omega_1\psi_s i_{Rq} \tag{4.92}$$

$$Q_s = 3\omega_1\psi_s i_{sd} = 3\omega_1\psi_s\left(\frac{\psi_s}{L_M} - i_{Rd}\right). \tag{4.93}$$

For a grid-flux-oriented system, where the voltage is aligned with the q axis, the expression in (4.92) and (4.93), still holds approximately since R_s can be considered as small. From (4.93) it can be seen that if

$$i_{Rd}^{\text{ref}} = \frac{\hat{\psi}_s}{\hat{L}_M} \tag{4.94}$$

the DFIG is operated at unity power factor.

Closed-Loop Reactive Power Control

Since the flux for a DFIG system can be considered as constant, there will be a static relationship between the reactive power and the d component of the rotor current, $G_{Qi_{Rd}}$. This means that IMC yields in an I controller, as

$$F_Q = \frac{\alpha_Q}{p}G_{Qi_{Rd}}^{-1} = -\frac{\alpha_Q}{3\omega_1\hat{\psi}_s}\frac{1}{p} \tag{4.95}$$

where α_Q is the bandwidth of the reactive power control loop. Moreover, since, in the steady state, $\hat{\psi}_s \approx E_{g,\text{nom}}/\omega_1$, the controller reduces to

$$F_Q = -\frac{\alpha_Q}{3E_{g,\text{nom}}}\frac{1}{p} \tag{4.96}$$

or as

$$i_{Rd}^{\text{ref}} = -\frac{\alpha_Q}{3E_{g,\text{nom}}}\int\left(Q_s^{\text{ref}} - Q_s\right)dt. \tag{4.97}$$

Of course, it would be possible to add a feed-forward term in order to compensate for the magnetizing current, i.e., ψ_s/L_M, in the above control law. However, since ψ_s/L_M is close to constant, the integration of the controller will compensate for the magnetizing current. Therefore, feed-forward compensation has not been considered for the reactive power control loop.

4.4.5 Sensorless Operation

"Sensorless" operation implies in this thesis that neither the rotor position nor the rotor speed is measured. This means that the stator frequency, ω_1, and the slip frequency, ω_2, and their corresponding angles, θ_1 and θ_2, must be estimated. The purpose of this section is to give an overview of some different estimation techniques that are available in literature. Note that if no stator variables exist in the control law, it might be unnecessary to estimate ω_1.

Estimation of Synchronous Frequency Angle

For a system which is oriented with the grid flux, or the voltage drop across the stator resistance is negligible, the angle $\hat{\theta}_1$ can easily be found by using a PLL, see Section 4.1.3, on the measured grid (stator) voltage. For a stator-flux-oriented control of the doubly-fed induction generator, where the voltage drop across the stator resistance can not be neglected, the stator flux can be estimated in stator coordinates using (4.36) as [46, 56]

$$\hat{\Psi}_s^s = \int (\mathbf{v}_s^s - \hat{R}_s \mathbf{i}_s^s) dt \tag{4.98}$$

and the estimate of the transformation angle, θ_1, can then be found from $\hat{\theta}_1 = \angle \hat{\Psi}_s^s$. The notation " ˆ " is used for estimated variables and parameters. Since the estimator in (4.98) is an open-loop integration, it is marginally stable. Thus, it has to be modified in order to gain stability. This could be done by replacing the open-loop integration with a low-pass filter [39]. It is also possible to estimate the transformation angle in synchronous coordinates. Starting with the stator voltage equation in stator coordinates and taking into account that for a stator-flux-oriented system, $\Psi_s^s = \psi_s e^{j\theta_1}$, yields

$$\mathbf{v}_s^s = R_s \mathbf{i}_s^s + \frac{d\Psi_s^s}{dt} = R_s \mathbf{i}_s^s + \frac{d\psi_s}{dt} e^{j\theta_1} + j\omega_1 \psi_s e^{j\theta_1}. \tag{4.99}$$

If $\mathbf{v}_s^s = \mathbf{v}_s e^{j\hat{\theta}_1}$ and $\mathbf{i}_s^s = \mathbf{i}_s e^{j\hat{\theta}_1}$, the above equation can be rewritten in synchronous coordinates as

$$\mathbf{v}_s = R_s \mathbf{i}_s + \frac{d\psi_s}{dt} e^{j\tilde{\theta}_1} + j\omega_1 \psi_s e^{j\tilde{\theta}_1} \tag{4.100}$$

where $\tilde{\theta}_1 = \theta_1 - \hat{\theta}_1$ is the angular estimation error. Taking the real part of the above equation and neglecting the flux dynamics yield

$$v_{sd} = R_s i_{sd} - \omega_1 \psi_s \sin(\tilde{\theta}_1). \tag{4.101}$$

Now, it is possible to form an error signal suitable for the PLL-type estimator, described in Section 4.1.3, as

$$\varepsilon = \sin(\theta_1 - \hat{\theta}_1) = \sin(\tilde{\theta}_1) = -\frac{v_{sd} - \hat{R}_s i_{sd}}{\omega_1 \psi_s} \approx -\frac{v_{sd} - \hat{R}_s i_{sd}}{v_s} \tag{4.102}$$

where the approximation is due to the fact that the stator is directly connected to the grid, so $\omega_1 \psi_s \approx v_s$.

Estimation of Slip-Frequency Angle

In the literature there are at least two methods to perform sensorless operation. In the first method, a set of variables is estimated or measured in one reference frame and then the variables are used in another reference frame to estimate the slip angle θ_2. Estimating the rotor currents from the flux and the stator currents can do this. In [15] the estimation of the rotor currents has been carried out in stator coordinates, while in [46, 68] it has been done in synchronous coordinates. The method will here be described in synchronous coordinates. Starting with the stator flux, which, in synchronous coordinates, is given by

$$\Psi_s = \psi_s = L_M(\mathbf{i}_s + \mathbf{i}_R) \tag{4.103}$$

and since the stator flux is known, i.e., it is to a great extent determined by the stator voltage, it is possible to use the above-mentioned equation to estimate the rotor current as follows:

$$\hat{\mathbf{i}}_R = \frac{\hat{\psi}_s}{\hat{L}_M} - \mathbf{i}_s \tag{4.104}$$

where the stator current has been measured and transformed with the transformation angle θ_1; see previous section for determination of this angle. The magnitude of the stator flux can be estimated as $\hat{\psi}_s = v_s/\omega_1$ [46]. Then, if the rotor current is measured in rotor coordinates the estimate of the slip angle can be found as

$$\hat{\theta}_2 = \angle \mathbf{i}_R^r - \angle \hat{\mathbf{i}}_R. \tag{4.105}$$

The second method is based on determining the slip frequency by the rotor circuit equation. In [56] a stator-flux-oriented sensorless control using the rotor voltage circuit equation is proposed. The rotor voltage equation is given by

$$\mathbf{v}_R = R_R \mathbf{i}_R + \frac{d\Psi_R}{dt} + j\omega_2 \Psi_R. \tag{4.106}$$

Neglecting the derivative of the flux, the slip frequency, ω_2, can be estimated from the imaginary part of the above equation as

$$\hat{\omega}_2 = \frac{v_{Rq} - \hat{R}_R i_{Rq}}{\psi_{Rd}} = \frac{v_{Rq} - \hat{R}_R i_{Rq}}{\psi_s + \hat{L}_\sigma i_{sd}}. \tag{4.107}$$

Then, the estimate of the slip angle, $\hat{\theta}_2$, can be found from integration of the estimate of the slip frequency, $\hat{\omega}_2$, as

$$\hat{\theta}_2 = \int \hat{\omega}_2 dt. \tag{4.108}$$

4.5 Control of Grid-Side Converter

The main objective of the grid-side converter is to control the dc-link voltage. The control of the grid-side converter consists of a fast inner current control loop, which controls the current through the grid filter, and an outer slower control loop that controls the dc-link voltage. The reference frame of the inner current control loop will be aligned with the grid flux. This means that the q component of the grid-filter current will control the active power delivered from the converter and the d component of the filter current will, accordingly, control the reactive power. This implies that the outer dc-link voltage control loop has to act on the q component of the grid-filter current.

4.5.1 Current Control of Grid Filter

In (4.44) the dynamics of the grid filter are described:

$$L_f \frac{d\mathbf{i}_f}{dt} = \mathbf{v}_f - (R_f + j\omega_1 L_f)\,\mathbf{i}_f - \mathbf{E}_g. \tag{4.109}$$

In order to introduce "active damping" and decouple the d and the q components of the grid-filter current, the applied grid-filter voltage, $\mathbf{v}_f$, is chosen as

$$\mathbf{v}_f = \mathbf{v}'_f - (R_{af} - j\omega_1 \hat{L}_f)\mathbf{i}_f. \tag{4.110}$$

This means that the inner closed-loop transfer function, assuming ideal parameters, becomes

$$G(p) = \frac{\mathbf{i}_f(p)}{\mathbf{v}'_f(p)} = \frac{1}{L_f p + R_f + R_{af}} \tag{4.111}$$

and, hence, by using IMC a PI controller can be determined with the bandwidth α_f. By choosing the active damping according to Section 4.1.5, i.e., $R_{af} = \alpha_f \hat{L}_f - \hat{R}_f$, the transfer function from grid voltage ("back emf"), $\mathbf{E}_g$, to the grid-filter current with ideal parameters then becomes

$$G_{\mathbf{E}_g \mathbf{i}_f}(p) = \frac{p}{L_f (p + \alpha_f)^2}. \tag{4.112}$$

Finally, the grid-filter current control law can now be written as

$$\mathbf{v}_f = \left(k_{pf} + \frac{k_{if}}{p}\right)(\mathbf{i}_f^{\text{ref}} - \mathbf{i}_f) - (R_{af} - j\omega_1 \hat{L}_f)\mathbf{i}_f \tag{4.113}$$

where

$$k_{pf} = \alpha_f \hat{L}_f \qquad k_{if} = \alpha_f(\hat{R}_f + R_{af}) = \alpha_f^2 \hat{L}_f \qquad R_{af} = \alpha_f \hat{L}_f - \hat{R}_f. \tag{4.114}$$

4.5.2 DC-Link Voltage Control

The dc-link voltage control in this thesis is essentially following [76]. One way of simplifying the control of the dc-link voltage is by utilizing feedback linearization, i.e., the nonlinear dynamics of the dc link are transformed into an equivalent linear system where linear control techniques can be applied [95]. This can be done by letting $W = v_{\text{dc}}^2$ [50, 76, 79]. The dc-link dynamics (4.48) are, thus, reduced to the following linear system

$$\frac{1}{2} C_{\text{dc}} \frac{dW}{dt} = -P_f - P_r \tag{4.115}$$

where, as mentioned earlier, P_f is the power delivered to the grid filter and P_r is the power delivered to the rotor circuit of the DFIG. If the power losses of the grid filter are small and the current control of the grid filter is aligned with the grid flux, the power delivered to the grid filter can be approximated as $P_f \approx 3E_{gq} i_{fq}$. Moreover, by assuming the current control loop to be fast, i.e., $i_{fq} = i_{fq}^{\text{ref}}$, and adding an "active damping" term as

$$i_{fq}^{\text{ref}} = i_{fq}'^{\text{ref}} + G_a W \tag{4.116}$$

where G_a is the gain of the "active damping," it is possible to write the dc-link dynamics as

$$\frac{1}{2}C_{\rm dc}\frac{dW}{dt} = -3E_g i'^{\rm ref}_{fq} - 3E_g G_a W - P_r. \tag{4.117}$$

The inner closed-loop transfer function becomes

$$G'(p) = \frac{W(p)}{i'^{\rm ref}_{fq}(p)} = \frac{-6E_g}{pC_{\rm dc} + 6E_g G_a}. \tag{4.118}$$

Then, by utilizing IMC, the following PI controller is obtained

$$F(p) = \frac{\alpha_w}{p}G^{-1}(p) = -\frac{\alpha_w \hat{C}_{\rm dc}}{6E_{g,\rm nom}} - \frac{\alpha_w G_a}{p} \tag{4.119}$$

where the magnitude of the grid voltage, E_g, is put to its nominal value, $E_{g,\rm nom}$, and α_w is the bandwidth of the dc-link voltage control loop. If the active damping is chosen as $G_a = \alpha_w \hat{C}_{\rm dc}/(6E_{g,\rm nom})$, a disturbance, i.e., P_r, will be damped as

$$G_{PW}(p) = \frac{-2p}{C_{\rm dc}(p^2 + 2\alpha_w \xi p + \alpha_w^2 \xi)} \tag{4.120}$$

where $\xi = E_{gq}/E_{g,\rm nom}$ and $\hat{C}_{\rm dc} = C_{\rm dc}$. With $E_{gq} = E_{g,\rm nom}$, i.e., $\xi = 1$, $G_{PW}(p)$ is reduced to

$$G_{PW}(p) = \frac{-2\alpha_w p}{C_{\rm dc}(p + \alpha_w)^2} \tag{4.121}$$

which means that a disturbance is damped with the same bandwidth as the dc-link voltage control loop. A block diagram of the dc-link voltage controller is depicted in Fig. 4.15.

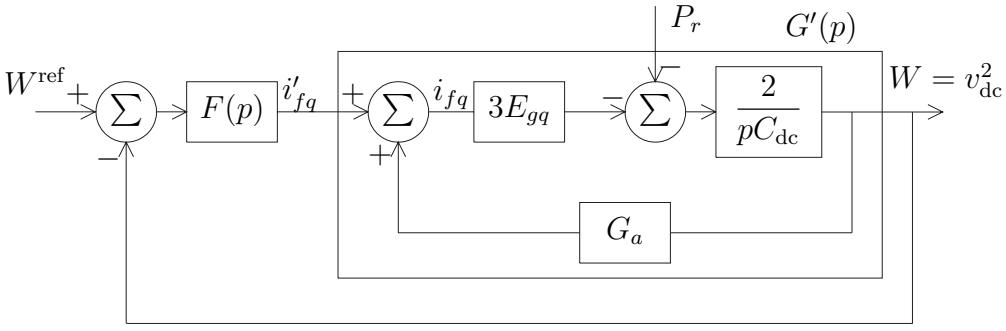

Fig. 4.15. DC-link voltage control loop.

Chapter 5

Evaluation of the Current Control of Doubly-Fed Induction Generators

In this chapter the current control law derived for the DFIG in the previous chapter is analyzed with respect to eliminating the influence of the back EMF, which is dependent on the stator voltage, rotor speed, and stator flux, in the rotor current. Further, stability analysis of the system is performed for different combinations of these terms in both a stator-flux and grid-flux-oriented reference frame, for both correctly known and erroneously parameters.

5.1 Stability Analysis

In order to investigate the influence of the feed-forward compensation of the back EMF and the influence of the "active resistance" on the stability of the system, an analysis is performed in this section. The analysis will be performed both for a stator-flux-oriented system and for a grid-flux-oriented system. In this section a full-order analysis of the system is performed, since one of the objectives is to study the impact of the current control law derived in the previous chapter.

5.1.1 Stator-Flux-Oriented System

Consider the system described by (4.66)–(4.68). Splitting (4.66) into real and imaginary parts, assuming stator-flux orientation, i.e., $\Psi_s^s = \psi_s e^{j\theta_1}$, the stator voltage equals the grid voltage, i.e., $\mathbf{v}_s = jE_g e^{j(\theta_g - \theta_1)}$. Making the variable substitution $\Delta\theta = \theta_g - \theta_1$, the system model can be rearranged as

$$\frac{d\mathbf{I}}{dt} = \mathbf{e} \tag{5.1}$$

$$\frac{d\psi_s}{dt} = -\frac{R_s}{L_M}\psi_s - E_g \sin(\Delta\theta) + R_s i_{Rd} \tag{5.2}$$

$$\frac{d\Delta\theta}{dt} = \frac{d\theta_g}{dt} - \frac{d\theta_1}{dt} = \omega_g - \frac{E_g \cos(\Delta\theta) + R_s i_{Rq}}{\psi_s} \tag{5.3}$$

$$\frac{d\mathbf{i}_R}{dt} = \frac{k_p\mathbf{e} + k_i\mathbf{I} + (j\hat{\omega}_2\hat{L}_\sigma - R_a)\mathbf{i}_R + k_{\mathbf{E}}\hat{\mathbf{E}}}{L_\sigma} - \frac{(R_R + R_s + j\omega_2 L_\sigma)\mathbf{i}_R + \mathbf{E}}{L_\sigma} \tag{5.4}$$

where

$$\mathbf{E} = \mathbf{E}_g - \Big(\frac{R_s}{L_M} + j\omega_r\Big)\Psi_s = jE_g e^{j\Delta\theta} - (\frac{R_s}{L_M} + j\omega_r)\psi_s. \tag{5.5}$$

In (5.1)–(5.4), the term $\mathbf{I}$ is the integration variable of the control error and $\mathbf{e} = \mathbf{i}_R^{\text{ref}} - \mathbf{i}_R$ is the control error. Note that (5.1) and (5.4) are complex-valued equations while (5.2) and (5.3) are real-valued equations. In the following analysis, the rotational speed ω_r will be assumed to be varying slowly, and is, therefore, treated as a parameter. Throughout this section, the machine model parameters will be assumed to be ideal and known.

If, for example, the rotor current is controlled by a high-gain feedback, it is possible to force the system to have both slow and fast time scales, i.e., the system behaves like a singularly perturbed system [57]. This means, that if the bandwidth of the current control loop is high enough, it is sufficient to study the system described by (5.2) and (5.3) in order to analyze the dynamic behavior of the DFIG. A stability analysis, assuming fast current dynamics, can be found in [13, 43]. Later on, analysis not neglecting the current dynamics will be compared to analysis neglecting the current dynamics; therefore a short summary will be presented. By linearization of the nonlinear system described by (5.2) and (5.3), the characteristic polynomial can be found. A first-order Taylor series expansion of the characteristic polynomial around $R_s = 0$ (as R_s is small, typically less than 0.1 p.u.) yields

$$p^2 + \frac{R_s}{L_M}\Big(2 - \frac{\omega_g L_M i_{Rd}^{\text{ref}}}{E_g}\Big)p + \Big(1 - \frac{R_s i_{Rq}^{\text{ref}}}{E_g}\Big)\omega_g^2 \tag{5.6}$$

where i_{Rq}^{ref} is the active current reference and i_{Rd}^{ref} is the magnetization current supplied from the rotor converter. Since R_s is small (< 0.1 p.u.), i_{Rq}^{ref} will only have a minor influence on the dynamics. However, i_{Rd}^{ref} will influence the dynamic performance. It is required that

$$i_{Rd}^{\text{ref}} < \frac{2E_g}{\omega_g L_M} \tag{5.7}$$

in order to maintain stability. A similar constraint can be found in [13, 43]. In order to operate the DFIG with unity power factor, one should select [99]

$$i_{Rd}^{\text{ref}} = \frac{\psi_s}{L_M} \approx \frac{E_g}{\omega_g L_M} \tag{5.8}$$

which value is half of the value in the condition in (5.7).

For the case when it is not possible to separate the time scales by a high-gain feedback in the current control loop, a full-order analysis should be performed. By linearizing the nonlinear system described by (5.1)–(5.4) in a similar manner as previously, the characteristic polynomial for the complete system can be found. A first-order Taylor series expansion of the characteristic polynomial around $R_s = 0$ yields

$$(p + \alpha_c)\Big(p + k_R\alpha_c + (1 - k_R)\frac{R_R}{L_\sigma}\Big)(p^4 + a_3p^3 + a_2p^2 + a_1p + a_0). \tag{5.9}$$

where expressions for the coefficients a_3 to a_0 become

$$a_3 = \alpha_c(1+k_R) + \frac{2R_s}{L_M} - \frac{R_s\omega_g i_{Rd}^{\text{ref}}}{E_g} + (1-k_R)\frac{R_R+2R_s}{L_\sigma} \tag{5.10}$$

$$\begin{aligned} a_2 = {} & \alpha_c^2 k_R + \omega_g^2 - \frac{i_{Rq}^{\text{ref}} R_s \omega_g^2}{E_g} + (1+k_R)\alpha_c R_s\Big(\frac{2}{L_M} - \frac{i_{Rd}^{\text{ref}}\omega_g}{E_g}\Big) \\ & + \frac{1-k_R}{L_\sigma}\alpha_c\Big(R_R+2R_s\Big) + \frac{1-k_R}{L_\sigma}R_R R_s\Big(\frac{2}{L_M} - \frac{i_{Rd}^{\text{ref}}\omega_g}{E_g}\Big) \end{aligned} \tag{5.11}$$

$$\begin{aligned} a_1 = {} & \frac{2\alpha_c^2 k_R R_s}{L_M} + (1-k_R)\frac{2\alpha_c R_R R_s}{L_M L_\sigma} - \frac{\alpha_c^2 k_R R_s i_{Rd}^{\text{ref}}\omega_g}{E_g} - (1-k_R)\frac{\alpha_c i_{Rd}^{\text{ref}} R_R R_s \omega_g}{L_\sigma E_g} \\ & - (1-k_{\mathbf{E}})\frac{R_s\omega_r\omega_g}{L_\sigma} + (1+k_R)\alpha_c\omega_g^2\Big(1 - \frac{i_{Rq}^{\text{ref}} R_s}{E_g}\Big) \\ & + (1-k_R)\omega_g^2\frac{R_R}{L_\sigma}\Big(1 - \frac{i_{Rq}^{\text{ref}} R_s}{E_g}\Big) + \frac{R_s}{L_\sigma}(1-2k_R+k_{\mathbf{E}})\omega_g^2 \end{aligned} \tag{5.12}$$

$$a_0 = \alpha_c^2\omega_g^2 k_R - \frac{\alpha_c^2 i_{Rq}^{\text{ref}} R_s \omega_g^2 k_R}{E_g} + \alpha_c\omega_g^2\frac{1-k_R}{L_\sigma}\Big(R_R + 2R_s - \frac{i_{Rq}^{\text{ref}} R_R R_s}{E_g}\Big). \tag{5.13}$$

The parameters k_E and k_R affect the roots of (5.9), directly and via a_0–a_3. The four different combinations of k_E and k_R available are, according to Table 5.1, termed Methods I–IV. Below, the characteristic polynomial (5.9) is investigated for the four different options.

TABLE 5.1. INVESTIGATED CURRENT CONTROL METHODS.

	k_E	k_R
Method I	0	0
Method II	0	1
Method III	1	0
Method IV	1	1

Methods I and II

Both methods give two real-valued poles (at $-\alpha_c$, $-R_R/L_M$ for Method I and two at $-\alpha_c$ for Method II) and four poles given by the fourth-degree factor. In Fig. 5.1, it is shown how one of the complex-conjugated poles given by the fourth-degree factor move with increasing bandwidth of the current control loop, α_c. The other complex-conjugated poles given by the fourth-degree factor are well damped and are therefore not shown in the figure. The IM is running as a generator at half of the rated torque, synchronous speed, and is magnetized from the rotor circuit. It can be seen in the figure that the poorly damped poles of Method II move with increasing bandwidth of the current control loop from stable to unstable and back to be stable again, while for Method I the poles are stable. Method II is unstable for bandwidths of the current control loop between 1.0–5.6 p.u. for the above mentioned operating point. Moreover, as shown in Fig. 5.1, the real part of the poorly damped pole is very small. This means that, when approximating fast current dynamics (marked with "x" in the figure), even a small error (due to the approximation of a fast current dynamics) may play a significant

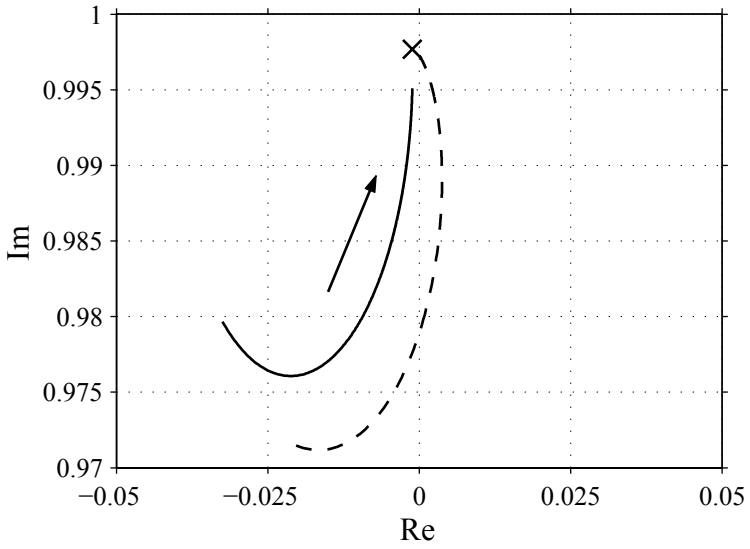

Fig. 5.1. Root loci of one of the poorly damped poles of the doubly-fed induction generator using current control methods without feed forward of the back EMF without "active resistance" (Method I, solid) and with "active resistance" (Method II, dashed). The arrow shows how the poles move with increasing bandwidth (0.5–15 p.u.) of the current control loop. The symbol "x" indicates the pole location when the current dynamics are neglected.

role for the result of the stability analysis. Hence, it is necessary to make a careful stability analysis, at least when using Methods I or II.

A similar approach, as will be performed in the next section, with Routh's table produces very large expressions of which it is difficult to determine any constrains for stability. Therefore, the approach with Routh's table is not carried out for Methods I and II.

Method III

When using *Method III*, i.e., feed forward of the back EMF, the characteristic polynomial in (5.9) is reduced to

$$(p+\alpha_c)^2\Big(p+\frac{R_R}{L_\sigma}\Big)(p^3+b_2p^2+b_1p+b_0). \tag{5.14}$$

The system has at least three real-valued poles, two located at $-\alpha_c$ and one at $-R_R/L_\sigma$. The coefficients in the third-degree factor become

$$b_2=\frac{2R_s}{L_M}+\frac{R_R+2R_s}{L_\sigma}-\frac{i_{Rd}^{\text{ref}}R_s\omega_g}{E_g} \tag{5.15}$$

$$b_1=\frac{(E_g-i_{Rq}^{\text{ref}}R_s)\omega_g^2}{E_g}+\frac{R_RR_s(2E_g-i_{Rd}^{\text{ref}}L_M\omega_g)}{L_ML_\sigma E_g} \tag{5.16}$$

$$b_0=\frac{\Big(-i_{Rq}^{\text{ref}}R_RR_s+(R_R+2R_s)E_g\Big)\omega_g^2}{L_\sigma E_g}. \tag{5.17}$$

As can be seen, the coefficients are not dependent on α_c for Method III.

TABLE 5.2. ROUTH'S TABLE.

p^3	1	b_1
p^2	b_2	b_0
p^1	$B = \dfrac{b_2 b_1 - b_0}{b_2}$	0
p^0	$\dfrac{Bb_0 - 0}{B} = b_0$	0

To investigate the stability of the system, Routh's table can be used [14], see Table 5.2. In order for the system to be stable, the coefficients in the first column must not change sign. Since the first coefficient in Routh's table is 1, all other coefficients must be positive in order to maintain stability. The expression for the coefficient B becomes quite complex; an approximation is

$$B \approx \frac{R_s\Big[2E_g - \omega_g L_M i_{Rd}^{\text{ref}}(R_R^2 + \omega_g^2 L_\sigma^2)\Big]}{L_M L_\sigma R_R E_g} \tag{5.18}$$

where a first-order Taylor series expansion of the coefficient B with respect to the stator resistance, R_s (around $R_s = 0$), has been carried out. The following constraint can be set on i_{Rd}^{ref} in order to keep the coefficient b_2 positive:

$$i_{Rd}^{\text{ref}} < \frac{E_g}{R_s \omega_g}\Big(\frac{2R_s}{L_M} + \frac{R_R + 2R_s}{L_\sigma}\Big). \tag{5.19}$$

For keeping the coefficient B positive, the following constraint has to be set

$$i_{Rd}^{\text{ref}} < \frac{2E_g}{\omega_g L_M}. \tag{5.20}$$

Since the term $-i_{Rq}^{\text{ref}} R_R R_s$ in b_0 is at least one order of magnitude lower than the term $(R_R + 2R_s)E_g$, b_0 can be considered to be positive. The constraint in (5.20) is "harder" than the constraint in (5.19). The constraint in (5.20) is identical to the constraint in (5.7) where the stability analysis was performed assuming fast current dynamics. The system has two poorly damped poles, caused by the flux dynamics, and the constraint on i_{Rd}^{ref} relates to the flux dynamics. Therefore, the constraint on i_{Rd}^{ref}, which relates to the flux dynamics, can be found more easily assuming fast current dynamics. Generally, a full-order analysis is still valuable, if the current dynamics are not fast, since other parameters also may influence the stability (for stability analysis assuming fast current dynamics).

Method IV

For *Method IV*, i.e., with feed forward of the back EMF and "active resistance," the characteristic polynomial in (5.9) is reduced to

$$(p + \alpha_c)^4\Big[p^2 + \frac{R_s}{L_M}\Big(2 - \frac{\omega_g L_M i_{Rd}^{\text{ref}}}{E_g}\Big)p + \Big(1 - \frac{R_s i_{Rq}^{\text{ref}}}{E_g}\Big)\omega_g^2\Big]. \tag{5.21}$$

The characteristic polynomial has four real roots located at $-\alpha_c$. The second-degree factor is identical to (5.6), where the current dynamics were neglected. Therefore, for Method IV, the same analysis as for the case with the assumption of fast current dynamics can be used.

5.1.2 Grid-Flux-Oriented System

The corresponding dynamics for the grid-flux-oriented system become

$$\frac{d\mathbf{I}}{dt} = \mathbf{e} \tag{5.22}$$

$$\frac{d\Psi_s}{dt} = \mathbf{E}_g - \left(\frac{R_s}{L_M} + j\omega_g\right)\Psi_s + R_s\mathbf{i}_R \tag{5.23}$$

$$\frac{d\mathbf{i}_R}{dt} = \frac{k_p\mathbf{e} + k_i\mathbf{I} + (j\hat{\omega}_2\hat{L}_\sigma - R_a)\mathbf{i}_R + k_{\mathbf{E}}\hat{\mathbf{E}}}{L_\sigma} - \frac{(R_R + R_s + j\omega_2 L_\sigma)\mathbf{i}_R + \mathbf{E}}{L_\sigma}. \tag{5.24}$$

Note that (5.22)–(5.24) are complex-valued equations. As for the case with stator-flux oriented analysis, the rotational speed ω_r will be assumed to be varying slowly and is therefore treated as a parameter. Throughout this section, parameters will exactly as in the previous section be assumed to be ideal and known.

If, as for the stator-flux orientation, the rotor current is controlled by a high-gain feedback, it is sufficient to study the dynamics described by (5.23), which have the following equilibrium points:

$$\psi_{sd0} = \frac{L_M\left(i_{Rd}^{\text{ref}}R_s^2 + L_M\left(i_{Rq}^{\text{ref}}R_s + E_g\right)\omega_g\right)}{R_s^2 + L_M^2\omega_g^2} \approx \frac{E_g + R_s i_{Rq}^{\text{ref}}}{\omega_g} \tag{5.25}$$

$$\psi_{qd0} = \frac{L_M R_s\left(i_{Rq}^{\text{ref}}R_s + E_g - i_{Rd}^{\text{ref}}L_M\omega_g\right)}{R_s^2 + L_M^2\omega_g^2} \approx \frac{R_s(E_g - i_{Rd}^{\text{ref}}L_M\omega_g)}{L_M\omega_g^2} \tag{5.26}$$

where the approximation is due to a first-order Taylor series expansion of R_s around $R_s = 0$. Then, the following characteristic polynomial can be determined:

$$p^2 + 2\frac{R_s}{L_M}p + \omega_g^2 + \frac{R_s^2}{L_M^2}. \tag{5.27}$$

In (5.27) it can be seen that the DFIG is poorly damped, and that the damping is only dependent of R_s and L_M. Moreover if the PLL-type estimator, described in Section 4.1.3 is used to track the grid voltage, the dynamics of the PLL will be separated from the flux dynamics in (5.27).

If the rotor currents cannot be neglected, a full-order analysis has to be performed. As in the previous section, the dynamic systems described by (5.22)–(5.24) consists of two parameters $k_{\mathbf{E}}$ and k_R that could be either set to zero or unity. This yields, in the same way as for the stator-flux-oriented system, four different options, Method I to Method IV, for the current control law, see Table 5.1.

Methods I and II

Linearizing of the non-linear system described by (5.22)–(5.24), its characteristic polynomial can be found. A first-order Taylor series expansion of the characteristic polynomial with respect to the stator resistance, R_s (around $R_s = 0$) yields

$$(p + \alpha_c)\left(p + k_R\alpha_c + (1 - k_R)\frac{R_R}{L_\sigma}\right)(p^4 + a_3p^3 + a_2p^2 + a_1p + a_0). \tag{5.28}$$

where the coefficients a_3 to a_0 become

$$a_3 = 2\frac{R_s}{L_M} + \alpha_c(1+k_R) - (k_R-1)\frac{R_R+2R_s}{L_\sigma} \tag{5.29}$$

$$a_2 = \alpha_c^2 k_R + \frac{2(1+k_R)\alpha_c R_s}{L_\sigma} - \frac{(k_R-1)\left(2R_R R_s + \alpha_c L_M(R_R+2R_s)\right)}{L_M L_\sigma} + \omega_g^2 \tag{5.30}$$

$$\begin{aligned} a_1 = {} & 2\frac{\alpha_c^2 k_R R_s}{L_M} + \alpha_c(1+k_R)\omega_g^2 \\ & - (k_R-1)\frac{2\alpha_c R_R R_s + (R_R+2R_s)L_M\omega_g^2}{L_M L_\sigma} - 2\frac{R_s\omega_g\omega_r}{L_\sigma} \end{aligned} \tag{5.31}$$

$$a_0 = \alpha_c^2 k_R \omega_g^2 - \frac{(k_R-1)(R_R+2R_s)\alpha_c\omega_g^2}{L_\sigma}. \tag{5.32}$$

In Fig. 5.2 it is shown how one of the complex-conjugated poles, as given by the fourth-order characteristic polynomial, move with increasing bandwidth of the current control loop, α_c. The second-complex conjugated poles are well damped and are therefore not shown in the figure. The operating condition is as in Fig. 5.1. It can be seen in the figure that

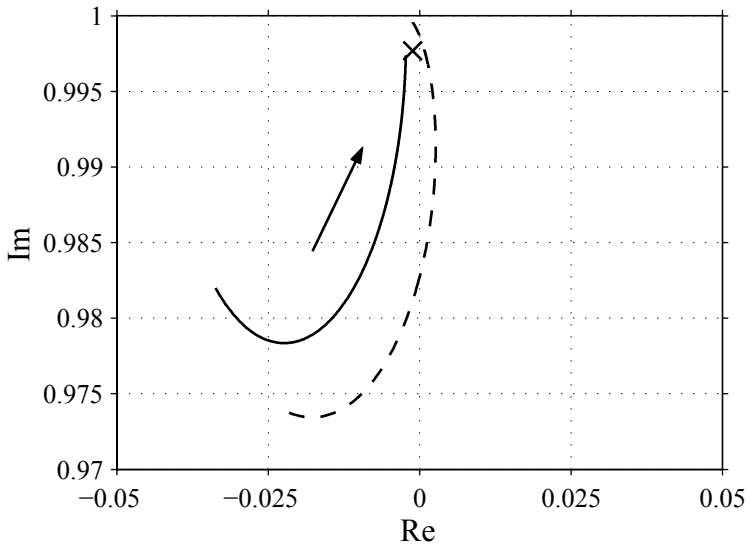

Fig. 5.2. Root loci of one of the poorly damped poles of the doubly-fed induction generator using current control methods without feed forward of the back EMF without "active resistance" (Method I, solid) and with "active resistance" (Method II, dashed). The arrow shows how the poles move with increasing bandwidth (0.5–15 p.u.) of the current control loop. The symbol "x" indicates the pole location when the current dynamics are neglected.

for Method I the poorly damped pole is stable and for Method II the poorly damped pole moves with increasing bandwidth of the current control loop from stable to unstable and back to be stable again. For the in the figure investigated case, the system is unstable for bandwidths between 1.1 p.u. and 3.8 p.u. for Method II. Of course, since the root loci are plotted with numerical values the result are only valid for the given operation conditions and for the investigated machine. As could also be seen for the stator-flux oriented case, a current control loop bandwidth of approximately 15 p.u. might not be high enough in order to be able to make the assumption of a fast current dynamics (marked with "x" in the figure),

at least for Method I, since the error is in the same order of magnitude as the real part of the pole, see Fig. 5.2.

Method III

When using *Method III*, i.e., feed forward of the back EMF, the characteristic polynomial can be found from the system (5.22)–(5.24) as

$$(p+\alpha_c)^2\left(p+\frac{R_R+R_s}{L_\sigma}\right)^2\left(p^2+2\frac{R_s}{L_M}p+\frac{R_s^2}{L_M^2}+\omega_g^2\right). \tag{5.33}$$

Note that the above characteristic polynomial has not been expanded by a Taylor series. The system has at least four real-valued poles, two located at $-\alpha_c$ and two at $-(R_R+R_s)/L_\sigma$.

Method IV

For *Method IV*, i.e., with feed forward of the back EMF and "active resistance," the characteristic polynomial becomes

$$(p+\alpha_c)^4\left(p^2+2\frac{R_s}{L_M}p+\frac{R_s^2}{L_M^2}+\omega_g^2\right). \tag{5.34}$$

Note that the above characteristic polynomial has not been expanded by a Taylor series. The characteristic polynomial has four real roots located at $-\alpha_c$. The second-degree factor is identical to the characteristic polynomial in (5.27) where the current dynamics were neglected, i.e., assumed to be much faster than the flux dynamics. Therefore, for Method IV, the same analysis as for the case with the assumption of fast current dynamics can be used.

5.1.3 Conclusion

It has been shown that by using grid-flux orientation the stability and the damping of the system is independent of the rotor current, in contrast to stator-flux orientation. This implies that for a grid-flux-oriented system, it is possible to magnetize the DFIG entirely from the rotor circuit without reducing the damping of the system. Moreover, for the grid-flux-oriented system, it is possible to produce as much reactive power as possible and still have a stable system with the same damping from a stability point of view.

By utilizing the feed-forward compensation, stability of the derived current control law is independent of the bandwidth of the current control loop and the order of the system to analyze is reduced. Further, as shown in Section 4.4.1, the inclusion of the "active resistance" improves significantly the damping of low-frequency disturbances, for higher bandwidths of the current control loop. Therefore, Method IV with both feed-forward compensation and "active resistance" can be assumed to be the best one of the investigated methods.

5.2 Influence of Erroneous Parameters on Stability

We now study how the closed-loop current-control transfer function, $G_{cl}(p)$, given by (4.73) and the transfer function from a disturbance to the rotor current, $G_{\mathbf{Ei}}(p)$, given by (4.74) are

influenced by non-ideal parameters. For ideal parameters the rotor current is determined by

$$\mathbf{i}_R = G_{cl}(p)\mathbf{i}_R^{\text{ref}} + G_{\mathbf{Ei}}(p)\mathbf{E}. \tag{5.35}$$

The methods where the back EMF is compensated for using feed forward (Methods III and IV), the back EMF will not be totally compensated for due to non-ideal parameters. This means that the conditions for impact of parameter variations also hold for the methods with feed forward of the back EMF, even though the effect might be less severe. Note that (5.35) is independent of the field orientation.

In the analysis below, the error in a parameter is denoted with the symbol $\tilde{}$, e.g. $\tilde{L}_\sigma = L_\sigma - \hat{L}_\sigma$. The parameters to be studied in the following are L_σ, R_s, and R_R. Since L_M is only included in the feed-forward compensation, it has no impact in the following analysis, and, hence, it is not included.

5.2.1 Leakage Inductance, L_σ

For errors in $\hat{L}_\sigma$, the rotor current, given by (5.35) for ideal parameters, is given by

$$\mathbf{i}_R \approx \frac{\alpha_c}{p+\alpha_c}\left(1 + j\tilde{L}_\sigma\omega_2 G_{\mathbf{Ei}}(p)\right)\mathbf{i}_R^{\text{ref}} + \left(1 - j\tilde{L}_\sigma\omega_2\frac{\alpha_c}{p+\alpha_c}\right)G_{\mathbf{Ei}}(p)\mathbf{E} \tag{5.36}$$

where the approximation is due to a first-order Taylor series expansion of $\tilde{L}_\sigma$ around $\tilde{L}_\sigma = 0$ and $L_\sigma \gg \tilde{L}_\sigma$. From (5.36) it can be seen that small values of $\tilde{L}_\sigma$ do not significantly influence the dynamic performance. A similar analytical expression for larger errors in $\hat{L}_\sigma$ is difficult to derive. In order to study the behavior for larger $\tilde{L}_\sigma$, root loci are shown in Fig. 5.3 for Method I with three different values of $\hat{L}_\sigma$. The operating condition corresponds to that of Fig. 5.1; however, the rotor speed is set to 1.3 p.u. so that the effect of the cross coupling between the d and the q components is included. It can be seen in Fig. 5.3 that the influence of errors in $\hat{L}_\sigma$ is small for the investigated 2-MW DFIG. However, for smaller DFIGs such as the 22-kW laboratory DFIG, the difference is larger. This is shown in Fig. 5.4. Clearly, it is preferable to overestimate $\hat{L}_\sigma$. One reason for this is that the proportional part of the controller will be increased, see (4.72). Hence, the bandwidth of the current control loop is increased if $\hat{L}_\sigma$ is overestimated.

5.2.2 Stator and Rotor Resistances, R_s and R_R

Since errors in R_s and R_R influence the performance in the same way, we will study the sum of the errors in the resistances: $\tilde{R} = \tilde{R}_s + \tilde{R}_R$.

For Methods II and IV where "active resistance" is used, the rotor current is given by (5.35) if $2\alpha_c L_\sigma \gg \tilde{R}$. This means that when using "active resistance," the system is not dependent on errors in R_s and R_R. For Methods I and III, the rotor current is found to be

$$\begin{aligned}\mathbf{i}_R \approx & \frac{\alpha_c(L_\sigma p + R_s + R_R - \tilde{R})}{L_\sigma p^2 + \alpha_c L_\sigma p + (R_s + R_R - \tilde{R})\alpha_c}\mathbf{i}_R^{\text{ref}} \\ & - \frac{p}{L_\sigma p^2 + \alpha_c L_\sigma p + (R_s + R_R - \tilde{R})\alpha_c}\mathbf{E}\end{aligned} \tag{5.37}$$

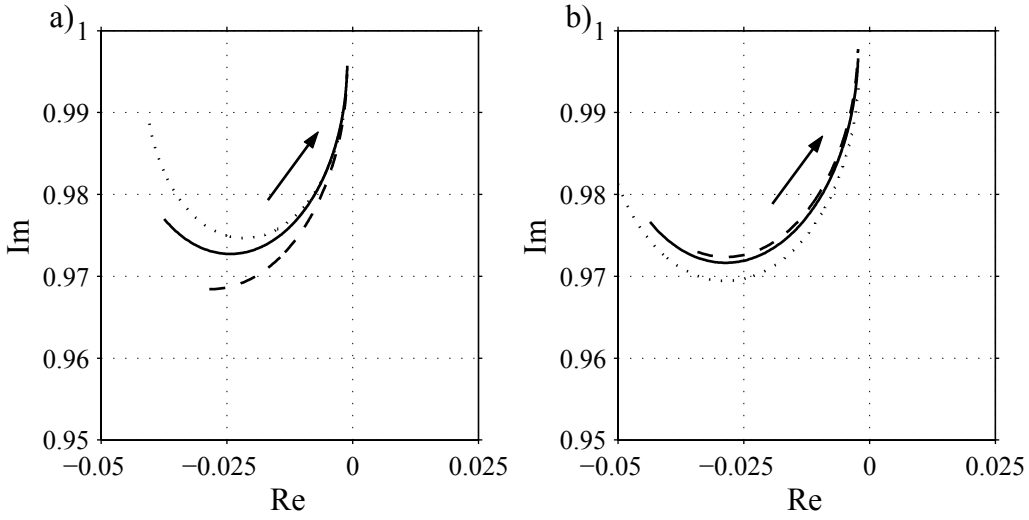

Fig. 5.3. Root loci of one of the poorly damped poles of the doubly-fed induction generator using Method I for three different errors in the leakage inductance parameter $\tilde{L}_\sigma$. Solid is $\tilde{L}_\sigma = 0$, dashed $\tilde{L}_\sigma = -0.5L_\sigma$, and dotted $\tilde{L}_\sigma = 0.5L_\sigma$. The arrow shows how the poles move with increasing bandwidth (0.5–15 p.u.) of the current control loop. a) Stator-flux orientation. b) Grid-flux orientation.

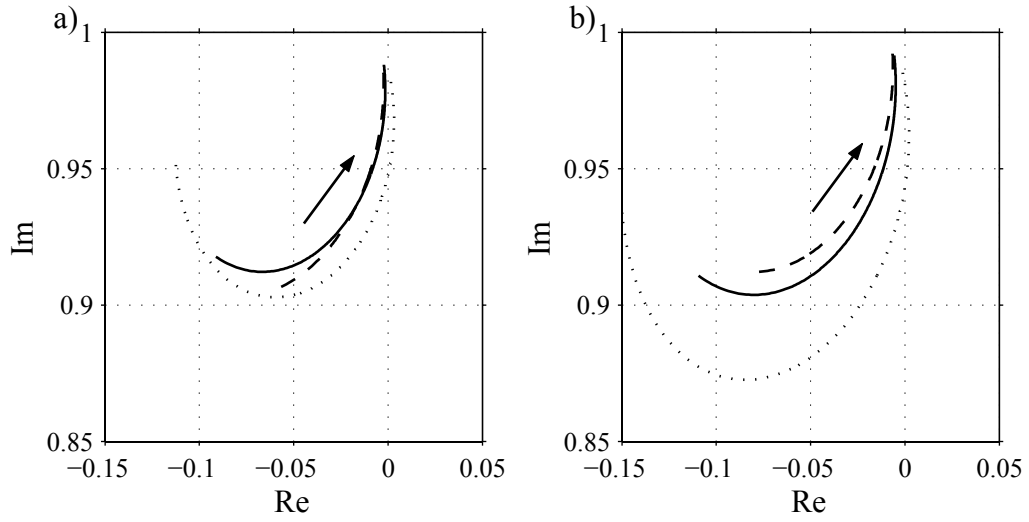

Fig. 5.4. Root loci of one of the poorly damped poles of the laboratory 22 kW doubly-fed induction generator using Method I for three different errors in the leakage inductance parameter $\tilde{L}_\sigma$. Solid is $\tilde{L}_\sigma = 0$, dashed $\tilde{L}_\sigma = -0.5L_\sigma$, and dotted $\tilde{L}_\sigma = 0.5L_\sigma$. The arrow shows how the poles move with increasing bandwidth (0.5–15 p.u.) of the current control loop. a) Stator-flux orientation. b) Grid-flux orientation.

the approximation assuming $\alpha_c L_\sigma \gg R_s + R_R$. In (5.37) it can be seen that if the resistances are overestimated, i.e., $\tilde{R} < 0$, the damping of the current dynamics are actually improved, i.e., the same phenomenon as using "active resistance." Fig. 5.5 shows the root loci for Method I of the investigated 2-MW DFIG. In the figure it can be seen that the influence of errors in the resistance is small. However, as for the case with errors in $\hat{L}_\sigma$, the difference is larger for smaller DFIGs, such as the 22-kW laboratory DFIG. This is shown in Fig. 5.4.

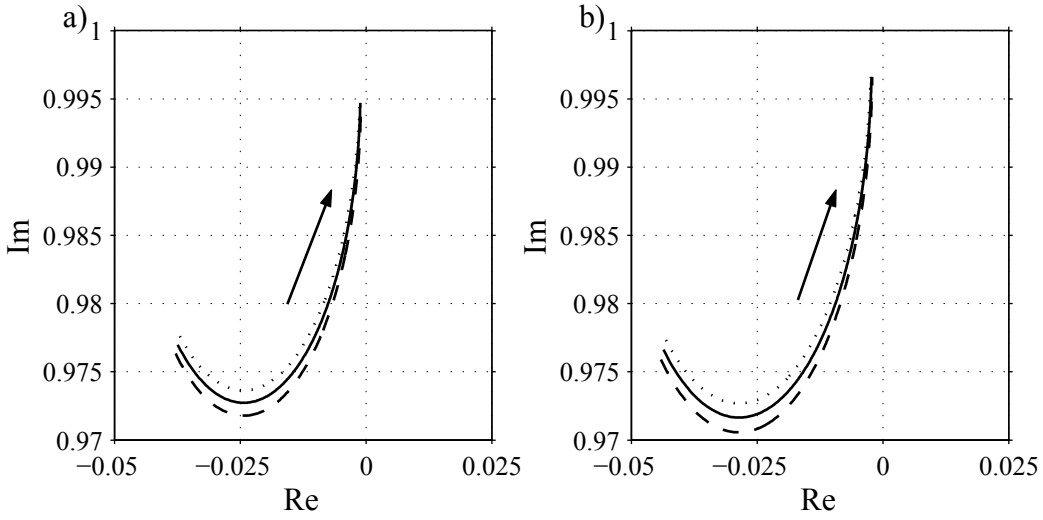

Fig. 5.5. Root loci of one of the poorly damped poles of the doubly-fed induction generator using Method I for three different errors in the stator and rotor resistances parameters $\tilde{R}$. Solid is $\tilde{R} = 0$, dashed $\tilde{R} = -0.5R$, and dotted $\tilde{R} = 0.5R$. The arrow shows how the poles move with increasing bandwidth (0.5–15 p.u.) of the current control loop. a) Stator-flux orientation. b) Grid-flux orientation.

Moreover, as shown previously when only using "active resistance" (Method II), the poorly damped poles (corresponding to the flux dynamics) could be unstable for certain operating conditions. Therefore, especially for Method I and smaller machines, the system can become

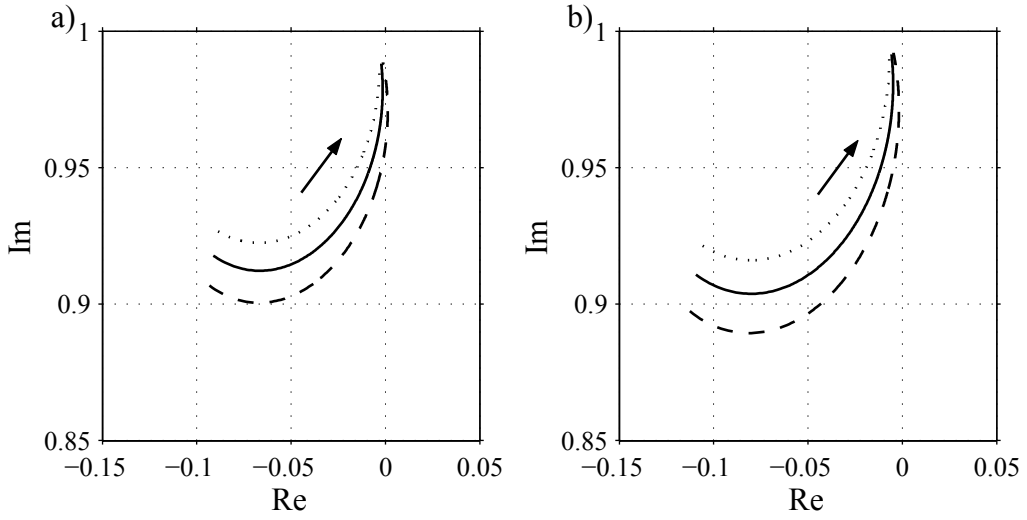

Fig. 5.6. Root loci of one of the poorly damped poles of the laboratory 22 kW doubly-fed induction generator using Method I for three different errors in the stator and rotor resistances parameters $\tilde{R}$. Solid is $\tilde{R} = 0$, dashed $\tilde{R} = -0.5R$, and dotted $\tilde{R} = 0.5R$. The arrow shows how the poles move with increasing bandwidth (0.5–15 p.u.) of the current control loop. a) Stator-flux orientation. b) Grid-flux orientation.

unstable if the resistances are overestimated, as illustrated in Fig. 5.6. It can also be seen in the figures that the grid-flux-oriented system seems, even though the difference is small, to

be less sensitive to overestimated $R = R_s + R_R$ in comparison to the stator-flux-oriented system.

5.3 Experimental Evaluation

The performance of the various current control methods are evaluated by reference step responses, see Fig. 5.7. See Appendix B.2 for data and parameters of the laboratory setup. This has been done by letting i_{Rq}^{ref} change from -0.25 p.u. to 0.25 p.u. when the rotor speed, ω_r, reaches 0.32 p.u., and vice versa when the rotor speed reaches 0.16 p.u. The DFIG is magnetized entirely from the stator, i.e., $i_{Rd}^{\text{ref}} = 0$, and is operated under no-load conditions. Further, the stator voltage of the DFIG was 230 V. Data have been sampled with 10 kHz and low-pass filtered with a cut-off frequency set to 5 kHz. In the measurements the bandwidth of the current control was set to 1.4 p.u. Offsets in the stator voltage measurements caused

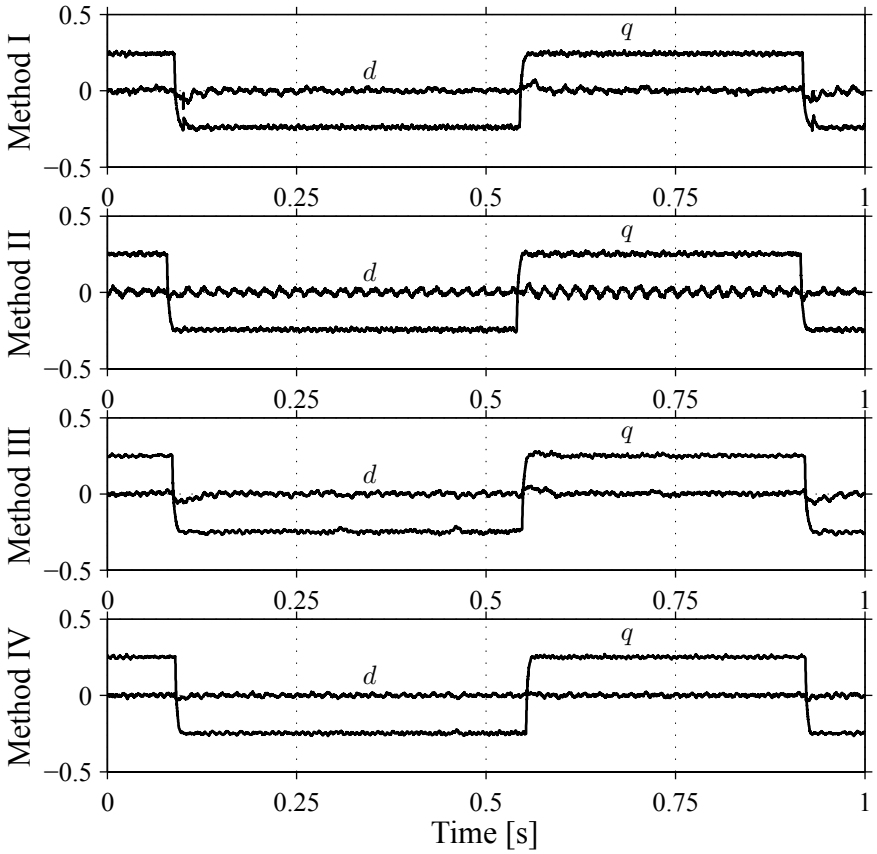

Fig. 5.7. Experiment of the stator-flux oriented current control step responses of the q component of the rotor current.

a 100-Hz frequency component in the stator voltage, which influenced the performances of the current control Methods III and VI, since the stator voltage is included in the control law. However, a notch filter limited the influence of the 100-Hz frequency component. A scrutiny investigation of Fig. 5.7 shows that Method II gives a 50-Hz ripple. The reason for this is that by using only "active resistance" to damp the back EMF, the system might be degraded, i.e., unstable, depending on the bandwidth of the current control loop, as shown earlier. Even

though the difference is fairly small, it can be seen in Fig. 5.7 that Method IV managed best to follow its reference values in this comparison.

5.3.1 Comparison Between Stator-Flux and Grid-Flux-Oriented System

The aim of this section is to experimentally verify the analytical result obtained in Section 5.1, that by using grid-flux orientation the stability and the damping of the system is independent of the rotor current, in contrast to stator-flux orientation

In Fig. 5.8 shows an experimental case of a stator-flux-oriented and a grid-flux-oriented rotor current control. In the figures the d component of the rotor current is increased from 0 p.u. to 1 p.u. after 0.1 s. The q component of the rotor current is set to 0.5 p.u. When i_{Rd} is

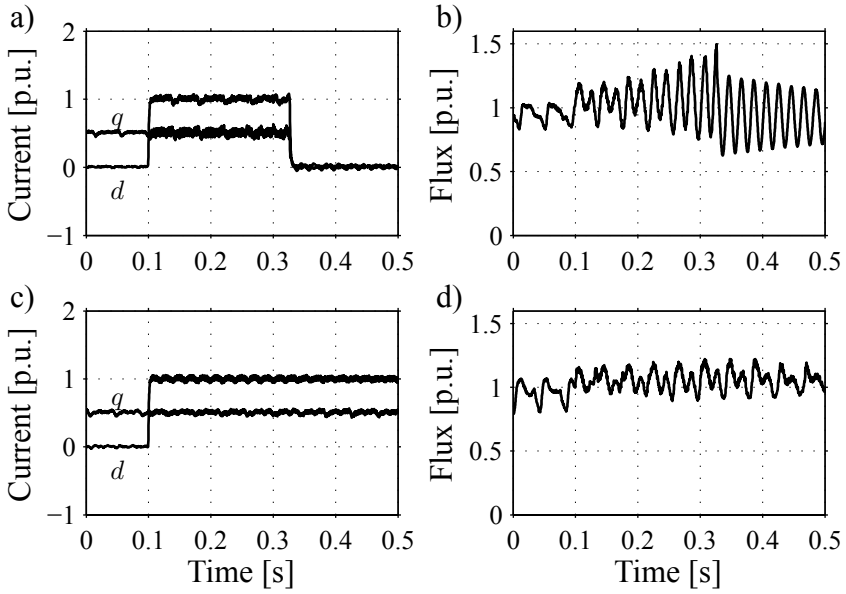

Fig. 5.8. Experimental comparison between stator-flux-oriented and grid-flux-oriented systems. a) Rotor current (stator-flux orientation). b) Stator-flux magnitude (stator-flux orientation). c) Rotor current (grid-flux orientation). d) Stator-flux magnitude (grid-flux orientation).

increased to 1 p.u. it can be seen that the stator-flux-oriented system becomes unstable with an increasing amplitude of the flux oscillations. After 0.32 s the rotor current is put to zero in order to put back the system into a stable operating condition. As expected from the analytical results, the grid-flux-oriented system remains stable throughout the whole experiment. During this evaluation, the bandwidth of the current control loop was set to 2.3 p.u. and the rotor speed, ω_r, was controlled by a d.c. machine to be 1 p.u.

5.4 Impact of Stator Voltage Sags on the Current Control Loop

Due to the poorly damped poles, in case of a voltage sag, the flux will enter a damped oscillation. It is essential that the magnitude of the rotor current is below the rated value of

the converter in order not to force the crowbar to go into action, and thereby lose control of the rotor currents and thus the power production.

Neglecting the current dynamics, the rotor voltage as given in (4.67) can be expressed as

$$\begin{aligned}\mathbf{v}_R &= (R_r + R_s + j\omega_2 L_\sigma)\mathbf{i}_R + \mathbf{v}_s - \Big(\frac{R_s}{L_M} + j\omega_r\Big)\psi_s \\ &\approx \mathbf{v}_s - j\omega_r\psi_s = jE_g e^{j(\theta_g-\theta_1)} - j\omega_r\psi_s.\end{aligned} \tag{5.38}$$

From this equation it can be noted that (since $\mathbf{v}_s \approx j\omega_g\psi_s$)

$$\begin{aligned}&\mathrm{Im}[\mathbf{v}_R] > 0 \quad \text{if}\, \omega_r < \omega_g \\ &\mathrm{Im}[\mathbf{v}_R] < 0 \quad \text{if}\, \omega_r > \omega_g \\ &\mathrm{Im}[\mathbf{v}_R] \approx 0 \quad \text{if}\, \omega_r = \omega_g.\end{aligned} \tag{5.39}$$

If the rotor voltage is $\mathbf{v}_{R,0}$ before the voltage sag, then the change in the rotor voltage will be $\Delta\mathbf{v}_R = \mathbf{v}_{R,0} - \mathbf{v}_R$. Assuming that the grid voltage (or stator voltage) drops from $E_{g,\mathrm{nom}}$ to E_g at t_{sag}, then, at the time instant t_{sag}, the rotor voltage will drop

$$\begin{aligned}\Delta\mathbf{v}_R(t = t_{\mathrm{sag}}) &= jE_{g,\mathrm{nom}}e^{j\Delta\theta_0} - jE_g e^{j\Delta\theta} \\ &\approx j(E_{g,\mathrm{nom}} - E_g) = j\Delta E_g\end{aligned} \tag{5.40}$$

since the stator flux and the rotor speed will not change instantaneously. From (5.39) and (5.40) it can be seen that for $\omega_r > \omega_g$, the magnitude of the rotor voltage will be instantaneously increased with ΔE_g. If $\omega_r < \omega_g$, then the value of the rotor voltage magnitude will, accordingly, be instantaneously decreased. This implies that the worst case occurs for $\omega_r > \omega_g$ according to (5.39) and (5.40). For example, if $\omega_r = 1.3$, implying $\mathbf{v}_R \approx -j0.3$ before the voltage sag, then, according to (5.40), the rotor voltage will be $\mathbf{v}_R(t = t_{\mathrm{sag}}) = \mathbf{v}_{R,0} + j\Delta E_g = -j0.3 - j0.4 = -j0.7$ for a grid voltage drop ΔE_g=0.4 p.u.

In Fig. 5.9, the maximum rotor voltage needed due to a symmetrical voltage sag for current control Methods I and IV can be seen. Method II is not considered, since it is actually unstable for certain operating conditions as indicated by Fig. 5.1 and Method III due that the results are relatively similar to those of Method IV. The DFIG is running as a generator at rated torque and is fully magnetized from the rotor circuit. The rotor speed is 1.3 p.u. This implies that the rotor voltage is approximately 0.3 p.u. immediately before the voltage sag occurs. For a wind turbine, this operating condition is disadvantageous since a rotor voltage of 0.3 p.u. is close to the maximum value needed in order to achieve the desired variable-speed range for a wind turbine. It can be seen that the maximum rotor voltage will increase with the size of the voltage sag. Further, the maximum rotor voltage is relatively independent of the bandwidth of the current control loop for Method IV. It can also be noted that, generally, Method I requires slightly more rotor voltage than Method IV, especially for low bandwidths. Further, for higher bandwidths of the current control loop, it can be seen that the increase in rotor voltage due to a voltage sag follows (5.40).

In Fig. 5.10, the corresponding maximum rotor current needed due to the voltage sag for Method I can be seen. Method IV is not shown in the figure, since it manages to keep the rotor current unaffected during the voltage sag, with known parameters. It can be seen in the figure that the maximum rotor current increases with the size of the voltage sag, especially for low bandwidths of the current control loop. For higher bandwidths, it can be seen that

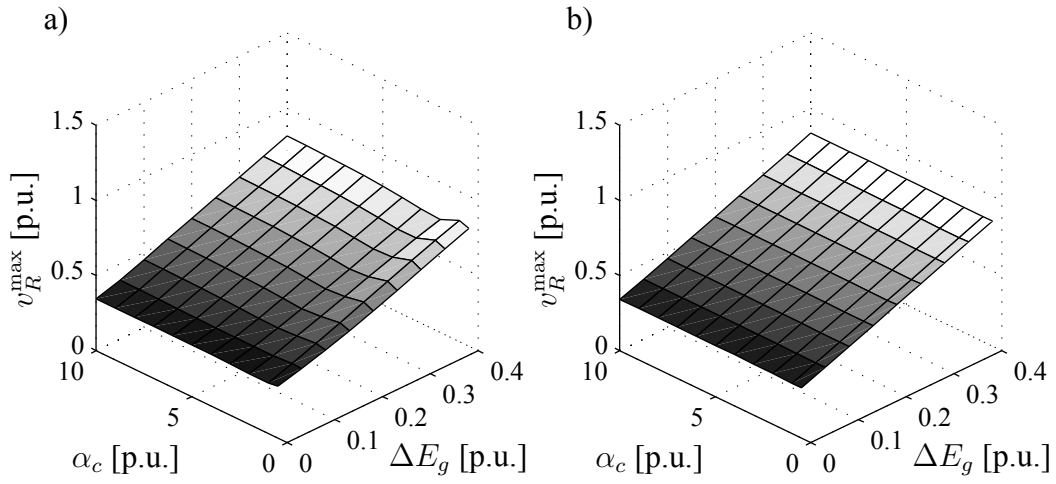

Fig. 5.9. Maximum rotor voltage, $v_R^{\max}$, due to a symmetrical voltage sag as a function of the sag size, ΔE_g, and the current control bandwidth, α_c. a) Method I (stator-flux-oriented system). b) Method IV (stator-flux-oriented system).

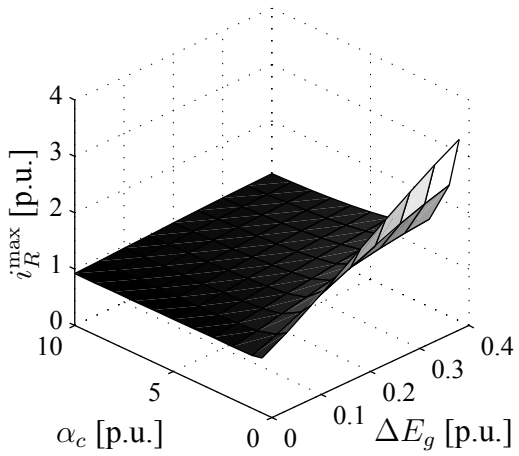

Fig. 5.10. Maximum rotor current, $i_R^{\max}$, for Method I, due to a symmetrical voltage sag as a function of the sag size, ΔE_g, and the current control bandwidth, α_c (stator-flux-oriented system).

the maximum rotor current is practically constant, independent of the voltage sag magnitude. The reason is that when the bandwidth is increased, the "need" for compensating the back EMF vanishes, see (4.74).

It is, thus, not only necessary to design the converter according to the desired variable-speed range, but also according to a certain voltage sag to withstand.

5.4.1 Influence of Erroneous Parameters

As mentioned earlier, the methods are mostly sensitive to an underestimated L_σ, mainly since the bandwidth of the current control loop then becomes lower than the desired. Simulations with $\tilde{L}_\sigma = 0.5L_\sigma$ shows that Method I is very sensitive to an underestimated L_σ during voltage sags, especially for low bandwidths of the current control loop, see Fig. 5.11. By using Method IV, the influence of an erroneous value of L_σ is, in principle, removed. If the current control loop bandwidth is below 2 p.u., the difference in the maximum rotor current

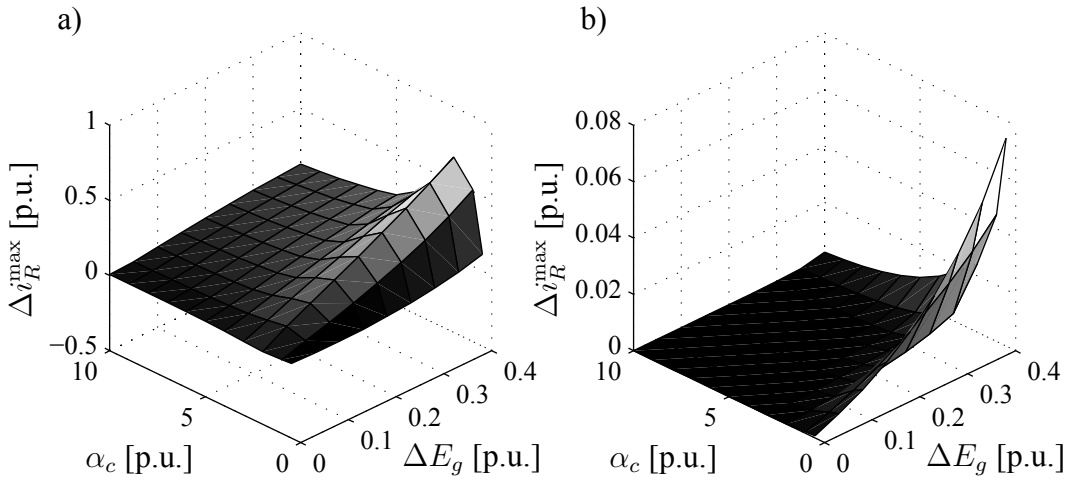

Fig. 5.11. Increased maximum rotor current, $\Delta i_R^{\max}$, for Method I (a) and Method IV (b), when the leakage inductance is underestimated, $\tilde{L}_\sigma = 0.5 L_\sigma$, due to a symmetrical voltage sag as a function of the sag size, ΔE_g, and the current control bandwidth, α_c (stator-flux-oriented system).

is below 0.02 p.u., as can be seen in Fig. 5.11.

For Method IV and variations in R_s, R_R, and L_M with $\pm 50\%$, the difference in maximum rotor current is insignificant; while for Method I, R_s and R_R have small impacts for smaller α_c. However, for higher values of α_c, this impact is also insignificant.

5.4.2 Generation Capability During Voltage Sags

As an example of this, Fig. 5.12 shows the minimum remaining grid voltage that can be handled without triggering the crowbar as a function of the power. The maximum rotor voltage is limited to 0.4 p.u. and the crowbar short circuits the rotor circuit when the rotor current is above 1.25 p.u. This means that when the current controller needs to put out a higher rotor voltage in order to compensate for the sag, it will lose control of the rotor current, and the crowbar may be triggered if the rotor current becomes too high. From the figure it can be seen that for low bandwidths of the current control loop (allowing a lower switching frequency), Method IV manages to survive deeper sags than Method I. However, as indicated by the figure, for higher bandwidths, the difference between the methods vanishes. A bandwidth of 7 p.u. for Method IV produces very similar results as a bandwidth of 1 p.u., and is therefore not shown in the figure.

5.5 Flux Damping

As previously mentioned there are different methods of damping the flux oscillations. As mentioned before, one method is to reduce the bandwidth of the current control loop [43]. In [107], a feedback of the derivative of flux was introduced in order to improve the damping of the flux. Another possibility is to use a converter to substitute the Y point of the stator winding, i.e., an extra degree of freedom is introduced that can be used to actively damp out the flux oscillations, [54].

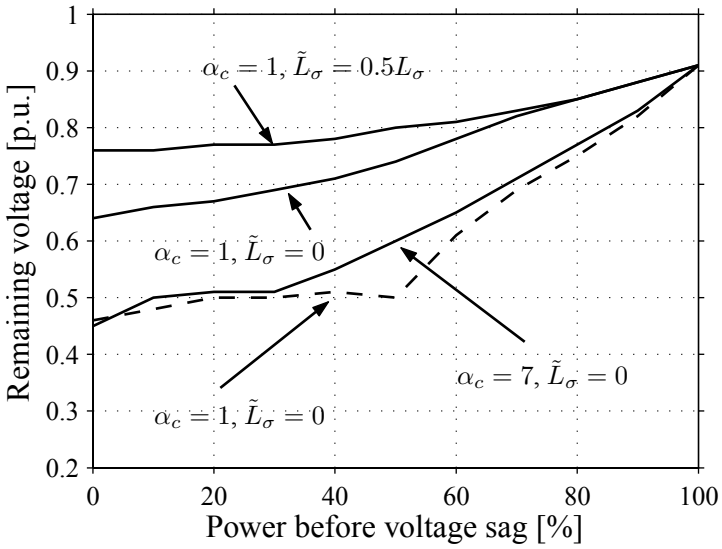

Fig. 5.12. Minimum remaining voltage without triggering the crowbar of a voltage sag, for Methods I (solid) and IV (dashed) as a function of the power. The maximum rotor voltage is set to 0.4 p.u. and a rotor current above 1.25 p.u. triggers the crowbar (stator-flux-oriented system).

Kelber made a comparison of different methods of damping the flux oscillations in [55]. The methods are 1) reducing the bandwidth of the current control loop, 2) compensation of the transformation angle (to synchronous coordinates), 3) feedback of the derivative of the flux, and 4) the method with a converter substituting the star point in the stator winding. It is concluded in [55] that the method of reducing the bandwidth works quite well, although it has the disadvantage of slowly damping of a grid disturbances. Compensation of the transformation angle method improves the damping only slightly. Feedback of the flux derivative method performs well and has a low cost; the disadvantage of this method is that the method cause relatively high rotor currents. The method with a converter in the star point of the stator winding performs very well, but the disadvantage of this method is the required addition in hardware and software. Since there is a need for another converter, the cost is also increased.

In this section, the flux oscillations will be damped by feedback of the derivative of the flux. The reason that this method is chosen is that it has low cost (i.e., no extra hardware), is easy to implement, and can damp the flux oscillations well. Due to the fact that the method with an extra converter connected to the Y point of the stator winding has to handle the stator current, implying an increase of the losses, and the increased cost for an extra converter this method, is not considered in this section since some of the benefits and reasons for the doubly-fed induction generator, e.g., smaller (cheaper) converter and lower losses, vanishes. However, later on in Chapter 7 where different methods for voltage sag ride-through are discussed and compared, the system with the converter in Y point becomes very interesting and is accordingly further investigated.

The q component of the rotor current is used for controlling the torque, but the d component of the current can be used to damp the oscillations and improve stability. If we add a

component $\Delta i_{Rd}^{\text{ref}}$ to the d component of the rotor current reference, which we control as

$$\Delta i_{Rd}^{\text{ref}}(p) = -\frac{p}{p+\alpha_{\text{co}}}\frac{\alpha_d}{\hat{R}_s}\psi_s = -\left(1-\frac{\alpha_{\text{co}}}{p+\alpha_{\text{co}}}\right)\frac{\alpha_d}{\hat{R}_s}\psi_s \tag{5.41}$$

then, a flux differentiation compensation term has been introduced, that will improve the damping of the system. In the above equation, a high-pass filter is used since a pure differentiation is not implementable. This means that i_{Rd}^{ref} is set to

$$i_{Rd}^{\text{ref}} = i_{Rd,0}^{\text{ref}} + \Delta i_{Rd}^{\text{ref}} \tag{5.42}$$

where $i_{Rd,0}^{\text{ref}}$ is used to control the reactive power as discussed in a previous chapter.

5.5.1 Stator-Flux Orientation

Under the assumption that the current dynamics are set much faster than the flux dynamics and α_{co} is small, the characteristic polynomial in (5.6) can be rewritten as (with correctly known parameters)

$$p^2 + \Big[\alpha_d + \frac{R_s}{L_M}\Big(2 - \frac{\omega_g L_M i_{Rd,0}^{\text{ref}}}{E_g}\Big)\Big]p + \Big(1 - \frac{R_s i_{Rq}^{\text{ref}}}{E_g} + \alpha_d R_s \frac{E_g - i_{Rd,0}^{\text{ref}} L_M \omega_g}{E_g L_M \omega_g^2}\Big)\omega_g^2. \tag{5.43}$$

With the inclusion of a flux damping, the constraint on the d component becomes

$$i_{Rd,0} < \Big(2 + \alpha_d \frac{L_M}{R_s}\Big)\frac{E_g}{\omega_g L_M} \tag{5.44}$$

in order to guarantee stability. Comparing to (5.7), it is seen that the constraint on the d component rotor current has increased $1 + \alpha_d L_M/(2R_s)$ times.

5.5.2 Grid-Flux Orientation

For a grid-flux-oriented system the characteristic polynomial in (5.27) is changed to (with correctly known parameters)

$$p^2 + \left(\alpha_d + 2\frac{R_s}{L_M}\right)p + \frac{\alpha_d R_s}{L_M} + \frac{R_s^2}{L_M^2} + \omega_g^2 \tag{5.45}$$

if α_{co} is small. Moreover, since R_s is small and L_M is large, see Table 2.1 for typical parameters, it is possible to approximate the above characteristic polynomial as

$$p^2 + \alpha_d p + \omega_g^2. \tag{5.46}$$

5.5.3 Parameter Selection

As can be seen in (5.41), the flux damping uses two parameters, α_d and α_{co}, that have to be determined. Obviously, the cut-off frequency, α_{co}, of the low-pass filter must be set lower than the oscillating frequency in order to be able to damp the oscillation at all. The damping term, α_d, must be chosen smaller than the bandwidth of the current control loop, α_c, so that the flux damper becomes slower than the current dynamics. Of course, if a flux estimator is used to determine the flux, the bandwidth of the damper, α_d, must be smaller than the bandwidth of the flux estimator.

5.5.4 Evaluation

Fig. 5.13 shows a simulation of a vector-controlled doubly-fed induction generator, according to Section 4.4.1 ($k_E = 1$ and $k_R = 1$), with and without flux damping. The reference frame is aligned with the stator flux. The reference value $i_{Rd,0}^{\text{ref}}$ is initially zero and is at 0.4 s changed to 0.5 p.u. The reference value of i_{Rq}^{ref} is initially zero and is at 0.1 s changed to 0.5 p.u., and at 0.7 s to -0.5 p.u. The bandwidth of the system, α_c, is set to 4.7 p.u., while

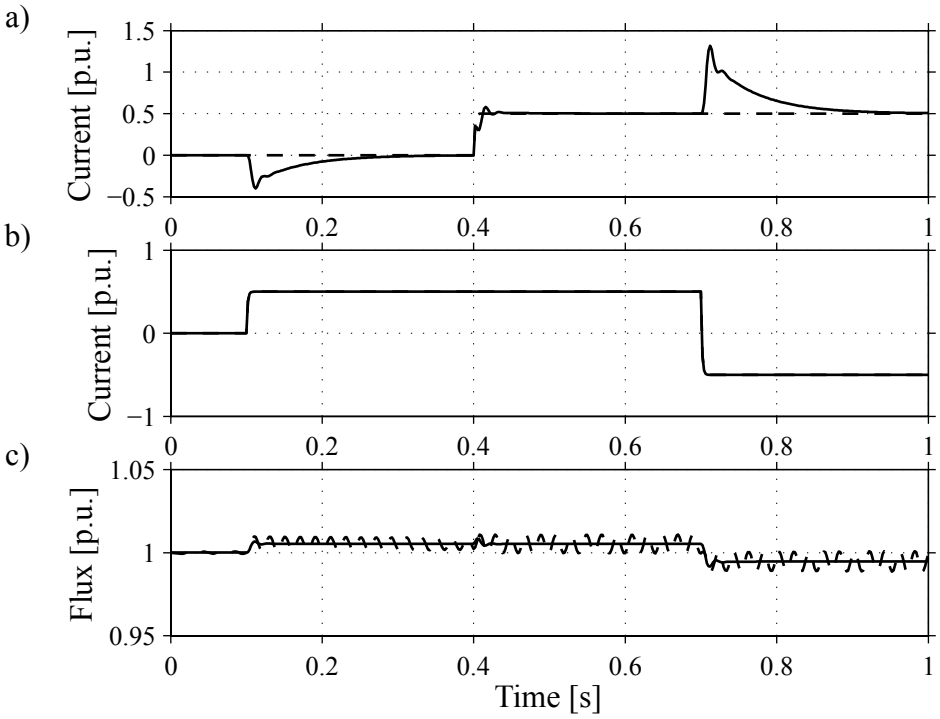

Fig. 5.13. Simulation of current control using a stator-flux oriented reference frame with (solid) and without (dashed) damping of the flux oscillations. a) i_{Rd}. b) i_{Rq}. c) ψ_s.

α_d is set to 0.7 p.u., and α_{co} is set to 0.05 p.u. In the simulation it is assumed that the flux can be determined from measurements of the stator and the rotor currents. The figure shows that the oscillations in the flux has been damped with the flux damper. Since it is difficult to see the effect of the flux damper in a measured time series, due to noise, a frequency spectra of the flux magnitude has been plotted instead in Fig. 5.14. In the figure the current control method with feed forward of the back EMF and with "active resistance" has been used, with and without flux damping. The frequency spectra is based on a 6 s long measurement on the laboratory DFIG setup described in Appendix B.2. The DFIG is operated as in Section 5.3. The bandwidth of the current control loop, α_c, was set to 2.3 p.u., the damping term, α_d, was set to 0.7 p.u. and, the cut-off frequency term, α_{co}, was set to 0.05 p.u. It can be seen in the figure that the 50-Hz component has been to a large extent damped, i.e., a factor of ten, by the flux damper.

5.5.5 Response to Symmetrical Voltage Sags

In this section the flux damper's response will be analyzed with respect to symmetrical voltage sags. It is assumed that before and directly after the voltage sag, the magnitude of the

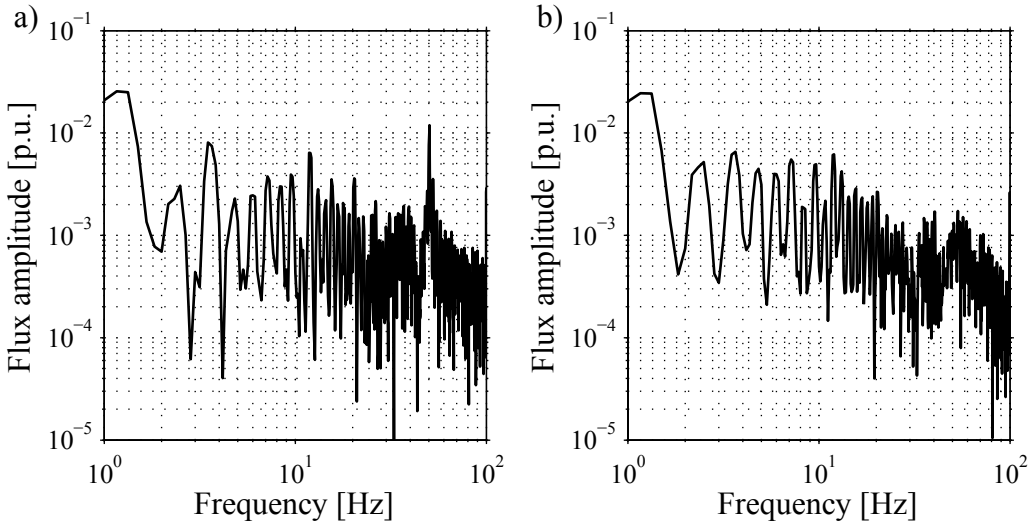

Fig. 5.14. Frequency spectra of the flux (data from measurements). The reference frame is aligned with the stator flux. a) Without flux damping. b) With flux damping.

stator flux can be expressed as

$$t < 0: \qquad \psi_s(t) = \psi_{s0} \tag{5.47}$$

$$t \geq 0: \qquad \psi_s(t) \approx \psi_{s0}\frac{V}{E_{g,\mathrm{nom}}} + \left(1 - \frac{V}{E_{g,\mathrm{nom}}}\right)\psi_{s0}e^{-\alpha_d t/2}\cos(\omega_g t) \tag{5.48}$$

where ψ_{s0} is the steady-state stator flux prior the voltage sag and V is the remaining voltage after the voltage sag. This means that the term $1 - V/E_{g,\mathrm{nom}}$ corresponds to the magnitude of the sag. Then, from (5.41) the response in Δi_{Rd} is estimated as

$$\Delta i_{Rd}^{\mathrm{ref}}(t) = \mathcal{L}^{-1}\left\{-\left(1 - \frac{\alpha_{\mathrm{co}}}{p + \alpha_{\mathrm{co}}}\right)\frac{\alpha_d}{R_s}\mathcal{L}\left\{\psi_s(t)\right\}\right\} \tag{5.49}$$

or as

$$\Delta i_{Rd}^{\mathrm{ref}}(t) = \mathcal{L}^{-1}\left\{-\frac{\alpha_d}{R_s}\left(\mathcal{L}\left\{\psi_s(t)\right\} - \frac{\alpha_{\mathrm{co}}}{p + \alpha_{\mathrm{co}}}\mathcal{L}\left\{\psi_s(t)\right\}\right)\right\}. \tag{5.50}$$

If α_{co} is considered small, i.e., the low-pass filter $\alpha_{\mathrm{co}}/(p + \alpha_{\mathrm{co}})$ has low bandwidth, it is possible to describe $\Delta i_{Rd}^{\mathrm{ref}}(t)$ after the voltage sag as

$$t \geq 0: \qquad \Delta i_{Rd}^{\mathrm{ref}}(t) \approx -\frac{\alpha_d}{R_s}\Delta\psi_s(t) = -\frac{\alpha_d}{R_s}\left(\psi_s(t) - \psi_{s0}\right) \tag{5.51}$$

which can be written as

$$t \geq 0: \qquad \Delta i_{Rd}^{\mathrm{ref}}(t) \approx \frac{\alpha_d}{R_s}\left(1 - \frac{V}{E_{g,\mathrm{nom}}}\right)\psi_{s0}\left(1 - e^{-\alpha_d t/2}\cos(\omega_g t)\right). \tag{5.52}$$

The above expression has a local maximum for $t = \arccos\left(-2\omega_g/\sqrt{\alpha_d^2 + 4\omega_g^2}\right)/\omega_g$. However, if $\alpha_d^2 \ll 4\omega_g^2$ it is possible to approximate t as $t \approx \arccos(-1)/\omega_g = \pi/\omega_g$. This means that the extreme value of $\Delta i_{Rd}^{\mathrm{ref}}(t)$ due to a symmetrical voltage sag can be expressed as

$$\Delta i_{Rd}^{\mathrm{ref}}(t = \pi/\omega_g) \approx \frac{\alpha_d}{R_s}\psi_{s0}\left(1 + e^{-\alpha_d\pi/(2\omega_g)}\right)\left(1 - \frac{V}{E_{g,\mathrm{nom}}}\right). \tag{5.53}$$

Consider the following values: $V = 0.9$ p.u., $\alpha_d = 0.7$ p.u., $\psi_{s0} = 1$ p.u., and $R_s = 0.01$ p.u. for a numerical example. This means that the maximum value of $\Delta i_{Rd}^{\text{ref}}$ due to the voltage sag is $\Delta i_{Rd}^{\text{ref}} = 0.7/0.01 \cdot 1 \left(1 + e^{-0.7\pi/(2\cdot 1)}\right)(1 - 0.9/1) = 9.3$ p.u. This value is, of course, an unrealistically high value. However, it indicates that the flux damper is very sensitive to voltage sags. In Fig. 5.15 the maximum value of $\Delta i_{Rd}^{\text{ref}}$ due to a voltage sag as a function of the bandwidth α_d of the flux damper can be seen. The results are presented for four different symmetrical voltage sags between $V = 0.8$ to $V = 0.95$ p.u. (note that V is the remaining voltage). In the figure both simulated results (using stator-flux orientation) as well as analytically results from (5.53) is shown. Both methods produce similar results, although the analytical results are generally slightly higher. The results in the figure shows that the flux damper is very sensitive to voltage sags. This means that if the flux damper should work during (small) voltage sags, the bandwidth, α_d, of the flux damper should be small. However, then some of the advantage of the flux damper is lost.

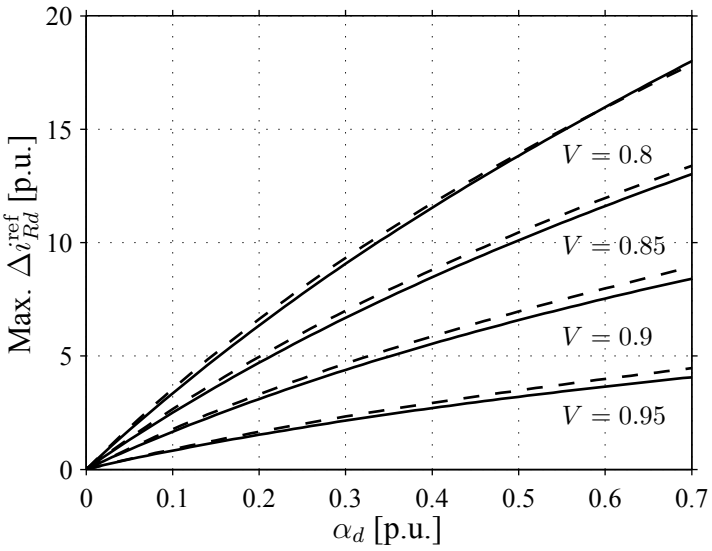

Fig. 5.15. Maximum of $\Delta i_{Rd}^{\text{ref}}$ due to a voltage sag as a function of α_d. Solid lines correspond to simulation and dashed lines correspond to results from an analytical expression.

5.6 Conclusion

In this chapter, the general rotor current control law derived in Chapter 4, with the option of including feed-forward compensation of the back EMF and "active resistance," in order to eliminate the influence of the back EMF on the rotor current, has been analyzed. It was found that the method that combines both the feed-forward compensation of the back EMF and the "active resistance" manages best to suppress the influence of the back EMF on the rotor current. Moreover, this method was found to be the least sensitive one to erroneous parameters and it manages to keep the rotor current close to unaffected, even with erroneous parameters, during a voltage sag. The choice of current control method is of greater importance if the bandwidth of the current control loop is low.

It has been shown that by using grid-flux orientation, the stability and the damping of the system is independent of the rotor current, in contrast to the stator-flux-oriented system.

This implies that for a grid-flux-oriented system it is possible to magnetize the DFIG entirely from the rotor circuit without reducing the damping of the system.

By utilizing feed-forward compensation, stability of the system resulting from the proposed current controller was found independent of the bandwidth of the current control loop, and the order of the system to analyze could be reduced. The introduction of an "active resistance" in the current control law improves the damping of low-frequency disturbances significantly.

Finally, it is shown that the design of the converter for a doubly-fed induction generator should also take into account a certain voltage sag to withstand and not only the desired variable-speed range.

Chapter 6

Evaluation of Doubly-Fed Induction Generator Systems

6.1 Reduced-Order Model

If, for example, the rotor current dynamics and the grid-filter current dynamics are controlled by a high-gain feedback, it is possible to force the system to have both slow and fast time scales, i.e., the system behaves like a singularly perturbed system [57]. This means, that the rotor and grid-filter current can be assumed to follow their reference values accurately.

As pointed out in the Introduction, the flux dynamics of the DFIG are strongly influenced by a pair of poorly damped poles, with an oscillating frequency close to 1 p.u., i.e. close to the line frequency. If the current control loop is much faster than the flux dynamics, it is sufficient to study only the flux dynamics and put the rotor current to its reference value, i.e.,

$$\frac{d\Psi_s}{dt} = \mathbf{E}_g - \left(\frac{R_s}{L_M} + j\omega_1\right)\Psi_s + R_s\mathbf{i}_R^{\text{ref}} \tag{6.1}$$

where the stator voltage has been put equal to the grid voltage. For a stator-flux-oriented system the above equation can be reduced to (5.2) and (5.3), where the equation is in polar form. While for a grid-flux oriented system the above equation can be used directly. However, the synchronous frequency, ω_1, must be determined. Either a PLL-estimator, as described in Section 4.1.3, can be used to track the frequency of the grid voltage, or, if the frequency of the grid is constant (or at least close to constant), the synchronous frequency can be put equal to the grid frequency, i.e. $\omega_1 = \omega_g$.

6.2 Discretization of the Doubly-Fed Induction Generator

If the simple-to-use forward Euler method, see Section 4.1.7, is used to simulate the system, care must be taken not to use a too long time step or sampling period, T_{sample}. For instance, in PSCAD/EMTDC [66], when writing user-defined modules, the module must be discretizised, and this often due to its simplicity results in using the forward Euler method. The forward Euler discretization is given by (4.35). As mentioned in Section 4.1.7, the poles must be inside a circle with a radius of $1/T_{\text{sample}}$ and the center point located at $(-1/T_{\text{sample}}, 0)$ in order for the forward Euler discretization to be stable.

It should be pointed out that in some other programs, for instance Simpow [1] and PSS/E [85], user-defined modules return expressions for the derivatives and advanced integration algorithms are used. In this case, the allowed time step can be made longer.

6.2.1 Stator-Flux Orientation

The solution to the characteristic polynomial for a stator-flux oriented system in (5.6) is found as

$$\begin{aligned} p_{1,2} &= -\frac{R_s}{2L_M}\Big(2-\frac{\omega_g L_M i_{Rd}^{\text{ref}}}{E_g}\Big) \\ &\pm\sqrt{\frac{R_s^2}{4L_M^2}\Big(2-\frac{\omega_g L_M i_{Rd}^{\text{ref}}}{E_g}\Big)^2-\Big(1-\frac{R_s i_{Rq}^{\text{ref}}}{E_g}\Big)\omega_g^2} \\ &\approx -\frac{R_s}{2L_M}\Big(2-\frac{\omega_g L_M i_{Rd}^{\text{ref}}}{E_g}\Big)\pm j\omega_g. \end{aligned} \tag{6.2}$$

In order for the discretization to be stable, the above-mentioned poles should be located inside the circle, i.e.,

$$\Big|\Big(-\frac{1}{T_{\text{sample}}},0\Big)-\Big(-\frac{R_s}{2L_M}\Big[2-\frac{\omega_g L_M i_{Rd}^{\text{ref}}}{E_g}\Big],\pm\omega_g\Big)\Big|<\frac{1}{T_{\text{sample}}} \tag{6.3}$$

which yields

$$T_{\text{sample}}<\frac{\dfrac{R_s}{L_M}\Big(2-\dfrac{\omega_g L_M i_{Rd}^{\text{ref}}}{E_g}\Big)}{\dfrac{\dfrac{R_s^2}{L_M^2}\Big(2-\dfrac{\omega_g L_M i_{Rd}^{\text{ref}}}{E_g}\Big)^2}{4}+\omega_g^2}<\frac{R_s}{\omega_g^2 L_M}\Big(2-\frac{\omega_g L_M i_{Rd}^{\text{ref}}}{E_g}\Big). \tag{6.4}$$

For unity power factor, i.e. $i_{Rd}^{\text{ref}}=\psi_s/L_M\approx E_g/(\omega_1 L_M)$, the above expression is reduced to

$$T_{\text{sample}}<\frac{R_s}{\omega_g^2 L_M}. \tag{6.5}$$

For the system investigated later on in this chapter and using the forward Euler method, the sampling period should be $T_s<4.6$ µs.

6.2.2 Grid-Flux Orientation

The solution to the characteristic polynomial in (5.27), corresponding to grid-flux-oriented system, is found as

$$p_{1,2}=\frac{R_s}{L_M}\pm j\omega_g \tag{6.6}$$

In order for the discretization to be stable, the above-mentioned poles should be located inside the circle, i.e.,

$$\left|\left(-\frac{1}{T_{\text{sample}}},0\right)-\left(-\frac{R_s}{L_M},\pm\omega_g\right)\right|<\frac{1}{T_{\text{sample}}}. \tag{6.7}$$

The solution to the above equation becomes

$$T_{\text{sample}} < \frac{2R_s}{L_M} \frac{1}{\frac{R_s^2}{L_M^2} + \omega_g^2} \approx \frac{2R_s}{L_M \omega_g^2} \tag{6.8}$$

which is twice the value obtained by (6.5). Moreover, the minimum sample time for the grid-flux-oriented system is independent, in contrast to a stator-flux-oriented system, of the d component of the rotor current.

6.3 Response to Grid Disturbances

In this section, simulations and experimental results of the response of a DFIG wind turbine to voltage sags are presented. The experiments were made on a VESTAS V-52 850 kW WT and in Appendix B.3 a short description of the used data acquisition setup is presented. Moreover, the simulations presented are carried out on a fictitious 850-kW DFIG WT. The following parameters were used in the simulations: $R_s = 0.0071$ p.u., $R_R = 0.01$ p.u., $L_M = 4.9$ p.u., and $L_\sigma = 0.21$ p.u. The grid filter for the grid-side converter $R_i = 0.01$ p.u. and $L_i = 0.07$ p.u. The dc-link capacitance is set to $C_{\text{dc}} = 2.8$ p.u. The simulations have been carried out both with a "full-order" model and a second-order model.

Fig. 6.1 shows experimental results of the response of a DFIG wind turbine to a voltage sag. The voltage drops down approximately 25%, i.e., a 75% sag, at t=0.1 s, and after 0.1 s the fault causing the voltage sag on the grid is cleared, and the voltage starts to recover. The wind turbine produces about 20% of the nominal power. The oscillation close to 50 Hz, caused by the poorly damped poles due to the voltage sag, is clearly seen. In Fig. 6.2, a simulation of the response to the same voltage sag, as shown in Fig. 6.1, is presented, for the full-order model. Fig. 6.3 shows the corresponding simulation with the reduced-order model of the system. It can be seen in the figure that the full-order model and the reduced-order model produce almost the same results. One reason for this is that the bandwidth of the current control loops (of the machine and grid-side converter) are set to 7 p.u., which is sufficiently higher than the eigenfrequency of the flux dynamics (close to 1 p.u.), shown in Section 5.1. Comparing the two figures it is seen that the agreement between the experiment and simulation is quite satisfactory. An exact agreement is not to be expected, since real machine parameters were unknown.

In Fig. 6.4, experimental results of the response due to an unsymmetrical voltage sag are presented. The WT now produces approximately 10% of its nominal power. Fig. 6.5 shows a simulation of the response to the same voltage sag as in Fig. 6.4, for the full-order model and Fig. 6.6 shows the corresponding simulation for the reduced-order model. Again, it is seen that the agreement is quite satisfactory.

In Fig. 6.7, a severe voltage disturbance is presented. In this case the disturbance is so large that the over voltage protection short-circuits the rotor and, after 40 ms, the breaker disconnects the stator from the grid. Before the disturbance the WT is producing approximately half of its rated power.

As mentioned earlier, the simulations shown in this section are carried out for a stator-flux-oriented system. However, similar results from simulations can also be found from a

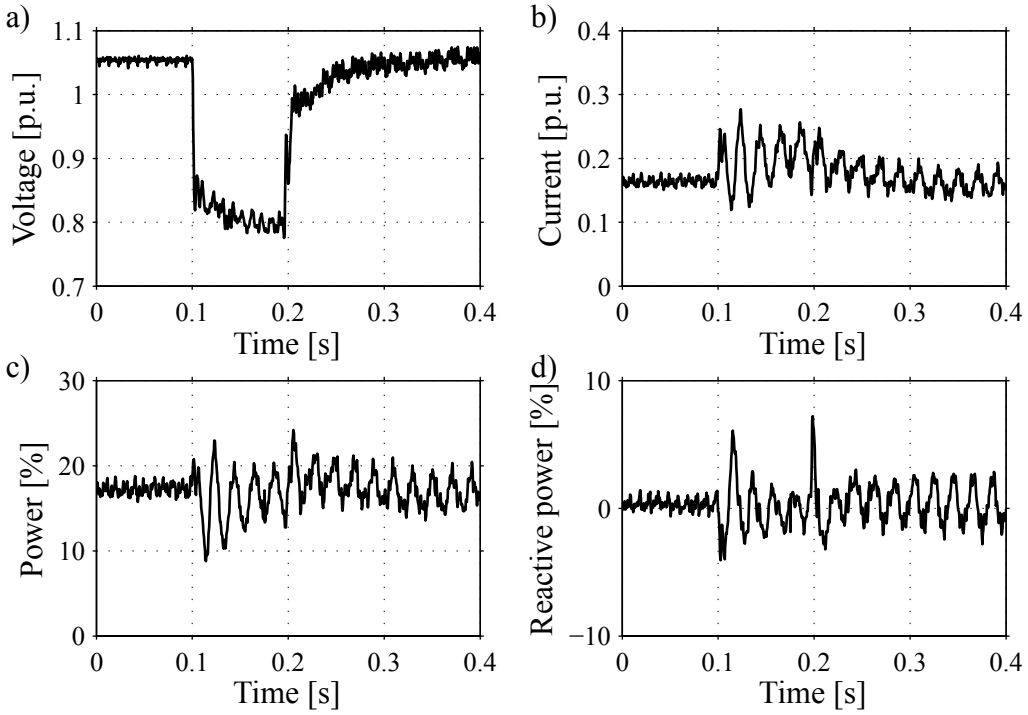

Fig. 6.1. Experiment of the response to a voltage sag. a) Grid-voltage magnitude. b) Grid-current magnitude. c) Active power. d) Reactive power.

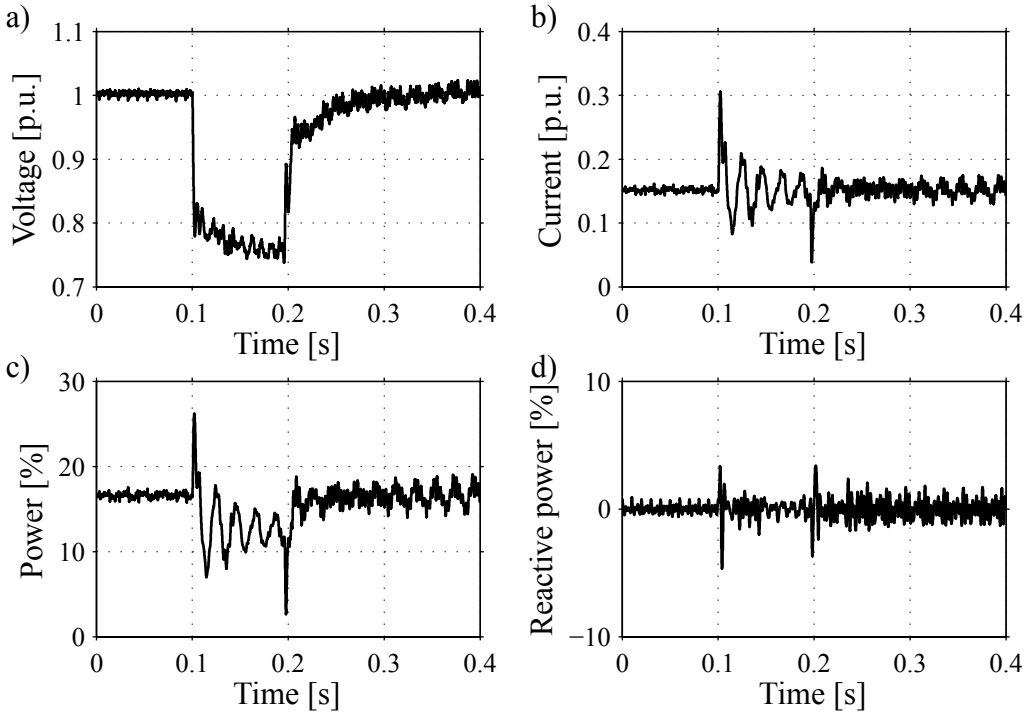

Fig. 6.2. Simulation of the response to a voltage sag with the full-order model. a) Grid-voltage magnitude. b) Grid-current magnitude. c) Active power. d) Reactive power.

stator-voltage oriented (or grid-flux oriented) system.

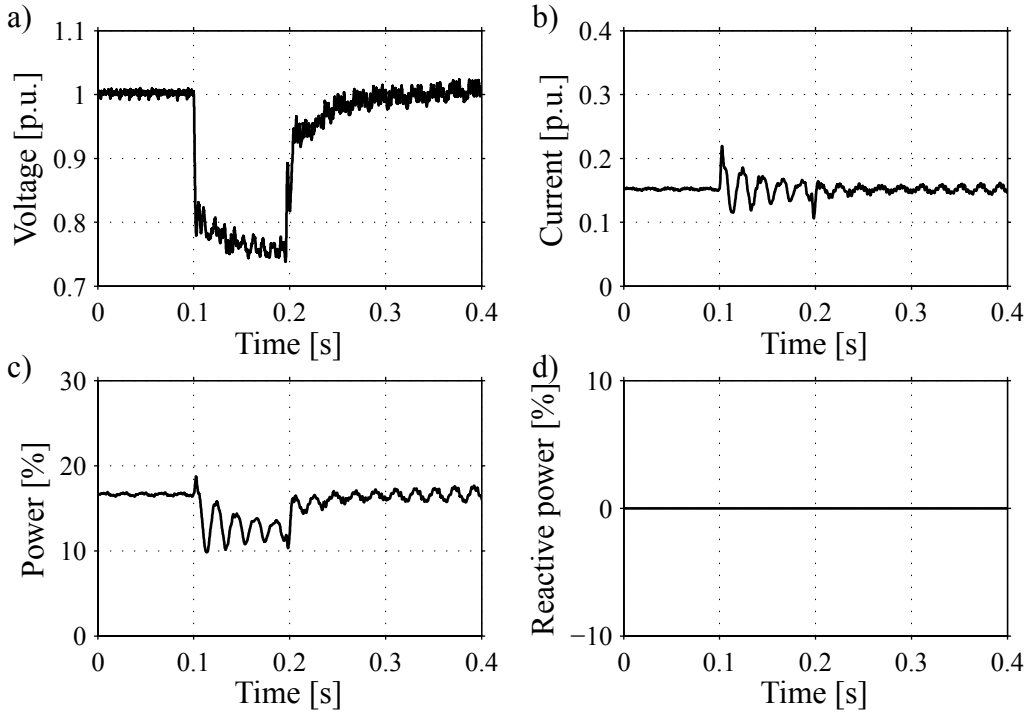

Fig. 6.3. Simulation of the response to a voltage sag with the reduced-order model. a) Grid-voltage magnitude. b) Grid-current magnitude. c) Active power. d) Reactive power.

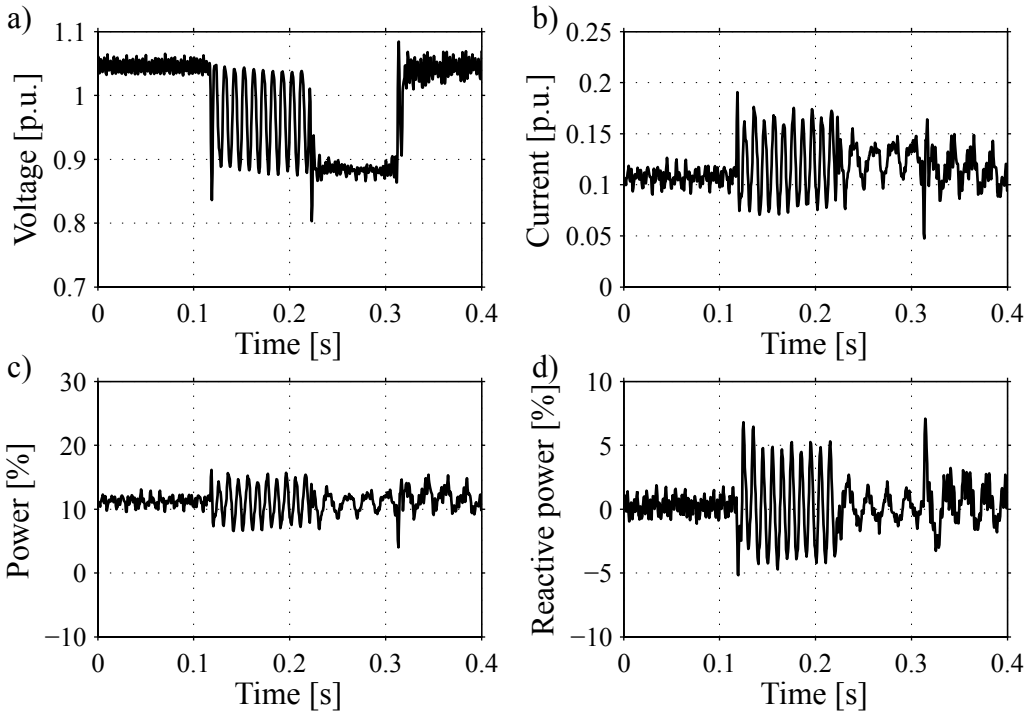

Fig. 6.4. Experiment of the response to a unsymmetrical voltage sag. a) Grid-voltage magnitude. b) Grid-current magnitude. c) Active power. d) Reactive power.

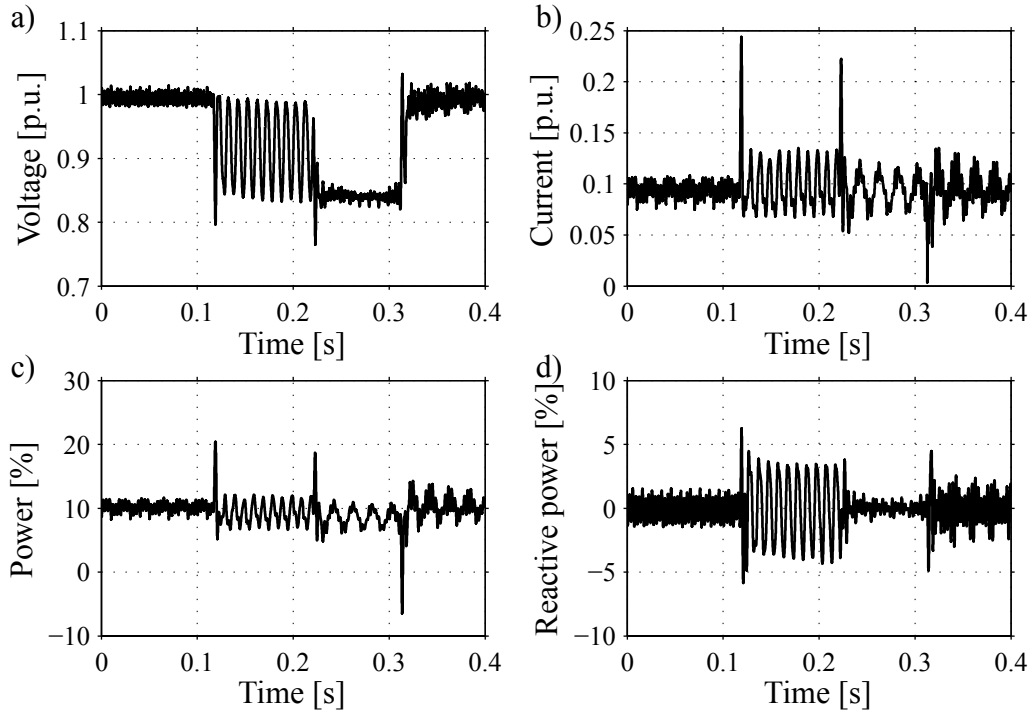

Fig. 6.5. Simulation of the response to an unsymmetrical voltage sag. The simulation has been performed with the full-order model. a) Grid-voltage magnitude. b) Grid-current magnitude. c) Active power. d) Reactive power.

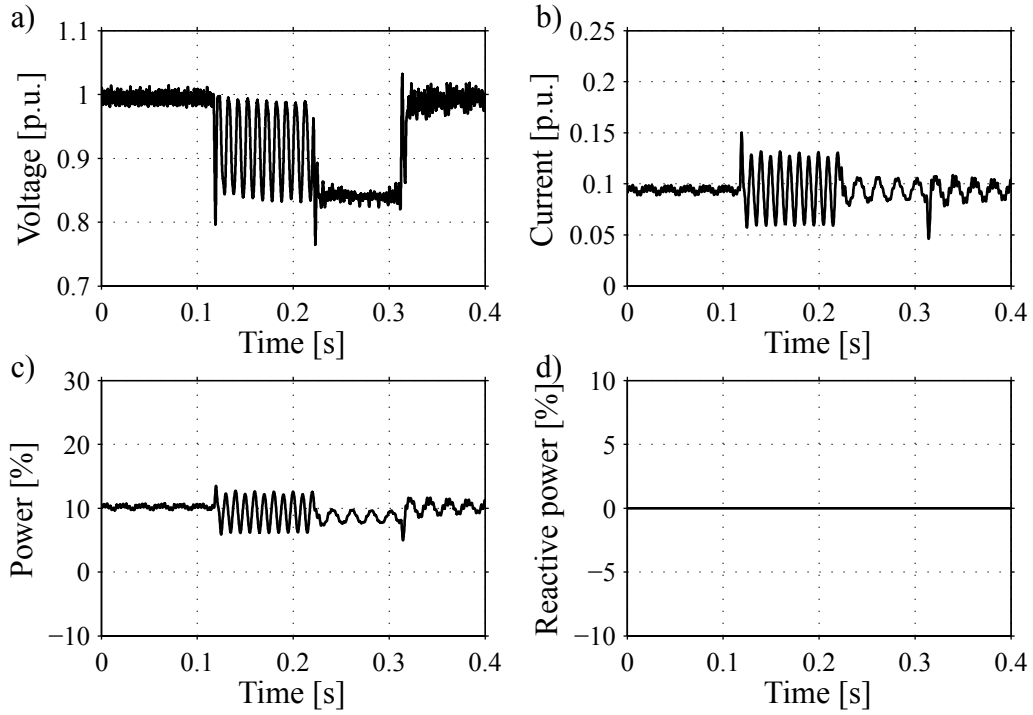

Fig. 6.6. Simulation of the response to an unsymmetrical voltage sag. The simulation has been performed with the reduced-order model. a) Grid-voltage magnitude. b) Grid-current magnitude. c) Active power. d) Reactive power.

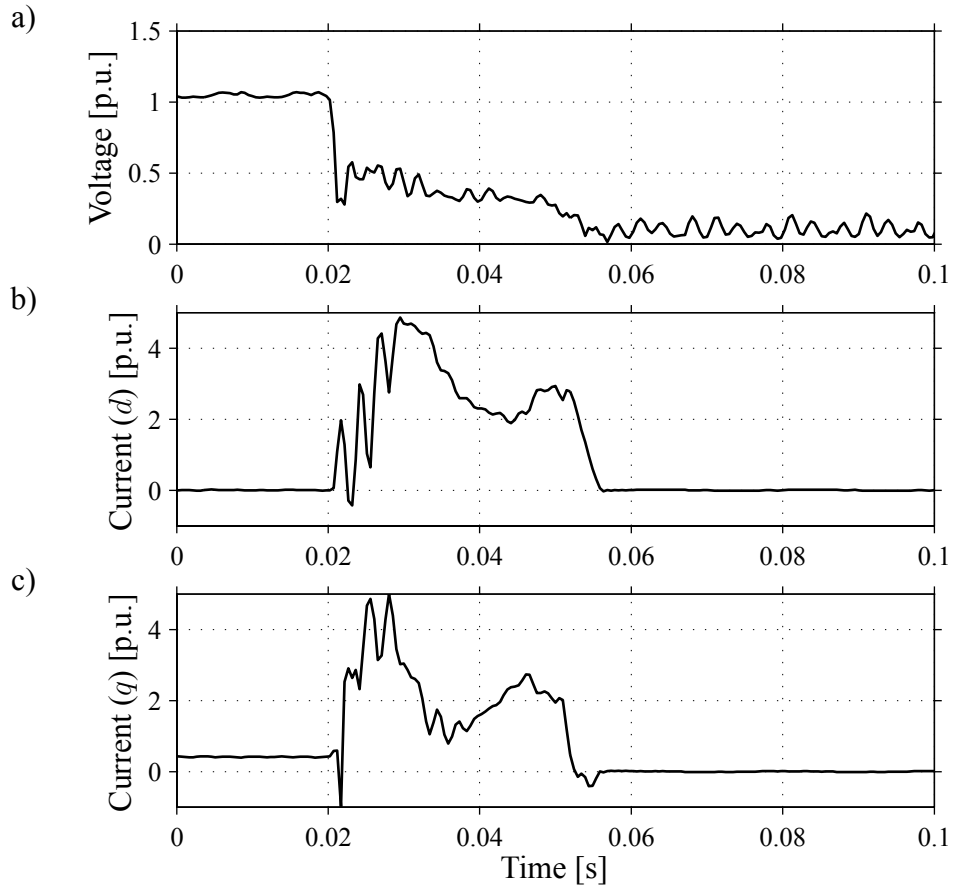

Fig. 6.7. Severe voltage disturbance. a) Grid voltage. b) d component of the grid current. c) q component of the grid current.

6.4 Implementation in Grid Simulation Programs

Some grid simulation programs can handle three-phase instantaneous quantities. Examples are EMTDC and Simpow. Other programs are designed to handle the voltages as phasors, and for these programs, 50-Hz oscillations in the output quantities cannot be captured, since the time step is often too large for these oscillations; an example is PSS/E. However, when handling simulations of large systems, it may not be possible to use such a short time step (about 5 μs) as is required in order to simulate the control of the DFIG system. The suggested approach is to simply ignore the 50-Hz oscillations when the DFIG system is implemented in simulations with long time steps, as long as the disturbances are small enough not to cause the rotor to be short-circuited. For this case, a steady-state model of the DFIG is sufficient. However, if a disturbance is large enough to cause the rotor to be short-circuited, the machine will act as a standard squirrel-cage induction machine which can be adequately modeled with a fifth-order model of the induction machine [83].

As pointed out in [84, 60], the stator flux transients may be negligible from the power system stability analysis point of view. This means that if stator flux transients are negligible a steady-state model of the DFIG dynamics are sufficient as long as the rotor circuit is not short-circuited due to a too large grid disturbance.

6.5 Summary

In this chapter, simulations and experimental verification of the dynamic response to voltage sags of a DFIG wind turbine were presented. Simulations were carried out using a full-order model and a reduced-order model. Both models produced acceptable results. Perfect correspondence with experiments were not expected since the simulations were carried out on a fictitious DFIG wind turbine. The response to symmetrical as well as unsymmetrical voltage sags was verified.

Chapter 7

Voltage Sag Ride-Through of Variable-Speed Wind Turbines

As mentioned in the Introduction, new grid codes are in progress both in Sweden and other countries. This means that new wind turbine installations have to stay connected to the grid for voltage sags above a certain reference sag, i.e., WTs have to *ride through* these voltage sags. In Fig. 7.1, the proposed Swedish requirements for voltage sags is depicted.

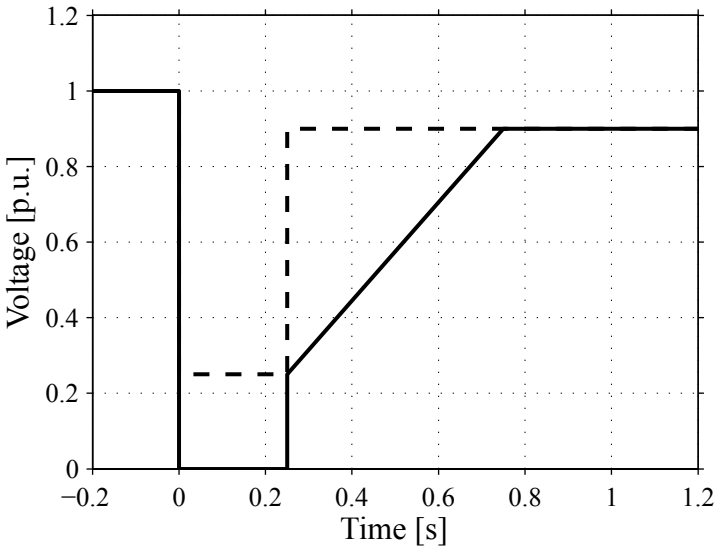

Fig. 7.1. Proposed regulations from the Swedish national grid company, Svenska Kraftnät [96]. Solid line is the requirement for wind parks with a rated power larger than 100 MW. Dashed line is the requirement for wind turbines and wind parks with a rated power between 0.3–100 MW.

First, simple space vector models will be presented for some common voltage sags that will be used in this chapter. Then, the voltage sag response of a WT that utilizes a full-power converter is investigated. This investigation will the serve as a basis for the comparison of DFIG ride-through systems. In the next sections the voltage sag response of the DFIG will be further analyzed, and systems for voltage sag ride-through will be investigated. Finally, these systems will be compared dynamically as well as for steady-state operation.

7.1 Voltage Sags

With the expression "voltage sag," it is normally implied that the grid rms voltage drops from 1 p.u. to 0.1–0.9 p.u. for a short period of time, i.e., 0.5–30 cycles. The duration of voltage sags is mainly determined by the clearing time of the protection used in the grid [9]. The fault clearing time for protective relays varies from 50 ms up to 2000 ms [9]. There are other protection devices, e.g., current-limiting fuses, that might have a shorter fault clearing time (less than one cycle). Voltage sags caused by these fuses are short and deep if the fault is in the local distribution network but if the fault is in a remote distribution network the sag is short and shallow [9]. The origin and classification of voltage sags are well explained in [9]. In this section, simple space vector models will be presented for some common voltage sags. These models are developed in [74] and the aim of the models are to estimate the moduli of the positive- and negative-sequence voltage vectors for different types of sags.

7.1.1 Symmetrical Voltage Sags

Symmetrical (or balanced) voltage sags implies an equally reduction of the rms voltage and, possibly, a "phase-angle jump" in all three phases [9]. Directly after a symmetrical voltage sag, the grid voltage vector can be expressed in the synchronous reference frame as

$$\mathbf{E}_g(t = 0_+) = jVe^{j\tilde{\theta}_0} = jVe^{j\phi} \tag{7.1}$$

where V is the remaining rms voltage in the faulted phases, $\tilde{\theta}_0$ is the initial error angle, and ϕ is the "phase-angle jump." The majority of all "phase-angle jumps" are smaller than $45°$ [9], and the remaining rms voltage can be as low as $V = 0$ for a direct-to-ground fault.

7.1.2 Unsymmetrical Voltage Sags

Unsymmetrical (or unbalanced) voltage sags are more difficult to model since, for instance, the impedance of each symmetrical component can be hard to derive. However, in order to simplify the derivation of models suitable for unsymmetrical voltage sags, the positive-, negative-, and zero-sequence impedance are assumed to be equal. For ground faults, it is assumed that the source and feeder impedance are much larger compared to the line-to-ground impedance. The impedance between the two faulted lines for a line-to-line fault is neglected. Zero sequences are not critical for a PWM rectifier since such sequences ideally disappear from the phase currents due to the absence of a neutral conductor.

Single-Line-to-Ground Fault

After a single-line-to-ground fault (SLGF) in the first phase the grid phase voltages can be expressed as

$$E_1(t = 0_+) = \sqrt{2}V\cos(\theta_g + \pi/2 + \phi) \tag{7.2}$$

$$E_2(t = 0_+) = \sqrt{2}E_{g,\text{nom}}\cos(\theta_g + \pi/2 - 2\pi/3) \tag{7.3}$$

$$E_3(t = 0_+) = \sqrt{2}E_{g,\text{nom}}\cos(\theta_g + \pi/2 + 2\pi/3) \tag{7.4}$$

where E_1, E_2, and E_3 are the grid phase voltages directly after the sag, and V and ϕ are the remaining rms voltage and "phase-angle jump" in the first phase, respectively. The space vector in a stationary reference frame that corresponds to (7.2)–(7.4) is then found as

$$\mathbf{E}_{g0}^{s} = j\left(\mathbf{E}_{p0}e^{j\theta_g} + \mathbf{E}_{n0}e^{-j\theta_g}\right) \tag{7.5}$$

where

$$\mathbf{E}_{p0} = \frac{1}{3}\left(2E_{\text{nom}} + Ve^{j\phi}\right),\ \mathbf{E}_{n0} = \frac{1}{3}\left(E_{\text{nom}} - Ve^{-j\phi}\right) \tag{7.6}$$

are the stationary parts of the positive- and negative-sequence voltage vectors, respectively. For perfect pre-sag field orientation, i.e., $\theta_1 = \theta_g$, (7.5) can be transformed to the synchronous reference frame by substituting $\mathbf{E}_{g0}^{s} = \mathbf{E}_{g0}e^{j\theta_g}$ and solving the resulting equation for $\mathbf{E}_{g0}$:

$$\mathbf{E}_{g0} = j\left(\mathbf{E}_{p0} + \mathbf{E}_{n0}e^{-j2\theta_g}\right). \tag{7.7}$$

As expected, the negative sequence becomes in the synchronous reference frame a component with a frequency of twice the fundamental frequency, i.e. $-2\omega_g$. From (7.6), it is seen that minimal modulus of the positive-sequence voltage vector is $E_p = 2E_{g,\text{nom}}/3$ and that the maximum negative-sequence voltage vector is $E_n = E_{g,\text{nom}}/3$. This occurs when $V = 0$, i.e., a total loss of voltage in the faulted phase.

The initial error angle of the positive-sequence voltage vector due to a SLGF is

$$\tilde{\theta}_0 = \arg(\mathbf{E}_{p0}) = \arctan\left(\frac{V\sin\phi}{2E_{g,\text{nom}} + V\cos\phi}\right). \tag{7.8}$$

Eventually, the PLL will track the position of the positive-sequence voltage vector, such that, ideally, $\mathbf{E}_p$ becomes real valued and, hence, $\tilde{\theta} \approx 0$. Consider the following values for a numerical example: $E_{g,\text{nom}} = 1$ p.u., $V = 0.5$ p.u. and $\phi = -45°$. This gives an initial error angle of $\tilde{\theta} = \arctan[-0.5 \cdot 0.71/(2 + 0.5 \cdot 0.71)] \approx -0.15$ rad $\approx -9°$. The initial error angle becomes even smaller if V is smaller than 0.5 p.u.; $\tilde{\theta}_0 = 0$ for $V = 0$, for instance.

Two-Lines-to-Ground Fault

After a two-lines-to-ground fault (TLGF) between the first and second phase, the grid phase voltages can be expressed as

$$E_1(t = 0_+) = \sqrt{2}V\cos(\theta_g + \pi/2 + \phi) \tag{7.9}$$

$$E_2(t = 0_+) = \sqrt{2}V\cos(\theta_g + \pi/2 - 2\pi/3 + \phi) \tag{7.10}$$

$$E_3(t = 0_+) = \sqrt{2}E_{g,\text{nom}}\cos(\theta_g + \pi/2 + 2\pi/3) \tag{7.11}$$

which correspond to the following space vector in the synchronous reference frame:

$$\mathbf{E}_{g0} = j\left(\mathbf{E}_{p0} + \mathbf{E}_{n0}e^{-j2\theta_g}\right) \tag{7.12}$$

where

$$\mathbf{E}_{p0} = \frac{E_{g,\text{nom}}}{3} + \frac{2}{3}Ve^{j\phi},\ \mathbf{E}_{n0} = \left(\mathbf{E}_{p0}^{*} - Ve^{-j\phi}\right)e^{-j\pi/3}. \tag{7.13}$$

From (7.12) and (7.13), it can be seen that the minimal modulus for the positive-sequence voltage vector is $E_p = E_{g,\text{nom}}/3$ and that the maximal modulus for the negative-sequence voltage vector is $E_n = E_{g,\text{nom}}/3$ for $V = 0$.

The initial error angle directly after a TLGF is

$$\tilde{\theta}_0 = \arg(\mathbf{E}_{p0}) = \arctan\left(\frac{2V\sin\phi}{E_{g,\text{nom}} + 2V\cos\phi}\right). \tag{7.14}$$

An initial error angle of -23° is obtained as a numerical example using the same values as in the previous section.

Line-to-Line Fault

Directly after a worst-case (no feeder impedance) line-to-line fault (LLF) between phases 2 and 3, the grid phase voltages are found as

$$E_1 = \sqrt{2}E_{g,\text{nom}}\cos(\theta_g + \pi/2) \tag{7.15}$$

$$E_2 = \frac{E_{g,\text{nom}}}{\sqrt{2}}\cos(\theta_g + \pi/2 - \pi) \tag{7.16}$$

$$E_3 = \frac{E_{g,\text{nom}}}{\sqrt{2}}\cos(\theta_g + \pi/2 - \pi) \tag{7.17}$$

which correspond to the following space vector in the synchronous reference frame:

$$\mathbf{E}_{g0} = j\left(1 - e^{-j2\theta_g}\right)\frac{E_{g,\text{nom}}}{2}. \tag{7.18}$$

Obviously, the modulus of the positive- and negative-sequence voltage vectors both equal $E_{g,\text{nom}}/2$, and the initial error angle moments after the LLF equals zero.

7.2 Full-Power Converter

In this section, the voltage sag response of PWM rectifiers, designed for the rated WT power, is analyzed. The system configuration consists of a generator and two converters connected "back-to-back" as depicted in Fig. 7.2. The main focus of this section is put on the PWM rectifier and the achieved results and conclusions are independent of the type of converter at the generator side. As a result of the analysis, accurate estimates of the transient and steady-state response of the grid current and dc-link voltage during voltage sags are provided. These results can be useful when designing a PWM rectifier for various grid codes and requirements.

7.2.1 Analysis

First, the dc-link voltage dynamics are analyzed for various disturbances and voltage sags. The dc-link voltage controller presented in Section 4.5.2 will be considered, with the exception of $P_r = -P_t$. Note that for this case, the grid-filter current equals the grid current. This exception indicates that the rotor power, P_r, used for the DFIG is changed to the total turbine power, P_t, for the full-power converter analyzed in this section. It is assumed that

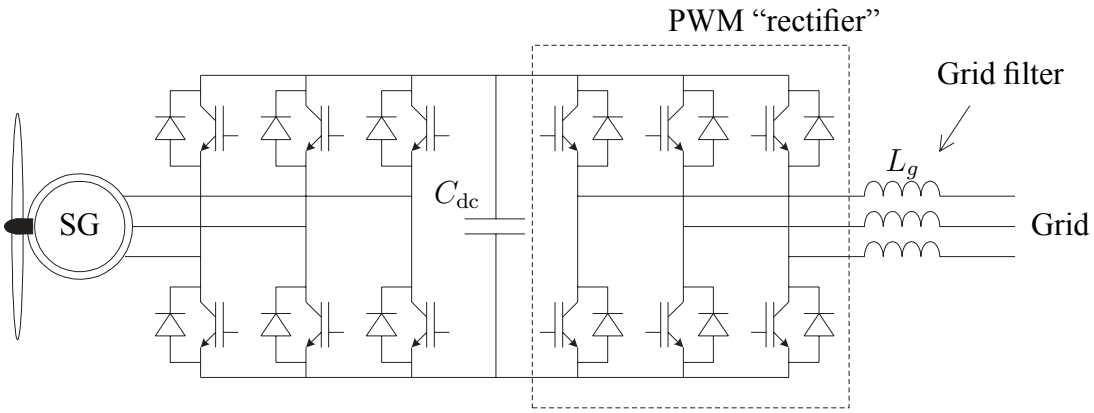

Fig. 7.2. Wind turbine with a full power rectifier.

the dc-link capacitance is accurately modeled, i.e., $\hat{C}_{\rm dc} = C_{\rm dc}$. The transfer function from the turbine power P_t to the error signal, $e_w = W_{\rm dc}^{\rm ref} - W_{\rm dc}$, will be considered which, with (4.120), becomes

$$G_{Pe}(p) = -G_{PW}(p) = \frac{-2p}{C_{\rm dc}\big(p^2 + 2\alpha_w\xi p + \alpha_w^2\xi\big)}. \tag{7.19}$$

Since the dc-link dynamics are considered to be much slower than the switching and sampling frequency, f_{sw}, of the PWM rectifier, the grid-filter current dynamics and the switching transients at the dc link are, thus, neglected. For instance, if the bandwidth of the dc-link voltage control loop is $\alpha_w = 0.2$ p.u. and the switching and sampling frequency is $f_{sw} = 4.9$ kHz. Then, for a 50-Hz grid, α_w is $4900/(0.2 \cdot 50) = 490$ times smaller than f_{sw}. Moreover, steady-state condition, symmetrical and nominal grid voltage, and perfect field orientation are assumed to precede the different disturbances.

Minimal DC-link Capacitance

In PWM rectifiers, the current in the dc-link capacitors is heavily distorted which gives rise to a small (compared to diode rectifiers) ripple in the dc-link voltage. To ensure that this voltage ripple remains below a tolerable value, the dc-link capacitance should be selected no smaller than [59]

$$C_{\rm dc,min} = \frac{\sqrt{3} i_{fq}^{\rm nom}}{8 f_{sw} \tilde{v}_{\rm dc}^{\rm p\text{-}p}} \tag{7.20}$$

where $i_{fq}^{\rm nom} = 1$ p.u. is the nominal q-axis current and $\tilde{v}_{\rm dc}^{\rm p\text{-}p}$ is the tolerable peak-to-peak ripple for the dc-link voltage. The value $\tilde{v}_{\rm dc}^{\rm p\text{-}p} = 0.028$ pu, which corresponds to 1 % peak-to-peak ripple at $v_{\rm dc}^{\rm ref} = 2.8$ and $f_{sw} = 4.9$ kHz, are considered for a numerical example. For a base frequency of $\omega_b = 314$ rad/s, these values yield $C_{\rm dc,min} = \sqrt{3} \cdot 1/(8 \cdot 4900/314 \cdot 0.028) \approx 0.5$ p.u. However, very high demands [50] are placed on the dc-link voltage control loop when using such small a dc-link capacitance, so (7.20) is mainly a benchmark that can be used for comparison to more realistic operating conditions. Henceforth, a dc-link capacitance of $C_{\rm dc} = 3.5$ p.u. is considered, which equals the capacitance of the experimental setup in Section 7.2.3.

Assessment of Turbine Power Reduction

The grid-voltage modulus is normally close to its nominal value. Therefore, it is natural to let $E_{gq} = E_{g,\text{nom}}$ when analyzing the capability of the dc-link voltage control loop to reject disturbances in P_t. Therefore, (7.19) is reduced to

$$G_{Pe}^{\text{nom}}(p) = G_{Pe}(p)\Big|_{E_{gq}=E_{\text{g,nom}}} = \frac{-2p}{C_{\text{dc}}(p+\alpha_w)^2}. \tag{7.21}$$

For a step in the turbine power, from $P_t(0_-) = 0$ to $P_t(0_+) = \Delta P$, the error, $e_w(t)$, becomes

$$e_w(t) = \mathcal{L}^{-1}\left\{G_{Pe}^{\text{nom}}(p)\frac{\Delta P}{p}\right\} = -\frac{2\Delta P}{C_{\text{dc}}}e^{-\alpha_w t}t. \tag{7.22}$$

Depending on whether ΔP is positive or negative, (7.22) has a local minimum or maximum for $t = 1/\alpha_w$ (determined by solving $\dot{e}_w(t) = 0$). Then, the maximum/minimum value of $e_w(t)$ is

$$e_w^{\max/\min}(t = 1/\alpha_w) = -\frac{2\Delta P}{\alpha_w C_{\text{dc}}}e^{-1} \approx -\frac{0.74\Delta P}{\alpha_w C_{\text{dc}}}. \tag{7.23}$$

The values $\Delta P = -1.5$ p.u. (50 % of nominal power), $\alpha_w = 0.2$ p.u. and $C_{\text{dc}} = 3.5$ p.u. are considered for a numerical example which yield a local maximum for $e_w(t)$ at $e_w^{\max} = 0.74 \cdot 1.5/(0.2 \cdot 3.5) \approx 1.6$ p.u. With $v_{\text{dc}}^{\text{ref}} = 2.8$ p.u., this corresponds to a minimum dc-link voltage of $v_{\text{dc}}^{\min} = ((v_{\text{dc}}^{\text{ref}})^2 - e_w^{\max})^{0.5} = (2.8^2 - 1.6)^{0.5} = 2.5$ p.u.

Response to Symmetrical Voltage Sags

As mentioned earlier, it is assumed that symmetrical voltage sags are preceded by symmetrical and nominal grid voltage, perfect field orientation and steady-state condition, i.e., $\dot{W} = 0$. This implies that:

$$t < 0: \quad 0 = -3E_{\text{g,nom}}i_{fq} + P_{t0} \tag{7.24}$$

where P_{t0} is the pre-sag turbine power. Moments after a symmetrical voltage sag occurs, it can be assumed that $E_{gq} = V$ while P_t remains at its pre-sag value. These assumptions imply the following dynamics for W:

$$t \geq 0: \quad \frac{1}{2}C\frac{dW}{dt} = -3Vi_{fq} + P_{t0} \tag{7.25}$$

after a sag at $t = 0$. Since the power to the grid filter is $P_f = 3E_{gq}(t)i_{fq}(v_{\text{dc}})$, where $E_{gq}(t)$ changes stepwise at $t = 0$ and $i_{fq}(v_{\text{dc}})$ is a function of the dc-link voltage (via the v_{dc} control loop), the dynamics in (7.25) appear to be time-varying. However, this is not the case, though, which can be deduced by multiplying (7.24) by $V/E_{\text{g,nom}}$:

$$t < 0: \quad 0 = -3Vi_{fq} + P_{t0}\frac{V}{E_{g,\text{nom}}}. \tag{7.26}$$

Then by introducing the "new" turbine power, $P_t'(t) = P_{t0}V/E_{g,\text{nom}}$, it follows from (7.25) and (7.26) that a symmetrical voltage sag is equivalent to a positive step in P_t', which changes from $P_t'(0_-) = P_{g0}V/E_{\text{g,nom}}$ to $P_t'(0_+) = P_{t0}$. This means that the net power step is $\Delta P' = (1 - V/E_{\text{g,nom}})P_{t0}$. Meanwhile, the q-axis grid voltage can considered to be constant at

$E_{gq} = V$ provided that accurate field orientation is maintained. The single exception to this power step equivalence is when $V = 0$, which corresponds to that power cannot be transferred to the utility grid.

Once the equivalence to turbine power steps has been revealed, the dynamics of e_w during symmetrical voltage sags are, hence, given by (7.19). By substituting $E_{gq} = V$, the poles of this transfer function are

$$p_{1,2} = -\frac{\alpha_w}{E_{g,\text{nom}}}\left(V \pm j\sqrt{E_{g,\text{nom}}V - V^2}\right). \tag{7.27}$$

For normal operation, i.e., $V = E_{g,\text{nom}}$, the poles are located at $-\alpha_w$, as seen in (7.21). Moreover, the poles of (7.27) are well damped for $V \geq E_{g,\text{nom}}/2$. More troublesome however, is that symmetrical voltage sags may require very large i_{fq} in order to counteract the reduction in the grid rms voltage such that $P_f = P_g$ in the steady state. Consider $P_t = 3$ p.u. (nominal power) and $V = 0.1$ p.u., for instance, which demands for $i_{fq} = 3/(3 \cdot 0.1) = 10$ p.u. in order to regain steady-state conditions during a sag. Remedies for avoiding severe overcurrents during symmetrical voltage sags are discussed in Section 7.2.2.

Provided that overcurrent is avoided, $e_w(t)$, after a symmetrical voltage sag, is obtained from the inverse Laplace transform of (7.19) multiplied by the step $\Delta P'/p$:

$$e_w(t) = \mathcal{L}^{-1}\left\{G_{Pe}(p)\frac{\Delta P'}{p}\right\} = -\frac{2\Delta P'}{\omega_w C}e^{-\alpha_w \xi t}\sin(\omega_w t) \tag{7.28}$$

where $\omega_w = \alpha_w\sqrt{(1-\xi)\xi}$. Depending on the sign of $\Delta P'$, (7.28) has a local minimum or maximum for $t = \arcsin(\sqrt{1-\xi})/\omega_w$. By substituting this instant in (7.28), the extreme value for $e_w(t)$ is obtained as

$$e_w = -\frac{2\Delta P'}{\omega_w C}\exp\left(-\sqrt{\frac{\xi}{1-\xi}}\arcsin\left(\sqrt{1-\xi}\right)\right)\sqrt{1-\xi}. \tag{7.29}$$

The values $C = 3.5$ p.u., $\alpha_w = 0.2$ p.u., $P_{t0} = -1.5$ p.u., $V = 0.6$ p.u. are considered for a numerical example. This means that $\Delta P' = -1.5 \cdot 0.4 = -0.6$ p.u., $\xi = 0.6$ and $\omega_w = 0.2\sqrt{0.4 \cdot 0.6} \approx 0.1$ p.u. This yields a local maximum of $e_w^{\max} \approx 0.94$ p.u. With $v_{\text{dc}}^{\text{ref}} = 2.8$ p.u., this corresponds to a minimal dc-link voltage of $v_{\text{dc}}^{\min} = \sqrt{2.8^2 - 0.94} \approx 2.6$ p.u., i.e., the dc-link voltage decreases by $0.2/2.8 \cdot 100 \approx 7$ %.

Response to "Phase-Angle Jumps"

For reasons of simplicity and clarity, it is assumed that the modulus of the grid voltage vector remains constant at $E_{g,\text{nom}}$, i.e., no voltage sag accompanies the "phase-angle jump." The response of PWM rectifiers to "phase-angle jumps" is, to a large extent, determined by the dynamics of the error angle. For a PLL tuned assuming a bandwidth of ρ, the time function of the error angle after a "phase-angle jump" can be modeled as

$$\tilde{\theta}(t) = \tilde{\theta}_0 e^{-\rho t}. \tag{7.30}$$

In the time interval when $\tilde{\theta}(t)$ converges exponentially to zero with the rise time $1/\rho$, the q-axis grid voltage varies as $E_{gq}(t) = E_{g,\text{nom}}\cos[\tilde{\theta}(t)]$ which yields the instantaneous grid-filter power as $P_f = 3E_{g,\text{nom}}i_{fq}(v_{\text{dc}})\cos[\tilde{\theta}(t)]$. Since P_f is a function of time and v_{dc}, the

dynamics of W, are time varying during "phase-angle jumps" in contrast to symmetrical voltage sags. As a remedy for this, the seemingly daring assumption of nearly constant dc-link voltage during "phase-angle jumps" is adopted. This assumption is validated by simulations and experiments in Section 7.2.3 which show that the approximation is, indeed, reasonable. With $\dot{W} \approx 0$, the "dynamics" after a "phase-angle jump" at $t = 0$ simplify to

$$t \geq 0: \; 0 \approx -3E_{g,\mathrm{nom}} i_{fq} \cos\tilde{\theta} + P_{t0} = -3E_{g,\mathrm{nom}} i_{fq} + \frac{P_{t0}}{\cos\tilde{\theta}}. \tag{7.31}$$

The approximated "dynamics" in (7.31) are time-invariant, since $P_f = 3E_{g,\mathrm{nom}} i_{fq}(v_{\mathrm{dc}})$ is a function of v_{dc} only. Therefore, from (7.24) and (7.31), a "phase-angle jump" is in close correspondence to a time varying P_t' which changes from $P_t'(0_-) = P_{t0}$ to $P_t'(t) = P_{t0}/\cos[\tilde{\theta}(t)]$ at constant $E_{gq} = E_{g,\mathrm{nom}}$. For small $\tilde{\theta}$, such that $1/\cos\tilde{\theta} \approx 1 + \tilde{\theta}^2/2$, the net change in P_t' is

$$\Delta P(t) = \left(1 + \frac{\tilde{\theta}^2(t)}{2}\right) P_{t0} - P_{t0} = \frac{\hat{\theta}_0^2}{2} e^{-2\rho t} P_{t0} \tag{7.32}$$

where the latter expression results from (7.30). The time function of the error signal can be derived by taking the inverse Laplace transform of the product of (7.21) and $\Delta P(p)$:

$$e_w(t) = \mathcal{L}^{-1}\{G_{Pe}^{\mathrm{nom}}(p)\mathcal{L}\{\Delta P(t)\}\} = \frac{2\tilde{\theta}_0^2 P_{t0}}{\rho C_{\mathrm{dc}}} \left(e^{-\rho t} + \frac{\rho}{2}t - 1\right) e^{-\rho t} \tag{7.33}$$

where $\alpha_w = \rho$ is assumed since proper rejection of the negative-sequence voltage requires a PLL bandwidth of $\rho \approx 0.2$ p.u. [76] (this happens to coincide with the selection of $\alpha_w = 0.2$ p.u. in the beginning of this section). Within a short time interval after a "phase-angle jump," $e_w(t)$ can be approximated by

$$e_w(t) \approx \frac{2\tilde{\theta}_0^2 P_{t0}}{\rho C_{\mathrm{dc}}} \left[e^{-\rho t} - 1\right] e^{-\rho t} = e_w'(t) \tag{7.34}$$

since $e^{-\rho t}$ initially decays faster than $\rho t/2$ increases. The error signal $e_w(t)$ has a local minimum/maximum for $t = \ln 2/\rho$. By substituting this instant in (7.33), the extreme value for $e_w(t)$ is found as

$$e_w \approx \frac{2\tilde{\theta}_0^2 P_{t0}}{\rho C_{\mathrm{dc}}} \left(\frac{1}{2} + \frac{\ln 2}{2} - 1\right) \frac{1}{2} \approx -\frac{0.15\tilde{\theta}_0^2 P_{t0}}{\rho C_{\mathrm{dc}}}. \tag{7.35}$$

The values $P_{t0} = -1.5$ p.u., $\tilde{\theta}_0 = -\pi/4$ rad, $\alpha_w = \rho = 0.2$ p.u. and $C_{\mathrm{dc}} = 3.5$ p.u. are considered for a numerical example, which gives a local maximum of $e_w^{\max} = 0.15 \cdot 1.5 \cdot \pi^2/(4^2 \cdot 0.2 \cdot 3.5) \approx 0.2$ p.u. With $v_{\mathrm{dc}}^{\mathrm{ref}} = 2.8$ p.u., this implies that the dc-link voltage decreases to $v_{\mathrm{dc}}^{\min} = (2.8^2 - 0.2)^{0.5} \approx 2.76$ p.u., i.e., a decrement by $0.04/2.8 \cdot 100 \approx 1$ %. From this analytic finding, which is supported by simulations and experiments in Section 7.2.3, it can be concluded that "phase-angle jumps" are believed not to be critical for PWM rectifiers.

Response to Unsymmetrical Voltage Sags

The response of PWM rectifiers to unsymmetrical voltage sags is partly similar to the response to symmetrical voltage sags, although less critical, since the remaining positive-sequence voltage of unsymmetrical sags is never as small as that of the worst-case symmetrical sag, as discussed previously. A unique property of unsymmetrical sags is, on the

other hand, that the negative-sequence voltage vector introduces a ripple in the instantaneous grid power. This power ripple in turn gives rise to ripple in the dc-link voltage and in i_{fq}, which can be expressed as $i_{fq} = i_{fq}^{\text{avg}} + \tilde{i}_{fq}$, where i_{fq}^{avg} is the average value of i_{fq} and $\tilde{i}_{fq}$ is the current ripple. Two simplifications are introduced in order to analyze these ripples. First shortly after an unsymmetrical sag it is assumed that the PLL recovers the position of the positive-sequence voltage vector, i.e., the q-axis grid voltage eventually varies as $E_{gq}(t) = E_p + E_n \cos(-2\theta_g + \varphi)$ where φ is the angle of the negative-sequence voltage vector for $\tilde{\theta} = t = 0$. Provided with this expression for E_{gq} and, secondly, small current ripple, such that $|i_{fq}^{\text{avg}}| \gg |\tilde{i}_{fq}|$, the dc-link voltage dynamics simplify to

$$\frac{1}{2}C_{\text{dc}}\frac{dW}{dt} \approx -3E_p i_{fq} - 3E_n i_{fq}^{\text{avg}} \cos(2\theta_g - \varphi) + P_t. \tag{7.36}$$

From (7.36), the power ripple can be treated as a turbine power disturbance, denoted by $\tilde{P}_t = 3E_n i_q^{\text{avg}} \cos(2\theta_g - \varphi) = \tilde{P}_t^{\text{pk}} \cos(2\theta_g - \varphi)$, with constant $E_{gq} = E_p$. The dc voltage ripple that results from $\tilde{P}_t$ are obtained from the static gain of $G_{Pe}(p)$ in (7.19) at the relevant frequency $2\omega_g$ and $E_{gq} = E_p$:

$$|G_{Pe}(j2\omega_g)| = \frac{4\omega_g}{C_{\text{dc}}\sqrt{(\alpha_w^2\xi_p - 4\omega_g^2)^2 + (4\omega_g\alpha_w\xi_p)^2}} \tag{7.37}$$

where $\xi_p = E_p/E_{g,\text{nom}}$. If α_w is selected at least three times smaller than ω_g, i.e., smaller than 0.3 p.u., such that $\omega_g^2 \gg \alpha_w^2$, then (7.37) can be approximated as

$$|G_{Pe}(j2\omega_g)| \approx \frac{4\omega_g}{C_{\text{dc}}\sqrt{(-4\omega_g^2)^2}} = \frac{1}{\omega_g C_{\text{dc}}}. \tag{7.38}$$

Hence, the ripple in e_w, due to an unsymmetrical voltage sag, is determined, to a large extent, by the dc-link capacitance. An LLF is considered for a numerical example. The values $E_n = 0.5$ p.u., $i_{fq}^{\text{avg}} = 1$ p.u., $v_{\text{dc}}^{\text{ref}} = 2.8$ p.u. and $C_{\text{dc}} = 3.5$ p.u. yield a peak ripple of $\tilde{e}_w^{\text{pk}} \approx \tilde{P}_t^{\text{pk}}/(\omega_g C_{\text{dc}}) = 3 \cdot 0.5 \cdot 1/(1 \cdot 3.5) = 0.43$ p.u. at a frequency of $2\omega_g$. The corresponding peak value of the v_{dc} ripple is $\tilde{v}_{\text{dc}}^{\text{pk}} = 2.8 - (2.8^2 - 0.43)^{0.5} \approx 0.08$ p.u., or a ripple of $0.08/2.8 \cdot 100 \approx 3$ %. This is a fairly small ripple which is not critical for the proper operation of a PWM rectifier. As for symmetrical sags, the modulus of the positive-sequence voltage vector is the most critical consequence. This indicates that if $E_p = 0.5$ p.u., a q-axis current of $i_{fq}^{\text{avg}} = 1$ p.u. yields $P_f = 3E_p i_{fq}^{\text{avg}} = 1.5$ p.u., whereas nominal power, i.e., $P_f = 3$ p.u., requires $i_{fq}^{\text{avg}} = 1/0.5 = 2$ p.u. This may be too large a current to be tolerated in a WT application; remedies for avoiding large q-axis currents are to be discussed in Section 7.2.2.

As previously discussed, the power ripple during unsymmetrical voltage sags also transfers to the q-axis current, via the dc voltage control system. In order to analyze the resulting q current ripple, which adds to the grid current distortion during faults, the transfer function from P_t to i_{fq} can be derived from Fig. 4.15, which results in

$$\begin{aligned} G_{Pi}(p) &= \frac{-2[G_a + F(p)]/(pC_{\text{dc}})}{1 - 6E_q[G_a + F(p)]/(pC_{\text{dc}})} \\ &= \frac{2\alpha_w(p + \alpha_w/2)}{3E_{g,\text{nom}}(p^2 + 2\alpha_w E_{gq}/E_{g,\text{nom}}p + \alpha_w^2 E_{gq}/E_{g,\text{nom}})}. \end{aligned} \tag{7.39}$$

By substituting $E_{gq} = E_p$ in this expression, the static gain of $G_{Pi}(p)$ at the relevant frequency $2\omega_g$ is obtained as

$$|G_{Pi}(j2\omega_g)| = \frac{\alpha_w}{3E_{g,\mathrm{nom}}}\sqrt{\frac{\alpha_w^2 + 16\omega_g^2}{(\alpha_w^2\xi_p - 4\omega_g^2)^2 + (4\omega_g\alpha_w\xi_p)^2}} \approx \frac{\alpha_w}{3\omega_g E_{g,\mathrm{nom}}} \tag{7.40}$$

where the latter approximation holds when α_w is selected at least three times smaller than ω_g. The relation in (7.40) implies that the resulting ripple in i_{fq} is mainly determined by the bandwidth of the dc voltage control system. Therefore, a less distorted grid current during unsymmetrical voltage sags can be obtained by selecting α_w smaller. This yields a peak ripple of $\tilde{i}_{fq}^{\mathrm{pk}} \approx \alpha_w \tilde{P}_t^{\mathrm{pk}}/(3\omega_g E_{g,\mathrm{nom}}) = 0.2 \cdot 1.5/3 = 0.1$ p.u. during an LLF, with identical values as previously and $\alpha_w = 0.2$ p.u. This is a fairly large ripple although the previous assumption on $|i_{fq}^{\mathrm{avg}}| \gg |\tilde{i}_{fq}|$ is still reasonable.

7.2.2 Discussion

In general, WTs using PWM rectifiers are robust towards voltage sags but large reductions in modulus of the positive-sequence voltage vector appear to be critical. For a voltage sag where the modulus reduces to V, no more than $P_f^{\mathrm{max}} = 3Vi_{fq}^{\mathrm{max}}$ can be transferred to the utility grid. Depending on the wind situation when the voltage sag occurs, it may happen that the turbine power is larger compared to P_f^{max}. For such operating conditions, the dc-link voltage begins to increase, unless the excess energy is somehow stored or dissipated. The design of such energy storages depends on several factors of which some are:

- Cost.
- Grid codes.
- The remaining modulus of the positive-sequence grid voltage vector and the duration of the voltage sag.

Depending on these factors, one, or possibly a combination, of the following four solutions may be applicable:

Rotor Energy Storage

In this solution, the turbine power is controlled to $P_t = P_f$ by changing the torque reference for the turbine. If the pre-sag grid power must be restored moments after the voltage sag is cleared, the blades should preferably remain in their pre-sag position, unless the WT approaches overspeed. If there is no need for instantaneous power restoration, the blades can be pitched out of the wind directly.

"Braking" Chopper

A "braking" chopper, acting as a load dump, can be installed at the dc link. The limiting factor of this solution is the heat generated by the "braking" resistor which may be troublesome to remove for long-duration voltage sags or interruptions.

DC-Link Energy Storage

A large dc-link capacitor bank can possibly be used, such that energy from the WT is buffered at the dc link during the sag. The required size of the capacitor bank can be calculated by substituting $\dot{W} = W_\Delta/t_\Delta$ in (7.25), assuming $i_{fq} = i_{fq}^{\max}$, and solving the resulting expression for $C_{\rm dc}$:

$$C_{\rm dc} = \frac{2\Delta t}{\Delta W}\left(-3Vi_{fq}^{\max} + P_t\right). \tag{7.41}$$

If the dc-link voltage is allowed to increase by no more than 10 %, then $W_\Delta = (1.1v_{\rm dc})^2 - (v_{\rm dc}^{\rm ref})^2 = 0.21(v_{\rm dc}^{\rm ref})^2$. The values $\Delta W = 0.21 \cdot 2.7^2 \approx 1.5$ p.u., $\Delta t = 0.25$ s, $V = 0$, $i_{fq}^{\max} = 1$ p.u. and $P_t = 3$ p.u. are considered for a numerical example, which gives $C_{\rm dc} = 2 \cdot 0.25 \cdot 314 \cdot 3/1.5 \approx 310$ p.u. This is a very large value, so a dc-link energy storage appears to be suitable mainly for small voltage sags that appear for a short period of time.

Overcurrent

The PWM rectifier can be designed for overcurrent, i.e., $i_{fq}^{\max} > 1$ pu. However, the thermal limit of the utility grid may not be designed for such overcurrent, especially if several WTs are connected to a common point.

7.2.3 Evaluation

This section presents simulated and experimental results of a PWM rectifier which is subjected to various disturbances and voltage sags. The base values are 85 A, 105 V, 50 Hz, and 1.2 Ω. The dc-link capacitance is $C_{\rm dc} = 9.2$ mF, which corresponds to $C_{\rm dc} = 3.5$ p.u. The PWM rectifier uses 4.9 kHz sampling and switching frequency and the reference for the dc-link voltage is normally 2.8 p.u. The PWM rectifier is loaded by a dc-link resistor which corresponds to $P_t = -1.5$ p.u. and $i_{fq} = -0.5$ pu at $v_{\rm dc} = 2.8$ p.u.

The closed-loop grid current and dc-link voltage control loops are tuned for the bandwidths 2.3 p.u. and $\alpha_w = 0.2$ p.u. respectively, which corresponds to a current rise time of 3 ms and a dc-link voltage rise time of 35 ms. The d current reference equals zero, the maximum current modulus allowed is 1 pu, and the PLL bandwidth is $\rho = 0.2$ p.u.

Fig. 7.3 shows the results from the first simulation and experiment. A pure "phase-angle jump" of $\phi = -45° \approx -0.8$ rad occurs at $t = 0.05$ s, which yields an initial error angle of $\tilde{\theta}_{0.05} = -0.8$ rad. As seen from $\tilde{\theta}$ in Fig. 7.3b), the PLL recovers accurate field orientation at approximately 40 ms after the "phase-angle jump" so the PWM rectifier is hardly affected by the "jump," as already concluded. A symmetrical voltage sag occurs in the time interval $t =$0.1–0.3 s, giving, eventually, $E_g = 0.5$ p.u. and requiring i_q to be close to 1 p.u. in the steady state. Moments after $t = 0.1$ s, the grid voltage modulus is $E_g \approx 0.6$ p.u. which causes the dc-link voltage to drop to $v_{\rm dc} = 2.65$ p.u. at $t = 0.12$ s. This is close to the predicted value $v_{\rm dc} = 2.6$ p.u., resulting from the numerical example in Section 7.2.1. The grid voltage is recovered at $t = 0.32$ s, causing the dc-link voltage to increase to $v_{\rm dc} = 3$ p.u.

Fig. 7.4 shows the results of an unsymmetrical voltage sag, characterized by $E_p = 0.6$ p.u. and $E_n = 0.4$ p.u. The sag occurs in the time interval $t =$0.1–0.3 s. In all other aspects, the simulation and corresponding experiment are carried out under similar conditions as in Fig. 7.3. The simulated and experimental waveforms are similar to those in Fig. 7.3 except

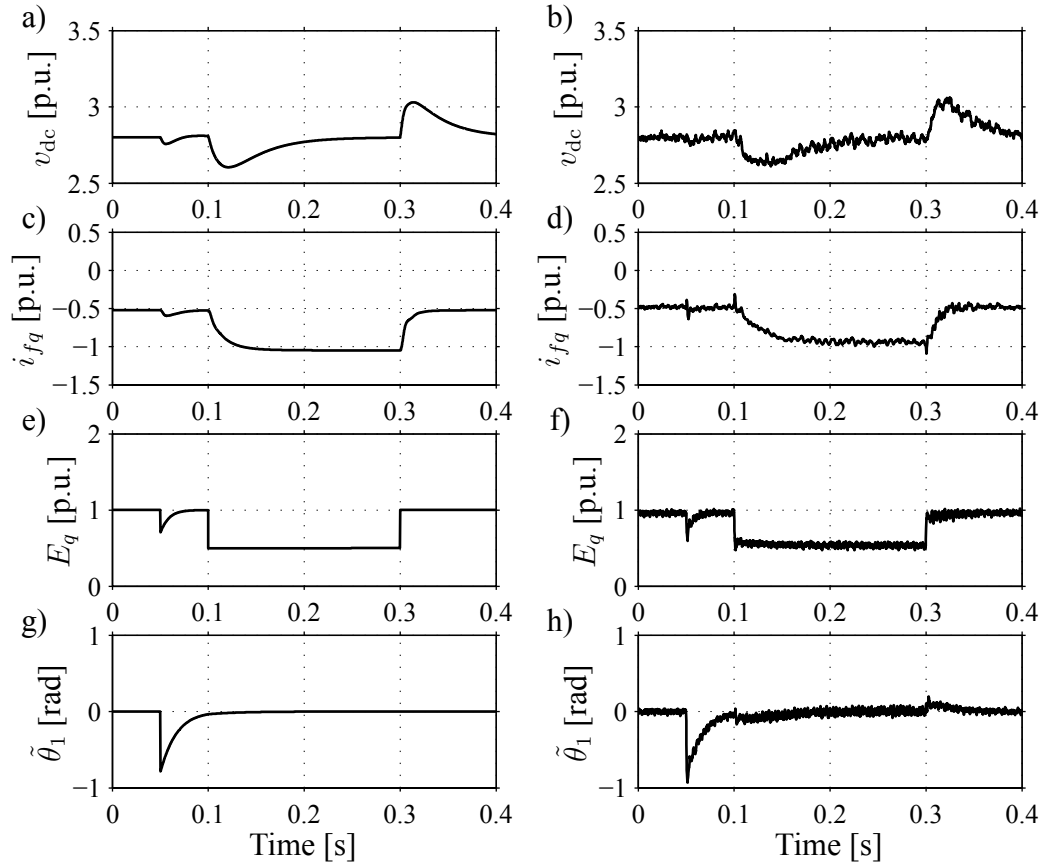

Fig. 7.3. Response to "phase-angle jump" and symmetrical voltage sag. a) DC-link voltage, $v_{\rm dc}$ (simulation). b) DC-link voltage, $v_{\rm dc}$ (experiment). c) Grid-filter current, i_{fq} (simulation). d) Grid-filter current, i_{fq} (experiment). e) Grid voltage, E_q (simulation). f) Grid voltage, E_q (experiment). g) PLL error angle, $\tilde{\theta}_1$ (simulation). h) PLL error angle, $\tilde{\theta}_1$ (experiment).

that a ripple of approximately 0.1 p.u. is superimposed on the dc-link voltage, and the ripple in the q-axis current is close to 0.12 p.u. These ripples are in close correspondence to the values predicted by the numerical example in the analysis section.

In the last experiment, the load power is stepped from $P_t = 0$ to $P_t = -1.5$ p.u. at $t = 0.1$ s, and 0.2 s later, the reference for the dc-link voltage changes stepwise from $v_{\rm dc}^{\rm ref} = 2.8$ p.u. to $v_{\rm dc}^{\rm ref} = 3$ p.u. Fig. 7.5 shows the results. The dc-link voltage reduces to 2.5 p.u., as predicted in Section 7.2.1, 15 ms after the load power step. The step response for $t > 0.3$ s is well damped and the dc voltage rise time (10–90 % of the final value) appears to equal the intended 35 ms.

7.2.4 Conclusion

The voltage sag response of PWM rectifiers has been investigated for a candidate dc-link voltage control system. A method of analysis was derived, which showed good agreement between analytical predictions and experimental results. For several types and magnitudes of voltage sags, the candidate dc-link voltage control system can successfully reduce disturbances from both symmetrical and unsymmetrical voltage sags such that nominal power

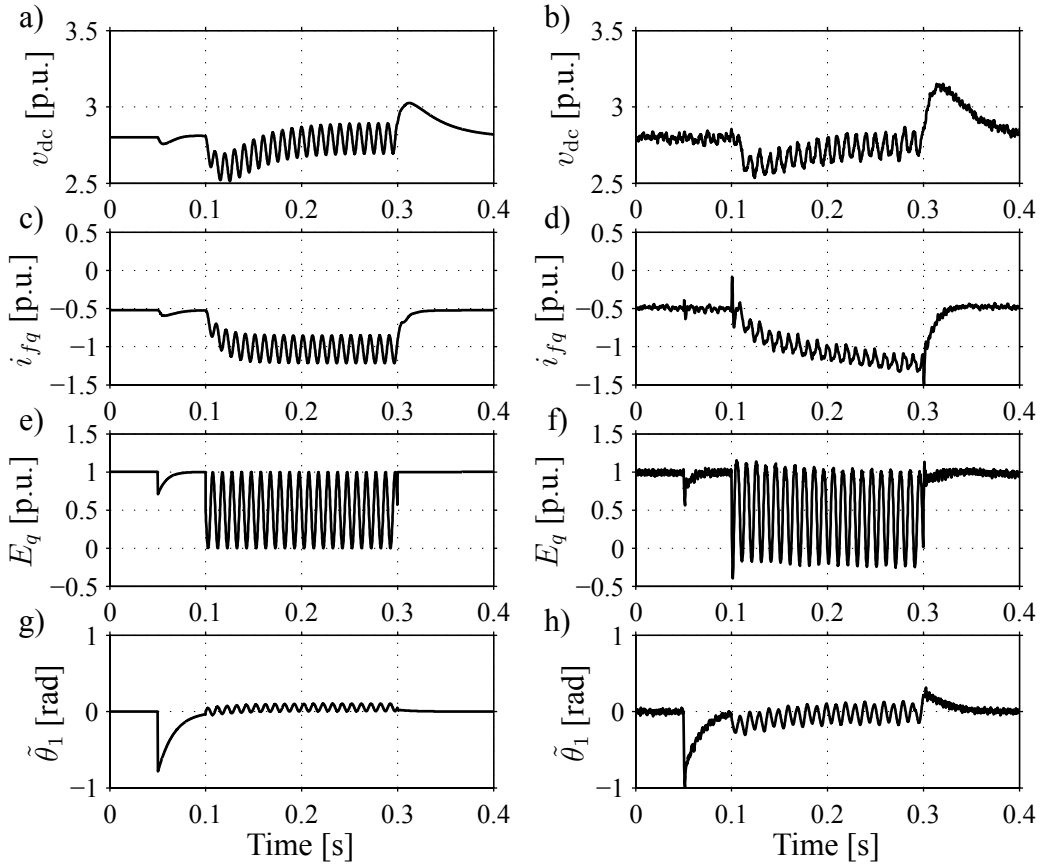

Fig. 7.4. Response to "phase-angle jump" and LLF unsymmetrical voltage sag. a) DC-link voltage, $v_{\rm dc}$ (simulation). b) DC-link voltage, $v_{\rm dc}$ (experiment). c) Grid-filter current, i_{fq} (simulation). d) Grid-filter current, i_{fq} (experiment). e) Grid voltage, E_q (simulation). f) Grid voltage, E_q (experiment). g) PLL error angle, $\tilde{\theta}_1$ (simulation). h) PLL error angle, $\tilde{\theta}_1$ (experiment).

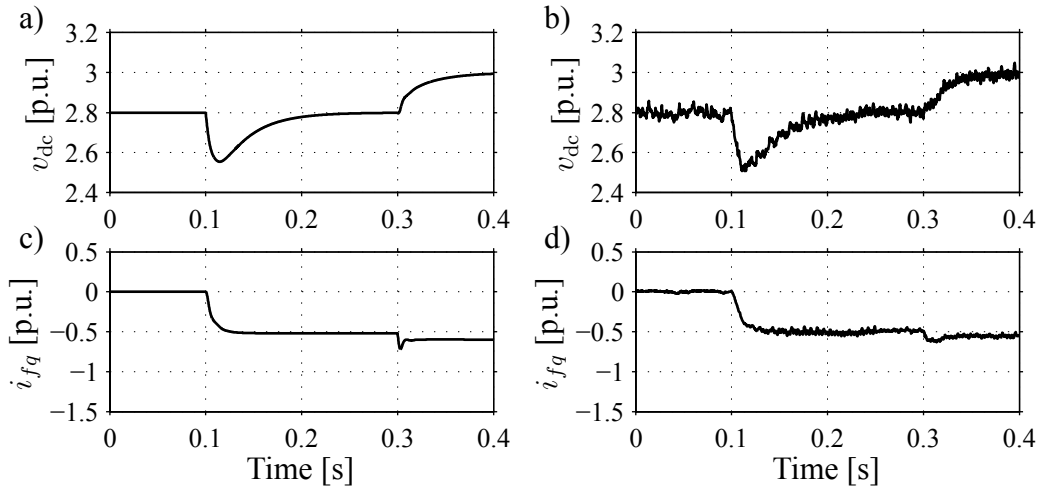

Fig. 7.5. Steps in P_s and $v_{\rm dc}^{\rm ref}$. a) DC-link voltage, $v_{\rm dc}$ (simulation). b) DC-link voltage, $v_{\rm dc}$ (experiment). c) Grid-filter current, i_{fq} (simulation). d) Grid-filter current, i_{fq} (experiment).

production can be restored once the grid voltage recovers. However, large reductions in the positive-sequence voltage were found to be critical. Unless suitable actions are taken, such a voltage reduction sag may result in a dc-link overvoltage since the transferable active power reduces with reducing grid voltage. Remedies for avoiding overvoltage at the dc link have also been discussed.

7.3 Doubly-Fed Induction Generator with Shunt Converter

Fig. 7.6 shows a principle sketch of the DFIG. In the figure a crowbar is also depicted, which short-circuits the rotor circuit in case of too large a grid disturbance causing high rotor current, and thereby protects the rotor converter. After such an action, rotor current control has been lost and the turbine must be disconnected from the grid. The crowbar in

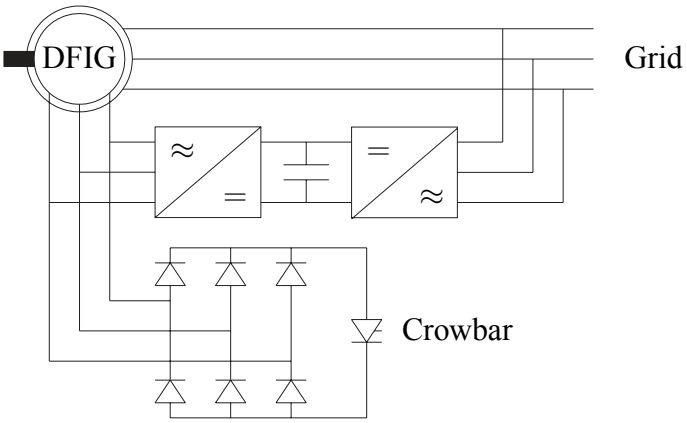

Fig. 7.6. Doubly-fed induction generator system with a crowbar.

Fig. 7.6 consists of a diode rectifier and a thyristor that is triggered when the rotor circuit should be short circuited. One disadvantage with this system is that once the crowbar has been triggered, the turbine must be disconnected from the grid, since the current through the thyristor is a continuous dc current and can only be interrupted if the turbine is disconnected from the grid [72]. However, one possibility is to still have a rotor converter, but one that can handle a higher current for a short period of time of some 100s of ms. Assuming such a short over-current time, this means that only the IGBT modules need to be designed for a higher current while the rotor winding and the converter (cooling etc) still can be designed according to the slip power only. This means that the converter shortly can handle a higher current and thereby stay connected to the grid longer without any crowbar action. Still, this system will have high fault currents from the stator during the voltage sag. Since the relatively low power losses in the power electronic equipment were a major reason for selecting a DFIG, it is accordingly important to study how the ride-through system influences the power losses, since additional hardware or modifications may reduce the efficiency.

Before explaining the candidate DFIG ride-through system, we will look further into the dynamics of the DFIG during a voltage sag.

7.3.1 Response to Small Voltage Sags

In order to explain what happens to the DFIG during and after a voltage sag, we will start by looking at the flux dynamics. First, we will assume that the converter is ideal an can supply the desired rotor voltage and current, and steady-state conditions are assumed to precede the voltage sag. As discussed several times before, the flux dynamics of the DFIG are poorly damped. As also previously shown a voltage sag will cause the stator flux to enter a poorly damped oscillation with an oscillating frequency close to the line frequency. The amplitude of the oscillation will be proportional to the size of the voltage sag, which can be realized from the fact that $\psi_s \approx E_g/\omega_g$. If the DFIG system survives the voltage sag, i.e., no crowbar action, the amplitude of the flux oscillations can, after the voltage sag, i.e., when the voltage returns, vary between zero and close to twice the flux oscillations in the beginning of the sag. The reason that the amplitude of the stator flux oscillation can almost vary between zero and twice the initial amplitude is that steady-state condition hardly precedes the returning of the voltage. This can be realized from Fig. 7.7, where a phase portrait and corresponding time series of the flux can be seen. Note, that in order to make the figure more lucid, the duration of the voltage sags in the time series is two periods longer. In the figure, two different voltage sags are shown, with the duration of the sag as the only difference. The cross marks the equilibrium point during normal operation and the circle marks the equilibrium point during the voltage sag. It can be seen in the figure that directly after the voltage sag has occurred, the flux will circularly approach the "new" equilibrium point (the circle) very slowly. This is indicated by the dashed lines in the figure. Then, when the voltage returns, the flux will again approach circularly the equilibrium point (the cross) indicated with the solid line. However, as indicated by the difference between Fig. 7.7a) and Fig. 7.7b), the duration of the sag is important. In Figs. 7.7a) and c), the voltage returns when the flux is close to the original equilibrium point (the cross), which leads to that the flux oscillations after the voltage sag are relatively small. However, as shown in Fig. 7.7b) and d), if the voltage returns at an unfortunate moment, when the flux is far away from the original equilibrium point (the cross), the oscillations become even worse when the voltage returns after the sag.

Symmetrical Voltage Sags

In this section, the dc-link dynamics of the DFIG system will be analyzed in a similar way as for the full-power converter system in Section 7.2. In the analysis below, it will be assumed that the "disturbance" is applied at $t = 0$ and that steady-state conditions precede the fault causing the voltage sag. In order to analyze the response to voltage sags we will assume that the magnitude of the stator flux can be expressed in a similar way as in (5.47) and (5.48) as

$$t < 0: \qquad \Psi_s(t) = \psi_{s0} \approx \frac{E_{g,\mathrm{nom}}}{\omega_g} \tag{7.42}$$

$$t \geq 0: \qquad \Psi_s(t) \approx \psi_{s0}\frac{V}{E_{g,\mathrm{nom}}} + \left(1 - \frac{V}{E_{g,\mathrm{nom}}}\right)\psi_{s0}e^{-R_s t/L_M}e^{-j\omega_g t} \tag{7.43}$$

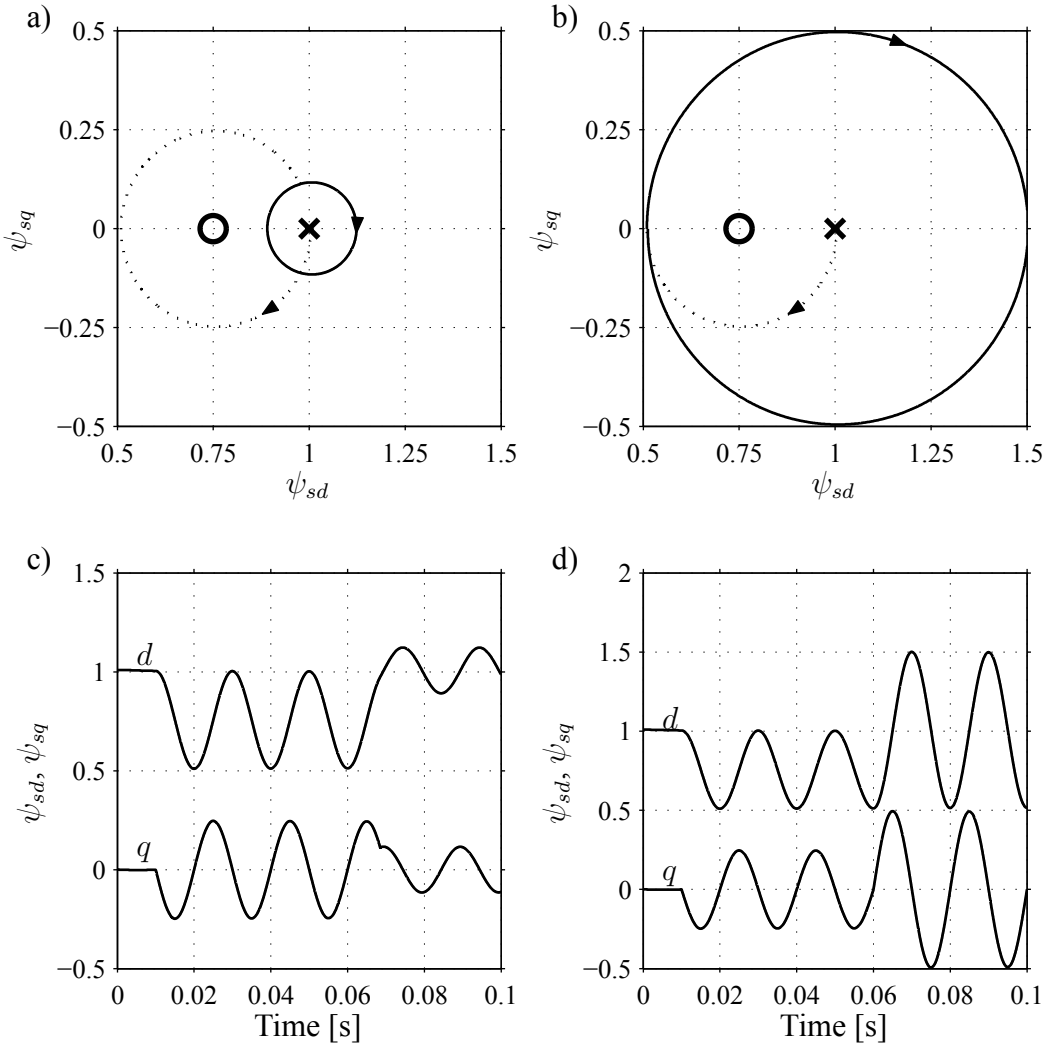

Fig. 7.7. Phase portrait and time series of the flux dynamics during a symmetrical voltage sag. For clarity of the figure, the voltage sag duration for the time series is two periods longer. a) 18.5 ms long voltage sag. b) 10 ms long voltage sag. c) Time series of the flux in a). d) Time series of the flux in b).

or as

$$t < 0: \qquad \Psi_s(t) = \psi_{s0} \approx \frac{E_{g,\mathrm{nom}}}{\omega_g} \tag{7.44}$$

$$t \geq 0: \qquad \Psi_s(t) \approx \psi_{s0}\frac{V}{E_{g,\mathrm{nom}}} + \psi_s^{\mathrm{pk}} e^{-R_s t/L_M} e^{-j\omega_g t} \tag{7.45}$$

where $\psi_s^{\mathrm{pk}} = (1 - V/E_{g,\mathrm{nom}})\psi_{s0}$ is the peak value of the stator flux oscillation. The expression for the stator flux in (7.43) and (7.45) can be found by solving the differential equation in (6.1). The dynamics of the dc-link are described by (4.48), and are governed both by the rotor power P_r and the grid-filter power P_f, which can be approximated as

$$P_r \approx 3E_{gq}i_{Rq} - 3\omega_r \mathrm{Re}[j\Psi_s \mathbf{i}_R^*] \approx 3E_{gq}i_{Rq} - 3\psi_s i_{Rq}\omega_r \tag{7.46}$$

$$P_f \approx 3E_{gq}i_{fq}. \tag{7.47}$$

The expression for P_r is derived from the fact that $P_r = \mathrm{Re}[3\mathbf{v}_R\mathbf{i}_R^*]$ and by using the approximation of the rotor voltage given by (5.38), i.e., $\mathbf{v}_R \approx E_{gq} - j\omega_r\Psi_s$, where the stator voltage has been changed to the grid voltage. This means that just before the voltage sag, P_r and P_f equal

$$P_r(t = 0_-) \approx 3E_{gq}i_{Rq} - 3\psi_{s0}i_{Rq}\omega_r \tag{7.48}$$

$$P_f(t = 0_-) \approx 3E_{gq}i_{fq}. \tag{7.49}$$

Moreover, since steady-state conditions are assumed to precede the sag, we have that $P_r(t = 0_-) = -P_f(t = 0_-)$, giving $i_{fq}(t = 0_-) = -(E_{gq}i_{Rq} - \psi_{s,0}i_{Rq}\omega_r)/E_{gq} \approx -(1-\omega_r/\omega_g)i_{Rq}$. Under the assumption that the rotor current controller and grid-filter controller manage to keep the current at (or at least close to) its reference value, moments after the sag has occurred, it is possible to express P_r and P_f as

$$t \geq 0: \qquad P_r(t) \approx 3Vi_{Rq} - 3\left(\frac{V}{E_{g,\mathrm{nom}}}i_{Rq}\omega_r\psi_{s0} + \psi_s^{\mathrm{pk}}i_R\omega_r e^{-R_s t/L_M}\sin(\omega_g t + \phi_r)\right) \tag{7.50}$$

$$t \geq 0: \qquad P_f(t) \approx 3Vi_{fq} \approx -3V\left(1 - \frac{\omega_r}{\omega_g}\right)i_{Rq} \tag{7.51}$$

where $i_R = |\mathbf{i}_R|$ and $\phi_r = \angle\mathbf{i}_R$. Then, as the stator flux prior to the voltage sag can be approximated as $\psi_{s0} \approx E_{g,\mathrm{nom}}/\omega_g$, the above expression can be further reduced as

$$t \geq 0: \qquad P_r(t) \approx 3V\left(1 - \frac{\omega_r}{\omega_g}\right)i_{Rq} - 3\psi_s^{\mathrm{pk}}i_R\omega_r e^{-R_s t/L_M}\sin(\omega_g t + \phi_r) \tag{7.52}$$

$$t \geq 0: \qquad P_f(t) \approx -3V\left(1 - \frac{\omega_r}{\omega_g}\right)i_{Rq}. \tag{7.53}$$

The dc-link dynamics in (4.48) are governed by the term $-P_r - P_f$. This means that the power drop in the first term of (7.52) is compensated for by the same drop in P_f as can be seen in (7.53). However, the second term in (7.52) will act as a disturbance to the dc-link, as

$$\tilde{P}_r = 3\psi_s^{\mathrm{pk}}i_R\omega_r e^{-R_s t/L_M}\sin(\omega_g t + \phi_r) = \tilde{P}_r^{\mathrm{pk}}e^{-R_s t/L_M}\sin(\omega_g t + \phi_r). \tag{7.54}$$

This disturbance will cause a ripple in the dc-link voltage with the frequency ω_g. In order to determine the amplitude of the ripple the static gain of (4.120), with $G_{Pe}(p) = -G_{PW}(p)$, at the relevant frequency can be used. This yields

$$|G_{Pe}(j\omega_g)| = \frac{2\omega_g}{C_{\mathrm{dc}}\sqrt{(\alpha_w^2\xi - \omega_g^2)^2 + (2\omega_g\alpha_w\xi)^2}} \tag{7.55}$$

where $\xi = V/E_{g,\mathrm{nom}}$. If $\omega_g \gg \alpha_w$, the above expression can be further approximated as

$$|G_{Pe}(j\omega_g)| \approx \frac{2}{C_{\mathrm{dc}}\omega_g}. \tag{7.56}$$

For example, consider a voltage sag with $V = 0.75$ p.u., and $C_{\mathrm{dc}} = 3.5$ p.u. This means that $\psi_s^{\mathrm{pk}} = (1 - V/E_{g,\mathrm{nom}})\psi_{s0} = (1 - 0.75) \cdot 1 = 0.25$ p.u., yielding $\tilde{P}_r^{\mathrm{pk}} = 3\psi_s^{\mathrm{pk}}i_R\omega_r =$

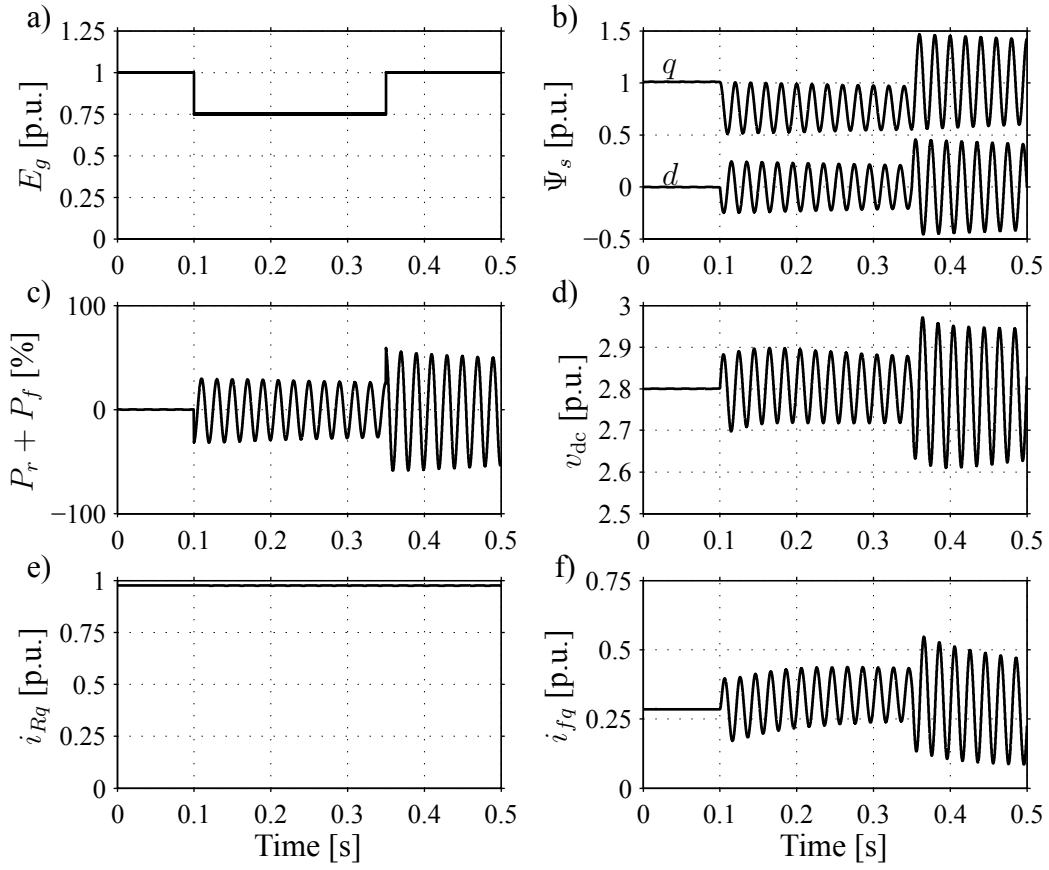

Fig. 7.8. Simulation of the response of the DFIG system to a small symmetrical voltage sag. a) Grid voltage. b) Stator flux. c) Sum of rotor and grid-filter power. d) DC-link voltage. e) q-component rotor current. f) q-component grid-filter current.

$3 \cdot 0.25 \cdot 1 \cdot 1 \cdot 1.3 = 0.98$ p.u. Then, according to (7.56), the peak ripple $\tilde{e}_w^{\rm pk}$ in the error signal $e_w = W_{\rm dc}^{\rm ref} - W_{\rm dc}$ will be $\tilde{e}_w^{\rm pk} = 2\tilde{P}_r^{\rm pk}/(C_{\rm dc}\omega_g) = 2 \cdot 0.98/(3.5 \cdot 1) = 0.56$ p.u. The corresponding peak value of the ripple in $v_{\rm dc}$ is $\tilde{v}_{\rm dc}^{\rm pk} = 2.8 - (2.8^2 - 0.56)^{0.5} = 0.1$ p.u. when $v_{\rm dc}^{\rm ref} = 2.8$ p.u. In Fig. 7.8, a corresponding simulation is shown. The simulation verifies the finding that the sum of the rotor and grid-filter powers consists of a corresponding oscillating power at a frequency of ω_g. Moreover, the ripple in the dc-link voltage is 0.1 p.u., which is according to the analytical result. However, as previously discussed, at the time when the voltage returns, the amplitude of the stator-flux oscillations can be close to twice the value at the beginning of the sag. This means, of course, that the amplitude in the dc-link voltage ripple will be increased accordingly. Since there is ripple in the dc-link voltage, this will also be transferred to i_{fq}, since it is used for controlling the dc-link voltage. With the transfer function in (7.39) the static gain of the ripple in i_{fq} can be calculated (note that $-G_{Pi}$ is actually used since here $P_t = -P_r$). This yields

$$|G_{Pi}(j\omega_g)| = \frac{\alpha_w}{3E_{g,\rm nom}}\sqrt{\frac{\alpha_w^2 + 4\omega_g^2}{(\alpha_w^2\xi_p - \omega_g^2)^2 + (2\omega_g\alpha_w\xi_p)^2}} \approx \frac{2\alpha_w}{3\omega_g E_{g,\rm nom}} \tag{7.57}$$

where the approximation holds if $\omega_g \gg \alpha_w$. For the example given above we have, with $\alpha_w = 0.2$, that $\tilde{i}_{fq}^{\rm pk} = 2\alpha_w\tilde{P}_r^{\rm pk}/(3\omega_g E_{g,\rm nom}) = 2 \cdot 0.2 \cdot 0.98/(3 \cdot 1 \cdot 1) = 0.13$ p.u. This value

is also confirmed by the simulation shown in Fig. 7.8. Moreover, the stator-flux oscillations will also cause a ripple in the stator current. The stator current can be found from (4.40) as

$$\mathbf{i}_s = \frac{\Psi_s}{L_M} - \mathbf{i}_R. \tag{7.58}$$

Then if the rotor current is controlled accurately, i.e., $\mathbf{i}_R = \mathbf{i}_R^{\text{ref}}$, the ripple in the stator current will be $\tilde{\imath}_s^{\text{pk}} = \psi_s^{\text{pk}}/L_M$, which, with $L_M = 4.6$ p.u., yields $\tilde{\imath}_s^{\text{pk}} = 0.25/4.6 = 0.05$ p.u.

"Phase-Angle Jumps"

In this section we will study how the DFIG system responds to small "phase-angle jumps." Moreover, in the analysis it will be assumed that the magnitude of the grid voltage remains at its nominal value after the "phase-angle jump." This has been done in order to study the effect of the actual "phase-angle jump" and not the influence of a voltage sag. After a pure "phase-angle jump," i.e, without any voltage sag, the grid voltage vector can be expressed as

$$\mathbf{E}_g = jE_{g,\text{nom}}e^{j\tilde{\theta}(t)} \approx jE_{g,\text{nom}}\left(1 + j\tilde{\theta}(t)\right) \approx jE_{g,\text{nom}}\left(1 + j\tilde{\theta}_0 e^{-\rho t}\right) \tag{7.59}$$

where $\tilde{\theta}(t)$ is the error angle and the approximation holds if $\tilde{\theta}(t)$ is small. In (7.59) the error angle $\tilde{\theta}(t)$ is modeled as in (7.30). Substituting (7.59) in (6.1) and solving the differential equation, the following solution is obtained

$$t < 0: \qquad \Psi_s(t) = \psi_{s0} \approx \frac{E_{g,\text{nom}}}{\omega_g} \tag{7.60}$$

$$t \geq 0: \qquad \Psi_s(t) \approx \frac{E_{g,\text{nom}}}{\omega_g} \frac{\omega_g^2 + \rho^2 + (1+j)\omega_g\rho\tilde{\theta}_0 e^{-\rho t} - \left(\omega_g\rho + j\omega_g^2\right)\tilde{\theta}_0 e^{-(R_s/L_M + j\omega_g)t}}{\omega_g^2 + \rho^2} \tag{7.61}$$

if the stator resistance in the solution is assumed to be zero—except in $e^{-R_s t/L_M}$—and $\psi_{s0} \approx E_{g,\text{nom}}/\omega_g$. If $\omega_g \gg \rho$, it is possible to further approximate the above equation as

$$t < 0: \qquad \Psi_s(t) = \psi_{s0} \approx \frac{E_{g,\text{nom}}}{\omega_g} \tag{7.62}$$

$$t \geq 0: \qquad \Psi_s(t) \approx \frac{E_{g,\text{nom}}}{\omega_g} + j\frac{E_{g,\text{nom}}}{\omega_g}\tilde{\theta}_0\left(e^{-\rho t} - e^{-R_s t/L_M}e^{-j\omega_g t}\right). \tag{7.63}$$

Using (7.46) and (7.47), the rotor and grid filter powers can be determined in a similar way as for the symmetrical voltage sag as

$$\begin{aligned} t \geq 0: \qquad P_r(t) \approx\, & 3E_{g,\text{nom}}\left(1 - \frac{\omega_r}{\omega_g}\right) i_{Rq} \\ & + 3E_{g,\text{nom}}\frac{\omega_r}{\omega_g}\tilde{\theta}_0\left(i_{Rd}e^{-\rho t} - i_R e^{-R_s t/L_M}\cos(\omega_g t + \phi_r)\right) \end{aligned} \tag{7.64}$$

$$t \geq 0: \qquad P_f(t) \approx -3E_{g,\text{nom}}\left(1 - \frac{\omega_r}{\omega_g}\right) i_{Rq}. \tag{7.65}$$

As for the case with symmetrical voltage sags, the dc-link dynamics in (4.48) are governed by the term $-P_r - P_f$. This means that the power drop in the first term of (7.64) is compensated

for by the same drop in P_f; see (7.65). However, the second term in (7.64) will act as a disturbance to the dc link, as

$$\tilde{P}_r = -3E_{g,\text{nom}}\tilde{\theta}_0\frac{\omega_r}{\omega_g}\left(i_{Rd}e^{-\rho t} - i_R e^{-R_s t/L_M}\cos(\omega_g t + \phi_r)\right). \tag{7.66}$$

In (7.66), the disturbance consists of two terms: one that depends on the bandwidth, ρ, of the PLL-type estimator and one that depends on the stator flux dynamics. It is difficult to use the disturbance in (7.66) in order to find the extreme value in the error signal e_w since it consists of two terms of which one is sinusoidal. One way of estimating the "worst case" impact of a specific "phase-angle jump" is to treat the two terms independently and then add them together. Of course, the result should be used with care since adding the results will not, generally, give mathematically correct results. However, the analysis will still give some valuable information of the system. The first term's impact on the dc-link dynamics can be found from the extreme value of

$$\begin{aligned} e_w(t) &= \mathcal{L}^{-1}\left\{G_{Pe}(p)\mathcal{L}\left\{-3E_{g,\text{nom}}\tilde{\theta}_0\frac{\omega_r}{\omega_g}i_{Rd}e^{-\rho t}\right\}\right\} \\ &= 3E_{g,\text{nom}}\tilde{\theta}_0\frac{\omega_r}{\omega_g}i_{Rd}\frac{(\alpha_w t - 2)te^{\alpha_w t}}{C_{\text{dc}}} \end{aligned} \tag{7.67}$$

where $G_{Pe}(p)$ is given by (7.21). The extreme value of (7.67) occurs for $t = (2-\sqrt{2})/\alpha_w$ if $\rho = \alpha_w$. This means that the extreme value of (7.67) becomes

$$e_w^{\max/\min} = 3E_{g,\text{nom}}\tilde{\theta}_0\frac{\omega_r}{\omega_g}i_{Rd}\frac{2(-1+\sqrt{2})e^{-2+\sqrt{2}}}{C_{\text{dc}}\alpha_w} \approx 3E_{g,\text{nom}}\tilde{\theta}_0\frac{\omega_r}{\omega_g}i_{Rd}\frac{0.46}{C_{\text{dc}}\alpha_w} \tag{7.68}$$

if $\rho = \alpha_w$. The second term in (7.66) will cause ripple in the dc-link voltage with the static gain according to (7.56).

The values $\tilde{\theta}_0 = -15^\circ \approx -0.26$ rad, $\alpha_w = \rho = 0.2$ p.u., $C_{\text{dc}} = 3.5$ p.u., $w_r = 1.3$ p.u., $i_R = 1$ p.u., and $i_{Rd} = 0.34$ (corresponding to unity power factor) are used for a numerical example. From (7.68) we have that $e_w^{\max/\min} = 3\cdot(-0.26)\cdot 1.3\cdot 0.34\cdot 0.46/(3.5\cdot 0.2) = -0.23$ p.u., which corresponds to a dc-link voltage of $v_{\text{dc}} = (2.8^2 - (-0.23))^{0.5} = 2.84$ p.u. The amplitude of the second term in (7.66) becomes $-3E_{g,\text{nom}}\tilde{\theta}_0\omega_r/\omega_g i_R = -3\cdot(-0.26)\cdot 1.3\cdot 1 = 1.01$ p.u., giving according to (7.56) a ripple with the amplitude $1.01\cdot 2/3.5 = 0.58$ p.u., which will cause a ripple in the dc-link voltage of $\tilde{v}_{\text{dc}}^{\text{pk}} = 2.8 - (2.8^2 - 0.58)^{0.5} = 0.11$ p.u. This means that the "worst case" dc-link voltage could be $v_{\text{dc}}^{\text{wc}} = 2.84 + 0.11 = 2.95$ p.u. In Fig. 7.9 shows a simulation of the "phase-angle jump" used in the example. It can be seen that the amplitude of the oscillation in the dc-link voltage and the maximum value of the dc-link voltage is close to the predicted values. Eq. (7.57) can be used to determine the amplitude of the oscillation in i_{fq}. Since the amplitude of the oscillation in $\tilde{P}_r$ is 1.01 p.u. the oscillation in i_{fq} becomes $\tilde{i}_{fq}^{\text{pk}} = 2\cdot 0.2\cdot 1.01/(3\cdot 1\cdot 1) = 0.13$ p.u.

For comparison to larger "phase-angle jumps" a corresponding simulation of a -45° "phase-angle jump" can be seen in Fig. 7.10. With the same analysis as above will give a dc-link voltage ripple of 0.33 p.u. and a "worst case" dc-link voltage of $v_{\text{dc}}^{\text{wc}} = 3.25$ p.u.

Unsymmetrical Voltage Sags

Similar analysis, as for symmetrical voltage sags and "phase-angle jumps," for unsymmetrical sags is more difficult to derive, since the system also will be excited with the negative-sequence voltage. Therefore, the analysis here will be limited to simulations. In Fig. 7.11

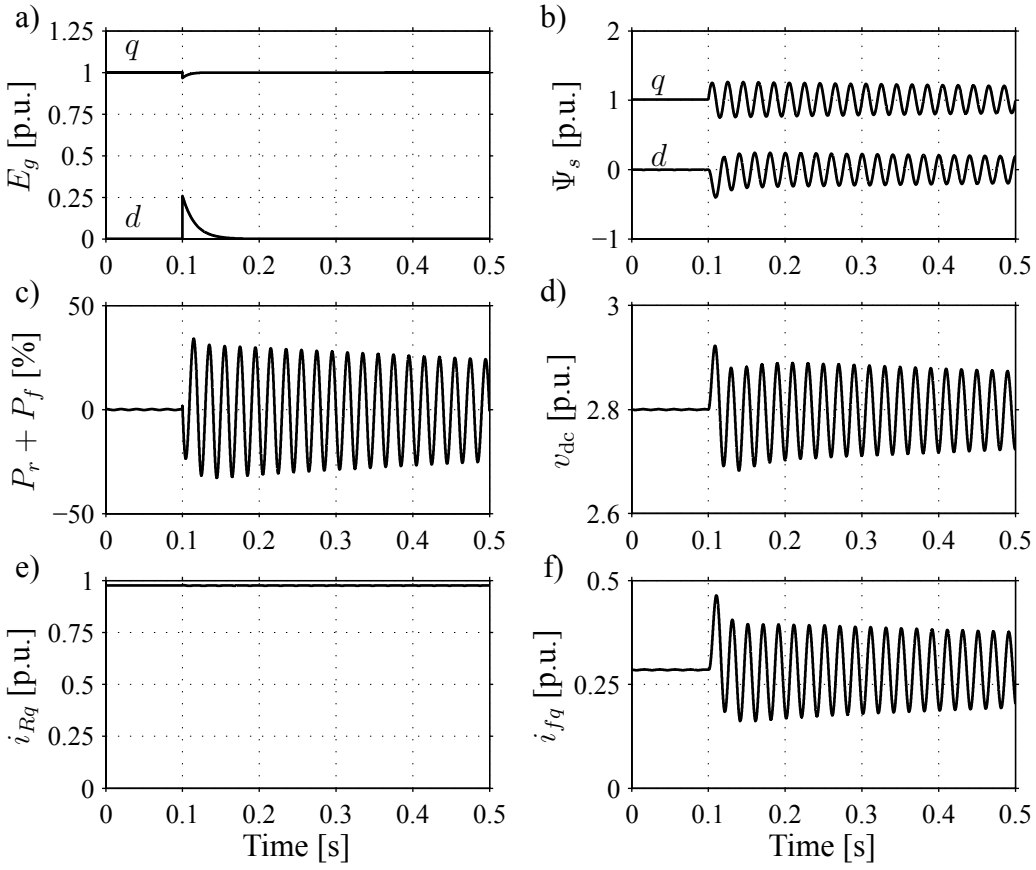

Fig. 7.9. Simulation of the response of the DFIG system to a small "phase-angle jump" of $-15°$. a) Grid voltage. b) Stator flux. c) Sum of rotor and grid-filter powers. d) DC-link voltage. e) q-component rotor current. f) q-component grid-filter current.

the response to an SLGF occurring at $t = 0.1$ ms with $V = 0.75$ p.u. is presented. In the figure it can be seen that in, for instance, the flux, the dc-link voltage, and in the grid-filter current oscillations with both frequencies of ω_g and $2\omega_g$. The oscillation with the frequency ω_g arises from the flux dynamics while the oscillation with the frequency $2\omega_g$ arises from the negative-sequence voltage. However, depending on the phase angle at the time instance of the sag the oscillation at ω_g can in principle be removed for an SLGF. This is indicated in Fig. 7.12 where the sag occurs at $t = 0.105$ ms, all other conditions are as in Fig. 7.11.

Summary

The response of the DFIG system due to different grid disturbances has been investigated. It has been shown that the amplitude of the flux oscillation when the voltage returns after a voltage sag can vary between zero and twice the initial amplitude of the flux oscillations due the sag. Moreover, the DFIG system has been analyzed for symmetrical voltage sags with good agreement. However, the response to "phase-angle jumps" and unsymmetrical voltage sags are analytically harder to derive. Moreover, the DFIG system is roughly as sensitive to "phase-angle jumps" as to symmetrical voltage sags.

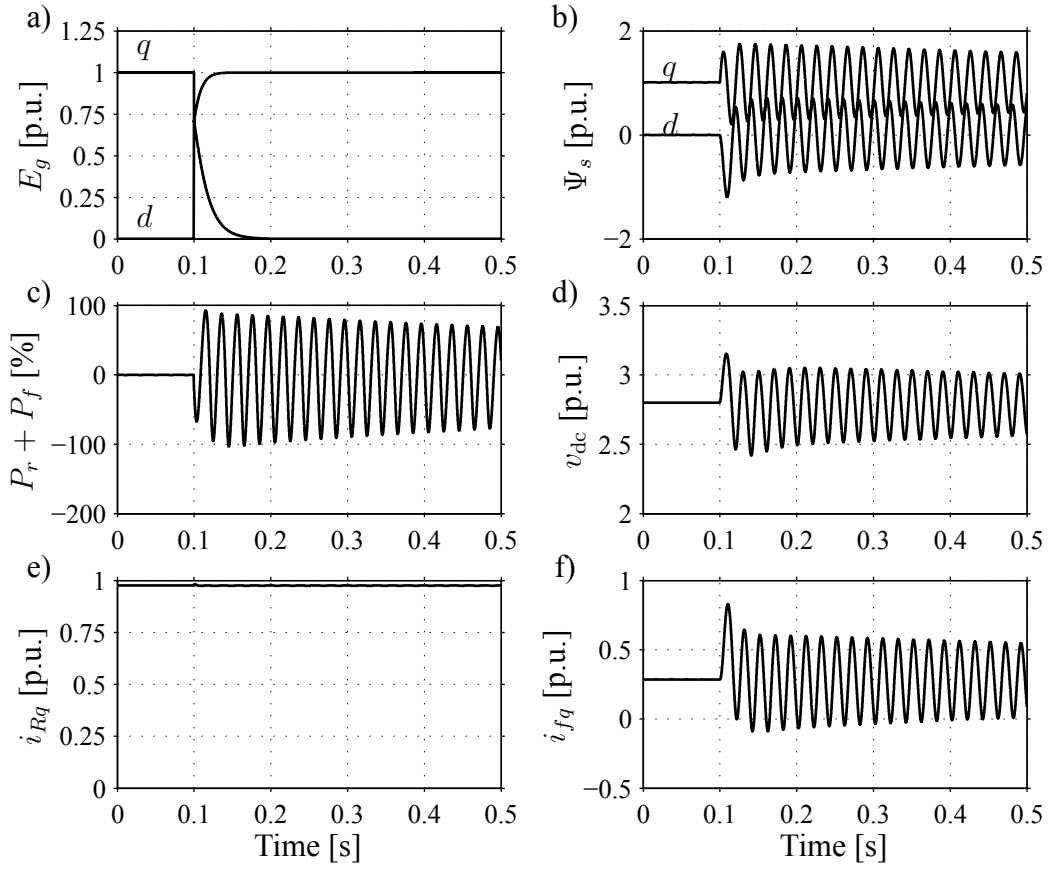

Fig. 7.10. Simulation of the response of the DFIG system to a "phase-angle jump" of $-45°$. a) Grid voltage. b) Stator flux. c) Sum of rotor and grid-filter powers. d) DC-link voltage. e) q-component rotor current. f) q-component grid-filter current.

7.3.2 Response to Large Voltage Sags

In previous section the voltage sags were assumed to be small enough, not causing the rotor converter to fail in controlling the rotor current. However, this cannot be assumed for larger voltage sags. As shown in (5.40), the rotor voltage will change in proportion to the depth of the voltage sag. So, for larger voltage sags, the rotor voltage will hit its maximum value and lose control of the rotor current. In this section, the DFIG system will be analyzed and it is assumed that the converter is large enough to handle excess currents. This has been done in order to study the behavior of the DFIG and not the influence of the converter and the crowbar. Still, the rotor voltage in the simulations is, anyhow, limited to ± 0.4 p.u. (referred to the stator circuit). This limitation of the rotor voltage is a major difference compared to the analysis in the previous section, since the converter will lose control of the rotor current.

In Fig. 7.13 a simulation of a symmetrical voltage sag (at 0.05 s) down to 0.25 p.u. is presented. Before the voltage sag the DFIG is running at rated power and a rotor speed of 1.3 p.u. The duration of the voltage sag in the simulation is 102 ms and 92 ms. In the figure it can be seen that the rotor voltage will hit its maximum value directly after the voltage sag. This means that the converter loses control of the rotor current, leading to an uncontrolled rotor current. As shown in Section 7.3.1 the situation might be even worse when the voltage returns. This is also indicated in Fig. 7.13, i.e., with two identical simulations

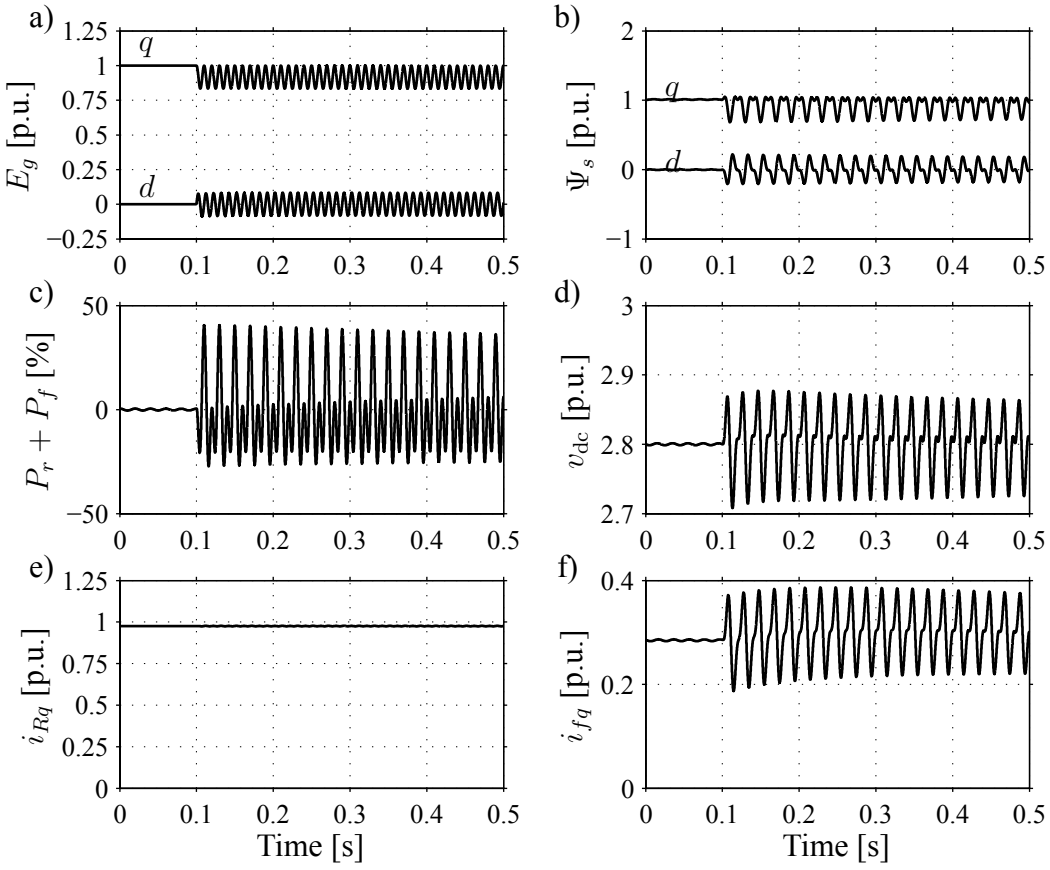

Fig. 7.11. Simulation of the response of the DFIG system to an unsymmetrical (SLGF) voltage sag. a) Grid voltage. b) Stator flux. c) Sum of rotor and grid-filter powers. d) DC-link voltage. e) q-component rotor current. f) q-component grid-filter current.

except the duration of the voltage sag. It can be seen that the maximum rotor current can be much higher when the voltage returns than when the voltage drops at the beginning of the disturbance, if the machine flux is in the wrong "direction." In Fig. 7.14, the maximum rotor current and the maximum rotor power due to a symmetrical voltage sag for three different operating conditions can be seen. In the figure, the effect of returning voltage has not been taken into consideration. From the figure it can be seen that the maximum rotor current due to a voltage sag will increase with the magnitude of the sag. Moreover, the maximum rotor power that is fed into the dc link can be up to almost 250% of nominal power. It should be kept in mind that for the ordinary DFIG system, the converter and dc link are only rated for 30–40% of the nominal power. This means that there is a huge rotor power that needs to be dealt with. Based on these findings a candidate ride-through system will be presented in the next section.

7.3.3 Candidate Ride-Through System

The aim of this section is to present a candidate ride-through DFIG system, based on the result in the previous section. The main idea is to overdimension the valves of the power electronic converter so that they can handle the rotor current occurring at deep voltage sags. However, as indicated in Fig. 7.13, the maximum rotor current actually might be much

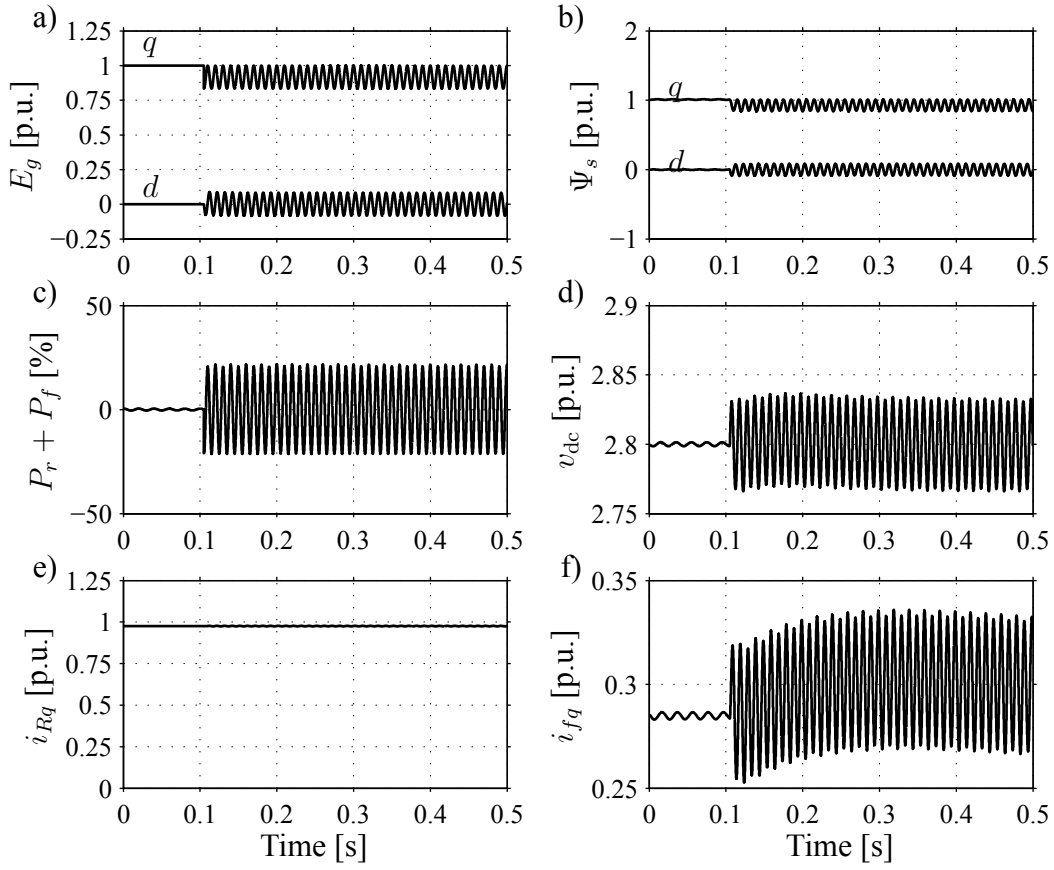

Fig. 7.12. Simulation of the response of the DFIG system to an unsymmetrical (SLGF) voltage sag. a) Grid voltage. b) Stator flux. c) Sum of rotor and grid-filter powers. d) DC-link voltage. e) q-component rotor current. f) q-component grid-filter current.

higher, i.e., up to twice as high, when the voltage returns than at the voltage drop. Of course, this means that the valves have to be even more overdimensioned. In order to avoid these high current when the voltage returns, anti-parallel thyristors can be connected in series with the stator in order to achieve a quick disconnection of the stator circuit [20]. By interrupting the stator circuit, the flux oscillation will also be interrupted. As soon as the flux is interrupted it is possible to remagnetize the DFIG quickly through the rotor converter and connect the stator circuit to the grid again. The converter needs not to be disconnected from the rotor circuit since the valves of the converter are overdimensioned. In order remove the excess power that is fed into the dc link, a "dc-link breaking chopper" is used to dissipate the excess power. Moreover, if required, the grid-side converter may provide the grid with reactive power during the sag. The system with anti-parallel thyristors is illustrated in Fig. 7.15. The anti-parallel thyristor switch can disconnect the stator within a half cycle, i.e., in 10 ms, [9, 20]. The anti-parallel thyristor switch needs to be equipped with a forced commutation unit in case of a dc component in the stator fault current [20]. Another option would be to have gate-turn-off thyristors; then, the disconnection time can be lowered. However, a complex driving circuit is needed, since typically a large negative gate current is required to turn off that device [67]. A third option would be to have anti-parallel IGBTs. Since a normal IGBT, a so-called punch-through IGBT, cannot handle reverse voltages as high as the forward blocking voltages, a diode has to be put in series with the IGBT. Instead of using the

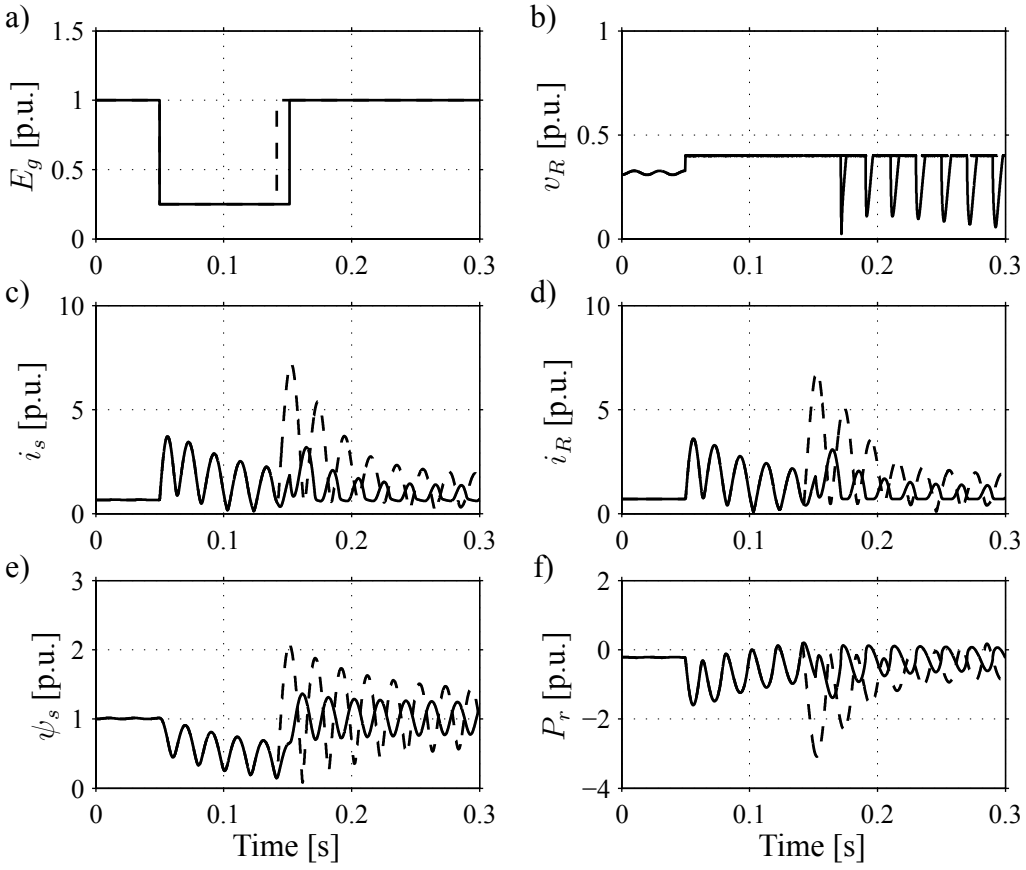

Fig. 7.13. Simulation of the response of a DFIG system to a voltage sag down to 0.25 p.u. Solid line correspond to a voltage sag of 102 ms and dashed line correspond to a voltage sag of 92 ms. a) Stator voltage. b) Rotor voltage magnitude. c) Stator current magnitude. d) Rotor current magnitude. e) Stator flux magnitude. f) Rotor power.

punch-through IGBT, the so-called non-punch through IGBT can be used. The non-punch through IGBT can handle a reverse voltage as high as the forward blocking voltage. However, this device has higher on-state losses [67]. One last option would be to have a contactor as a circuit breaker. However, the disconnection time for the contactor will be longer, while on the other hand, in principle, without losses.

Thus, the IGBT modules of the machine-side converter are designed for a higher current rating, in order to withstand voltage sags. Moreover, in order to avoid the possible higher rotor currents when the voltage returns, the stator circuit is disconnected from the grid. Then, after a disconnection, the rotor current controller re-magnetizes the DFIG, and then the DFIG can be synchronized to the grid as soon as the voltage has returned to an acceptable, predefined, level. For the investigated system, the maximum rotor current and rotor power due to symmetrical voltage sag is shown in Fig. 7.16, if the stator circuit is disconnected within 10 ms.

Of course, for IGBT modules that can handle higher currents temporarily, the stator circuit can be disconnected less often due to voltage sags. Fig. 7.17 shows the maximum rotor current and rotor power when the stator is not disconnected from the grid and the grid voltage returns at the worst instance around 50 ms. This means that the duration of the voltage sag is approximately 50 ms. It can be seen in the figure that for voltage sags down to

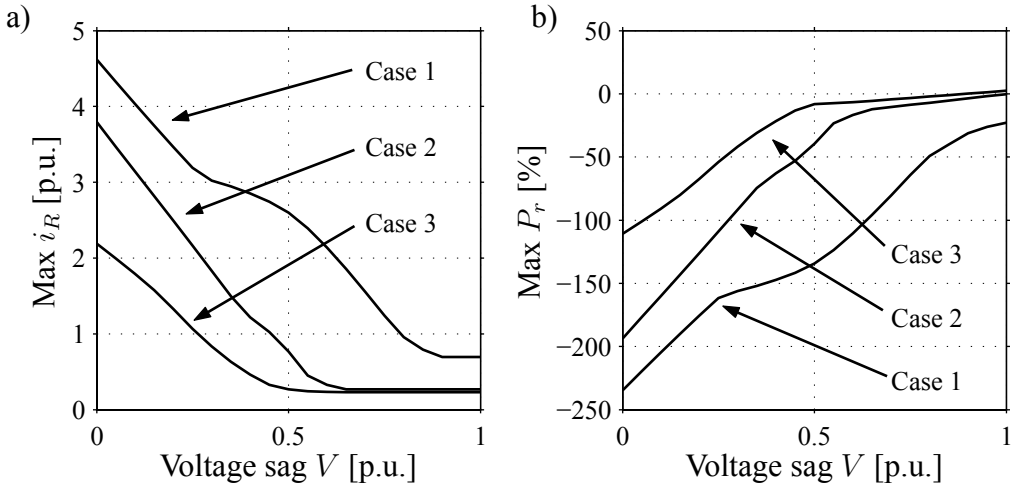

Fig. 7.14. Maximum rotor current and rotor power for three different operating conditions. Case 1 corresponds to rated power and a rotor speed of 1.3 p.u. Case 2 corresponds to 23% of rated power and a rotor speed of 1.0 p.u. Case 3 corresponds to 11% of rated power and a rotor speed of 0.7 p.u. a) Maximum rotor current. b) Maximum rotor power (Note that negative rotor power means that the power is fed into the dc link).

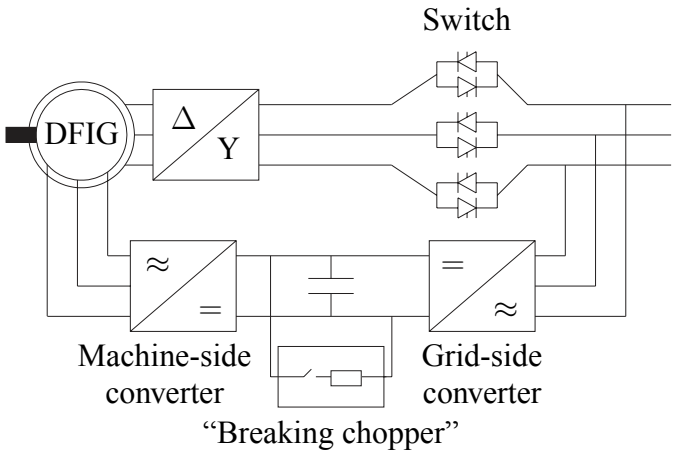

Fig. 7.15. DFIG with anti-parallel thyristors in the stator circuit.

0.5 p.u. the maximum rotor current is approximately as large as the maximum rotor current when the stator is disconnected. However, the maximum rotor power fed to the dc link becomes higher compared to when the stator circuit is disconnected.

7.3.4 Evaluation of the Ride-Through System

The aim of this section is to make a theoretical case study on the candidate voltage sag ride-through system presented in the previous section. This study will focus on the energy production and energy production cost of such a system for a 2-MW DFIG WT.

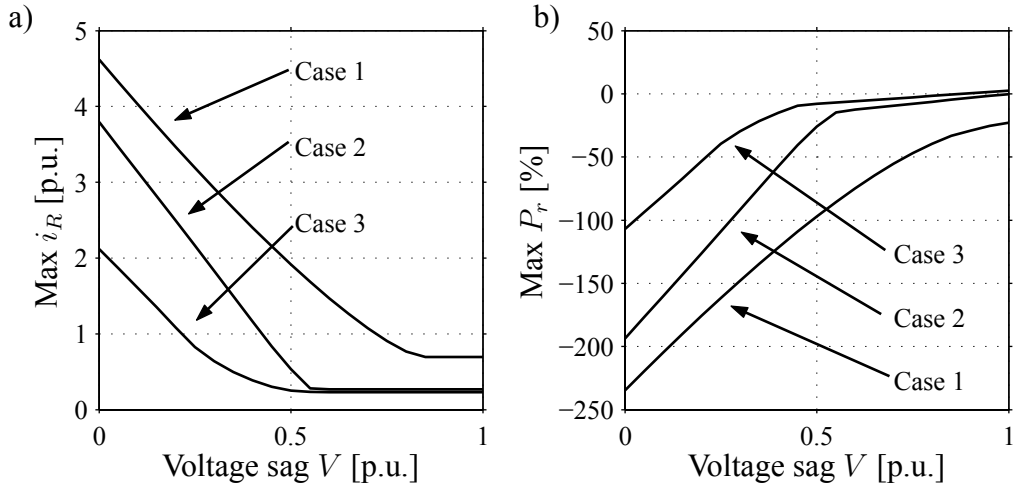

Fig. 7.16. Maximum rotor current and rotor power for three different operating conditions if the stator circuit is disconnected within 10 ms. Case 1 corresponds to rated power and a rotor speed of 1.3 p.u. Case 2 corresponds to 23% of rated power and a rotor speed of 1.0 p.u. Case 3 corresponds to 11% of rated power and a rotor speed of 0.7 p.u. a) Maximum rotor current. b) Maximum rotor power (note that negative rotor power means that the power is fed into the dc link).

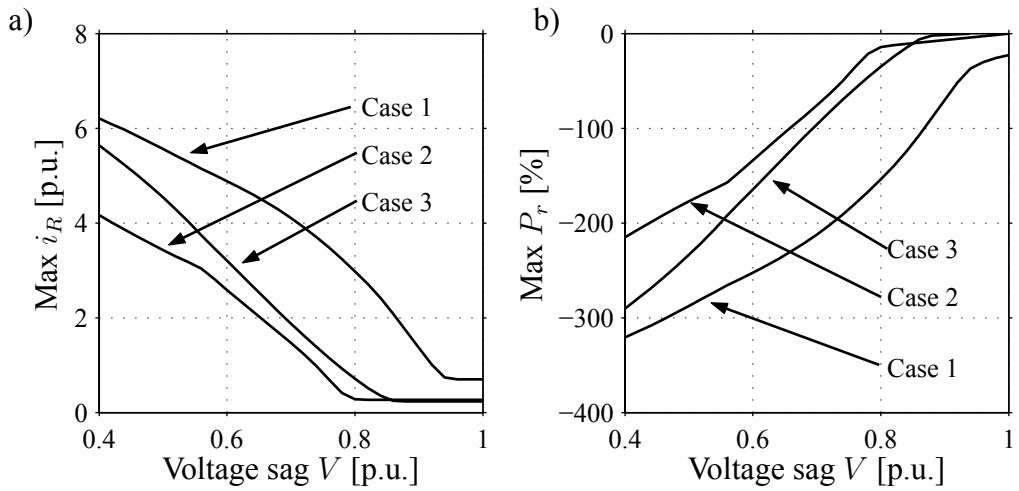

Fig. 7.17. Maximum rotor current and rotor power fed to the dc link for three different operating conditions with returning voltage at the worst instance around 50 ms. Case 1 corresponds to rated power and a rotor speed of 1.3 p.u. Case 2 corresponds to 23% of rated power and a rotor speed of 1.0 p.u. Case 3 corresponds to 11% of rated power and a rotor speed of 0.7 p.u. a) Maximum rotor current. b) Maximum rotor power (note that negative rotor power means that the power is fed into the dc link).

Calculation of Power Losses

The losses taken into consideration are the losses in the aerodynamic conversion, gearbox, generator and in the semiconductor devices, i.e., the same losses as in Chapter 3. The calculation of the will also follow the loss models used in Chapter 3.

The losses in the anti-parallel thyristor switch used in the stator circuit, see Fig. 7.15, can

be described by (3.4). Since the switching occurs at zero current and at low frequency (the grid frequency), the switching losses in the switch will be neglected. The parameters for the thyristors used here are $r_{\mathrm{Thy}} = 0.164$ mΩ and $V_{\mathrm{Thy}} = 0.88$ V [93]. The dc-link "chopper" is not used during normal operation; hence, it will not influence the energy production.

In Fig. 7.18 the losses in the semiconductor devices are shown. It can be noticed in Fig.

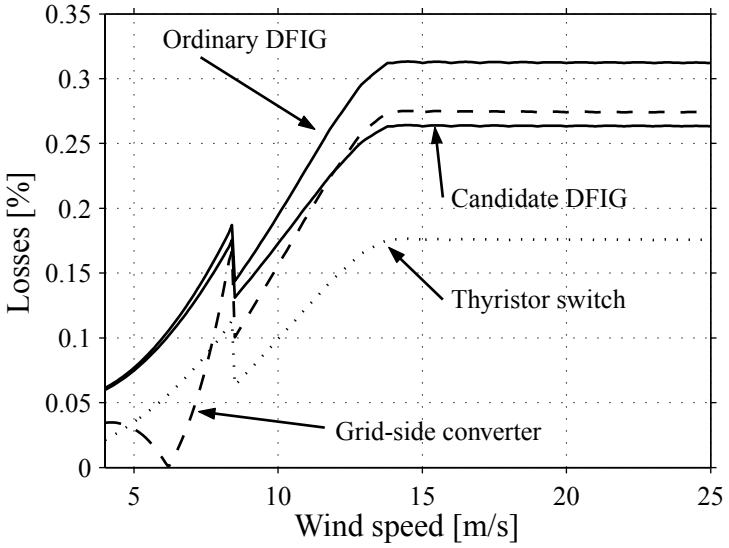

Fig. 7.18. The losses in the semiconductor devices used in this work. The solid lines show the losses in the MSC for ordinary and the candidate DFIG system. The dashed line shows the losses for the GSC and the dotted line shows the losses in the anti-parallel thyristor switch.

7.18, that the losses of the MSC can be reduced by approximately 0.05 percentage units at rated operation by increasing the current rating of the valves. This reduction is only due to that the resistance in the valves decreases with an increasing current rating. However, the losses of the thyristor switch are much larger than the reduction of losses due to the increased current rating of the valves. The steps in the curves at 7.8 m/s are due to that the stator of the generator is switch from a Y connection to a Δ connection, as discussed in Section 2.3.4.

In Fig. 7.19 the expected efficiency of the candidate DFIG system as a function of the average wind speed is presented. In the figure expected efficiencies of the ordinary DFIG system as well as a system that utilizes a full power electronic converter can also be seen. In the figure it can be seen that the ordinary DFIG system has the highest efficiency, even though the difference towards the candidate DFIG system is relatively small. See Section 2.1.1 for details of calculation of the expected efficiency.

Energy Cost

For the calculation of the energy production cost, it has been assumed that the standard 2-MW DFIG WT costs €1600000 [65] and that one IGBT converter and the anti-parallel thyristor switch costs €6000/p.u. current. The cost of the IGBTs is an estimate based on cost information obtain from some IGBT manufactures. In Fig. 7.20, the relative energy production cost of the candidate system normalized with the energy production cost of the ordinary DFIG system can be seen. As could be expected, the energy production cost of the candidate system is higher than for the ordinary DFIG system. The energy production cost

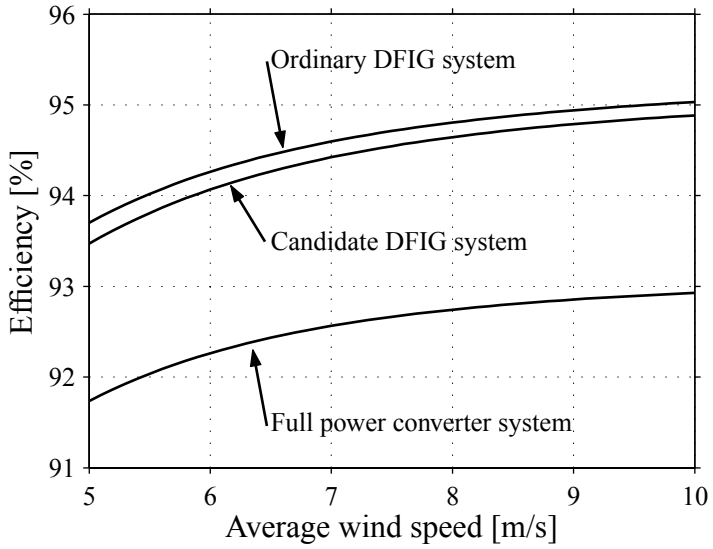

Fig. 7.19. Expected efficiency as a function of the average wind speed for the candidate DFIG system, the ordinary DFIG system, and a system with a full-power converter.

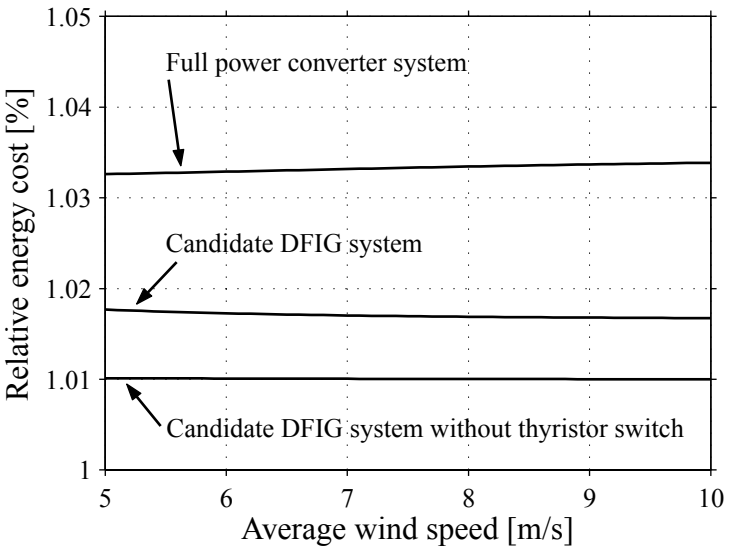

Fig. 7.20. Energy cost of the candidate DFIG, candidate DFIG without thyristor switch, and the system that utilizes a full-power converter. The energy cost is related to the ordinary DFIG system.

of the candidate system is approximately two percentage units higher then for the ordinary DFIG system. A full power electronic conversion, which handles the total power, has approximately three percentage units higher energy cost than the ordinary DFIG system. The increase in energy production cost is due to the lower energy production of the candidate system, but it is mainly due to the increased cost of the valves. In Fig. 7.20 the normalized energy production cost of a modified candidate system, i.e., without anti-parallel thyristor switch in the stator circuit, is also shown.

Conclusion

The influence on the energy production of a DFIG ride-through system has been investigated. This system is based on increased current rating of the converter and anti-parallel thyristors in the stator circuit. It has been found that the increased cost for a ride-through system for a DFIG turbine might be reasonable, in comparison to the cost of full-power converter system connected to a cage-bar induction generator.

7.4 Doubly-Fed Induction Generator with Series Converter

After a voltage sag, the stator flux of the DFIG will start to oscillate. This oscillation often causes very high rotor currents, which necessitates a disconnection of the WT. Today, the grid-side converter is connected to the grid in a shunt configuration, see Fig. 7.21. This means that the converter injects a current into the grid. However, if the converter is instead connected in series with the grid, a voltage is introduced in series with the stator voltage, i.e., the stator voltage of the DFIG is the sum of the grid and converter voltages. Then, the series voltage can be used in order to control the stator flux of the machine and prevent, for instance, high rotor current with resulting disconnection of the turbine. Kelber has shown that such a system can effectively damp the flux oscillations caused by voltage sags [55].

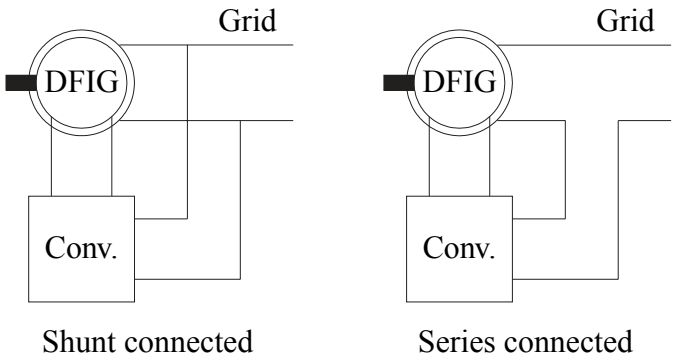

Fig. 7.21. Schematic figure showing shunt- and series-connected converters for doubly-fed induction generator systems.

The contribution and purpose of this section is to analyze and present the advantages and drawbacks of a DFIG system for a wind-turbine application with a series converter with the focus on handling voltage sags. In addition, a goal is also to study the energy efficiency, and, in particular, compare it to a system that utilizes a full-power converter. The reason for comparing these two systems is that they are both capable of voltage sag ride-through.

7.4.1 Possible System Configurations

As mentioned in the Introduction, the idea is to have a converter connected in series with the stator circuit and the grid. Fig. 7.21 shows both the ordinary DFIG system where the converter is connected in shunt to the grid, and the system where it is connected in series. The purpose of the series-connected converter is to control the stator flux of the DFIG, and in this way be able to control the DFIG during voltage sags. By having the converter connected

in series, the stator voltage $\mathbf{v}_s$ of the DFIG is, ideally, the sum of grid voltage $\mathbf{E}_g$ and the voltage $\mathbf{v}_c$ from the series converter:

$$\mathbf{v}_s = \mathbf{E}_g + \mathbf{v}_c. \tag{7.69}$$

Some of the demands on the series converter for a DFIG system may be:

- A sufficiently fast stator-flux control in order to damp the oscillations and control the stator flux.
- Accurate control of the dc-link voltage.

There are at least two methods of accomplishing this series voltage, which are presented below.

Series-Injection Transformer

In this configuration, the voltage source converter is connected to the grid via a series-injection transformer, as depicted in Fig. 7.22. This configuration of a series-injection transformer and a voltage source converter is also used in dynamic voltage restorers (DVRs) [27, 49]. The protection system of such a system is complicated since a simple disconnection does not work [70]. Normally the system is equipped with an LC filter with the objective of reducing voltage and current harmonics generated from the voltage source converter. Note that the LC filter can be placed on either side of the transformer [49]. The series-injection transformer is necessary for galvanic insulation. Moreover, in order to avoid magnetic saturation, the series-injection transformer must be rated to handle twice the nominal flux [27]. Another option, in order to avoid the series-injection transformer, is to have a converter for each phase with separate dc links [63]. For DVRs, there are, at least, three

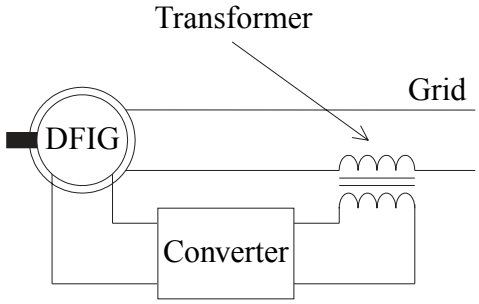

Fig. 7.22. Doubly-fed induction generator (DFIG) with the grid-side converter connected in series via a series-injection transformer.

methods of controlling the series voltage: 1) in an open-loop manner [45], 2) directly control the series voltage [71], and 3) by two control loops, i.e., an inner fast current control loop that controls the current through the inductance and an outer cascade loop controlling the capacitor (series) voltage [10]. One advantage of controlling both the inductor current and capacitor voltage is that it is easy to avoid the resonant frequency of the LC filter. However, a drawback for the DFIG is that bandwidth is lost for the stator-flux controller, since the stator flux is then controlled in cascade with both the capacitor (series) voltage and the inductor current. For example, if it is desired to separate the control loops by one decade,

the bandwidth of the flux control loop is a factor of hundred lower than the current control loop. This means that a very high bandwidth of the current control loop is necessary and, accordingly, a very high switching frequency is needed.

Converter in the Y Point of the DFIG

The second method of accomplishing a series voltage for the DFIG is to connect a voltage source converter where the Y point of the stator circuit usually is [54, 55]. Hereafter, this will be referred to as the Y point. In [54, 55], this is accomplished using an additional (third) converter, which is only used to damp the occurring stator flux oscillations. During normal operation, the extra converter voltage is zero. In [54, 55], the converter in the Y point of the DFIG system is only used to damp disturbances, while here it can also be used to control the magnitude of the stator flux and the dc-link voltage.

Fig. 7.23 shows a principle sketch of the system when a voltage source converter is connected to the Y point of the stator circuit of the DFIG. For this system, the converter

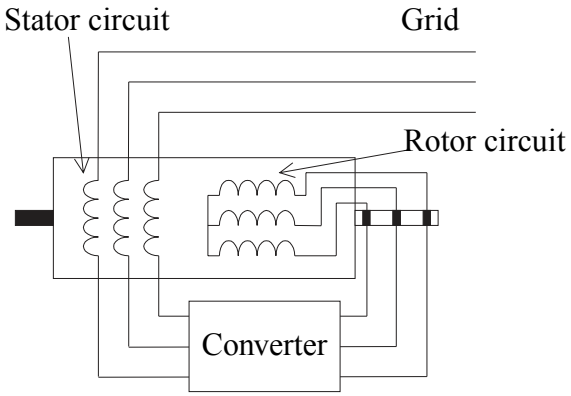

Fig. 7.23. Doubly-fed induction generator (DFIG) with the grid-side converter connected to the Y point of the stator circuit.

voltage is directly used to control the stator flux in the machine, while the rotor current is controlled by the machine-side converter. One disadvantage of this method is that all of the stator current is passed through the Y-point converter, which may cause additional high losses in the power electronic equipment.

7.4.2 System Modeling

As mentioned earlier the stator voltage is ideally the sum of the grid and series voltage. This means that (4.38) and (4.39) become

$$\mathbf{v}_s = \mathbf{E}_g + \mathbf{v}_c = R_s \mathbf{i}_s + \frac{d\Psi_s}{dt} + j\omega_1 \Psi_s \tag{7.70}$$

$$\mathbf{v}_R = R_R \mathbf{i}_R + \frac{d\Psi_R}{dt} + j\omega_2 \Psi_R \tag{7.71}$$

where $\mathbf{v}_c$ is the series voltage. The dc-link dynamics are described by

$$\frac{C_{\mathrm{dc}}}{2}\frac{dv_{\mathrm{dc}}^2}{dt} = v_{\mathrm{dc}} C_{\mathrm{dc}} \frac{dv_{\mathrm{dc}}}{dt} = -P_r - P_c \tag{7.72}$$

where P_r is the rotor power and P_c is the power from the grid-side converter, which are given by

$$P_r = 3\mathrm{Re}\left[\mathbf{v}_R \mathbf{i}_R^*\right] \tag{7.73}$$
$$P_c = 3\mathrm{Re}\left[\mathbf{v}_c \mathbf{i}_s^*\right] \tag{7.74}$$

or as

$$P_r = 3\left(R_R i_{Rq}^2 + R_R \frac{\psi_{sd}^2}{L_M^2} + \psi_{sd} i_{Rq} \omega_2\right) \tag{7.75}$$
$$P_c = 3\left(R_s i_{Rq}^2 + E_g i_{Rq} - \psi_{sd} i_{Rq} \omega_1\right) \tag{7.76}$$

in the steady state if $\psi_{sq} = 0$, i.e., controlled to be zero. Moreover, in the above equations the d component of the rotor current is controlled so that the system operates at unity power factor, i.e., $i_{Rd} = \psi_{sd}/L_M$.

Steady-State Operation

For a constant dc-link voltage it is required that $P_r = -P_c$. This means that ψ_{sd} must be used to control the dc-link voltage, and in the steady state ψ_{sd} approximately becomes

$$\psi_{sd} \approx \frac{E_g}{\omega_r} \tag{7.77}$$

where the approximation is that the stator resistance has been neglected. Since the magnetizing losses depend on the flux in the machine, (7.77) indicates that the system will have an undesirable feature. At low wind speeds (low power), the rotor speed is also low, causing the flux to be high and thereby also the magnetizing losses to increase. At high wind speeds (high power), the rotor speed is low, which means that the stator flux is low. Since the stator flux is low, a higher torque-producing current is needed.

In the steady state, the rotor voltage can be expressed as

$$\mathbf{v}_R = \left(R_R + j\omega_2 L_\sigma\right) \mathbf{i}_R^{\mathrm{ref}} + j\omega_2 \Psi_s = \left(R_R + j\omega_2 L_\sigma\right) \mathbf{i}_R^{\mathrm{ref}} + j\omega_2 \psi_{sd}. \tag{7.78}$$

If $\psi_{sd} = E_g/\omega_r$, (7.78) becomes

$$\mathbf{v}_R = \left(R_R + j\omega_2 L_\sigma\right) \mathbf{i}_R^{\mathrm{ref}} + j\omega_2 \frac{E_g}{\omega_r} \tag{7.79}$$
$$= \left(R_R + j\omega_2 L_\sigma\right) \mathbf{i}_R^{\mathrm{ref}} + j\left(\frac{\omega_1}{\omega_r} - 1\right) E_g \tag{7.80}$$
$$\approx j\left(\frac{\omega_1}{\omega_r} - 1\right) E_g. \tag{7.81}$$

For example, we have, with $\omega_1 = E_g = 1$ p.u.

$$\mathbf{v}_R \approx \begin{cases} 0.43 \text{ p.u.} & \text{for } \omega_r = 0.7 \text{ p.u.} \\ -0.23 \text{ p.u.} & \text{for } \omega_r = 1.3 \text{ p.u.} \end{cases} \tag{7.82}$$

showing that the rotor voltage is not symmetrically distributed around the synchronous speed, as for the case with constant stator flux.

The series voltage $\mathbf{v}_c$ of the grid-side converter is given by

$$\mathbf{v}_c = R_s \mathbf{i}_s + j\omega_1 \Psi_s - \mathbf{E}_g \approx j\omega_1 \Psi_s - \mathbf{E}_g \tag{7.83}$$

in steady state. Then, as $\psi_{sq} = 0$ and $\mathbf{E}_g = jE_g$, we have

$$\mathbf{v}_c \approx j\omega_1 \psi_{sd} - jE_g = j\omega_1 \frac{E_g}{\omega_r} - jE_g = j\left(\frac{\omega_1}{\omega_r} - 1\right) E_g. \tag{7.84}$$

As seen in (7.81) and (7.84), the rotor voltage will approximately equal the converter voltage, i.e., $\mathbf{v}_R \approx \mathbf{v}_c$.

Close to No-Load Operation

It is required that (7.72) equals zero at steady-state operation in order to have a constant dc-link voltage. If the rotor current and stator flux are controlled with high-gain feedback, we have that

$$R_R i_{Rq}^2 + R_R \frac{\psi_{sd}^2}{L_M^2} + \psi_{sd} i_{Rq} \omega_2 + R_s i_{Rq}^2 + E_g i_{Rq} - \psi_{sd} i_{Rq} \omega_1 = 0 \tag{7.85}$$

in order to have a constant dc-link voltage. Note that in (7.85), $\psi_{sq} = 0$. Eq. (7.85) can be rewritten as

$$\psi_{sd}^2 - \omega_r i_{Rq} \frac{L_M^2}{R_R} \psi_{sd} + \frac{L_M^2}{R_R} \left[(R_s + R_R) i_{Rq}^2 + E_g i_{Rq}\right] = 0 \tag{7.86}$$

which has the following solution:

$$\psi_{sd} = \omega_r i_{Rq} \frac{L_M^2}{2R_R} \pm \sqrt{\omega_r^2 i_{Rq}^2 \frac{L_M^4}{4R_R^2} - \frac{L_M^2}{R_R}\left[(R_s + R_R) i_{Rq}^2 + E_g i_{Rq}\right]}. \tag{7.87}$$

The expression under the square root cannot be negative, implying that

$$\frac{L_M^2}{R_R} i_{Rq} \left[\left(\omega_r^2 \frac{L_M^2}{4R_R} - (R_s + R_R)\right) i_{Rq} - E_g\right] \geq 0 \tag{7.88}$$

or

$$|i_{Rq}| \geq \frac{E_g}{\dfrac{\omega_r^2 L_M^2}{4R_R} - (R_s + R_R)} \approx \frac{4E_g R_R}{\omega_r^2 L_M^2}. \tag{7.89}$$

If $|i_{Rq}| < 4E_g R_R/(\omega_r^2 L_M^2)$, ψ_{sd} cannot keep the dc-link voltage constant. For the values given in the Appendix, the constraint becomes $|i_{Rq}| < 4 \cdot 1 \cdot 0.009/(1^2 \cdot 4.6^2) = 0.0017$ p.u., which is a small value. In order to handle this problem an extra converter that controls the dc-link voltage is added. It might be possible to use either a diode rectifier (depending on the power flow) or an IGBT converter as the extra converter. However, later on when the losses

and efficiency are calculated, an IGBT converter has been used. Here two different sizes of this extra converter will be investigated:

Option 1. In this case, the extra converter is designed to be as small as possible. However, since this converter would be small and only used at very low powers another way could be to increase energy storage on the dc-link, and thereby make the third converter unnecessary.

Option 2. For this option the extra converter is designed so that it is used in the whole operating region. This means that for this option the stator flux is not used for controlling the dc-link voltage. Kelber *et al.* used this option [54, 55]. However, in contrast to [54, 55], the stator flux is here controlled to reduce the magnetizing losses. This means as the extra converter controls the dc-link voltage, the stator-flux reference value is set to minimize the losses of the generator. Note, that for this option the flux does not follow (7.77).

7.4.3 Control

The basic idea of the control system is to have an inner fast rotor current controller. The rotor current is controlled with the machine-side converter. With the rotor current it is possible to control the active and reactive powers. Then, the stator flux is controlled using the grid-side converter. The stator-flux control loop is about a decade slower than the current control loop. Then, finally, the dc-link voltage is controlled in cascade with the stator flux in order to keep the dc-link voltage constant.

As mentioned in the previous section, to be able to control the dc-link voltage with the stator flux there is a minimum rotor current. Therefore, when designing the control laws it will be assumed that an additional power electronic device keeps the dc-link voltage constant when i_{Rq} is small. This means that when i_{Rq} is below a certain value, ψ_{sd} is not used to control the dc-link voltage anymore. For this case, the stator flux can be controlled "arbitrarily," meaning that the stator flux can be controlled so that the losses are reduced.

Rotor Current Control

The d component of the rotor current, i_{Rd}, is used to control the reactive power while the q component of the rotor current, i_{Rq}, controls the active power or the torque, for details see Chapter 4.

Stator-Flux Control

The stator voltage equation (7.70) can be rewritten as

$$\mathbf{E}_g + \mathbf{v}_c = -R_s \mathbf{i}_R^{\text{ref}} + \frac{d\Psi_s}{dt} + \left(\frac{R_s}{L_M} + j\omega_1 \right) \Psi_s \tag{7.90}$$

where the rotor current has been put to its reference value. Then, $\mathbf{v}_c = \mathbf{v}_c' - \mathbf{E}_g + (j\omega_1 - \Omega_a)\Psi_s$ is chosen where Ω_a is the "active damping." The above equation then reduces to

$$\mathbf{v}_c' = -R_s \mathbf{i}_R^{\text{ref}} + \frac{d\Psi_s}{dt} + \left(\frac{R_s}{L_M} + \Omega_a \right) \Psi_s. \tag{7.91}$$

The term $R_s\mathbf{i}_R^{\text{ref}}$ is treated as a disturbance and the transfer function from $\mathbf{v}_c'$ to Ψ_s is found as

$$G(p) = \frac{\Psi_s(p)}{\mathbf{v}_c'(p)} = \frac{1}{p + R_s/L_M + \Omega_a}. \tag{7.92}$$

IMC yields the following PI controller tuned for a closed-loop bandwidth α_f

$$F(p) = \frac{\alpha_f}{p} G^{-1}(p) = \alpha_f + \alpha_f \frac{R_s/L_M + \Omega_a}{p}. \tag{7.93}$$

If the "active damping" is set to $\Omega_a = \alpha_f - R_s/L_M$ a disturbance is damped with the same bandwidth as the closed-loop stator-flux control loop, i.e., the transfer function from a disturbance, $D(p)$, to Ψ_s is

$$G_{D\Psi_s}(p) = \frac{\Psi_s(p)}{D(p)} = \frac{p}{(p + \alpha_f)^2}. \tag{7.94}$$

DC-Link Voltage Control

For a dc-link voltage controller with a shunt converter, see Section 4.5.2. If the resistive losses are treated as a disturbance, the dc-link dynamics in (7.72) can be written as

$$\frac{C_{\text{dc}}}{2}\frac{dv_{\text{dc}}^2}{dt} = 3i_{Rq}\left(\psi_{sd}\omega_r - E_g\right) + D \tag{7.95}$$

where D is the disturbance. Moreover, if the variable substitution $W = v_{\text{dc}}^2$ is made, the following system is obtained

$$\frac{C_{\text{dc}}}{2}\frac{dW}{dt} = 3i_{Rq}^{\text{ref}}\left(\psi_{sd}^{\text{ref}}\omega_r - E_g\right) + D. \tag{7.96}$$

where i_{Rq} and ψ_{sd} are put to their reference values. By choosing the reference value of the flux as

$$\psi_{sd}^{\text{ref}} = \frac{\psi_{sd}^{\prime\text{ref}} - G_a W}{i_{Rq}^{\text{ref}}\omega_r} + \frac{E_g}{\omega_r} \tag{7.97}$$

the dc-link dynamics are reduced to

$$\frac{C_{\text{dc}}}{2}\frac{dW}{dt} = 3\psi_{sd}^{\prime\text{ref}} - 3G_a W + D. \tag{7.98}$$

In (7.97), G_a is the "active damping." Then, the transfer function, treating D as a disturbance, becomes

$$G(p) = \frac{W(p)}{\psi_{sd}^{\prime\text{ref}}} = \frac{3}{C_{\text{dc}}/2p + 3G_a}. \tag{7.99}$$

By using IMC, we obtain the following PI controller

$$F(p) = \frac{\alpha_{\text{dc}}}{p} G^{-1}(p) = \frac{C_{\text{dc}}\alpha_{\text{dc}}}{6} + \frac{G_a\alpha_{\text{dc}}}{p}. \tag{7.100}$$

Then, if $G_a = C_{\text{dc}}\alpha_{\text{dc}}/6$, the transfer function from D to W becomes

$$\frac{W(p)}{D(p)} = \frac{G}{1 + FG} = \frac{p}{\frac{C_{\text{dc}}}{2}(p + \alpha_{\text{dc}})^2}. \tag{7.101}$$

This means that a disturbance is damped with the same bandwidth as the dc-link voltage control loop.

Simulation of Electromechanical Torque Steps

In the simulation shown here, it is assumed that the rotor speed can by the pitch mechanism of the wind turbine, if desired, be controlled with a bandwidth of α_s.

Fig. 7.24 shows a simulation of the investigated system during current (or torque) control mode. After 50 ms, i_{Rq} is stepped from -0.9 p.u. to -0.1 p.u., and between 0.5 s and 1.0 s the rotor speed is ramped from 1.2 p.u. down to 0.8 p.u. using pitch control. Finally, at 1.25 s, i_{Rq} is stepped back to -0.9 p.u. It can be seen in the figure that the control system manages

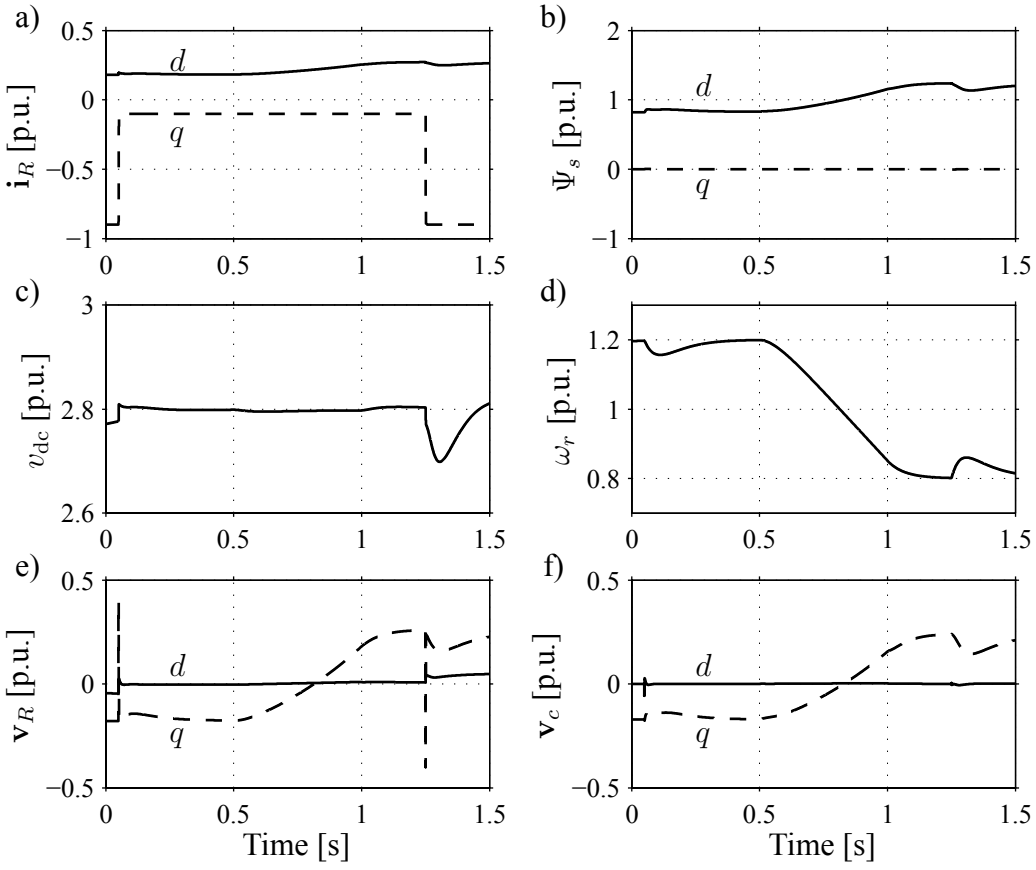

Fig. 7.24. Simulation of the system when the DFIG is in current control (or torque) mode. a) Rotor current. b) Stator flux. c) DC-link voltage. d) Rotor speed. e) Rotor voltage. f) Series voltage.

to control i_{Rd}, i_{Rq}, and v_{dc} well. Moreover, the simulation verifies the result previously presented in Section 7.4.2, which indicated that the q component of the rotor voltage and converter voltage are close to identical. There is a small difference in the d component due to the fact that the rotor converter also supplies the magnetizing current.

7.4.4 Speed Control Operation

At low wind speeds, the pitch angle of the turbine is fixed and the DFIG is operated in speed control operation. In this section, a rotor speed control law will be derived using IMC. The

mechanical dynamics are given by

$$\frac{J}{n_p}\frac{d\omega_r}{dt} = T_e - T_s \tag{7.102}$$

where T_e is the electromechanical torque, T_s is the shaft torque, J is the inertia and, n_p is the number of pole pairs. Assuming $\psi_{sq} = 0$, the electromechanical torque can be expressed as $T_e = -3n_p\psi_{sd}i_{Rq}$. Then, since $\psi_{sd} \approx E_g/\omega_r$, (7.102) can be expressed as

$$\frac{J}{n_p}\frac{d\omega_r}{dt} = -3n_p\frac{E_g}{\omega_r}i_{Rq}^{\text{ref}} - T_s \tag{7.103}$$

where i_{Rq} has been changed to its reference value. Now, we choose

$$i_{Rq}^{\text{ref}} = \frac{\omega_r}{3n_pE_g}\left(i_{Rq}'^{\text{ref}} + B_a\omega_r\right) \tag{7.104}$$

where B_a is the "active damping." This means that the mechanical dynamics can be rewritten as

$$\frac{J}{n_p}\frac{d\omega_r}{dt} = -i_{Rq}'^{\text{ref}} - B_a\omega_r - T_s. \tag{7.105}$$

Then, with IMC, the following controller is obtained

$$F(p) = k_p + \frac{k_i}{p} = -\alpha_s\frac{J}{n_p} - \alpha_s\frac{B_a}{p} \tag{7.106}$$

and if $B_a = \alpha_s J/n_p$, a change in T_s is damped with the same bandwidth, α_s, as the speed control loop:

$$G_{T\omega}(p) = \frac{P}{\frac{J}{n_p}(p+\alpha_s)^2} \tag{7.107}$$

Fig. 7.25 shows an example of the proposed DFIG series system with the DFIG operated in speed-control mode. In order to validate the performance, the machine is exposed to shaft torque steps of 30% to 100% of rated torque. These torque steps are much faster than what would be the case in reality and they are performed for verification purposes only. The rotor speed is controlled by the DFIG to be 0.8 p.u. during the whole simulation. It can be seen in the figure that the control system manages to control i_{Rd}, ω_r, and v_{dc} well.

7.4.5 Response to Voltage Sags

Fig. 7.26 shows the response to a 0% voltage sag, i.e., the remaining voltage is 0 p.u. The voltage drops after 0.1 s and the sag has a duration of 250 ms. This is an extreme voltage sag and if the system manages this sag, it manages the Swedish transmission system operator's demands for large production facilities [96]. During the simulation, the DFIG is operated at $i_{Rq} = -1$ p.u. which corresponds to generator operation at rated current (full power). In this case, the rotor speed is controlled by the pitch mechanism to 1.2 p.u. During the sag, the stator flux is controlled by the series-connected converter to be close to zero. The rotor

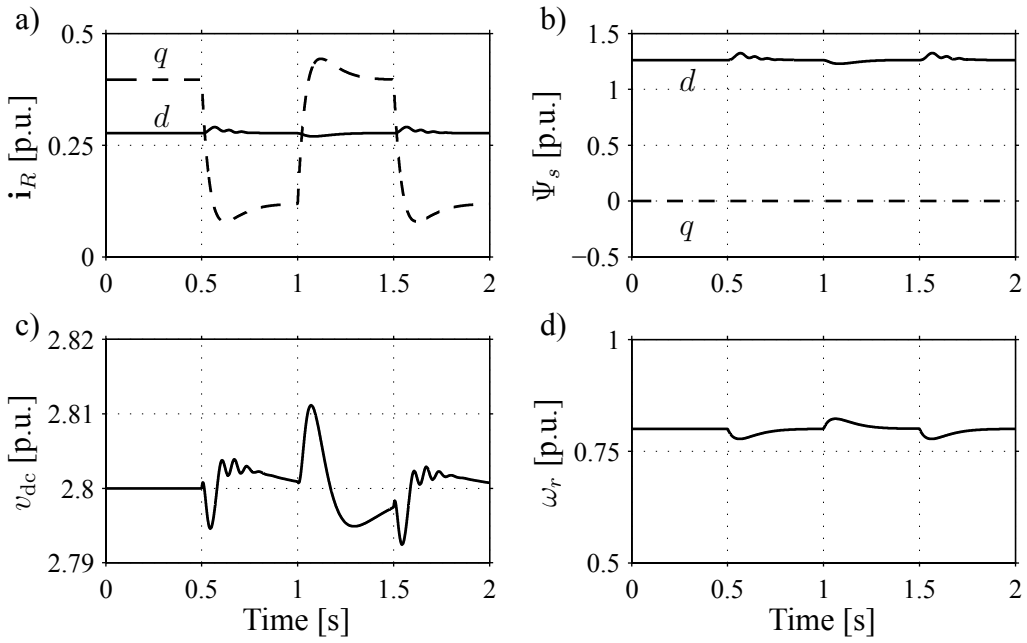

Fig. 7.25. Simulation of the system when the DFIG is in speed-control mode. a) Rotor current. b) Stator flux. c) DC-link voltage. d) Rotor speed.

current is practically constant during the sag. Some minor current transients can be observed at the instant of the sag and at the instant where the voltage returns. The main reason for this is that both the rotor and converter voltages have been limited to their maximum values. Otherwise, the dynamic performance of the system is promising.

Although the sag in the simulation is only 250 ms, the system can stay connected to the grid for indefinitely long voltage sags. This can be realized from the fact that the stator flux is controlled down to an appropriate level. The system then returns to a steady-state operating condition, in this case at a voltage level of 0 p.u. However, one issue that must be kept in mind is that, since the stator flux is reduced according to the voltage sag, the maximum torque that can be handled by the generator is reduced in proportion to the voltage sag. This means that the pitch mechanism must reduce the incoming torque accordingly, as otherwise overspeed occurs and the overspeed protection trips the turbine.

7.4.6 Steady-State Performance

As mentioned in the Introduction, the main reasons for choosing a DFIG system are cost and efficiency. Therefore, when modifying the DFIG system it is necessary to evaluate how the modifications affects both cost and efficiency. In Chapter 3, the average efficiency of the ordinary DFIG WT system has been calculated and compared to other electrical configurations used in wind turbine systems. This study serves as a basis for the efficiency calculations and comparisons in this section. Details of the calculations methods used here are described in Chapter 3. Moreover, the systems are compared to an ordinary DFIG system and a system that utilizes a full-power converter.

In this section, the efficiency will be calculated for the two options presented in the last part of Section 7.4.2.

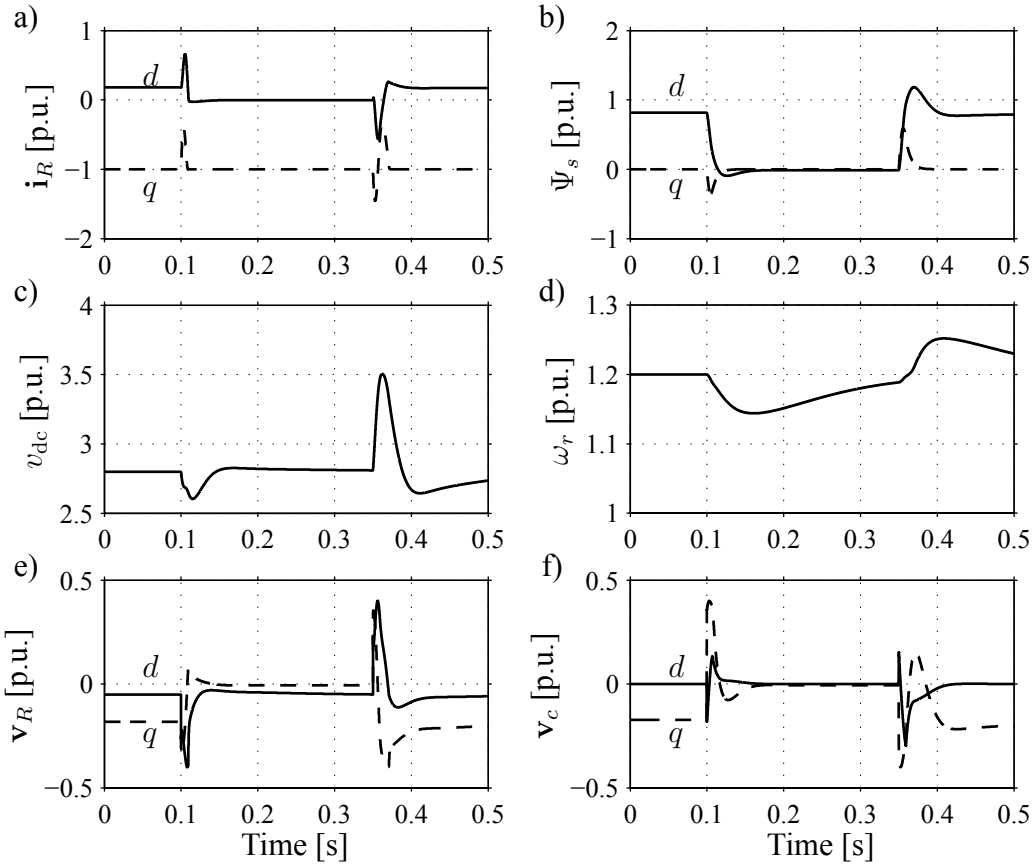

Fig. 7.26. Response to a 0% symmetrical voltage sag. a) Rotor current. b) Stator flux. c) DC-link voltage. d) Rotor speed. e) Rotor voltage. f) Series voltage.

Series-Injection Transformer

Fig. 7.27 shows the converter losses for the ordinary DFIG system, and in addition it presents the losses of the series-injection transformer for the two options of the DFIG series system presented earlier.

In Fig. 7.28, the average efficiencies of the ordinary DFIG system, the series system with the two options, and a system with a full-power converter are shown as functions of the average wind speed. As seen in Fig. 7.28, the efficiency of the standard DFIG system is highest. The efficiency of the DFIG series system with Option 1 is roughly same as the system that utilizes a full-power converter, although the efficiency is slightly lower at low average wind speeds and slightly higher at higher average wind speeds. The efficiency of the DFIG series system with Option 2 is between the ordinary DFIG system and the full-power converter system. Accordingly, this is the most energy efficient system with voltage sag ride-through facility.

Converter in the Y Point of the DFIG

Fig. 7.29 shows the magnetizing and resistive losses of the generator and the converter losses for the ordinary DFIG system and for the two options of the DFIG series system.

In Fig. 7.30, the efficiencies of the ordinary DFIG system, full-power converter system,

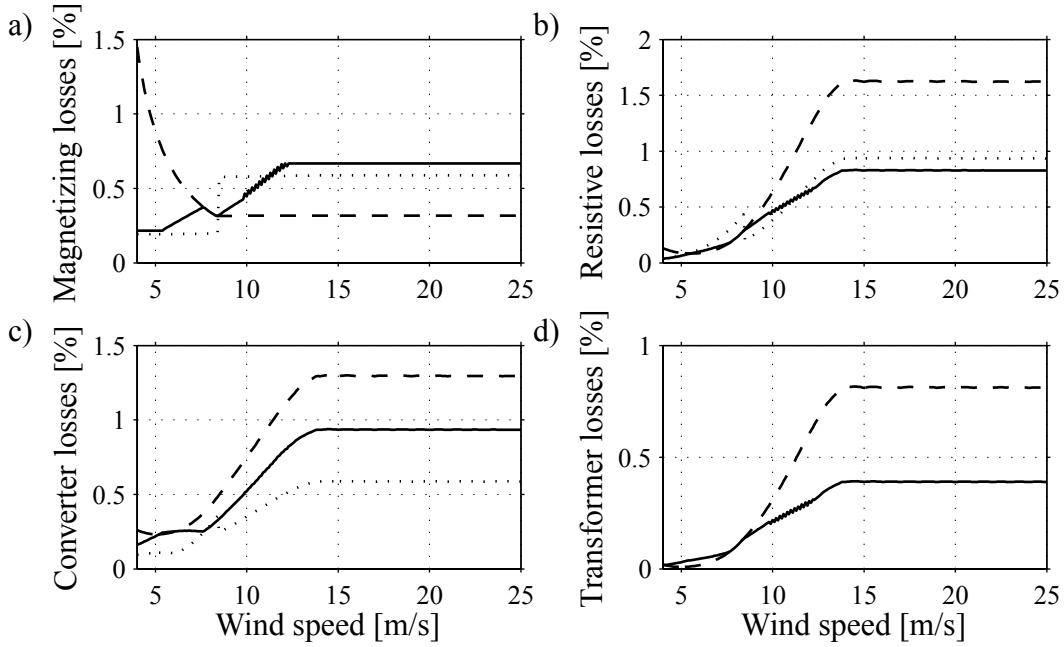

Fig. 7.27. Losses of the system with a series-injection transformer with the same turns ratio as the stator-to-rotor turns ratio. Dashed lines correspond to the series DFIG system with Option 1, solid line to the series DFIG with Option 2, and dotted line to the ordinary DFIG system. a) Magnetizing loses of the generator. b) Resistive losses of the generator. c) Converter losses. d) Transformer losses.

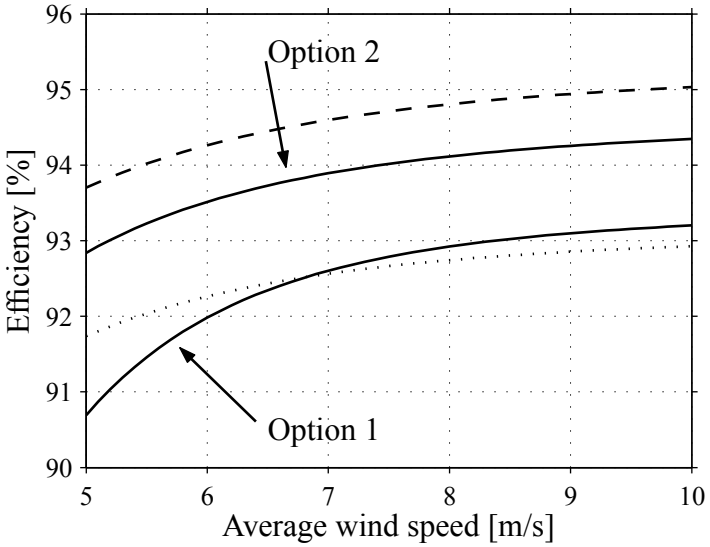

Fig. 7.28. Expected efficiency as a function of the average wind speed for the system with a series-injection transformer. Dashed line corresponds to the ordinary DFIG system, solid line to the DFIG series system, and dotted line to a system with a full-power converter.

and the two different options for the series DFIG system are shown as functions of the average wind speed. If Fig. 7.30 is compared to Fig. 7.28, it can be seen that the results are almost identical when connecting the converter to the Y point of the stator circuit. One reason for this is that the increased losses in the converter are almost the same as the losses of

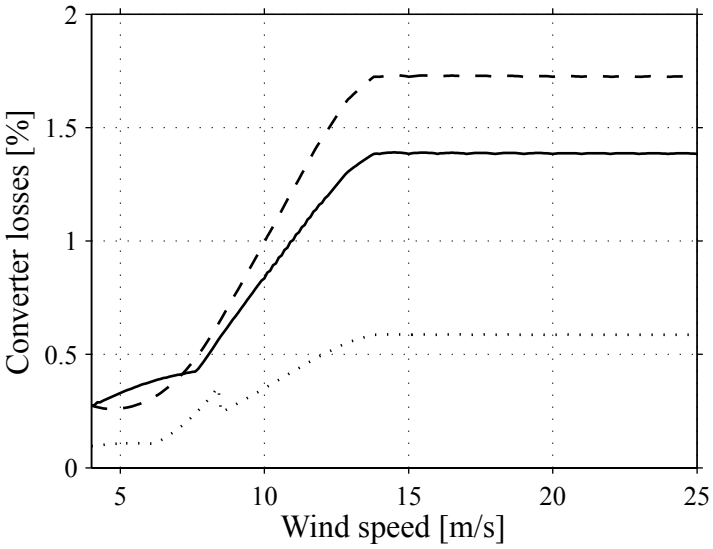

Fig. 7.29. Converter losses when the converter is connected to the Y point of the stator circuit of the DFIG. Dashed line is the series DFIG system with Option 1, solid line is the series DFIG with Option 2, and dotted line is the ordinary DFIG system. The generator losses are identical to that of Fig. 7.27.

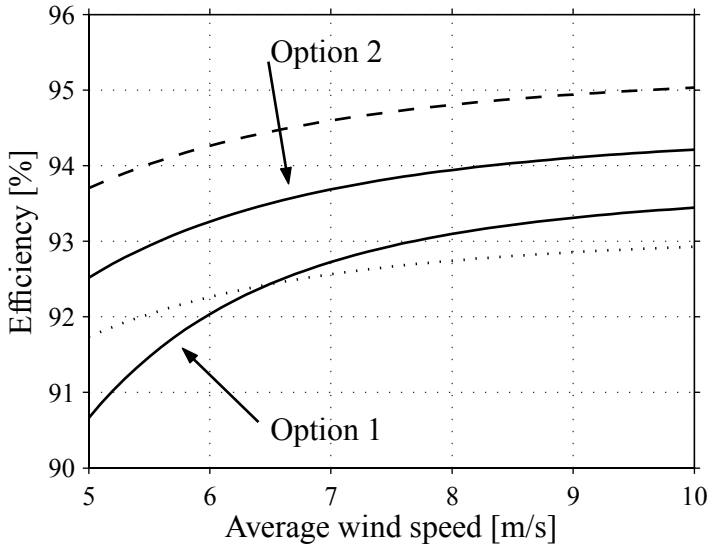

Fig. 7.30. Expected efficiency as a function of the average wind speed. The converter is connected to the Y point of the stator circuit of the DFIG. Dashed line corresponds to the ordinary DFIG system, solid line to the DFIG series system, and dotted line to a system with a full-power converter.

the series-injection transformer.

Energy Production Cost

Fig. 7.31 shows the relative energy cost of the DFIG series system in comparison to the ordinary DFIG system. From an initial cost perspective, an extra converter for the DFIG series system seems to be disadvantageous. However, as indicated in Fig. 7.31, from the

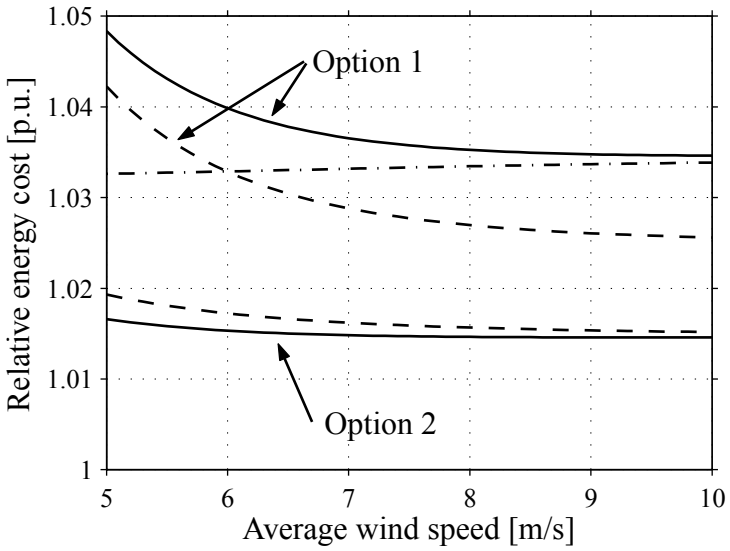

Fig. 7.31. Energy cost of the DFIG series system. The energy cost is related to the ordinary DFIG system. Solid lines are with the series-injection transformer, dashed lines are with the converter connected to the Y point, and dashed-dotted line is the system that utilize a full-power converter.

energy cost point of view it is beneficial to use the extra (third) converter to control the dc-link voltage. In the figure it is shown that the increased energy cost for this series system using Option 2 is approximately 1.5 percentage units. Moreover, as seen in the figure, for the system with a full-power converter the corresponding energy cost is approximately 1.5 percentage unit higher than for the series system with Option 2.

7.4.7 Discussion and Conclusion

A control law for the doubly-fed induction generator with the grid side converter connected in series with the stator circuit has been derived. The rotor current (torque and power factor), stator flux, and dc-link voltage are controlled. Simulations showed that the dynamic performance of the system is promising both during normal operation and during conditions when voltage sags are present in the grid. The derived control law is not capable of controlling the dc-link voltage at very low loads. As a remedy for this, two different options using an additional converter to solve this problem have been proposed and investigated. It was found that the best option was to use an additional converter for controlling the dc-link voltage in the whole operating area. Then, the series-connected converter can be used to control the flux to an optimal value from an overall efficiency point of view.

Two different methods of connecting the series converter resulted in almost the same efficiency. The efficiency of the DFIG series system with the best performance was found to be between the ordinary DFIG system and a system that utilizes a full-power converter system, i.e., a cage-bar induction generator equipped with a back-to-back converter.

7.5 Conclusion

In this chapter, voltage sag ride-through of variable-speed wind turbines has been investigated. It has been shown that a variable-speed wind turbine with a full-power converter system, e.g., a cage-bar induction generator with a back-to-back converter, can successfully reduce disturbances from both symmetrical and unsymmetrical voltage sags. Two candidate methods, with one shunt-connected and one series-connected grid-side converter respectively, of improving the voltage sag ride-through of DFIG variable-speed wind turbines have also been investigated. The shunt connected DFIG system with ride-through capabilities still suffers, at least initially, from high fault currents, while the series-connected DFIG system seems to have similar dynamic performance as the full-power converter system. However, the control of the DFIG series system is much more complicated than that of the full-power converter system. Another drawback of the series-connected DFIG system in comparison to the full-power converter system is that the maximum torque that can be handled by the generator is reduced in proportion to the voltage sag.

The energy production cost of the full-power converter system was found to be three percentage units higher than that of the ordinary DFIG system. The shunt DFIG system and the series system have approximately the same energy production cost, which is approximately 1.5 percentage unit higher compared to the ordinary DFIG system.

Chapter 8

Flicker Reduction of Stalled-Controlled Wind Turbines using Variable Rotor Resistances

Although there will be very large wind power installations, the installations of small-scale wind turbines (WTs) will most likely proceed. Small WTs, 1 MW and below, have been developed successfully using the fixed-speed stall-regulated concept, and will probably dominate the small-turbine market also in the near future. Worth pointing out is that fixed-speed WTs have the same energy production given a certain rotor diameter as variable-speed WTs (see Chapter 3).

The power quality impact, for instance the flicker (or voltage fluctuations) contribution, of WTs is an important concern for grid owners. For individual installations of these types of WTs, the flicker contribution can be the limiting factor from a power quality point of view, especially in weak grids [64]. One possibility to reduce flicker from a stall-controlled WT with an induction generator (IG) directly connected to the grid could be to introduce a variable rotor resistance. In other words, the rotor resistance could be used to control the rotor speed in a limited range and, in this way, absorb torque fluctuations and thereby reduce the flicker emission. The purpose of this chapter is to derive a rotor resistance control law, with the objective of minimizing torque fluctuations and flicker, for a stall-controlled WT.

8.1 Modeling

In Fig. 8.1, the system with turbine, gearbox, generator, and external rotor resistances, is presented. It is possible to control the slip of the IG with the external rotor resistances. The value of the external rotor resistances is adjusted with the power electronic equipment. However, in this chapter the power electronic equipment is not included in the model, i.e., it is assumed to be ideal. Therefore, the external rotor resistances can be treated as a continuous variable.

One way of representing the IG dynamically is to the use the so called Γ model as de-

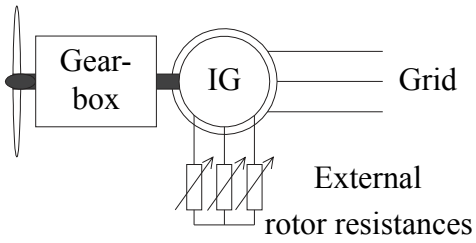

Fig. 8.1. Wind turbine with variable-rotor-resistance induction generator.

scribed in Section 4.2.1. The mechanical dynamics are described by

$$\frac{J}{n_p}\frac{d\omega_g}{dt} = T_g - \frac{T_t}{g_r} \tag{8.1}$$

where T_g is the electromechanical torque produced by the generator, T_t is the torque produced by the turbine, on the low-speed side of the gearbox, and g_r is the gear ratio of the gearbox. The drive train (soft axis) is not included in the model, since the objective is to investigate the relative performance of the derived control law and, for instance, absolute flicker values are of minor importance.

For the 1-MW IG considered in this chapter, operated at 690 V and 50 Hz the following parameters are used: R_s=0.007 p.u., $R_R^{\max}$=0.05 p.u., $R_R^{\min}$=0.01 p.u., R_R^{avg}=0.03 p.u., L_M=5 p.u., L_σ=0.2 p.u., n_p =2, g_r=61, and, J=32000 p.u. (without turbine J=3000 p.u.).

8.1.1 Reduced-Order Model

A common way to reduce the order of the induction machine model in (4.38) and (4.39) is to neglect the stator-flux dynamics. Then, the electrical dynamics of the induction machine dynamics are described by (4.39). Eliminating ψ_R from (4.39) yields

$$0 = (R_R + j\omega_2 L_\sigma)\mathbf{i}_R + L_\sigma\frac{d\mathbf{i}_R}{dt} + j\omega_2\mathbf{\Psi}_s. \tag{8.2}$$

Note that in the above equation, the stator-flux dynamics have also been neglected. Further, if i_{Rd} can be assumed constant or at least small, and $\mathbf{\Psi_s} \approx \psi_{sd} \approx \dfrac{v_s}{\omega_1}$, the dynamic system reduces to

$$L_\sigma\frac{di_{Rq}}{dt} = -R_R i_{Rq} - (\omega_1 - \omega_g)L_\sigma i_{Rd} - (\omega_1 - \omega_g)\frac{v_s}{\omega_1} \tag{8.3}$$

$$\frac{J}{n_p}\frac{d\omega_g}{dt} = -k_T i_{Rq} - \frac{T_t}{g_r} \tag{8.4}$$

where $k_T = 3v_s n_p/\omega_1$. This means that the model has been reduced to the second order, i.e., one electrical and one mechanical equation.

In Fig. 8.2, simulations of the induction machine are presented, both with the fifth-order and the second-order model of the system. In the simulations, the rotor resistance is increased by 40% after 50 ms and, after 250 ms, the shaft torque is increased from half of the rated torque to rated. Note that in this simulation, only the inertia of the generator has been taken into account and not the inertia of the turbine. This has been done in order to get a quicker

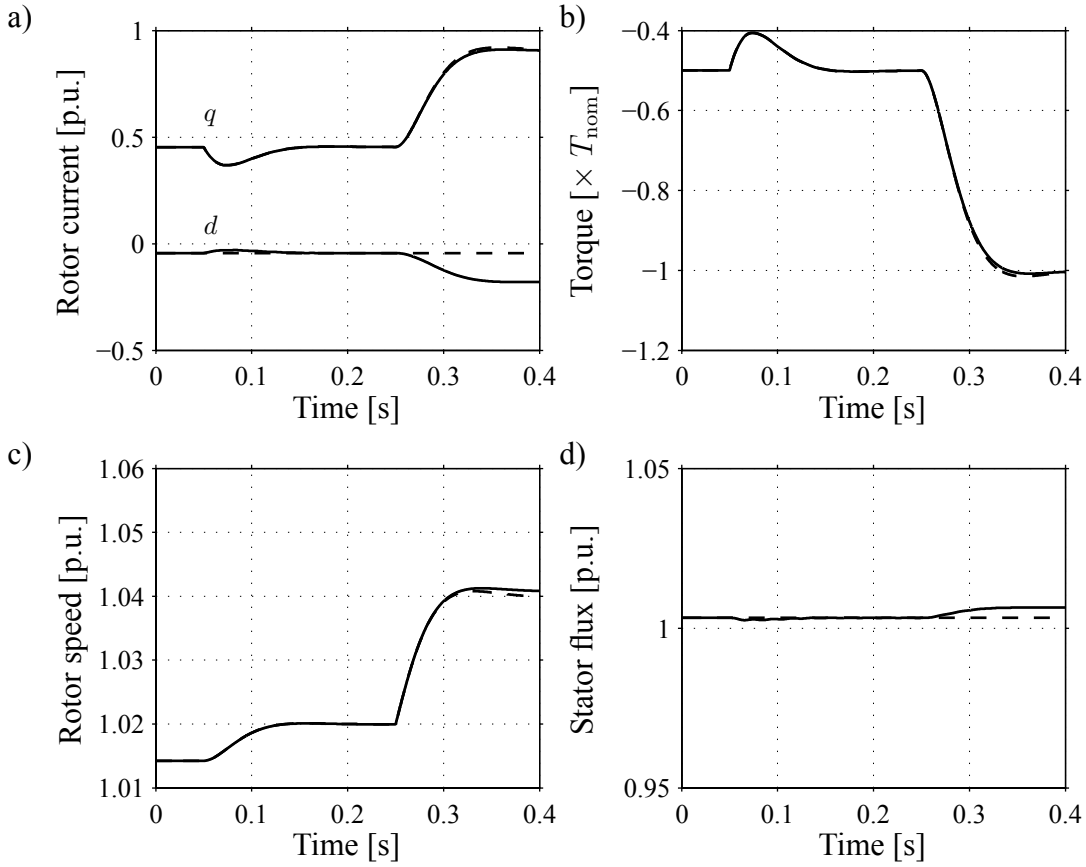

Fig. 8.2. Example of the response of the induction machine due to a step in the rotor resistance. The rotor resistance is increased 40% after 50 ms and after 250 ms the shaft torque is increased to the rated torque. Solid lines correspond to the fifth-order model while dashed lines correspond to the second-order model. a) Rotor current, b) Torque, c) Rotor speed and d) Stator flux.

response of the rotor speed and thereby a more lucid figure. The figure shows that both models produce approximately the same results. However, there is a small deviation in the d component of the rotor current. This reduced-order model will be used to derive the control law.

8.2 Current Control

In order to remove the multiplication between the R_R and i_{Rq}, i.e., the term $R_R i_{Rq}$, in (8.3), we will introduce the following non-linear control law

$$R_R^{\rm ref} = \frac{R'_R + R_{Ra} i_{Rq}}{i_{Rq}} \qquad i_{Rq} \neq 0 \tag{8.5}$$

where R_{Ra} is an "active damping," which can be used damp disturbances as described earlier. How to chose R_{Ra} will be described in the next section. Substitution of the above control

law in (8.3) yields

$$L_\sigma \frac{di_{Rq}}{dt} = -R'_R - R_{Ra} i_{Rq} + D \tag{8.6}$$

$$\begin{aligned} D &= -(\omega_1 - \omega_t) i_{Rd} L_\sigma - (\omega_1 - \omega_t)\frac{v_s}{\omega_1} \\ &= -\omega_2 \Big(i_{Rd} L_\sigma + \frac{v_s}{\omega_1} \Big) \end{aligned} \tag{8.7}$$

where a term D has been introduced. By treating the term D as a disturbance the following open-loop transfer function can be found

$$G_{\mathrm{ol}}(p) = \frac{i_{Rq}(p)}{R'_R(p)} = \frac{-1}{L_\sigma p + R_{Ra}}. \tag{8.8}$$

Then, by using IMC, the following current controller is obtained

$$F_c(p) = k_{pc} + \frac{k_{ic}}{p} = -L_\sigma \alpha_c - \frac{R_{Ra}\alpha_c}{p} \tag{8.9}$$

where α_c is the closed-loop bandwidth of the current control loop. A block diagram of the current control loop is shown in Fig. 8.3.

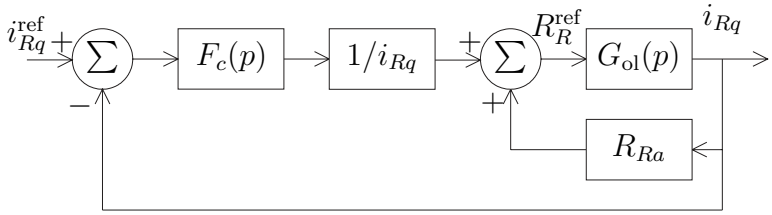

Fig. 8.3. Current Control Block Diagram.

Determination of the Active Damping

The transfer function, from a disturbance D to the current i_{Rq}, is found as

$$G_{D,i_{Rq}}(p) = \frac{-p}{L_\sigma p^2 + (R_{Ra} + L_\sigma \alpha_c)p + R_{Ra}\alpha_c}. \tag{8.10}$$

If $R_{Ra} = L_\sigma \alpha_c$, the above transfer function is reduced to

$$G_{D,i_{Rq}}(p) = \frac{-p}{L_\sigma (p + \alpha_c)^2}. \tag{8.11}$$

This choice of R_{Ra} causes a disturbance to be damped with the same time constant as the current control loop. A Bode diagram of (8.11) can be seen in Fig. 8.4 for three different values of the current control loop bandwidth α_c.

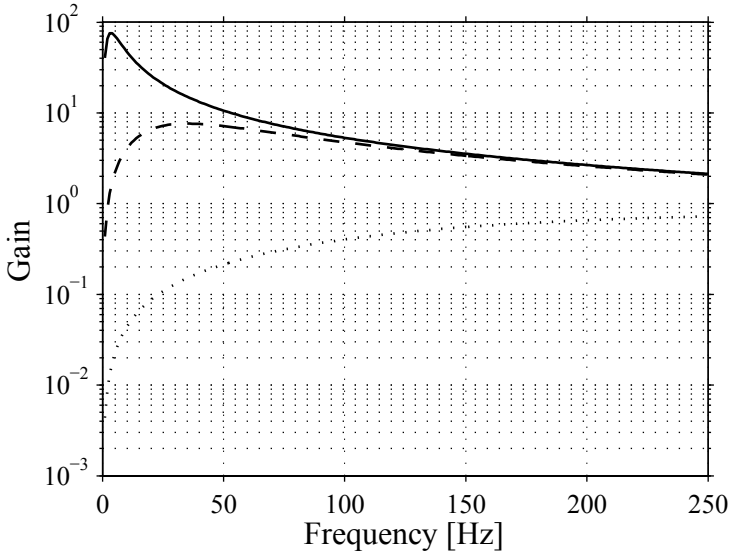

Fig. 8.4. Bode diagram. Solid α_c=22 rad/s, dashed α_c=220 rad/s and dotted α_c=2200 rad/s.

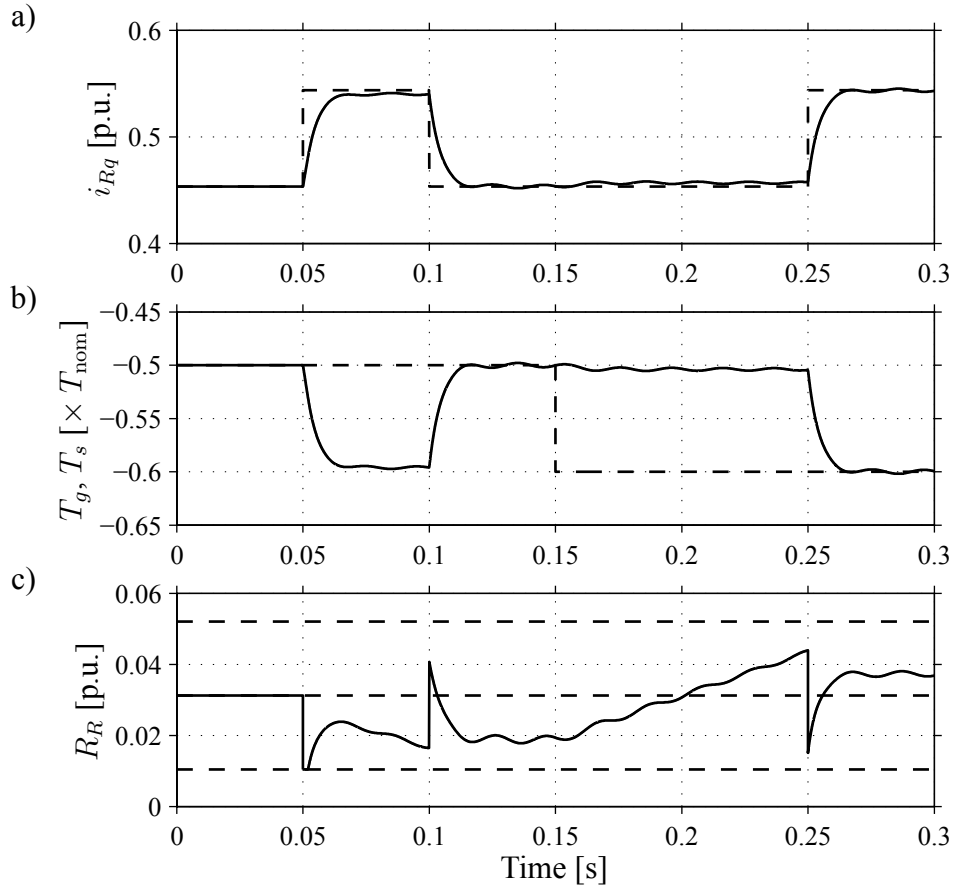

Fig. 8.5. Example of current control of an IG with external rotor resistances. a) q component of the rotor current (dashed line is the reference value), b) Torque (dashed line is the shaft torque), c) Rotor resistance (dashed line is the minimum, average and maximum value of the available rotor resistance).

8.2.1 Evaluation

Fig. 8.5 shows a simulation with the above derived rotor current control law. In the simulation the bandwidth of the current control loop is set to 220 rad/s which corresponds to a (10–90%) rise time of 10 ms. In the figure, it is seen that the current controller manages to control the rotor current with the desired bandwidth. Moreover, the controller manages to keep the generator torque at the shaft torque step (at 150 ms) until the current reference is adjusted according to the new shaft torque (at 250 ms). However, the rotor resistance varies over its entire range even for small current variations and shaft torque steps, as seen in the figure. It is also seen that when the shaft and generator torques differ (between 150–250 ms), the rotor resistance is constantly increased (or decreased for opposite sign of the torque difference). If the rotor resistance has to be limited, the current controller will not manage to keep the rotor current and thereby the generator torque. Because of the limited range in which the rotor resistance can vary, the setting of the current reference will be of great importance for the over-all performance of the system. How to set the rotor current reference will be further addressed in the next section. First, however, in this section, a brief analytical investigation of how the rotor resistance varies due to a shaft torque step is made.

By controlling the rotor current with a high-gain feedback, the rotor-current dynamics in (8.3) can be expressed as

$$L_\sigma \frac{di_{Rq}}{dt} = -R_R^{\text{ref}} i_{Rq} - \omega_2 \left(L_\sigma i_{Rd} + \frac{v_s}{\omega_1} \right) = 0. \tag{8.12}$$

This implies that the rotor-resistance reference value varies as

$$\begin{aligned} R_R^{\text{ref}} &= -\frac{\omega_2}{i_{Rq}^{\text{ref}}} \left(L_\sigma i_{Rd} + \frac{v_s}{\omega_1} \right) \approx -\frac{\omega_2}{i_{Rq}^{\text{ref}}} \frac{v_s}{\omega_1} \\ i_{Rq}^{\text{ref}} &\neq 0. \end{aligned} \tag{8.13}$$

From (8.13), it is seen that the rotor resistance is depending on the slip, ω_2, and the operating condition, i.e. i_{Rq}^{ref}. Moreover, if the generator is exposed to a shaft-torque step, ΔT_t, the generator speed becomes according to (8.1)

$$\frac{J}{n_p} \frac{d\omega_g}{dt} = -\frac{\Delta T_t}{g_r} \tag{8.14}$$

if the system initially was in the steady state and the electromechanical torque, T_g, is kept constant. This means that (8.13) can be rewritten as

$$\begin{aligned} R_R^{\text{ref}} &\approx -\frac{v_s}{\omega_1 i_{Rq}^{\text{ref}}} \int \frac{n_p}{J g_r} \Delta T_t dt \\ i_{Rq}^{\text{ref}} &\neq 0 \end{aligned} \tag{8.15}$$

since $\omega_g = \omega_1 - \omega_2$ and $d\omega_1/dt = 0$. The integral can be evaluated easily since ΔT_t is constant. This means that rotor resistance has changed ΔR_R over the time

$$\Delta t = -\frac{J g_r \omega_1}{n_p v_s} \frac{i_{Rq}^{\text{ref}}}{\Delta T_t} \Delta R_R. \tag{8.16}$$

For the shaft torque step at 150 ms in Fig. 8.5, the increase in rotor resistance ($\Delta R_R = 0.024$) would, according to the above formula, take 0.2 s, which also can be seen in the figure. Moreover, if $\pm\Delta R_R^{\max}$ is the maximum available rotor resistance, the time, $\Delta t^{\lim}$, to reach maximum or minimum value of the rotor resistance becomes

$$\Delta t^{\lim} = \frac{J g_r \omega_1}{n_p v_s} \frac{i_{Rq}^{\text{ref}}}{\Delta T_t} \Delta R_R^{\max}. \tag{8.17}$$

This means that for a given step in the shaft torque, the time until the rotor resistance must be limited depends on i_{Rq}^{ref}. That is, smaller values of i_{Rq}^{ref} imply a shorter time until the rotor resistance must be limited. This nonlinearity makes the setting of the rotor current reference i_{Rq}^{ref} more difficult.

8.3 Reference Value Selection

In the steady state, the rotor resistance should be (or at least close to) its desired value, R_{R0}. One idea is to set i_{Rq}^{ref} as

$$i_{Rq}^{\text{ref}} = k_R \int (R_{R0} - R_R) dt - B_a \omega_2 \tag{8.18}$$

where only an integration term of the error in the rotor resistance is used in order to avoid an algebraic loop. If the current control loop is fast, i.e., $i_{Rq} = i_{Rq}^{\text{ref}} = k_R I - B_a \omega_2$, where I is the integration of the error in the rotor resistance, the system becomes

$$\frac{J}{n_p} \frac{d\omega_2}{dt} = k_T i_{Rq}^{\text{ref}} + \frac{T_t}{g_r} = k_T (k_R I - B_a \omega_2) + \frac{T_t}{g_r} \tag{8.19}$$

$$\frac{dI}{dt} = R_{R0} - R_R. \tag{8.20}$$

Note that the slip dynamics are found from (8.1), $\omega_g = \omega_1 - \omega_2$ and $d\omega_1/dt = 0$. Moreover, since the bandwidth of the current control loop is fast, it can be assumed that $R_R = R_R^{\text{ref}}$. Therefore, according to (8.13), R_R equals to

$$R_R = R_R^{\text{ref}} \approx -\frac{\omega_2}{i_{Rq}^{\text{ref}}} \frac{v_s}{\omega_1} = -\frac{\omega_2}{k_R I - B_a \omega_2} \frac{v_s}{\omega_1}. \tag{8.21}$$

This means, finally, that the following system must be analyzed

$$\frac{J}{n_p} \frac{d\omega_2}{dt} = k_T (k_R I - B_a \omega_2) + \frac{T_t}{g_r} \tag{8.22}$$

$$\frac{dI}{dt} = R_{R0} + \frac{\omega_2}{k_R I - B_a \omega_2} \frac{v_s}{\omega_1}. \tag{8.23}$$

The above system has an equilibrium point at

$$\omega_{2,0} = \frac{R_{R0} T_{t0} \omega_1}{g_r k_T v_s} \tag{8.24}$$

$$I_0 = \frac{T_{t0}(\omega_1 R_{R0} B_a - v_s)}{g_r k_R k_T v_s}. \tag{8.25}$$

Linearization and insertion around the equilibrium point yields

$$\Delta\dot{x} = \begin{bmatrix} -B_a k_T n_p/J & k_R k_T n_p/J \\ \dfrac{g_r k_T(\omega_1 R_{R0} B_a - v_s)}{T_{t0}\omega_1} & \dfrac{-g_r k_R k_T R_{R0}}{T_{t0}} \end{bmatrix} \Delta x + \begin{bmatrix} \dfrac{n_p}{g_r J} \\ 0 \end{bmatrix} \Delta u \tag{8.26}$$

where

$$\Delta x = \begin{bmatrix} \Delta\omega_2 \\ \Delta I \end{bmatrix} \qquad \Delta u = \Delta T_t. \tag{8.27}$$

Now, it is interesting to see how a change in the incoming torque influences the rotor resistance. Therefore, one option is to study the error in the rotor resistance, $e = R_{R0} - R_R$. However, e cannot be found directly from the state variables but since I is the integration of e, it is possible to use the derivative of I. This means that

$$G_{T_t e} = p\, G_{T_t I}(p) \tag{8.28}$$

where $G_{T_t I}(p)$ is the transfer function from T_t to I which can be found from the system in (8.26). If k_R and B_a are chosen as

$$k_R = \frac{\alpha_R^2 J T_{t0}\omega_1}{g_r k_T^2 n_p v_s} \tag{8.29}$$

$$B_a = -\frac{\alpha_R^2 J^2 R_{R0}\omega_1 - 2a_R J k_T n_p v_s}{k_T^2 n_p^2 v_s} \tag{8.30}$$

where α_R is a parameter that can be set "freely," the above transfer function $G_{T_t e}(p)$ becomes

$$G_{T_t e}(p) = -\frac{(k_T n_p v_s - \alpha_R J R_{R0}\omega_1)^2}{J k_T n_p v_s \omega_1 T_{t0}} \frac{p}{(p+\alpha_R)^2} \tag{8.31}$$

which is a band-pass filter centered at α_R. Moreover, the damping of the above transfer function and the parameter k_R is dependent on the operating condition, i.e., T_{t0}.

8.3.1 Evaluation

For a given operating condition it possible to express (8.31) as

$$G_{T_t e}(p) = K\frac{p}{(p+\alpha_R)^2} \tag{8.32}$$

where K is a constant that depends on the operating condition. If the system is exposed to a step, we will get

$$e(t) = \mathcal{L}^{-1}\left[\frac{1}{p} G_{T_t e}(p)\right] = K t e^{-\alpha_R t} \tag{8.33}$$

where $\mathcal{L}$ is the Laplace transformation symbol. From the above equation, it is seen that after a torque step, the rotor resistance returns to its desired value R_{R0}, i.e., $e(t \to \infty) = 0$.

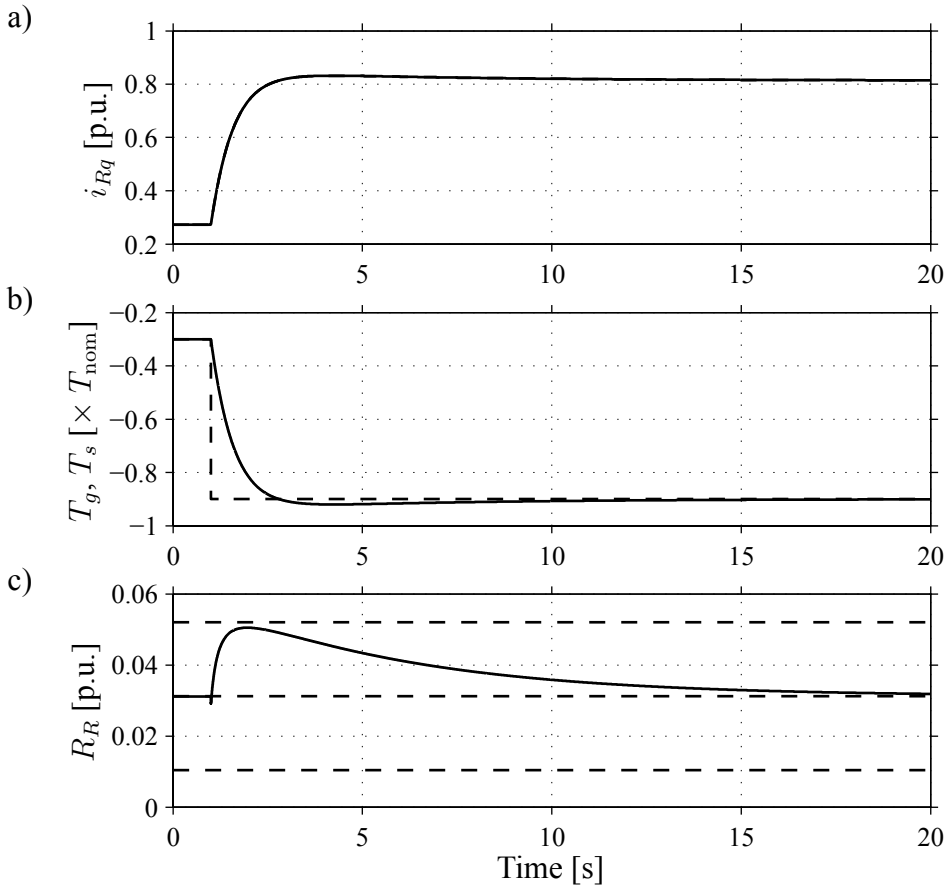

Fig. 8.6. Example of outer reference selection control loop. a) q component of the rotor current (dashed line is the reference value), b) Torque (dashed line is the shaft torque), c) Rotor resistance (dashed line is the minimum, average and maximum value of the available rotor resistance).

Moreover, by looking at the derivative of the above function it is possible to determine that the function has a maximum at

$$t\big(\max(R_R)\big) = \frac{1}{\alpha_R}. \tag{8.34}$$

Fig. 8.6 shows a simulation of the system with the reference selection control loop. The bandwidth of the current control loop is set to a high value (2200 rad/s) and the parameter α_R is set to 1 rad/s. It is seen in the figure that after the torque step (at $t = 1$ s) the rotor resistance has its maximum value after 1 s (at $t = 2$ s), which is also verified by the expression (8.34). Moreover, after the torque step the rotor resistance is returning to its desired value.

8.4 Evaluation

In order to evaluate the derived control law, the flicker emission is compared to a similar system with uncontrolled rotor resistances, i.e., R_R is fixed. Flicker emission or rapid voltage fluctuations can be described with the dimensionless quantity P_{st}: the short-term severity index. In the standard IEC 61000-21, it is described how this value is determined [51]. The

system is simulated for 10 minutes, since the 10 minute P_{st}-value is used. The applied shaft torque has been precalculated using blade element momentum theory with different average wind speeds and turbulence intensities. Then the P_{st} value has been calculated on a fictive grid with a short-circuit power of 50 times the nominal power of the WT and with an X/R ratio of 0.5. The average torque, corresponding to the average wind speed, for each 10 minute period is used to set the parameters that are dependent on the operating condition, i.e., k_R. Naturally, in a real system, they can be adjusted according to a changing operating condition. However, since this should be done on a much slower time scale than the bandwidths of the control loops, it has been ignored in the simulation presented here.

Fig. 8.7 shows an example of how the derived rotor resistance control law operates for a short piece of one of the above mentioned 10-minute simulation. The average wind speed in the 10 minute simulation was 14 m/s and the turbulence intensity was 25%. The bandwidth

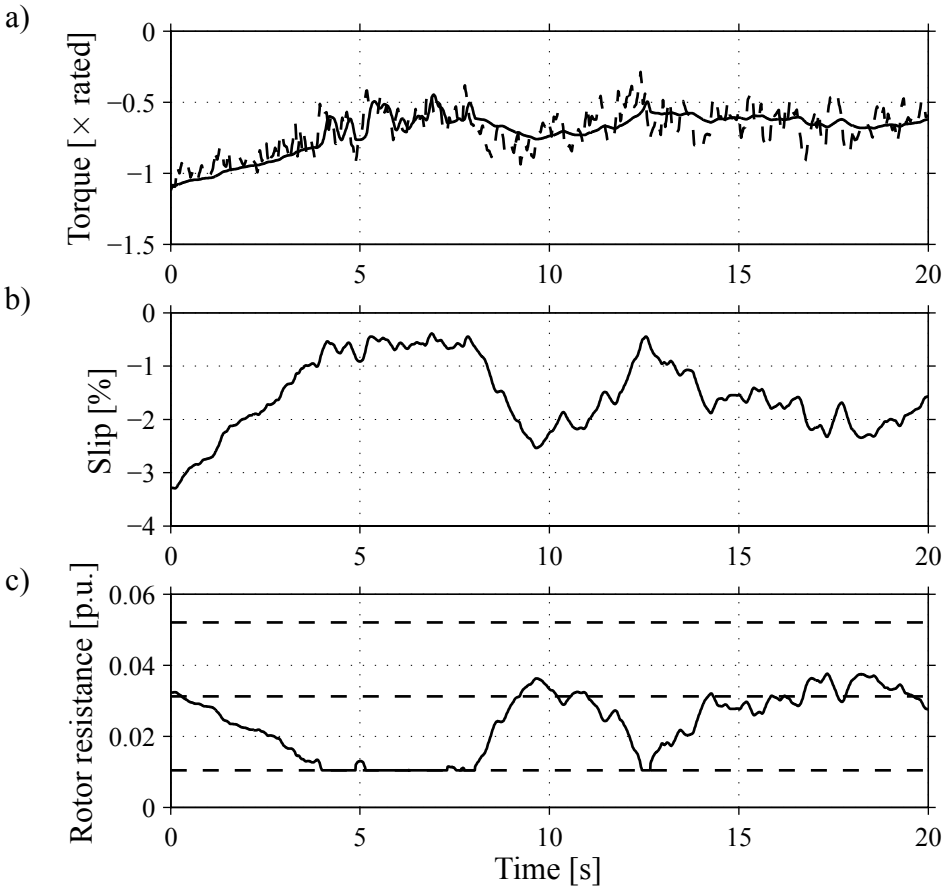

Fig. 8.7. Example of the behaviour of the derived control law. a) Torque (generator torque is solid and turbine torque is dashed), b) Slip and c) Rotor resistance.

of the current control loop, α_c, is 2200 rad/s and the parameter α_R, of the reference value selection control loop is 0.5 rad/s. The set point value for the rotor resistance, R_{R0}, has been set to the average value of the available rotor resistance R_R^{avg}.

8.4.1 Flicker Contribution

In Fig. 8.8, the P_{st} value is seen for a system with fixed rotor resistance and with the derived control law as a function of the turbulence intensity and for different average wind speeds. The control parameter is as in Fig. 8.7, except for the parameter α_R that is 1 rad/s. In the

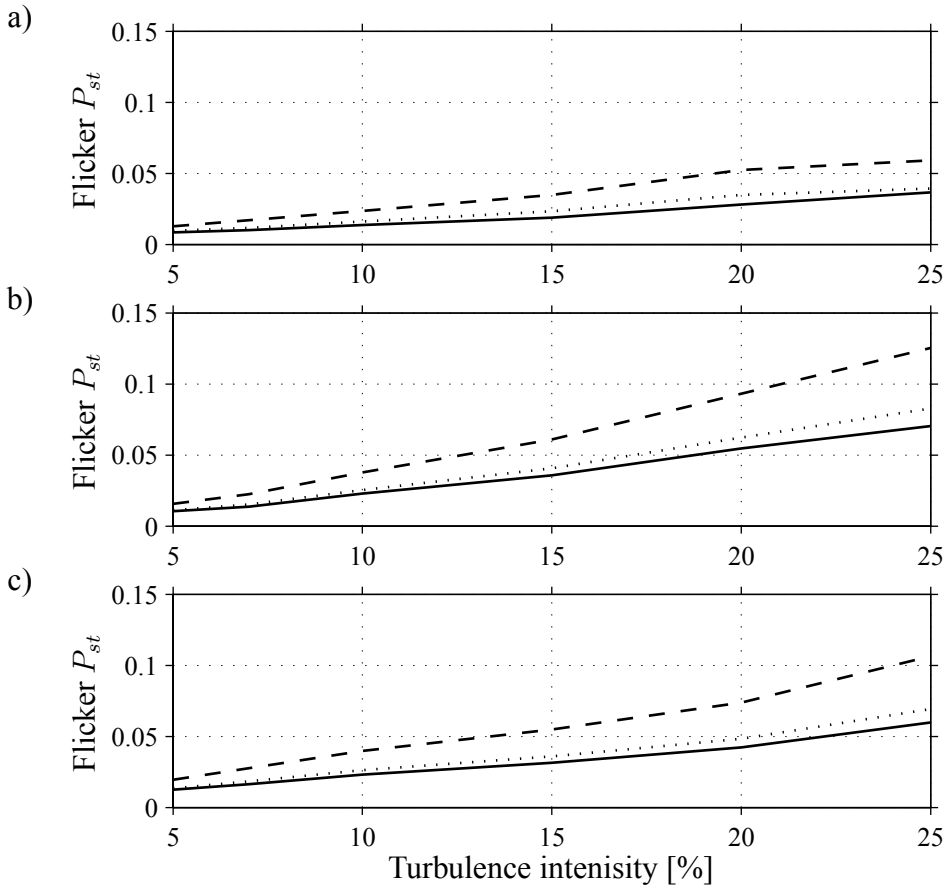

Fig. 8.8. Flicker as a function of the turbulence intensity. Solid line is WT with controlled rotor resistance, dashed line is with fixed rotor resistance, $R_R = R_R^{\text{avg}}$ and dotted line is with fixed rotor resistance, $R_R = R_R^{\max}$. The average wind speed is a) 6 m/s, b) 14 m/s and c) 20 m/s.

figure, the system with fixed rotor resistance has been simulated with two different values of the rotor resistance, i.e., the average value, R_R^{avg}, and the maximum value (in continuous operation), $R_R^{\max}$, of the available rotor resistance. It can be seen that the derived control law produces lower P_{st} values than the system with fixed rotor resistance. Even though the P_{st} value for the fixed rotor resistance system with $R_R = R_R^{\max}$ is close to the system with controlled rotor resistances, it suffers from a drawback, namely, that the higher the rotor resistance is, the higher the losses in the rotor resistance will be. These higher losses imply that it will be necessary to increase the cooling of the generator. Finally, during the simulation, the average value of the rotor resistance R_R is very close to R_R^{avg}.

8.4.2 Flicker Reduction

In Fig. 8.9 the relative flicker contribution for the proposed controller for five different values of a_R is shown. The flicker in the comparison is related to a system with a fixed rotor resistance. The rotor resistance of this system is set to the average value of the available rotor resistance, i.e., $R_R = R_R^{\text{avg}}$. A relative flicker of 1 corresponds to a flicker contribution equal to that of the fixed rotor resistance system. Lower values of the relative flicker imply a lower flicker contribution and vice versa. The relative flicker is given as a function of turbulence intensities for an average wind speed of 6 m/s. In general, it can be seen that the

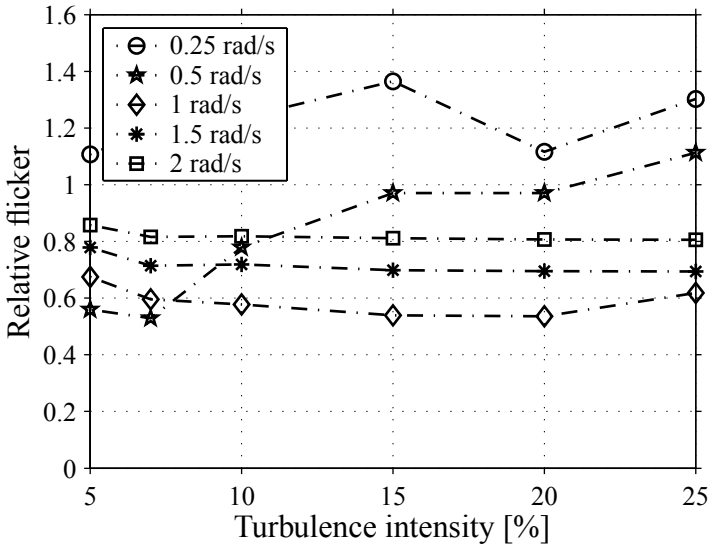

Fig. 8.9. Reduction in flicker for different bandwidths of α_R. The average wind speed is 6 m/s.

lower the parameter α_R is, the more reduction in the P_{st} value is achieved. However, if the frequency is too low or the turbulence intensity is too high, the rotor resistance will hit its maximum or minimum value to a high extent which will make the result worse. For example, for the case with α_R put to 0.5 rad/s in the figure, the number of times the rotor resistance has to be limited is rapidly increased from a turbulence intensity of 7% and upwards. For the case with α_R equal 0.25 rad/s the rotor resistance has been limited to its maximum or minimum value between 20–70% of the total simulation time depending on the turbulence intensity. Due to this fact, the P_{st} value is actually worse for this case than for the case with fixed rotor resistance.

In Figs. 8.10 and 8.11 the corresponding diagrams for an average wind speed of 14 and 20 m/s are shown. It is seen that when the turbulence intensity becomes higher, for low values of α_R, the rotor resistance can not follow its reference value and has to be limited to a higher and higher degree (i.e., the same phenomena as in Fig. 8.9). This will have a negative impact on the performance.

As mentioned earlier, the damping of the flicker (or the torque fluctuation) is dependent on the operating condition. This is also verified by the simulation since it is possible to reduce more of the flicker at higher average wind speeds (i.e., higher average torques). On the other hand, the flicker contribution is lower at lower average wind speeds. Moreover, from the figures it can be seen that in order to have an "optimal" reduction in flicker, over the whole operating area, with the derived control law, the parameter α_R should be a function of

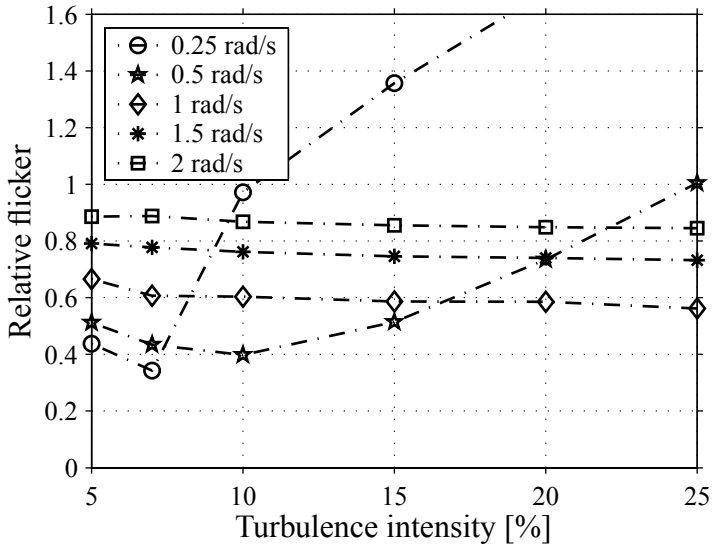

Fig. 8.10. Reduction in flicker for different bandwidths of α_R. The average wind speed is 14 m/s.

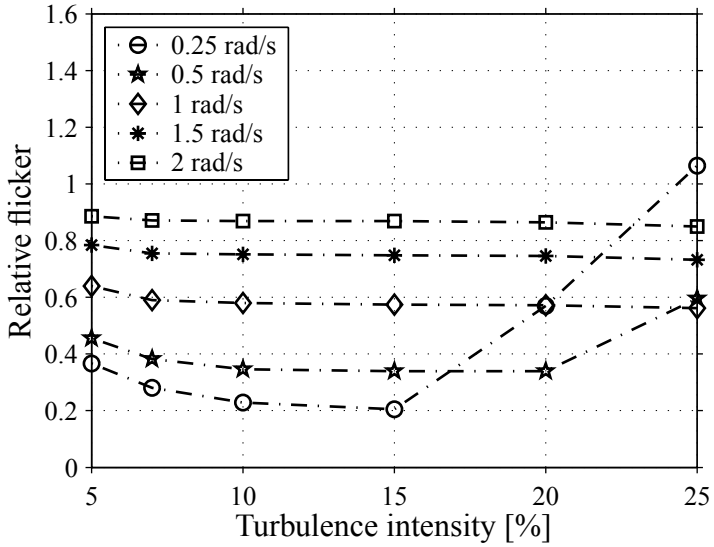

Fig. 8.11. Reduction in flicker for different bandwidths of α_R. The average wind speed is 20 m/s.

both the average torque and turbulence intensity.

8.5 Conclusion

A non-linear rotor resistance control law has been derived with the objective of minimizing the flicker contribution of a stall-controlled fixed-speed wind turbine to the grid.

It was shown that it is possible to reduce the flicker contribution by utilizing the derived rotor resistance control law with 40–80% depending on the operating condition. However, since the rotor resistance can be varied only within a limited range, the reduction in the flicker contribution will be dependent on the operating condition. Moreover, the non-linearity of the system will make an “optimal” reduction in flicker, over the whole operating area, difficult.

Chapter 9

Conclusion

The electrical energy efficiency of wind turbine systems equipped with doubly-fed induction generators in comparison to other wind turbine generator systems has been investigated. It was found that the energy efficiency of a doubly-fed induction generator system is a few percentage units higher compared to a system using a cage-bar induction generator, controlled by a full-power converter. In comparison to a direct-driven permanent-magnet synchronous generator, controlled by a converter or a two-speed generator system the difference in energy efficiency was found to be small. Moreover, the converter losses of the doubly-fed induction generator can be reduced if the available rotor-speed range is made smaller. However, the aerodynamic capture of the wind turbine is reduced with a smaller rotor-speed range. This means that the increased aerodynamic capture that can be achieved by a larger converter has, thus, a greater impact than the increased converter losses. Finally, two methods to reduce the magnetizing losses of the doubly-fed induction generator system, have been investigated. It was found that the method, utilizing a Y-Δ switch in the stator circuit had the largest gain in energy, of the two investigated methods.

In order to evaluate different methods of reducing the influence of the back EMF on the rotor current control loop, a general rotor current control law has been derived with the option of having feed-forward compensation of the back EMF and "active resistance." It was found that the method that combines both the feed-forward compensation of the back EMF and the "active resistance" manages to suppress the influence of the back EMF on the rotor current best and was found to be the least sensitive to erroneous parameters. The choice of current control method is of greater importance if the bandwidth of the current control loop is low. Moreover, it has been shown that by using grid-flux orientation, the stability and the damping of the system is independent of the rotor current, in contrast to the stator-flux oriented system.

Dynamic models of the DFIG wind turbines have been experimentally verified, with a 850-kW wind turbine. Simulations and experimental results of the dynamic response to symmetrical as well as unsymmetrical voltage sags of a DFIG wind turbine were presented. Simulations were carried out both with a full-order model, and also with a reduced-order (second-order) model. Both models produced acceptable results.

Voltage sag ride-through capabilities of some different variable-speed wind turbines have been investigated and compared. A variable-speed wind turbine with a full-power converter

system can handle voltage sags very well. Two candidate methods for improving the voltage sag ride-through capability of DFIG variable-speed wind turbines have been investigated. One of the methods still suffers, at least initially, from high fault currents, while the other method seems to have similar dynamical performance as the full-power converter system. However, the control of the latter method is much more complicated than that of the full-power converter system. In addition, the maximum torque that can be handled by the generator is reduced in proportion to the voltage sag. The energy production cost of the full-power converter system was found to be three percentage units higher than that of the ordinary DFIG system without ride through capability. The two DFIG candidate methods have approximately the same energy production cost, which is approximately 1.5 percentage units higher in comparison to the ordinary DFIG system.

Finally, a non-linear rotor resistance control law has been derived with the objective of minimizing the flicker contribution of a stall-controlled fixed-speed wind turbine to the grid. It has been found that the flicker contribution can be reduced with 40–80%, depending on the operating condition, with the derived control law.

9.1 Future Research

The following candidate topics are proposed for future research:

- Development of a unified estimator for both stator-flux and grid-flux field orientation. Since the flux dynamics are poorly damped, a desired property would be a relatively good damping of the flux dynamics.
- More thorough dynamic, steady-state, and experimental analysis of the voltage sag ride-through systems for the DFIG wind turbine. In addition, it is essential to study the hardware configuration of the voltage sag ride-through systems.
- Development of mathematical models of wind turbines with voltage sag ride-through properties. Experimental evaluation of the developed models with commercial wind turbines with voltage sag ride-through properties.
- Derivation of analytical expressions for the response of the DFIG to unsymmetrical voltage sags.

References

[1] *SIMPOW Power System Simulation Software*, Brochure, ABB Power Systems Analysis, Västerås, Sweden.

[2] F. Abrahamsen, "Energy optimal control of induction motor drives," Ph.D. dissertation, Aalborg Univ., Aalborg, Denmark, Feb. 2000.

[3] T. Ackermann and L. Söder, "An overview of wind energy-status 2002," *Renew. Sustain. Energy Rev.*, vol. 6, no. 1–2, pp. 67–128, Feb./Apr. 2002.

[4] H. Akagi and H. Sato, "Control and performance of a doubly-fed induction machine intended for a flywheel energy storage system," *IEEE Trans. Power Electron.*, vol. 17, no. 1, pp. 109–116, Jan. 2002.

[5] H. Akagi, Y. Kanazawa, and A. Nabae, "Instantaneous reactive power compensators comprising switching devices without energy storage components," *IEEE Trans. Ind. Applicat.*, vol. 20, no. 3, pp. 625–630, May/June 1984.

[6] J. Bendl, M. Chombt, and L. Schreier, "Adjustable-speed operation of doubly fed machines in pumped storage power plants," in *Proc. Ninth International Conference on Electrical Machines and Drives*, Sep., 1–3, 1999, pp. 223–227.

[7] I. Boldea and S. A. Nasar, *Electric Drives*. CRC Press LCC, 1999.

[8] S. Bolik, "Grid requirements challenges for wind turbines," in *Proc. Int. Work. Large-Scale Integration Wind Power Transmission Networks Offshore Wind Farms*, Billund, Denmark, Oct., 20–21, 2003.

[9] M. H. Bollen, *Understanding Power Quality Problems: Voltags Sags and Interuptions*. Piscataway, NJ, USA: IEEE Press, 2002.

[10] M. Bongiorno, "Control of voltage source converters for voltage dip mitigation in shunt and series configuration," Chalmers University of Technology, Göteborg, Sweden, Licentiate Thesis 515L, Nov. 2004.

[11] T. Burton, D. Sharpe, N. Jenkins, and E. Bossanyi, *Wind Energy Handbook*. John Wiley & Sons, Ltd, 2001.

[12] O. Carlson, J. Hylander, and K. Thorborg, "Survey of variable speed operation of wind turbines," in *Proc. of European Union Wind Energy Conference*, Göteborg, Sweden, May, 20–24, 1996, pp. 406–409.

[13] L. Congwei, W. Haiqing, S. Xudong, and L. Fahai, "Research of stability of double fed induction motor vector control system," in *Proc. of the Fifth International Conference on Electrical Machines and Systems*, vol. 2, Shenyang, China, Aug., 18–20, 2001, pp. 1203–1206.

[14] R. L. Cosgriff, *Nonlinear Control Systems*. McGraw-Hill, 1958.

[15] R. Datta and V. T. Ranganathan, "A simple position-sensorless algorithm for rotor-side field-oriented control of wound-rotor induction machine," *IEEE Trans. Ind. Electron.*, vol. 48, no. 4, pp. 786–793, Aug. 2001.

[16] ——, "Variable-speed wind power generation using doubly fed wound rotor induction machine-a comparison with alternative schemes," *IEEE Trans. Energy Conversion*, vol. 17, no. 3, pp. 414–421, Sept. 2002.

[17] ——, "Decoupled control of active and reactive power for a grid-connected doubly-fed wound rotor induction machine without position sensors," in *Proc. Conference Record of the 1999 IEEE Industry Applications Conference*, vol. 4, Phoenix, AZ, USA, Oct. 1999, pp. 2623–2628.

[18] F. B. del Blanco, M. W. Degner, and R. D. Lorenz, "Dynamic analysis of current regulators for ac motors using complex vectors," *IEEE Trans. Ind. Applicat.*, vol. 35, no. 6, pp. 1424–1432, Nov./Dec. 1999.

[19] DEWIND. (2005, Jan.) The D8 series. Brochure. [Online]. Available: http://www.dewind.de/en/downloads/D8-2000-100-eng.pdf

[20] A. Dittrich and A. Stoev, "Grid voltage fault proof doubly-fed induction generator system," in *Proc. Power Electronics and Applications (EPE)*, Toulouse, France, Sep. 2003.

[21] J. L. Duarte, A. V. Zwam, C. Wijnands, and A. Vandenput, "Reference frames fit for controlling pwm rectifiers," *IEEE Trans. Power Electron.*, vol. 46, no. 3, pp. 628–630, June 1999.

[22] J. B. Ekanayake, L. Holdsworth, and N. Jenkins, "Comparison of 5th order and 3rd order machine models for doubly fed induction generator (DFIG) wind turbines," *Electric Power Systems Research*, vol. 67, pp. 207–215, Dec. 2003.

[23] Elforsk. (2005) Driftuppföljning av vindkraftverk december 2004. [Online]. Available: http://www.elforsk.se/varme/underlag/vstat0412.pdf

[24] Elsam. (2003, Oct.) Horns rev offshore wind farm. Brochure. [Online]. Available: http://www.hornsrev.dk/nyheder/brochurer/Horns_Rev_GB.pdf

[25] (2004) Enercon website. [Online]. Available: http://www.enercon.de/

[26] A. Feijóo, J. Cidrás, and C. Carrillo, "A third order model for the doubly-fed induction machine," *Electric Power Systems Research*, vol. 56, pp. 121–127, Nov. 2000.

[27] C. Fitzer, A. Arulampalam, M. Barnes, and R. Zurowski, "Mitigation of saturation in dynamic voltage restorer connection transformers," *IEEE Trans. Power Electron.*, vol. 17, no. 6, pp. 1058–1066, Nov. 2002.

[28] J. Fortmann, "Validation of DFIG model using 1.5 MW turbine for the analysis of its behavior during voltage drops in the 110 kV grid," in *Proc. Int. Work. Large-Scale Integration Wind Power Transmission Networks Offshore Wind Farms*, Billund, Denmark, Oct. 2003.

[29] GE Wind Energy. (2005, Jan.) 3.6s offshore wind turbine. Brochure. [Online]. Available: http://www.gepower.com/prod_serv/products/wind_turbines/en/downloads/ge_36_brochure.pdf

[30] ——. (2005, Jan.) Low voltage ride-thru technology. Brochure. [Online]. Available: http://www.gepower.com/businesses/ge_wind_energy/en/downloads/ge_lvrt_brochure.pdf

[31] T. Glad and L. Ljung, *Reglerteori: flervariabla och olinjära metoder*. Lund, Sweden: Studentlitteratur, 1997, (in Swedish).

[32] A. Grauers and S. Landström, "The rectifiers influence on the size of direct-driven generators," in *Proc. of European Wind Energy Conference and Exhibition (EWEC´99)*, Nice, France, Mar., 1–5, 1999.

[33] A. Grauers, "Synchronous generator and frequency converter in wind turbine applications: system design and efficiency," Chalmers University of Technology, Göteborg, Sweden, Licentiate Thesis 175L, May 1994. [Online]. Available: http://www.elteknik.chalmers.se/Publikationer/EMKE.publ/Abstracts/old/Grauers_Lic.pdf

[34] ——, "Design of direct-driven permanent-magnet generators for wind turbines," Ph.D. dissertation, Chalmers University of Technology, Göteborg, Sweden, Nov. 1996. [Online]. Available: http://www.elteknik.chalmers.se/Publikationer/EMKE.publ/Abstracts/old/Grauers_PhD_Thesis.pdf

[35] ——, "Efficiency of three wind energy generator systems," *IEEE Trans. Energy Conversion*, vol. 11, no. 3, pp. 650–657, Sept. 1996.

[36] L. H. Hansen, L. Helle, F. Blaabjerg, E. Ritchie, S. Munk-Nielsen, H. Bindner, P. Sørensen, and B. Bak-Jensen, "Conceptual survey of generators and power electronics for wind turbines," Risø National Laboratory, Roskilde, Denmark, Tech. Rep. Risø-R-1205(EN), ISBN 87-550-2743-8, Dec. 2001.

[37] L. Harnefors and H.-P. Nee, "A general algorithm for speed and position estimation of ac motors," *IEEE Trans. Ind. Electron.*, vol. 47, no. 1, pp. 77–83, Feb. 2000.

[38] L. Harnefors, "On analysis, control and estimation of variable-speed drives," Ph.D. dissertation, Royal Institute of Technology, Stockholm, Sweden, 1997.

[39] ——, *Control of Variable-Speed Drives*. Västerås, Sweden: Department of Electronics, Mälardalen University, 2002.

[40] L. Harnefors and H.-P. Nee, "Model-based current control of ac machines using the internal model control method," *IEEE Trans. Ind. Applicat.*, vol. 34, no. 1, pp. 133–141, Jan./Feb. 1998.

[41] L. Harnefors, K. Pietiläinen, and L. Gertmar, "Torque-maximizing field-weakening control: design, analysis, and parameter selection," *IEEE Trans. Ind. Electron.*, vol. 48, no. 1, pp. 161–168, Feb. 2001.

[42] S. Hartge and V. Diedrichs, "Ride-through capability of ENERCON-wind turbines," in *Proc. Int. Work. Large-Scale Integration Wind Power Transmission Networks Offshore Wind Farms*, Billund, Denmark, Oct. 2003.

[43] M. Heller and W. Schumacher, "Stability analysis of doubly-fed induction machines in stator flux reference frame," in *Proc. of 7th European Conference on Power Electronics and Applications*, vol. 2, Brussels, Belgium, Sept., 8–10, 1997, pp. 707–710.

[44] K. Hentabli, M. E. H. Benbouzid, and D. Pinchon, "CGPC with internal model structure: Application to induction motor control," in *Proc. of the 1997 IEEE International Conference on Control Applications*, Hartford, CT, USA, Oct., 5–7, 1997, pp. 235–237.

[45] N. G. Hingorani and L. Gyugyi, *Understanding FACTS: Concepts and Technology of Flexible AC Transmission Systems*. Piscataway, NJ, USA: IEEE Press, 2000.

[46] B. Hopfensperger, D. J. Atkinson, and R. A. Lakin, "Stator-flux-oriented control of a doubly-fed induction machine with and without position encoder," *IEE Proc. Electr. Power Appl.*, vol. 147, pp. 241–250, July 2000.

[47] B. Hopfensperger, D. Atkinson, and R. A. Lakin, "Stator flux oriented control of a cascaded doubly-fed induction machine," *IEE Proc. Electr. Power Appl.*, vol. 146, no. 6, pp. 597–605, Nov. 1999.

[48] B. Hopfensperger and D. Atkinson, "Doubly-fed a.c. machines: classification and comparsion," in *Proc. Power Electronics and Applications (EPE)*, Graz, Austria, Aug., 27–29, 2001.

[49] C.-J. Huang, S.-J. Huang, and F.-S. Pai, "Design of dynamic voltage restorer with disturbance-filtering enhancement," *IEEE Trans. Power Electron.*, vol. 18, no. 5, pp. 1202–1210, Sep. 2003.

[50] N. Hur, J. Jung, and K. Nam, "A fast dynamic dc-link power-balancing scheme for a PWM converter–inverter system," *IEEE Trans. Ind. Electron.*, vol. 48, no. 4, pp. 794–803, Aug. 2001.

[51] *Measurement and assessment of power quality characteristics of grid connected wind turbines (11/2000)*, International Electrotechnical Commission Std. IEC 61 000-21, 2000.

[52] M. G. Ioannides and J. A. Tegopoulos, "Optimal efficiency slip-power recovery drive," *IEEE Trans. Energy Conversion*, vol. 3, no. 2, pp. 342–348, June 1988.

[53] G. L. Johnsson, *Wind Energy Systems*. Englewood Cliffs, N.J., USA.: Prentice-Hall, 1985.

[54] C. R. Kelber and W. Schumacher, "Active damping of flux oscillations in doubly-fed ac machines using dynamic variation of the system's structure," in *Proc. Power Electronics and Applications (EPE)*, Graz, Austria, Aug., 27–29 2001.

[55] C. R. Kelber, "Aktive dämpfung der doppelt-gespeisten Drehstrommaschine," Ph.D. dissertation, Technishen Universität Carolo-Wilhelmina, 2000, (in German).

[56] E. H. Kim, S. B. Oh, Y. H. Kim, and C. H. Kim, "Power control of a doubly fed induction machine without rotational transducers," in *Proc. of 3rd International Conference on Power Electronics and Motion Control*, vol. 2, Beijing, China, Aug., 15–18, 2000, pp. 951–955.

[57] P. Kokotović, H. K. Khalil, and J. O'Reilly, *Singular Perturbation Methods in Control: Analysis and Design*. London: Academic Press, 1986.

[58] Å. Larsson, P. Sørensen, and F. Santjer, "Grid impact of variable speed wind turbines," in *Proc. of European Wind Energy Conference and Exhibition (EWEC'99)*, Nice, France, Mar., 1–5, 1999.

[59] A. Lasson and P. Lundberg, "Trefas självkommuterade strömriktare anslutna till elnätet—En inledande studie," Chalmers University of Technology, Göteborg, Sweden, Tech. Rep., 1990.

[60] P. Ledesma and J. Usaola, "Effect of neglecting stator transients in doubly fed induction generator models," *IEEE Trans. Energy Conversion*, vol. 19, pp. 459–461, June 2004.

[61] W. Leonhard, *Control of Electrical Drives*, 2nd ed. Berlin, Germany: Springer-Verlag, 1996.

[62] M. Lindgren, "Modeling and control of voltage source converters connected to the grid," Ph.D. dissertation, Chalmers University of Technology, Göteborg, Sweden, Nov. 1998. [Online]. Available: http://www.elteknik.chalmers.se/Publikationer/EMKE.publ/Abstracts/old/Lindgren_PhD_Thesis.pdf

[63] B. Li, S. Choi, and D. Vilathgamuwa, "Transformerless dynamic voltage restorer," *IEE Proceedings Generation, Transmission and Distribution*, vol. 149, no. 3, pp. 1202–1210, May 2002.

[64] S. Lundberg, T. Petru, and T. Thiringer, "Electrical limiting factors for wind energy installations in weak grids," *International Journal of Renewable Energy Engineering*, vol. 3, no. 2, pp. 305–310, Aug. 2001.

[65] S. Lundberg, "Performance comparison of wind park configurations," Department of Electric Power Enginering, Chalmers University of Technology, Department of Electric Power Enginering, Göteborg, Sweden, Tech. Rep. 30R, Aug. 2003.

[66] *EMTDC Users's Guide*, On-line help, Manitoba HVDC Research Centre Inc., Winnipeg, Manitoba, Canada, 1998.

[67] N. Mohan, T. Undeland, and W. Robbins, *Power Electronics Converter, Applications and Design*. New York, USA: John Wiley & Sons, 1995.

[68] L. Morel, H. Godfroid, A. Mirzaian, and J. Kauffmann, "Double-fed induction machine: converter optimisation and field oriented control without position sensor," *IEE Proc. Electr. Power Appl.*, vol. 145, no. 4, pp. 360–368, July 1998.

[69] P. Mutschler and R. Hoffmann, "Comparison of wind turbines regarding their energy generation," in *Proc. 2002 IEEE 33rd Annual IEEE Power Electronics Specialists Conference*, vol. 1, Cairns, Qld., Australia, June, 23–27, 2002, pp. 6–11.

[70] M. J. Newman and D. G. Holmes, "An integrated approach for the protection of series injection inverters," *IEEE Trans. Ind. Applicat.*, vol. 38, no. 3, pp. 679–687, May/June 2002.

[71] J. G. Nielsen, M. Newman, H. Nielsen, and F. Blaabjerg, "Control and testing of a dynamic voltage restorer (DVR) at medium voltage level," *IEEE Trans. Power Electron.*, vol. 19, no. 3, pp. 806–813, May 2004.

[72] J. Niiranen, "Voltage dip ride through of doubly-fed generator equipped with active crowbar," in *Proc. Nordic Wind Power Conference (NWPC)*, Göteborg, Sweden, Mar., 1–2 2004.

[73] Nordex. (2005, Jan.) N80/2500 kW N90/2300 kW. Brochure. [Online]. Available: http://www.nordex-online.com/_e/online_service/download/_dateien/PB_N80_GB.pdf

[74] R. Ottersten, A. Petersson, and K. Pietiläinen, "Voltage sag response of PWM rectifiers for variable-speed wind turbines," in *Proc. IEEE Nordic Workshop on Power and Industrial Electronics (NORpie'2004)*, Trondheim, Norway, June, 14–16 2004.

[75] R. Ottersten, "Vector control of a double-sided PWM converter and induction machine drive," Chalmers University of Technology, Göteborg, Sweden, Licentiate Thesis 368L, Dec. 2000. [Online]. Available: http://www.elteknik.chalmers.se/Publikationer/EMKE.publ/Abstracts/old/otterstenLic/ottersten_lic_thesis.pdf

[76] ——, "On control of back-to-back converters and sensorless induction machine drives," Ph.D. dissertation, Chalmers University of Technology, Göteborg, Sweden, June 2003. [Online]. Available: http://www.elteknik.chalmers.se/Publikationer/EMKE.publ/Abstracts/2003/RolfPhD.pdf

[77] M. P. Papadopoulos, S. A. Papathanassiou, N. G. Boulaxis, and S. T. Tentzerakis, "Voltage quality change by grid-connected wind turbines," in *European Wind Energy Conference*, Nice, France, 1999, pp. 783–785.

[78] R. Pena, R. Cardenas, G. Asher, J. Clare, J. Rodriguez, and P. Cortes, "Vector control of a diesel-driven doubly fed induction machine for a stand-alone variable speed energy system," in *IEEE Annual Conference of the Industrial Electronics Society*, vol. 2, Nov., 5–8, 2002, pp. 985–990.

[79] R. Pena, R. Cardenas, R. Blasco, G. Asher, and J. Clare, "A cage induction generator using back to back PWM converters for variable speed grid connected wind energy system," in *Proc. IEEE IECON'01*, vol. 2, Denver, CO, Nov. 2001, pp. 1376–1381.

[80] R. Pena, J. C. Clare, and G. M. Asher, "Doubly fed induction generator using back-to-back PWM converters and its application to variable-speed wind-energy generation," *IEE Proc. Electr. Power Appl.*, vol. 143, pp. 231–241, May 1996.

[81] A. Petersson, "Analysis, modeling and control of doubly-fed induction generators for wind turbines," Chalmers University of Technology, Göteborg, Sweden, Licentiate Thesis 464L, Feb. 2003. [Online]. Available: http://www.elteknik.chalmers.se/Publikationer/EMKE.publ/Abstracts/2003/AndreasLic.pdf

[82] T. Petru and T. Thiringer, "Active flicker reduction from a sea-based 2.5 MW wind park connected to a weak grid," in *Proc. Nordic Workshop on Power and Industrial Electronics*, Aalborg, Denmark, June, 13–16, 2002.

[83] ——, "Modeling of wind turbines for power system studies," *IEEE Trans. Power Syst.*, vol. 17, pp. 1132–1139, Nov. 2002.

[84] M. A. Pöller, "Doubly-fed induction machine models for stability assessment of wind farms," in *Proc. IEEE Bologna Power Tech*, Bologna, Italy, June, 23–26 2003.

[85] *PSS/E-Introduction to Dynamic Simulation*, Manual, Power Technologies, Inc., Schenectady, NY, U.S.A., 2001.

[86] B. Rabelo and W. Hofmann, "Optimal active and reactive power control with the doubly-fed induction generator in the MW-class wind-turbines," in *Proc. International Conference on Power Electronics and Drives Systems*, vol. 1, Denpasar, Indonesia, Oct., 22–25, 2001, pp. 53–58.

[87] R. Richter, *Electrische Machinen*, 2nd ed. Basel/Stuttgart: Verlag Birkhäuser, 1954, (in German).

[88] B. Schmidtbauer, *Analog och digital reglerteknik*, 2nd ed. Lund, Sweden: Studentlitteratur, 1995, (in Swedish).

[89] Semikron. (2004, Dec.) SKiiP 1203GB172-2DW. Data sheet. [Online]. Available: http://www.semikron.com/internet/ds.jsp?file=1266.html

[90] ——. (2004, Dec.) SKiiP 1803GB172-3DW. Data sheet. [Online]. Available: http://www.semikron.com/internet/ds.jsp?file=1264.html

[91] ——. (2004, Dec.) SKiiP 2403GB172-4DW. Data sheet. [Online]. Available: http://www.semikron.com/internet/ds.jsp?file=1261.html

[92] ——. (2004, Dec.) SKiiP 513GD172-3DUL. Data sheet. [Online]. Available: http://www.semikron.com/internet/ds.jsp?file=1268.html

[93] ——. (2004, Dec.) Thyristor SKT 2400. Data sheet. [Online]. Available: http://www.semikron.com/internet/ds.jsp?file=516.html

[94] G. R. Slemon, "Modelling of induction machines for electric drives," *IEEE Trans. Ind. Applicat.*, vol. 25, no. 6, pp. 1126–1131, Nov./Dec. 1989.

[95] J.-J. E. Slotline and W. Li, *Applied Nonlinear Control*. Upper Saddle River, New Jersey, USA: Prentice Hall, 1991.

[96] Svenska Kraftnät, "Affärsverket svenska kraftnäts föreskrifter om driftsäkerhetsteknisk utformning av produktionsanläggningar," Svenska Kraftnät, Vällingby, Sweden, Tech. Rep., 2004, Draft version. [Online]. Available: http://www.svk.se/upload/3645/Foreskriftprod_remiss.pdf

[97] Swedish Energy Agency, "Climate report 2001," Swedish Energy Agency, Tech. Rep. ER 6:2002, 2002. [Online]. Available: http://www.stem.se/web/biblshop.nsf/FilAtkomst/ER62002.pdf/$FILE/ER62002.pdf?OpenElement

[98] ——, "The energy market 2004," Swedish Energy Agency, Tech. Rep. ET 29:2004, 2004. [Online]. Available: http://www.stem.se/web/biblshop.nsf/FilAtkomst/ER62002.pdf/$FILE/ER62002.pdf?OpenElement

[99] Y. Tang and L. Xu, "Flexible active and reactive power control strategy for a variable speed constant frequency generating system," *IEEE Trans. Power Electron.*, vol. 10, no. 4, pp. 472–478, July 1995.

[100] T. Thiringer and J. Linders, "Control by variable rotor speed of a fixed-pitch wind turbine operating in a wide speed range," *IEEE Trans. Energy Conversion*, vol. 8, no. 3, pp. 520–526, Sept. 1993.

[101] T. Thiringer and J. Luomi, "Comparison of reduced-order dynamic models of induction machines," *IEEE Trans. Power Syst.*, vol. 16, no. 1, pp. 119–126, Feb. 2001.

[102] J. L. Thomas and M. Boidin, "An internal model control structure in field oriented controlled vsi induction motors," in *Proc. of the 4th European Conference on Power Electronics and Applications*, vol. 2, 1991, pp. 202–207.

[103] K. Thorborg, *Power Electronics – in Theory and Practice*. Lund, Sweden: Studentlitteratur, 1997.

[104] Vestas. (2004, May) V52-850 kW. Brochure. [Online]. Available: http://www.vestas.com/produkter/pdf/updates_020304/V52_UK.pdf

[105] ——. (2005, Jan.) V120-4.5 MW Offshore leadership. Brochure. [Online]. Available: http://www.vestas.com/pdf/produkter/AktuelleBrochurer/v120/V120%20UK.pdf

[106] A. K. Wallace, R. Spee, and G. C. Alexander, "The brushless doubly-fed machine: its advantages, applications and design methods," in *Sixth International Conference on Electrical Machines and Drives)*, Oxford, UK, Sept., 8–10, 1993, pp. 511–517.

[107] S. Wang and Y. Ding, "Stability analysis of field oriented doubly-fed induction machine drive based on computer simulation," *Electric Machines and Power Systems*, vol. 21, no. 1, pp. 11–24, 1993.

[108] S. Williamson, A. C. Ferreira, and A. K. Wallace, “Generalised theory of the brushless doubly-fed machine. part 1: Analysis,” *IEE Proc. Electr. Power Appl.*, vol. 144, no. 2, pp. 111–122, Mar. 1997.

[109] L. Xu, F. Liang, and T. A. Lipo, “Transient model of a doubly excited reluctance motor,” *IEEE Trans. Energy Conversion*, vol. 6, no. 1, pp. 126–133, Mar. 1991.

[110] L. Xu and C. Wei, “Torque and reactive power control of a doubly fed induction machine by position sensorless scheme,” *IEEE Trans. Ind. Applicat.*, vol. 31, no. 3, pp. 636–642, May/June 1995.

[111] D. Zhou and R. Spee, “Field oriented control development for brushless doubly-fed machines,” in *Proc. IEEE Industry Applications Conference*, vol. 1, Oct., 6–10, 1996, pp. 304–310.

[112] D. S. Zinger and E. Muljadi, “Annualized wind energy improvement using variable speeds,” *IEEE Trans. Ind. Applicat.*, vol. 33, no. 6, pp. 1444–1447, Nov./Dec. 1997.

Appendix A

Nomenclature

Symbols

A_r	swept area
C	capacitor
C_p	power coefficient
$\mathbf{E}$	back EMF
E_g, $\mathbf{E}_g$	grid-voltage modulus and space vector
F	controller
$f(w)$	probability density function
G	transfer function
g_r	gearbox ratio
$\mathbf{I}$	steady-state complex-valued current
i, $\mathbf{i}$	current modulus and space vector
J	inertia
j	$\sqrt{-1}$
k_E, k_R	coefficients in the rotor current control law
k_p, k_i	proportional and integral gain
L	inductance
$\mathcal{L}$	Laplace transform
$\mathcal{L}^{-1}$	inverse Laplace transform
n_p	number of pole pairs
n_s/n_r	stator-to-rotor turns ratio
P	active power
p	d/dt
Q	reactive power
R	resistance
S	apparent power
s	slip
T_e, T_s	electromechanical and shaft torque
T_{sample}	sample time
$\mathbf{V}$	steady-state complex-valued voltage
V	remaining voltage
v, $\mathbf{v}$	voltage modulus and space vector

α	closed loop bandwidth
β	pitch angle
λ	tip-speed ratio
ρ	density of air or bandwidth of PLL
Ψ	flux space vector or steady-state complex-valued flux
ψ	flux modulus
ω_1, θ_1	synchronous frequency and angle
ω_2	slip frequency
ω_g, θ_g	grid frequency and angle
ω_r	(electrical) rotor speed of generator
$\tilde{}$	error
$\hat{}$	estimated

Superscripts

avg	average
max	maximum
min	minimum
s	stator-oriented reference frame
pk	peak
ref	reference

Subscripts

cl	closed loop
co	cut off
d	real part of synchronous-frame space vector
f	(grid-) filter or flux
g	grid
GB	gearbox
m	mutual
M	mutual (Γ representation)
mech	mechanical
n	negative sequence
nom	nominal
R	rotor (Γ representation)
r	rotor
s	stator
sw	switch
t	turbine
q	imaginary part of synchronous-frame space vector
p	positive sequence
λ	leakage
σ	leakage (Γ-representation)

Abbreviations

DFIG	doubly-fed induction generator
EMF	electromotive force
FSIG	fixed-speed wind turbine with an induction generator
G	generator
GSC	grid-side converter
IG	induction generator
IGBT	insulated gate bipolar transistor
IMC	internal model control
LLF	line-to-line fault
MSC	machine-side converter
PLL	phase-locked loop
PMSG	permanent-magnet synchronous generator
p.u.	per unit
PWM	pulse width modulation
RMS	root mean square
SG	synchronous generator
SLGF	single-line-to-ground fault
TLGF	two-lines-to-ground fault
VSIG	variable-speed wind turbine with an induction generator and a full-power converter
WT	wind turbine

Appendix B

Data and Experimental Setup

B.1 Data of the DFIG

These data and parameters of the DFIG are used throughout the thesis if not otherwise stated. In Table B.1, Table B.2, and in Table B.3 the nominal values, base values, and the parameters of the DFIG are shown respectively.

TABLE B.1. NOMINAL VALUES OF THE DFIG.

Rated voltage (Y)	$V_{n,p-p}$	690 V
Rated current	I_n	1900 A
Rated frequency	f_n	50 Hz
Rated power	P_n	2 MW
Number of pole pairs	n_p	2

TABLE B.2. BASE VALUES.

Base voltage (phase-neutral)	V_b	400 V
Base current	I_b	1900 A
Base frequency	ω_b	$2\pi \cdot 50$ Hz
Base impedance	$Z_b = V_b/I_b$	0.21 Ω

TABLE B.3. PARAMETERS OF THE INDUCTION MACHINE.

Stator resistance	R_s	0.0022 Ω	⇔	0.01 p.u.
Rotor resistance	R_r	0.0018 Ω	⇔	0.009 p.u.
Rotor resistance (Γ equivalent)	R_R	0.0019 Ω	⇔	0.0093 p.u.
Stator leakage inductance	$L_{s\lambda}$	0.12 mH	⇔	0.18 p.u.
Rotor leakage inductance	$L_{r\lambda}$	0.05 mH	⇔	0.07 p.u.
Leakage inductance (Γ equivalent)	L_σ	0.18 mH	⇔	0.27 p.u.
Magnetizing resistance	R_m	42 Ω	⇔	198 p.u.
Magnetizing inductance	L_m	2.9 mH	⇔	4.4 p.u.
Magnetizing inductance (Γ equivalent)	L_M	3.1 mH	⇔	4.6 p.u.

A dc-link capacitor of $C_{\mathrm{dc}} = 53$ mH $= 3.5$ p.u. is used.

B.2 Laboratory Setup

The laboratory setup consists of one slip-ringed wound rotor induction machine, one voltage source converter, two measurement boxes, one digital signal processing (DSP) system and one measurement computer. Data of the induction machine is given in Section B.2.1. Fig. B.1 shows a principle sketch of the laboratory setup. In the measurement boxes voltages and

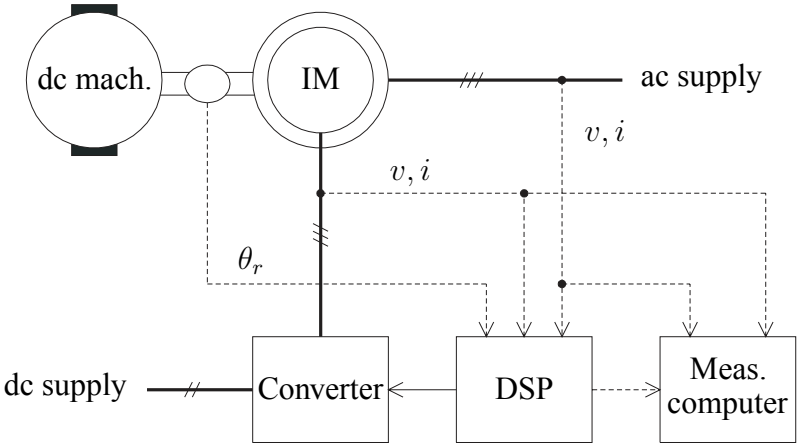

Fig. B.1. Laboratory setup. Thick lines indicates cables with power while dashed lines implies measurements signals.

currents are measured. One measurement box is attached to the stator circuit while the other measure the rotor circuit. There is also a resolver that measure the rotor position, θ_r, of the induction machine. When running the machine as doubly-fed the stator circuit is directly connected to the grid (during the experiments in this thesis the stator circuit was connected to a 230-V, 50-Hz source, note that the nominal voltage of the induction machine is 380 V). Normally, the converter operates as a back-to-back converter, but during the experiments the converter was directly fed by a dc source of 450 V dc. Although the converter here is fed directly from a dc source, it is possible to run it as a back-to-back converter. The loading dc machine is fed through a thyristor inverter and could be both speed or torque controlled.

The control laws were all written in the C-language and downloaded to the DSP-unit (Texas TMS320c30). The DSP-unit has 16 analog input channels, for measurement signals, and 8 analog output channels, for signals that is desired to be fed to the measurement computer. The voltage references to the converter are modulated digitally and via optic fibers sent to the converter.

The measurement system consists of one filter box and one computer equipped with the LabView software. With this system it is possible to measure up to 16 channels, i.e., from the measurements boxes or from the DSP unit.

A more thorough description of the laboratory set up can be found in [75].

B.2.1 Data of the Induction Generator

In Table B.4, Table B.5, and in Table B.6 the nominal values, base values, and the parameters of the laboratory DFIG are shown respectively.

TABLE B.4. NOMINAL VALUES OF THE INDUCTION GENERATOR.

Rated voltage (Y)	$V_{n,p-p}$	380 V
Rated current	I_n	44 A
Rated frequency	f_n	50 Hz
Rated rotor speed	n_n	1440 rpm
Rated power	P_n	22 kW
Rated torque	T_n	145 Nm
Power factor		0.89

TABLE B.5. BASE VALUES.

Base voltage (phase-neutral)	V_b	220 V
Base current	I_b	44 A
Base frequency	ω_b	$2\pi \cdot 50$ Hz
Base impedance	$Z_b = V_b/I_b$	5 Ω

TABLE B.6. PARAMETERS OF THE INDUCTION MACHINE.

Stator resistance	R_s	0.115 Ω	⇔	0.0230 p.u.
Rotor resistance	R_r	0.184 Ω	⇔	0.0369 p.u.
Stator leakage inductance	$L_{s\lambda}$	1.65 mH	⇔	0.104 p.u.
Rotor leakage inductance	$L_{r\lambda}$	1.68 mH	⇔	0.106 p.u.
Magnetizing resistance	R_m	224 Ω	⇔	44.9 p.u.
Magnetizing inductance	L_m	46.6 mH	⇔	2.93 p.u.
Inertia	J	0.334 kgm^2	⇔	178 p.u.

B.3 Jung Data Acquisition Setup

The experiments were made on a VESTAS V-52 850 kW WT, located at the inland (≈ 100 km from the west coast) in the southern part of Sweden. The wind turbine is located in a flat surroundings and is connected to the 10-kV distribution grid via a transformer, which transforms the voltage to the wind-turbine voltage of 690 V. See Fig. B.2 for a picture of the turbine and the data acquisition computer. In Table B.7 some data of VESTAS V-52 850 kW WT is given. The currents and voltages are measured using transformers, which transform

TABLE B.7. DATA OF VESTAS V-52 850 KW WT [104].

Rated voltage (Y)	690 V
Rated power	850 kW
Rotor diameter	52 m
Rotor speed	14.0–31.0 rpm (26 rpm)
Cut-in wind speed	4 m/s
Nominal wind speed	16 m/s
Maximum wind speed	25 m/s

the current to 5 A and the voltage to 110 V. In addition, the stator currents are also measured directly using LEM modules.

Fig. B.2. Jung wind turbine and the data acquisition computer.